

# **Ionospheric Signatures of Ultra Low Frequency Waves**

Thesis submitted for the degree of

Doctor of Philosophy

at the University of Leicester

by

**James David Borderick**

Radio and Space Plasma Physics Group

Department of Physics and Astronomy

University of Leicester

November 2010

© James David Borderick, 11 November 2010

This thesis is copyright material and no quotation from it may be published without proper acknowledgement.

# **Ionospheric Signatures of Ultra Low Frequency Waves**

Thesis submitted for the degree of

Doctor of Philosophy

at the University of Leicester

by

**James David Borderick**

Radio and Space Plasma Physics Group

Department of Physics and Astronomy

University of Leicester

November 2010

© James David Borderick, 11 November 2010

This thesis is copyright material and no quotation from it may be published without proper acknowledgement.

## **To Mum and Dad**

*"Thus the yeoman work in any science, and especially physics, is done by the experimentalist, who must keep the theoreticians honest."*

**Michio Kaku**

# **Abstract**

## **Ionospheric Signatures of Ultra Low Frequency Waves**

**James David Borderick**

Ultra Low Frequency (ULF) waves have been studied for many years and the observation and modelling of such phenomena reveals important information about the solar-terrestrial interaction. Being ubiquitous in the collisionless terrestrial space plasma environment, ULF waves represent important physical processes in the transfer of energy and momentum. This thesis comprises three distinct studies to observe, model and analyse ULF phenomena.

The first two studies focus on ULF wave observations at high-latitudes in the terrestrial ionosphere using a collection of both space- and ground-based instruments. The first study provides a detailed analysis of the time evolution of a ULF wave using the characteristics of the observed ULF wave as input-parameters to a 1-D numerical model. As the wave signature evolves towards a Field Line Resonance (FLR) a change in the incident wave mode from a partially Alfvénic wave to a purely shear Alfvénic wave is observed. The second study presents statistics of 25 large spatial-scale ULF waves with observations from a high-latitude Doppler sounder and ground-based magnetometers, complemented by model results.

The third and final study describes the implementation of a well established radar technique ("double-pulse"), which is new for the Super Dual Auroral Radar Network (SuperDARN), which aims to provide an unprecedented temporal resolution for ULF wave studies. The new pulse sequence increases the temporal resolution of SuperDARN by a factor of three. Preliminary findings suggest this technique yields impressive results for ionospheric scatter with steady phase values but that the method cannot be used for data when the phase is rapidly changing or if the data originates from slowly decorrelating plasma irregularities. The running of two independent pulse sequences on the stereo channels of the Hankasalmi radar has also enabled, for the first time, the observation of cross-contamination between the radar channels.

## Declarations

The research undertaken during the course of this doctoral programme has led to the publication of the following scientific papers in refereed journals:

**Borderick, J. D.**, Yeoman, T. K., Waters, C. L., and Wright, D. M.: Observations and modelling of the wave mode evolution of an impulse-driven 3 mHz ULF wave, *Ann. Geophys.*, 28, 9, 1723-1735, 2010.

## **Acknowledgments**

I wish to thank my supervisor, Professor T. K. Yeoman, for all the guidance and encouragement he has given me while I have been a student at the University of Leicester. I give many thanks to Professor M. Lester who influenced my decision to study for a PhD in the Radio Space Plasma Physics group, and Professor S. W. H. Cowley for making this possible. I also greatly thank my mother and father for all their love and support.

# Contents

<b>1</b>	<b>An Introduction to Solar-Terrestrial Physics</b>	<b>1</b>
1.1	Introduction . . . . .	1
1.2	The Sun . . . . .	2
1.3	The Solar Wind . . . . .	2
1.4	The Terrestrial Bow Shock . . . . .	4
1.5	Solar-Terrestrial Coupling . . . . .	6
1.5.1	The Closed Magnetosphere . . . . .	7
1.5.2	The Open Magnetosphere . . . . .	9
1.6	The Ionosphere . . . . .	12
1.6.1	Ionospheric Currents . . . . .	15
1.6.2	Ionospheric Conductivity . . . . .	17
1.6.3	Twin Cell Convection . . . . .	17
<b>2</b>	<b>Waves in the Magnetosphere: Theory, Previous Observations and Modelling</b>	<b>20</b>
2.1	Introduction . . . . .	20
2.2	Magnetohydrodynamic Wave Theory . . . . .	22
2.2.1	Cold Plasma Waves . . . . .	23
2.2.2	Warm Plasma Waves . . . . .	25
2.3	Ionospheric Boundary Conditions . . . . .	28
2.4	The Ionospheric Reflection Coefficient . . . . .	32
2.5	Field Line Resonances . . . . .	33
2.5.1	The Box Model of the Magnetosphere . . . . .	33
2.5.2	Illustration of Field Line Resonances . . . . .	37
2.6	Ultra Low Frequency Wave Generation Mechanisms . . . . .	39
2.6.1	Internal Mechanisms . . . . .	39
2.6.2	External Mechanisms . . . . .	40
2.7	High-Frequency Radio Wave Sounding of the Ionosphere . . . . .	46
2.7.1	The Altar-Appleton-Hartree Equation . . . . .	46
2.7.2	HF Doppler Ultra Low Frequency Wave Modelling . . . . .	47
2.7.3	HF Doppler Ultra Low Frequency Wave Observations . . . . .	51
2.8	Summary . . . . .	59
<b>3</b>	<b>Instrumentation</b>	<b>62</b>
3.1	Introduction . . . . .	62
3.2	The Super Dual Auroral Radar Network . . . . .	62
3.2.1	Introduction . . . . .	62
3.2.2	Standard Super Dual Auroral Radar Network Operations . . . . .	63
3.2.3	Ionospheric Sounding by Pulsed Radars . . . . .	65

3.2.4	The Standard SuperDARN pulse sequence . . . . .	66
3.2.5	TMS Super Dual Auroral Radar Network Operations . . . . .	71
3.3	The Doppler Pulsation Experiment . . . . .	74
3.4	Ground Magnetic Measurements . . . . .	78
3.4.1	Fluxgate Magnetometers . . . . .	78
3.4.2	The International Monitor for Auroral Geomagnetic Effects . . . . .	80
3.5	The Tromsø Dynasonde . . . . .	82
3.6	The Tromsø Heater . . . . .	83
3.7	The Advanced Composition Explorer . . . . .	85
3.8	The Interplanetary Monitoring Platform -8 . . . . .	85
<b>4</b>	<b>An Introduction to the Numerical Model and Example Results</b>	<b>86</b>
4.1	The 1-D Ultra Low Frequency Wave Numerical Model . . . . .	86
4.1.1	Introduction . . . . .	86
4.1.2	The 1-D Numerical Model - A Mathematical Description . . . . .	88
4.2	The Sutcliffe and Poole Model . . . . .	91
4.2.1	Introduction . . . . .	91
4.2.2	The Magnetic Mechanism ( $V_I$ ) . . . . .	92
4.2.3	The Advection Mechanism ( $V_{II}$ ) . . . . .	93
4.2.4	The Compressional Mechanism ( $V_{III}$ ) . . . . .	93
4.2.5	The 1-D Numerical Model - Running the Model . . . . .	94
4.3	Testing the 1-D Ultra Low Frequency Wave Numerical Model . . . . .	99
4.3.1	Introduction . . . . .	99
4.3.2	The Sutcliffe-Poole Model Results . . . . .	99
4.3.3	The Sutcliffe-Poole Model Results at High-Latitude . . . . .	105
4.3.4	A Sample Event . . . . .	109
4.3.5	Model Dependence on Key Parameters . . . . .	114
4.4	Summary . . . . .	129
<b>5</b>	<b>Observations and Modelling of the Wave Mode Evolution of an Impulse-Driven 3 mHz Ultra Low Frequency Wave</b>	<b>132</b>
5.1	Introduction . . . . .	132
5.2	Observations . . . . .	133
5.2.1	Interplanetary Magnetic Field Analysis . . . . .	133
5.2.2	Ionospheric and Ground Data Observations . . . . .	136
5.2.3	Wave Evolution . . . . .	140
5.3	The Numerical Model . . . . .	143
5.3.1	Observational Inputs . . . . .	143
5.3.2	The Model Output . . . . .	144
5.4	Discussion . . . . .	150
5.4.1	Wave Evolution . . . . .	151
5.4.2	The Advection Mechanism . . . . .	152
5.5	Summary . . . . .	153
<b>6</b>	<b>Observations and Modelling of High-Latitude HF Doppler Measurements of Large-Scale Ultra Low Frequency Waves</b>	<b>155</b>
6.1	Introduction . . . . .	155
6.2	Basic Event Statistics . . . . .	156

6.3	Doppler Shift Amplitude Dependence on Mechanisms . . . . .	158
6.4	Normalised Doppler Amplitude . . . . .	162
6.4.1	Normalised Model Doppler Shift . . . . .	162
6.4.2	Normalised Observed Doppler Shift . . . . .	167
6.4.3	Conductivity Effects on Doppler Shift . . . . .	169
6.5	Doppler Shift Phase . . . . .	170
6.6	Analysis of Incident Wave Mode . . . . .	173
6.7	Discussion and Summary . . . . .	177
<b>7</b>	<b>Double-Pulse Operations with the Super Dual Auroral Radar Network</b>	<b>181</b>
7.1	A Case for a Greater Super Dual Auroral Radar Network Temporal Res- olution . . . . .	181
7.2	Emulation of Double-Pulse Operations . . . . .	182
7.2.1	Emulated Ionospheric Scatter Results . . . . .	182
7.2.2	Emulated Ground Scatter Results . . . . .	187
7.2.3	Lag Zero Power as a Data Quality Discriminator . . . . .	189
7.3	Implementing a Double-Pulse Radar Mode on the Super Dual Auroral Radar Network . . . . .	192
7.3.1	Enhanced Temporal Resolution with TMS . . . . .	192
7.3.2	The Reproduction of Standard Radar Mode Data . . . . .	195
7.3.3	Increasing Temporal Resolution using TMS . . . . .	197
7.3.4	Double-Pulse Lag Zero Power . . . . .	200
7.3.5	Cross-Contamination between Channels A and B . . . . .	204
7.3.6	Double-Pulse Velocity Analysis . . . . .	207
7.4	Summary . . . . .	209
<b>8</b>	<b>Summary and Further Work</b>	<b>211</b>
8.1	Introduction . . . . .	211
8.2	Summary I- Large Spatial-Scale ULF Waves . . . . .	211
8.3	Future Work I- Large Spatial-Scale ULF Waves . . . . .	213
8.4	Summary II- Double-Pulse Operations . . . . .	214
8.5	Future Work II- Double-Pulse Operations . . . . .	214
	<b>Bibliography</b>	<b>215</b>

# Chapter 1

## An Introduction to Solar-Terrestrial Physics

### 1.1 Introduction

This thesis examines the behaviour of high-latitude Ultra Low Frequency (ULF) magnetohydrodynamic (MHD) waves within the terrestrial magnetosphere and ionosphere. ULF waves are so called because their common frequency range is lower than the natural frequency of the propagation medium, plasma. ULF waves are of interest, since they transport energy, contained originally within the solar wind, into the terrestrial magnetosphere. The coupling of ULF waves to terrestrial "closed" magnetic field lines, that are fixed at each end to conjugate ionospheres on the Earth, causes the terrestrial field lines to resonate akin to a stretched string held fixed at both ends.

The aurorae colourfully demonstrate how the Sun affects our planet and have been a subject of fascination throughout history. In the northern-hemisphere the aurora is known as the aurora borealis. The Roman goddess of dawn was known as "Aurora" and the Greek translation of "Boreas" is "north-wind." Throughout the ages, mankind has attempted an understanding of these phenomena without success. It was not until 1733 that Anders Celsius suggested that there was a connection between the aurorae and the terrestrial magnetic field. His findings were reported in a collection of 316 observations of the aurora borealis.

It was to be a further 128 years until a set of revolutionary equations were published that would unite the fields of electricity and magnetism (Maxwell, 1861). The combination of Newton's laws of motion (Newton, 1686) and the Maxwell equations, therefore, were known to Physicists for more than 50 years before it was found that electromagnetic (EM) waves may propagate in a conducting fluid. The MHD wave solutions were eventually derived and form the foundation of ULF wave research (Alfvén, 1942).

## 1.2 The Sun

The Sun provides energy, heat, and light for our planet and has allowed the vast abundance, and variation, of life to exist that is seen today. The star itself is a "typical" yellow dwarf and is located approximately  $1.5 \times 10^8$  km (1 AU (Astronomical Unit)) away such that light takes just under 500 s to reach Earth from the solar surface. Not surprisingly, the Sun accounts for 99.86% of the mass of the Solar System. The Sun was formed approximately 4.57 billion years ago due to the collapse of a hydrogen molecular cloud, and is now over halfway through its main sequence. Figure 1.1 presents a schematic of the solar interior with the salient features labelled. At the current rate of nuclear fusion, within approximately 5 billion years, the Sun will become a red giant. Before this happens, physicists have plenty of time to investigate the solar-terrestrial interaction and study the powerful effect that the nearest star has on our planet.

## 1.3 The Solar Wind

The Sun not only outputs heat and light in the form of electromagnetic radiation but constantly streams out plasma in the form of the solar wind. The solar wind plasma is composed of protons and alpha particles, together with approximately equal numbers of electrons such that the solar wind is overall electrically neutral. The solar wind outflow carries the Sun's magnetic field with it and, therefore, the solar magnetic field is said to be fixed or "frozen-in" to the solar wind plasma. The embedded magnetic field is called

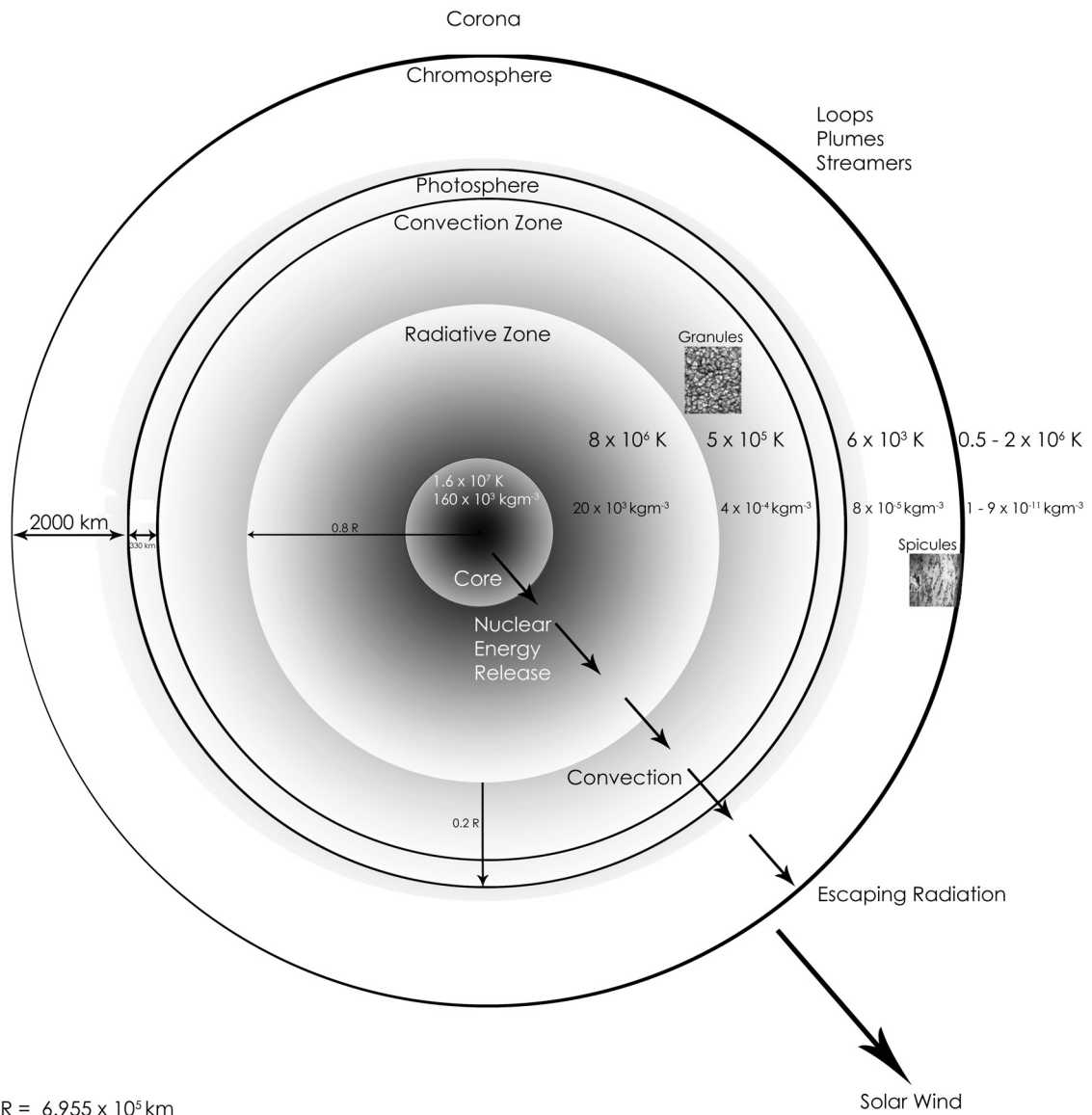


Figure 1.1: A schematic of the solar interior. Nuclear fusion reactions consume hydrogen to form helium within the solar core. The energy released from fusion is eventually emitted from the solar surface as electromagnetic radiation. Energy transport immediately outwards from the core takes place via radiation. This zone is therefore called the radiative zone. Convective fluid motion occurs in the convective zone as the fluid heats then cools. The photosphere is the visible surface of the Sun as seen from Earth. Beyond the photosphere lies the corona and is located within the outer solar atmosphere. The corona is visible during total eclipses of the Sun. A variety of features exist within the corona such as loops, plumes and streamers.

the Interplanetary Magnetic Field (IMF). The solar wind outflow is purely radial. The foot of each field line is fixed to the solar surface, which is rotating with a period of roughly 27 days. The rotational period is, in fact, faster at the equator and decreases with latitude. Since the surface is rotating, a spiral pattern is produced: the plasma element at the Sun's surface begins to flow radially outwards at the solar wind speed. At a later time, the magnetic field line is still linked to the plasma and the same location on the solar surface. Figure 1.2 presents the Archimedean spiral pattern that is produced. This pattern is called the Parker Spiral (Parker, 1958). The large spiral structure, dubbed the ballerina's skirt, creates the heliospheric current sheet, which is the largest known structure within the solar system. Figure 1.3 illustrates the spiral-like nature of the current sheet. The solar magnetic dipole axis,  $M$ , in relation to the solar rotation axis,  $\Omega$ , is highlighted in the figure.

## 1.4 The Terrestrial Bow Shock

The solar wind flow speed exceeds the Alfvén, sound and magnetosonic speeds. Solar wind deflection around any bodies encountered takes place either by Lorentz forces or by collisions. Electromagnetic forces control these flows. Such a deflection must be accompanied by an MHD shock wave. A shock is important because it modifies the properties of the solar wind flow before the flow interacts with a solar system body, such as the Earth. Across the shock the flow is slowed, compressed, and heated, forming a layer of turbulent plasma outside the magnetopause called the magnetosheath. Qualitatively, the bow shock is a non-linearly steepened bow wave. The propagation speed of many wave modes depends on the wave amplitude. The wave amplitudes can increase their gradients non-linearly and form shocks. The position and shape of the bow shock, as well as the nature of the shock transition, depend on the ram pressure, the solar wind Alfvén mach number, and the angle between the upstream flow velocity and the magnetic field (Spreiter et al., 1966). Figure 1.5 highlights the position of the bow shock, which is situated upstream of Earth on the dayside. Unlike conventional shocks found in fluid

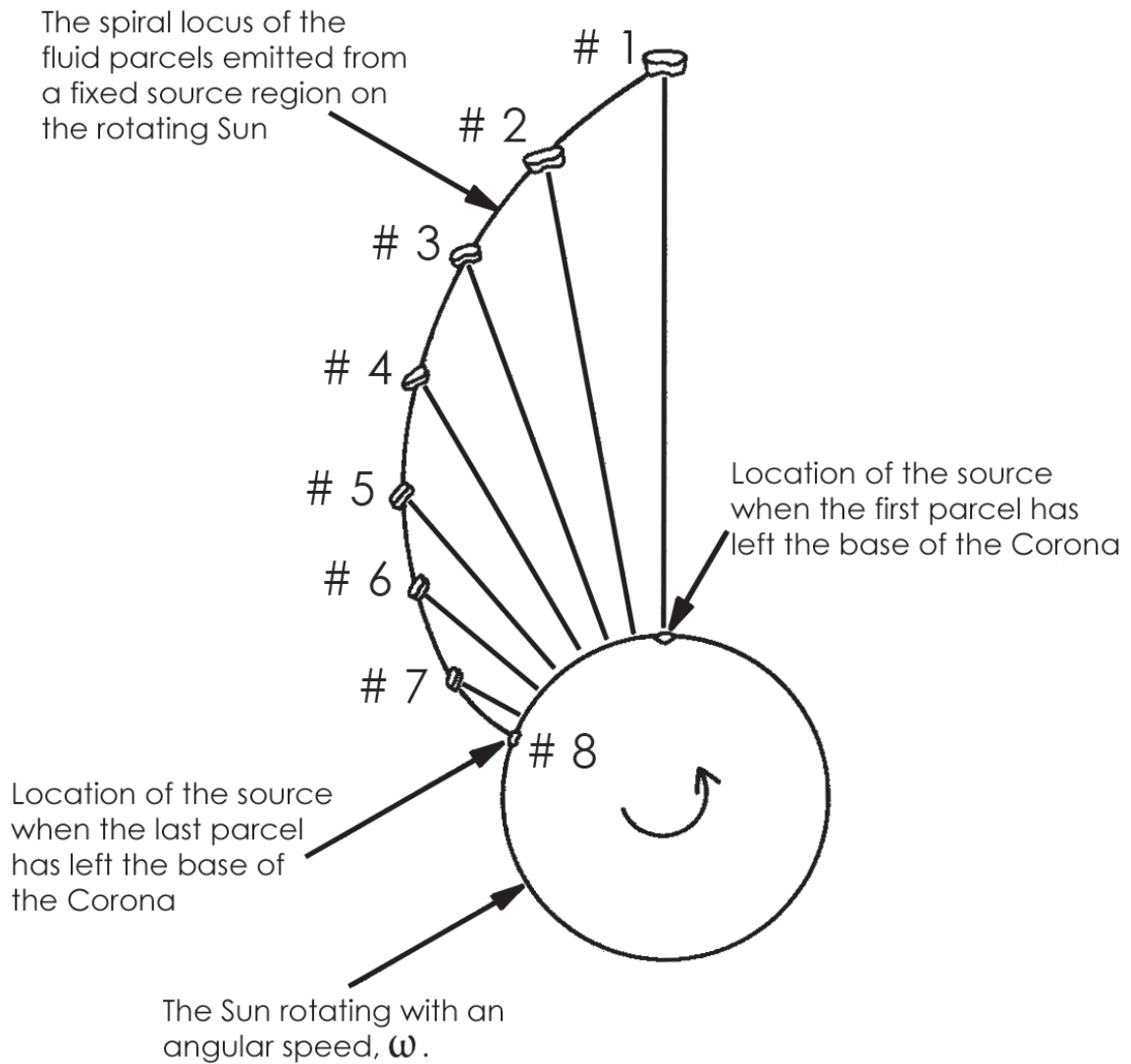


Figure 1.2: A succession of fluid parcels are emitted at constant speed from a source region, which is fixed on the rotating solar surface (Kivelson and Russell, 1997).

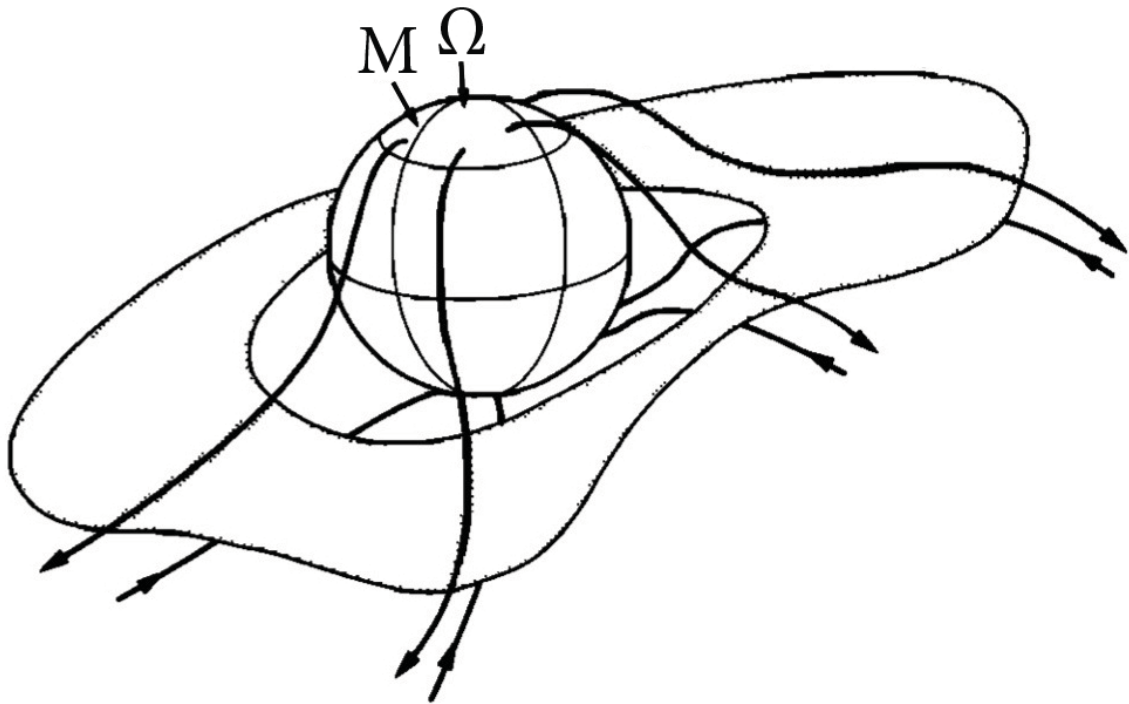


Figure 1.3: The solar sector structure and the ballerina's skirt. The solar rotation is given by  $\Omega$  and the solar magnetic dipole, in relation to this rotation, is given by  $M$  (Smith et al., 1978).

dynamics, the bow shock is a collisionless shock. Most space plasmas are collisionless. This means that the plasma is so rarefied that coulomb collisions between the particles happen so rarely that collisional effects are not significant. Collisions are of importance in the lower solar and planetary atmospheres where the plasma and neutral gas densities are high. However, in the solar wind and in the planetary magnetospheres, the mean free path is of order of 1 AU for protons, and so collisions may be discounted.

## 1.5 Solar-Terrestrial Coupling

Solar-terrestrial relations involves the coupling of two principal components. These are the terrestrial magnetic field and the IMF. The terrestrial magnetic field is generated by currents flowing in the core of the Earth. Outside the Earth, the magnetic field is roughly dipolar and is tilted to the axis of rotation by about  $11^\circ$ . The solar wind plasma confines the terrestrial magnetic field into the protective "bubble" known as the magnetosphere.

The geometry of the magnetosphere clearly affects the level of protection from the solar wind. A three-dimensional illustration of the terrestrial magnetosphere depicting its currents, plasma regions and fields is presented in Figure 1.4. There are two basic models to help explain the solar-terrestrial interaction, which are known as the closed and open magnetospheres.

### 1.5.1 The Closed Magnetosphere

The concept of the magnetosphere was first developed by Sydney Chapman and his student, at the time, Vincenzo Ferraro (Chapman and Ferraro, 1931). Chapman suggested that the plasma and magnetic field behave essentially as if they are "frozen" together. Thus, the magnetic fields are transported by flowing plasmas. Even though the IMF has a weak magnetic field strength of roughly 5 nT close to the Earth, this field still plays a critical role in solar-terrestrial relations. To a first approximation, the "frozen-in" condition implies that the entire magnetospheric cavity is "closed." Therefore, the plasma populations contained within the terrestrial ionosphere and solar wind do not mix, but instead form separate regions. The thin boundary separating these plasma populations is known as the magnetopause and according to Chapman carries a current, later to be known as the "Chapman-Ferraro" current. This theory implies that the solar wind confines the terrestrial magnetic field preventing entry of plasma from the solar wind and is shown graphically in panel (a) of Figure 1.5.

The magnetic field has a tension, which resists field line bending, and a pressure, which resists compression. The magnetic pressure force on the plasma is proportional to the square of the field strength. This magnetic pressure force resists the rarefactions and compressions of the field. The size of the magnetospheric cavity is determined by pressure balance at the boundary between the solar wind on one side, and the magnetic pressure of the planetary field on the other. The ram pressure,  $P_{ram}$ , dictates both the shape and position of the magnetopause and may be expressed as

$$P_{ram} = \rho_{SW} V_{SW}^2 \quad (1.1)$$

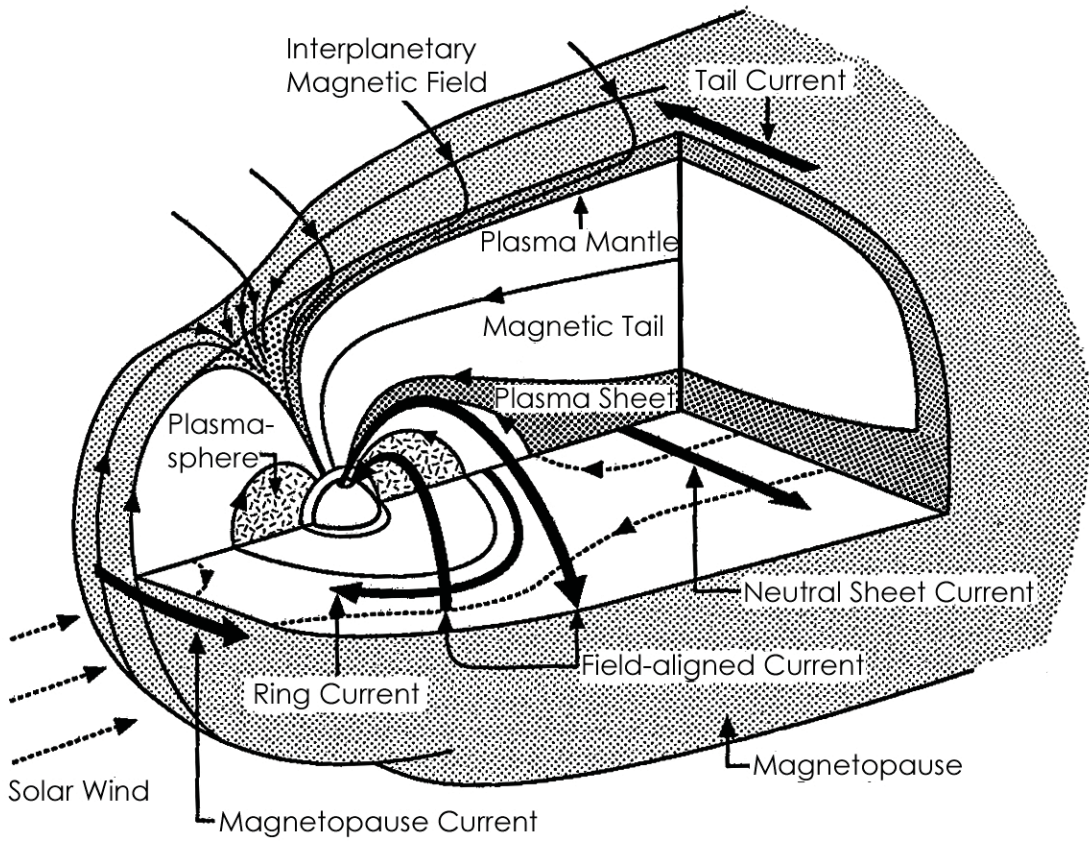


Figure 1.4: A three-dimensional representation of the terrestrial magnetosphere (Kivelson and Russell, 1997).

where  $\rho_{SW}$  is the solar wind mass density (often approximated to just the proton number density since the small electron mass contribution may be neglected) and  $V_{SW}$  is the velocity of the solar wind. If the sum of the gas and magnetic pressures are equal on either side of the magnetopause and the IMF magnetic pressure and the magnetospheric plasma pressure are neglected, the standoff distance,  $R_{mp}$ , for the magnetopause may be written as

$$R_{mp} = R_E \left( \frac{B_{eq}^2}{\mu_0 \rho_{SW} V_{SW}^2} \right)^{\frac{1}{6}}, \quad (1.2)$$

(Kivelson and Russell, 1997) where  $R_E$  is the radius of the Earth,  $B_{eq}$  is the surface magnetic field and  $\mu_0$  is the permeability of free space and has the value  $4\pi \times 10^{-7}$  H m<sup>-1</sup>. Panel (a) of Figure 1.5 also highlights that the nightside magnetosphere extends into

a long "tail." This is known as the magnetotail.

## 1.5.2 The Open Magnetosphere

The processes acting at the magnetopause are the ones finally responsible for determining how much energy the magnetosphere receives from the solar wind. To a first approximation, the magnetosphere contains two magnetically neutral points called "cusps," which are located at approximately  $77^\circ$  magnetic latitude (Wing et al., 2005) where solar wind particles gain direct access to lower altitudes within the magnetosphere and may propagate into the ionosphere. However, a more complete picture of solar-terrestrial coupling was described by the Dungey cycle, which will be outlined shortly. Clearly, the magnetosphere is not a closed system, with no entry points, but is in fact a highly dynamic region of flowing plasma guided by the terrestrial magnetic field, which at times connects to the IMF allowing an entry point for plasma, energy and momentum. The mathematics of "frozen-in" flow will be considered in more detail in the second chapter of this thesis, however the overall results are presented here for convenience. The induction equation may be expressed as

$$\frac{\partial \mathbf{B}}{\partial t} = \nabla \wedge \mathbf{V} \wedge \mathbf{B} + \frac{\nabla^2 \mathbf{B}}{\mu_0 \sigma} \quad (1.3)$$

where  $\mathbf{B}$  is the magnetic field in Tesla,  $t$  is the time in seconds,  $\mathbf{V}$  is the velocity vector,  $\sigma$  is the conductivity and  $\mu_0$  is the permeability of free space. For a material in motion, with negligible electrical resistance and assuming that the plasma obeys ideal MHD then the second term, the diffusion term, vanishes leaving the "frozen-in" flow equation,

$$\frac{\partial \mathbf{B}}{\partial t} = \nabla \wedge \mathbf{V} \wedge \mathbf{B}. \quad (1.4)$$

If  $\mathbf{V} = 0$  and the plasma has a finite conductivity, then the "frozen-in" condition no longer applies and equation 1.3 becomes,

$$\frac{\partial \mathbf{B}}{\partial t} = \frac{\nabla^2 \mathbf{B}}{\mu_0 \sigma}, \quad (1.5)$$

which is a diffusion equation and mathematically implies that the fields can diffuse relative to the plasma, and any oppositely directed fields moving towards one another will decay. The diffusion equation is essentially how the IMF and the terrestrial field lines connect through the boundary as shown in panel (b) of Figure 1.5, which presents the open magnetosphere with a southward-directed IMF. The process of field lines from different sources connecting together is called "magnetic reconnection" (Dungey, 1963). The dayside reconnection rate, and hence the transfer of interplanetary magnetic flux into the magnetosphere, is strong when the IMF points south (opposite in direction to the equatorial terrestrial field) and the reconnection site is then near to the subsolar point. A magnetic tension force is exerted on the plasma when the field lines become bent after reconnection. This force causes the plasma to be accelerated away from the reconnection region. Panel (b) of Figure 1.5 also shows the magnetosheath where open magnetic field lines are dragged antisunward by the plasma flow. After some time, the open magnetic field lines reconnect again on the nightside in the magnetotail. These newly reconnected field lines then contract back sunward towards and beyond the Earth on the dayside where this cycle may begin again. This cycle is referred to as the Dungey cycle. The Dungey cycle occurs in the outer regions of the magnetosphere, but, close to the Earth, between  $4 R_E$  (Earth radii) -  $6 R_E$ , the cold dense plasma population that permeates the region known as the plasmasphere dominates. The sharp terminating boundary of the plasmasphere is known as the plasmopause. Also trapped on closed field lines are the energetic particles associated with the Van Allen particles, which reside in the famous Van Allen belts. These Van Allen particles are some of the most energetic in the magnetosphere and can even affect ionisation in the upper terrestrial atmosphere. Beyond  $6 R_E$ , the magnetospheric plasma density decreases due to the ionospheric plasma being lost during each succession of the Dungey cycle. However, the magnetospheric cavity also consists of hot tenuous plasma, which is accelerated sunward on the nightside along the newly closed magnetic field lines. The acceleration of plasma is caused by the second reconnection point in the magnetotail.

If the IMF is directed northward, equatorial reconnection is no longer possible on the

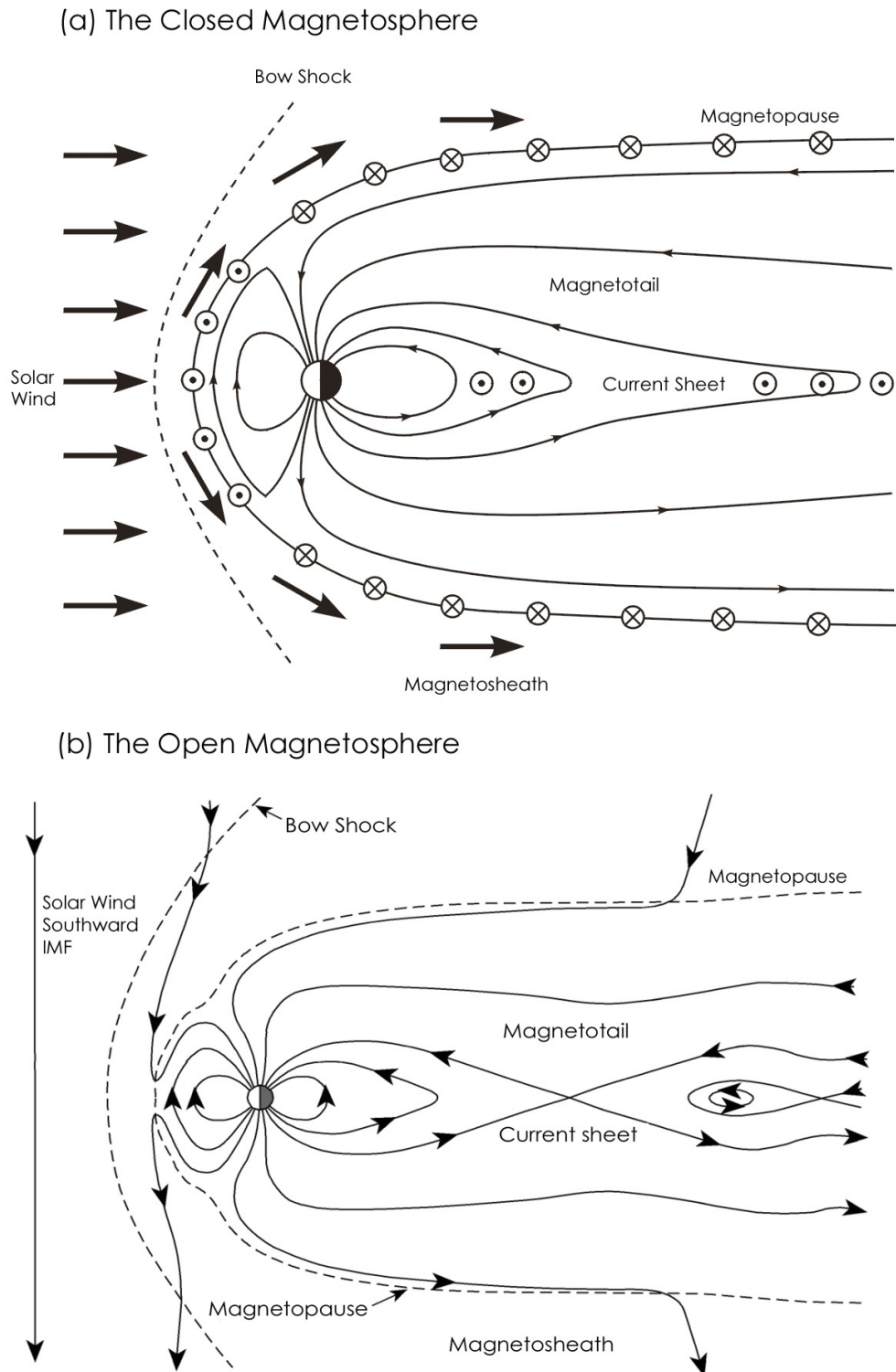


Figure 1.5: **(a and b)** Schematics of the closed and open magnetosphere. Panel (a) shows the closed magnetosphere and highlights the fundamental regions (Hughes, 1995). Panel (b) shows the open magnetosphere, which allows for the entry of particles, energy and momentum from sources external to the magnetospheric cavity (adapted from Cowley et al., 2003).

dayside and the Dungey cycle cannot take place. However, lobe reconnection may occur instead at high-latitudes (e.g., Sandholt et al., 1996; Imber et al., 2006). The magnetospheric and ionospheric flow strengths, therefore, are governed by variations in the strength and orientation of the IMF.

## 1.6 The Ionosphere

The terrestrial atmosphere comprises atoms and molecules, which vary in abundance with altitude. Ultra-violet rays from the Sun ionise the upper atmosphere, creating the electrically-conducting ionosphere and a source of plasma for the magnetosphere. The ionisation is highly dependent on the amount of solar radiation received from the Sun. A solar dependence implies that there are diurnal, seasonal, and geographical effects associated with the levels of ionisation within the terrestrial ionosphere, as well as a dependence on solar activity. Panel (a) of Figure 1.6 presents the variation of molecular composition with altitude up to 1000 km. The ionosphere stretches from a height of roughly 60 km to over 1000 km. Below approximately 60 km, loss processes dominate, but above 60 km free electrons exist for considerable amounts of time. Panel (b) of Figure 1.6 shows vertical profiles of electron density in the mid-latitude ionosphere. The solid and dashed lines show the profiles for sunspot maximum and minimum, respectively.

The ionosphere is divided into a number of layers. The first layer to be identified, the E layer, was discovered in 1924 by E. V. Appleton. Later he identified a second layer at higher altitude. Logically he used the symbol F for this layer. Furthermore, since, at an even later date, a lower layer was detected below the first identified E-layer, it was also logical to name this region the D-region. Figure 1.6 highlights the D-, E- and F-regions as well as the two peaks in electron density,  $F_1$  and  $F_2$ . The critical frequency of a plasma, the frequency at which electromagnetic waves are reflected, may be related to the electron concentration by the following expression

$$f_{critical} = \left( \frac{n_0 e^2}{4\pi^2 \epsilon_0 m} \right)^{\frac{1}{2}}, \quad (1.6)$$

where  $n_0$  is the electron density concentration,  $e$  is the electron charge, and  $m$  is the electron mass. Since all parameters on the right hand side of equation 1.6 are constants apart from the electron concentration, the equation may be expressed as  $f_{critical} \sim 9n_0^{\frac{1}{2}}$  for rough ionospheric sounding calculations.

The magnetic field causes "double refraction" or birefractivity of the ionospheric medium and the transmitted electromagnetic wave is decomposed into two modes, which are known as the ordinary (O-) and extraordinary (X-) High Frequency (HF) radio wave modes. The mathematical treatment of these modes, and their origin, will be dealt with in the next chapter. The highest frequency at which an O-mode wave may achieve reflection in the F2 region ionosphere is known as FoF2. There is a similar peak frequency, FxF2, for X-mode waves that will not be discussed in detail in this thesis. Equation 1.6 implies that if a radio wave propagating from the ground is incident on the ionosphere, with a frequency less than the critical frequency, it will be reflected. The maximum usable frequency (MUF), therefore, is a frequency that may "just" be reflected. For vertical sounding, the MUF is just given by equation 1.6. However, for oblique sounding with an angle of attack,  $\alpha$ , the MUF becomes

$$f_{MUF} = \left( \frac{n_0 e^2}{4\pi^2 \epsilon_0 m \sin^2 \alpha} \right)^{\frac{1}{2}}. \quad (1.7)$$

The electron density of the F2 region is, therefore, a very important consideration for radio wave sounding of the ionosphere. As already established, the terrestrial geomagnetic field lines at high-latitudes may reconnect to outer magnetospheric field lines. Since this coupling process is driven by the solar wind, the dynamics of the high-latitude ionosphere may vary greatly compared with the ionosphere at mid- to low-latitudes where the inner magnetosphere effectively corotates with the Earth. Other activity at high-latitude, such as the auroral zones and substorms, make this location particularly dynamic.

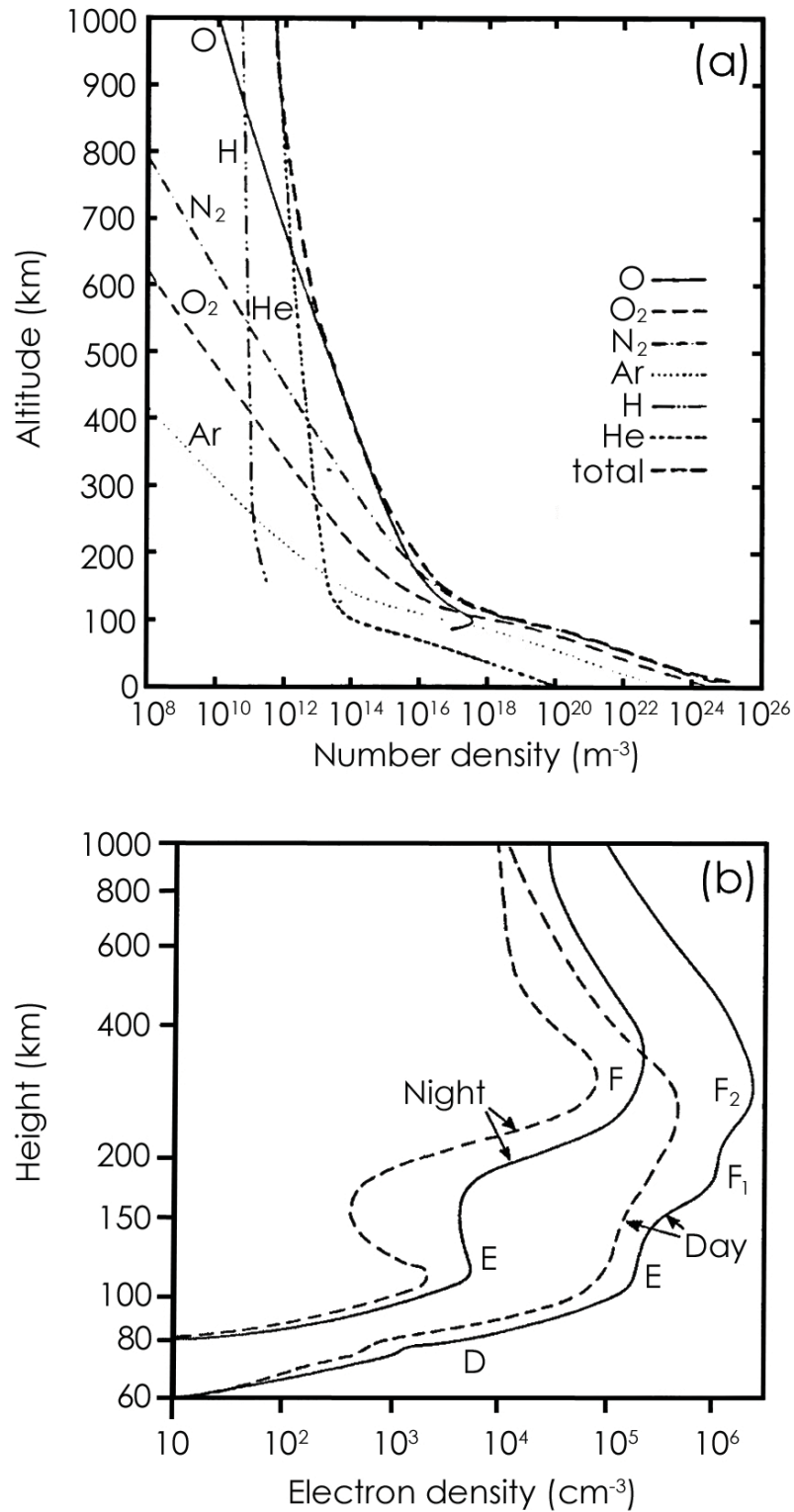


Figure 1.6: **(a and b)** Atmospheric and electron density variations with altitude. Panel (a) shows the variation of atmospheric composition to an altitude of 1000 km for a typical temperature profile (after COESA, 1976). Panel (b) shows example electron density profiles in the mid-latitude ionosphere. The solid line shows the profile for sunspot maximum while the dot-dashed line shows the profile for sunspot minimum (Hargreaves, 1979).

### 1.6.1 Ionospheric Currents

Electron and ion motion in magnetic and electric fields give rise to distinct finite conductivities and their respective currents. When a magnetic and electric field is present particles experience the Lorentz force,  $\mathbf{F}_{\text{Lorentz}}$ . If the particle is moving with a velocity,  $\mathbf{v}$ , and has a charge,  $q$ , then the Lorentz force may be expressed as

$$\mathbf{F}_{\text{Lorentz}} = q(\mathbf{E} + \mathbf{v} \wedge \mathbf{B}), \quad (1.8)$$

where  $\mathbf{E}$  and  $\mathbf{B}$  are the electric and magnetic field vectors, respectively. Equation 1.8 also reveals that when no electric field is present, the Lorentz force causes the particles to gyrate around magnetic field lines. The frequency of this motion is known as the cyclotron frequency,  $f_{\text{cyclotron}}$ . This frequency is governed by the particles mass,  $m$ , and may be written as

$$f_{\text{cyclotron}} = \frac{qB}{m}, \quad (1.9)$$

and clearly the period,  $t_{\text{cyclotron}}$ , of gyration may be expressed as

$$t_{\text{cyclotron}} = \frac{m}{qB}. \quad (1.10)$$

Equation 1.8 suggests that the path of an electron in a uniform magnetic field is helical. The guiding centre of this motion will also drift due to an applied electric field. This additional perpendicular drift is orthogonal to the magnetic and electric fields. The perpendicular drift,  $\mathbf{v}_{\text{drift}}$ , of the guiding centre may be written as

$$\mathbf{v}_{\text{drift}} = \frac{\mathbf{E} \wedge \mathbf{B}}{B^2}, \quad (1.11)$$

where the force associated with the electric field,  $\mathbf{E}$ , is  $q\mathbf{E}$ . Therefore, particles will drift as well as gyrate around magnetic field lines. Equation 1.11 is known simply as  $\mathbf{E} \wedge \mathbf{B}$  drift.

The motion of electrons and ions are also mediated by their frequency of colliding with

neutrals. Clearly, if collisions are unimportant, the electrons and ions will gyrate and drift according to equation 1.11. However, in regions where collisions are important, such as the D-region, the electrons and ions move with fewer completions of their respective gyrocycle before a collision occurs. After a collision has taken place the ion or electron then starts a new gyrocycle.

The currents arising from the particle motions described previously are characteristically separated into three components, namely the direct, Pedersen and Hall currents. Panel (a) of Figure 1.7 presents an altitude profile highlighting the relative drifts of electrons and ions. The arrows on the figure show the net horizontal particle drift with respect to  $\mathbf{E} \wedge \mathbf{B}$  and  $\mathbf{E}$ , assuming a vertical magnetic field. The currents within each of the three regions will now be described with the aid of Figure 1.7 in ascending altitude from the D- to the F-region.

### **D-region Currents**

Horizontal currents flow in the D-region, the electrons drift in the direction of the electric field and it is here where collision processes dominate due to the weakly ionised nature of this region. The gyrofrequency is less than the ion-neutral collision frequency implying that  $\mathbf{E} \wedge \mathbf{B}$  drift breaks down. If the collision frequency is too high compared with the gyrofrequency, as occurs in the D-region, then the electrons and ions will move in the direction of the electric field.

### **E-region Currents**

As the altitude is increased towards the E-region, the ionisation increases accordingly. The E-region contains the strongest currents of all three regions mainly due to the relative drift between electrons and ions as shown in panel (a) of Figure 1.7. As the altitude increases, the electrons and ions move with greater completions of their respective gyrocycle before a collision occurs.

As the collision frequency decreases with altitude, then the ions will move with a velocity with a component in the  $\mathbf{E} \wedge \mathbf{B}$  direction. Figure 1.7 shows that the ion drift direction

changes from parallel to the electric field in the lower E-region to the  $\mathbf{E} \wedge \mathbf{B}$  direction at the top of the region. The electrons drift in the  $\mathbf{E} \wedge \mathbf{B}$  direction throughout this region.

### **F-region Currents**

In the F-region both ions and electrons drift in the  $\mathbf{E} \wedge \mathbf{B}$  direction as can be seen from panel (a) of Figure 1.7. The gyrofrequency is higher than the collision frequency for both ions and electrons in this region and so the Hall and Pedersen conductivities are much smaller in the F-region than in the E-region.

## **1.6.2 Ionospheric Conductivity**

As panel (a) of Figure 1.7 clearly showed, the E-region contains the largest relative drifts between ions and electrons. These relative drifts give rise to finite conductivities, namely the direct,  $\sigma_{\parallel}$ , Hall,  $\sigma_H$ , and Pedersen,  $\sigma_P$ .

It is these conductivities, which govern the direct, Pedersen and Hall currents, respectively. Panel (b) of Figure 1.7 shows the Hall and Pedersen conductivity altitude profiles. The Hall current is largest in the E-region due to a greater Hall conductivity. The F-region, however, contains a Pedersen conductivity, which is larger than the Hall conductivity.

## **1.6.3 Twin Cell Convection**

The electric field imposed on the magnetosphere will cause motion of the ionospheric plasma with an associated flow of ionospheric currents. The magnetospheric motion and ionospheric currents are mediated by Field Aligned Currents (FACs) (Birkeland, 1908). The Dungey cycle, described in section 1.5.2, results in a characteristic convection pattern in the ionosphere, dubbed the twin cell convection pattern. Figure 1.8 presents the twin cell convection pattern during southward IMF conditions in the northern hemisphere. The antisunward flow resulting from magnetopause reconnection travels towards the footprint of the reconnection site in the magnetotail, which causes a flow reversal.

The location of the Open-Closed field line Boundary (OCB) is marked with the dashed

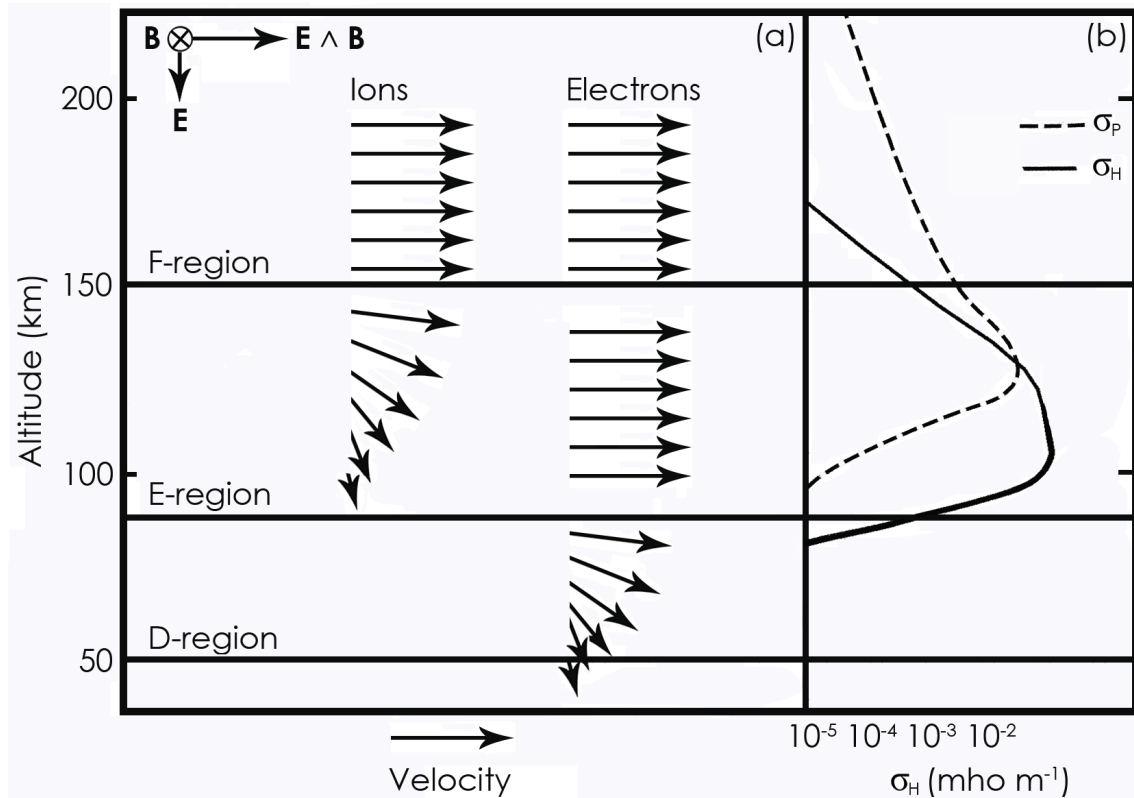


Figure 1.7: **(a and b)** Altitude profiles showing the relative electron and ion drift and the corresponding conductivity profiles. Panel (a) presents an altitude profile, which shows the relative drifts of electrons and ions. The arrows on the figure show the net horizontal particle drift with respect to  $\mathbf{E} \wedge \mathbf{B}$  and  $\mathbf{E}$ , assuming a vertical magnetic field. Panel (b) shows the Hall,  $\sigma_H$ , and Pedersen,  $\sigma_P$ , conductivity profiles (after Grocott, 2002).

line. The circular symbols highlight the direction of the FAC flow. The circled crosses show downward currents into the ionosphere and the circled dots indicate the outward flow. The "Region 1" and "Region 2" field aligned currents associated with the Dungey cycle flow are also highlighted as are the ionospheric Hall,  $J_H$ , and Pedersen,  $J_P$ , currents. The Pedersen currents are perpendicular to the plasma streamlines, indicating a current parallel to the electric field, while the Hall currents are anti-parallel to the plasma streamlines, indicating the current flow is orthogonal to both the electric and magnetic fields as described in section 1.6.3. Current continuity requires that the upward and downward FACs close with the aid of the horizontally flowing Pedersen currents in the ionosphere.

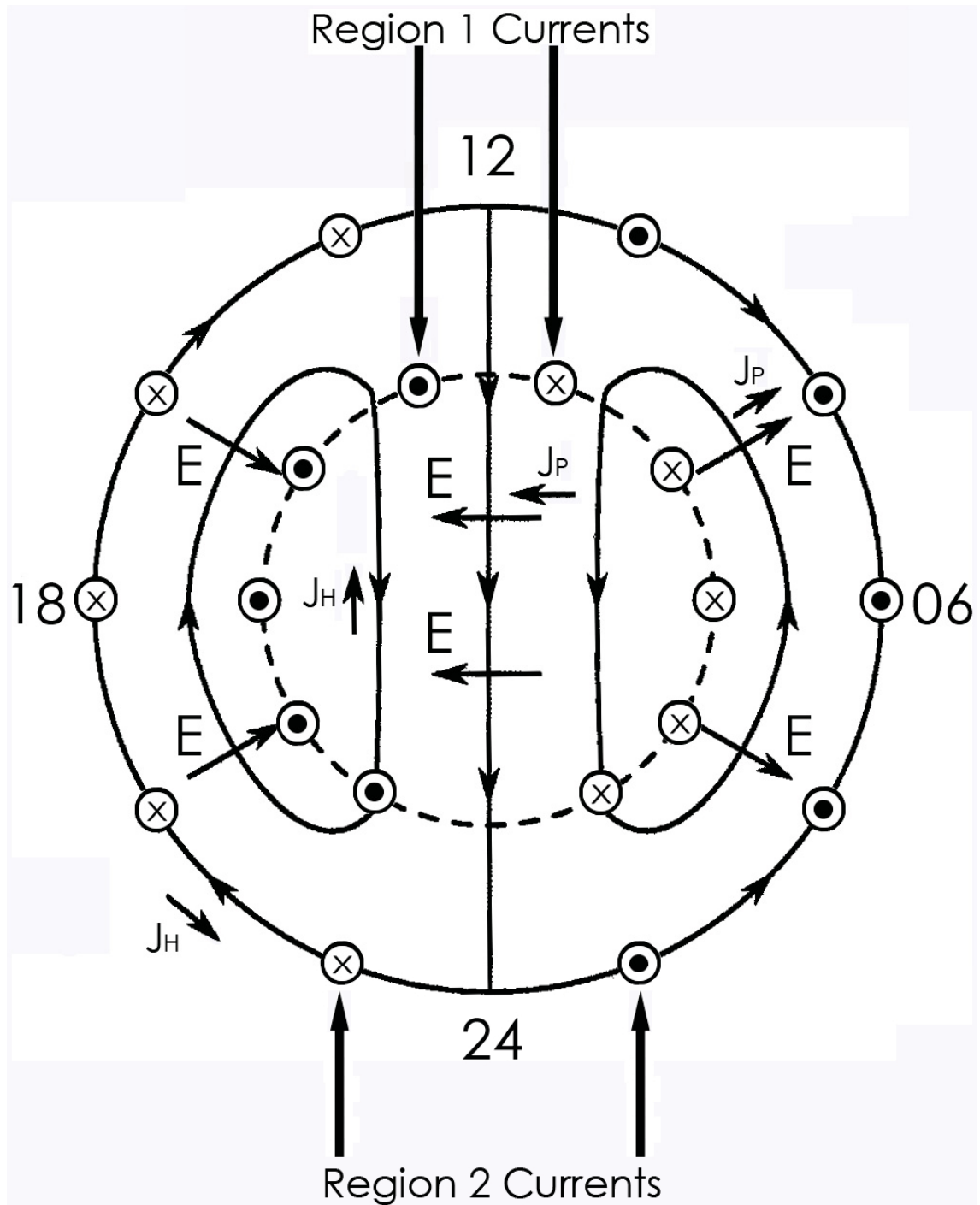


Figure 1.8: A schematic of the Dungey cycle mapped onto the ionosphere. The long solid and short solid arrows show the plasma streamlines and the electric field direction, respectively. The dashed line shows the location of the Open-Closed field line Boundary (OCB). The Field Aligned Currents (FACs) are given as circular symbols. The circled crosses show downward currents into the ionosphere and the circled dots indicate the outward current flow. The "Region 1" and "Region 2" currents associated with the Dungey cycle flow are also highlighted as are the Hall,  $J_H$ , and Pedersen,  $J_P$ , currents (after Cowley, 2000).

# Chapter 2

## Waves in the Magnetosphere: Theory, Previous Observations and Modelling

### 2.1 Introduction

Magnetohydrodynamics is the theory of time-varying magnetic fields that induce electrical currents in a moving conductive fluid, which then affect the original magnetic field. In 1942, the MHD wave solutions were derived (Alfvén, 1942). Direct observation of these waves to substantiate the theory proved difficult as the decay rate of these waves is too fast for direct observation in the laboratory. Over almost the next seven decades topics such as wave modes, damping and excitation of ULF waves in the terrestrial magnetosphere have been studied in great detail (see for example the review by Southwood and Hughes, 1983).

Many types of wave in the ULF band may be observed in the magnetosphere, ionosphere and on the ground. Important physical processes in the near-Earth plasma environment may be understood by studying these wave phenomena. The ionosphere, introduced in chapter 1, greatly affects the ULF wave signatures recorded on the ground and a number of authors have investigated the effect that the ionosphere has on their propagation. This chapter reviews previous geomagnetic pulsation research, considers ULF wave generation mechanisms and details observations of high-latitude ULF wave signatures.

ULF waves are commonly known as geomagnetic pulsations as first reported in 1861 at Kew observatory (Stewart, 1861). These pulsations are, in fact, oscillations of the terrestrial magnetic field, and are known to be ubiquitous in the terrestrial magnetosphere, occurring at all times of day. Typical periods of these waves are between 0.2 s - 600 s. The waves are categorised into different frequency bands (Jacobs et al., 1964). Table 2.1 highlights the classes of geomagnetic pulsation that occur. The waves most relevant to this high-latitude study are in the Pc5 category. Pc5 waves are continuous pulsations within the frequency range of 2 mHz - 7 mHz. The types of Pc5 waves investigated here have large azimuthal scale-sizes and are thought to be driven by processes external to the magnetospheric cavity. Of particular interest to this study are ionospheric observations of Field Line Resonances (FLRs). FLRs are large-scale toroidal mode waves, which display a characteristic amplitude peak and a 180° phase change as a function of latitude across the resonant peak. FLRs are characterised by the fact that they are observed at the same frequency on field lines covering a wide range of latitudes. Small azimuthal scale-size waves are generally poloidal in nature, are thought to be driven internally to the magnetosphere through wave-particle interactions, and shall not be considered further within this thesis.

Continuous Pulsations					
Pulsation Class	Pc1	Pc2	Pc3	Pc4	Pc5
T (s)	0.2 - 5.0	5.0 - 10.0	10.0 - 45.0	45.0 - 150.0	150.0 - 600.0
f (mHz)	200.0 - 5000.0	100.0 - 200.0	22.0 - 100.0	7.0 - 22.0	2.0 - 7.0

Irregular Pulsations		
Pulsation Class	Pi1	Pi2
T (s)	1.0 - 45.0	40.0 - 150.0
f (mHz)	25.0 - 1000.0	2.0 - 25.0

Table 2.1: The classification of geomagnetic micropulsations where Pc refers to regular continuous pulsations and Pi denotes irregular damped pulsations (Jacobs et al., 1964).

## 2.2 Magnetohydrodynamic Wave Theory

In physical terms, magnetospheric ULF waves are associated with the fluid motion of the plasma. Therefore, MHD plasma theory is required to describe the particle dynamics. The next section of this thesis details a full mathematical description of MHD waves. All MHD wave theory has a solid foundation built upon the four Maxwell equations, which may be expressed in their differential form as

$$\nabla \cdot \mathbf{E} = \frac{\rho_q}{\varepsilon_0}, \quad (2.1)$$

$$\nabla \cdot \mathbf{B} = 0, \quad (2.2)$$

$$\nabla \wedge \mathbf{E} = -\frac{\partial \mathbf{B}}{\partial t}, \quad (2.3)$$

and

$$\nabla \wedge \mathbf{B} = \mu_0 \mathbf{J} + \mu_0 \varepsilon_0 \frac{\partial \mathbf{E}}{\partial t}, \quad (2.4)$$

where  $\mathbf{E}$  is the electric field vector in Volts  $\text{m}^{-1}$ ,  $\mathbf{B}$  is the magnetic field vector in Tesla,  $\rho_q$  is the charge density in coulombs  $\text{m}^{-3}$ ,  $t$  is the time in seconds (s),  $\mathbf{J}$  is the current density in Amps  $\text{m}^{-2}$ ,  $\varepsilon_0$  is the permittivity of free space ( $8.85 \times 10^{-12} \text{ F m}^{-1}$ ) and  $\mu_0$  is the permeability of free space. Starting from these four simple equations an entire mathematical description of ULF waves may be undertaken. There are a number of different wave modes that may propagate in magnetised plasmas. Some of these modes are governed by the plasma pressure,  $P$ . If the plasma pressure is much less than the magnetic pressure then the plasma pressure term may be neglected and the condition for cold plasma waves is revealed. If however, magnetic pressure does not dominate over the plasma pressure then warm plasma waves are the outcome.

### 2.2.1 Cold Plasma Waves

In a cold plasma, if the plasma pressure is much smaller than the magnetic pressure,  $\frac{B^2}{2\mu_0}$ , then  $P$  may be neglected.

If an infinite uniform liquid is considered, which is permeated by a uniform magnetic field,  $\mathbf{B}$ , and a velocity vector field,  $\mathbf{V}$ , is produced within this fluid due to a small magnetic disturbance, then ignoring viscosity and conductivity, the induction, continuity and momentum equations may be written as

$$\frac{\partial \mathbf{b}}{\partial t} = \nabla \wedge \mathbf{V} \wedge \mathbf{B}, \quad (2.5)$$

$$\frac{\partial \rho}{\partial t} + \nabla \cdot (\rho \mathbf{V}) = 0, \quad (2.6)$$

and

$$\rho \frac{D\mathbf{V}}{Dt} = -\nabla P + \mathbf{J} \wedge \mathbf{B}, \quad (2.7)$$

respectively. Using the Maxwell equations, neglecting displacement currents, linearising equations 2.5 and 2.7 and Fourier analysing in time and space reveals

$$\omega \mathbf{b} = (\mathbf{k} \cdot \mathbf{V})\mathbf{B} - (\mathbf{B} \cdot \mathbf{k})\mathbf{V} \quad (2.8)$$

and

$$\mu_0 \rho \omega \mathbf{V} = \mathbf{k}(\mathbf{b} \cdot \mathbf{B}) - (\mathbf{B} \cdot \mathbf{k})\mathbf{b}, \quad (2.9)$$

where  $\mathbf{k}$  is the wavevector,  $\omega$  is the angular frequency, and  $\rho$  from now on denotes the mass density.

### Fast Compressional Wave Mode

There are two wave modes associated with cold plasma waves. These are known as the fast and Alfvén modes. Taking the dot product of equations 2.8 and 2.9 with  $\mathbf{B}$  and  $\mathbf{k}$ , respectively, yields the dispersion relationship for fast mode waves in a cold plasma as

$$\omega^2 = V_A^2 k^2, \quad (2.10)$$

where  $V_A$  is defined as

$$V_A = \left( \frac{B^2}{\mu_0 \rho} \right)^{\frac{1}{2}}, \quad (2.11)$$

and is known as the Alfvén velocity. Equation 2.10 reveals that fast mode waves are not restricted to move just along magnetic field lines. The group velocity of the fast mode shows that energy and information may be carried in any direction, hence, fast mode waves are isotropic in propagation if the plasma is "cold." The perturbations, for the fast mode, are at an angle to the background magnetic field, and the oblique phase fronts yield varying separations between the perturbed field lines.

### Alfvén Wave Mode

Taking the cross product of equations 2.8 and 2.9 with  $\mathbf{k}$ , taking a dot product with  $\mathbf{B}$  on one of the resulting equations and incorporating the parallel component of the wavevector yields the dispersion relationship for Alfvén mode waves as

$$\omega^2 = V_A^2 k^2 \cos^2 \theta, \quad (2.12)$$

where  $\theta$  is the angle between  $\mathbf{B}$  and  $\mathbf{k}$ .

The Alfvén and fast mode dispersion relationships both depend on the magnetic field magnitude and the plasma density. The Alfvén dispersion relation depends only on the parallel component of the wavevector,  $\mathbf{k}$ , due to the anisotropic nature of the magnetic forces. The group velocity of Alfvén mode waves indicates that both information and

energy may not propagate across the background magnetic field. The Alfvén wave is analogous to waves on a string where energy is only transmitted along the string. Importantly, the Alfvén wave perturbations are orthogonal to the background field, and the distances between the individual perturbed field lines are constant.

### 2.2.2 Warm Plasma Waves

In a warm plasma the plasma pressure,  $P$ , may not be neglected with respect to the magnetic pressure and the sound speed,  $S$ , is not so small as to be neglected compared to the Alfvén velocity since the sound speed is proportional to the root of the gas pressure,  $P$ . There are now interactions between the magnetic field and the effects of compressibility. As for the cold plasma waves gravity will be neglected and an initially constant magnetic field in the  $Z$  direction only will be assumed. If  $\nabla \cdot \mathbf{V} \neq 0$  the adiabatic, induction and momentum equations may be expressed as

$$\gamma p \left( \frac{\delta \rho}{\rho} \right) = S^2 \delta \rho, \quad (2.13)$$

$$\frac{\partial \mathbf{b}}{\partial t} = \nabla \wedge \mathbf{V} \wedge \mathbf{B} = B \frac{\partial \mathbf{V}}{\partial z} - \mathbf{B}(\nabla \cdot \mathbf{V}), \quad (2.14)$$

and

$$\rho \frac{\partial \mathbf{V}}{\partial t} = -\nabla \delta p + \frac{B_0}{\mu_0} \frac{\partial \mathbf{b}}{\partial z} - \frac{\nabla(\mathbf{B}_0 \cdot \mathbf{b})}{\mu_0}, \quad (2.15)$$

respectively. Taking the partial derivative with respect to time of equation 2.15, using equation 2.13 in conjunction with the fact that  $\frac{\partial \delta \rho}{\partial t} = -\rho(\nabla \cdot \mathbf{V})$  and equation 2.14, yields the following second order differential in the velocity vector.

$$\frac{\partial^2 \mathbf{V}}{\partial t^2} = S^2 \nabla(\nabla \cdot \mathbf{V}) + V_A^2 \left[ \frac{\partial}{\partial z} \left( \frac{\partial \mathbf{V}}{\partial z} - (\nabla \cdot \mathbf{V})_Z \right) - \nabla \left( \frac{\partial V_z}{\partial z} - \nabla \cdot \mathbf{V} \right) \right], \quad (2.16)$$

where the  $Z$  subscript shows that the field-parallel component of the divergence in the velocity vector is used. Taking the  $Z$  component of equation 2.16 yields

$$\frac{\partial^2 V_z}{\partial t^2} = S^2 \frac{\partial(\nabla \cdot \mathbf{V})}{\partial z}, \quad (2.17)$$

since the latter two terms on the right hand side of equation 2.16 cancel out upon evaluation. Taking the divergence of equation 2.16 makes the first term in the square brackets zero, and may be expressed as

$$\frac{\partial^2(\nabla \cdot \mathbf{V})}{\partial t^2} = S^2 \nabla^2 \nabla \cdot \mathbf{V} + V_A^2 \nabla^2 (\nabla \cdot \mathbf{V} - \frac{\partial V_z}{\partial z}), \quad (2.18)$$

which is a second order differential in the divergence of the velocity vector. The Z component of the velocity vector is eliminated from equations 2.17 and 2.18 by differentiating equation 2.18 twice with respect to time and substituting equation 2.17 giving

$$\frac{\partial^4(\nabla \cdot \mathbf{V})}{\partial t^4} - (V_A^2 + S^2) \frac{\partial^2}{\partial t^2} (\nabla^2 \nabla \cdot \mathbf{V}) + V_A^2 S^2 \frac{\partial^2}{\partial z^2} (\nabla^2 \nabla \cdot \mathbf{V}) = 0, \quad (2.19)$$

which is a fourth order differential in the divergence of the velocity vector. For disturbance variables proportional to  $\exp^{i(\omega t - \mathbf{k} \cdot \mathbf{r})}$ , where  $\mathbf{r}$  is the position coordinate vector, equation 2.19 may be reduced to

$$\omega^4 - (V_A^2 + S^2) k^2 \omega^2 + V_A^2 S^2 k^4 \cos^2 \theta = 0, \quad (2.20)$$

which is a quartic in the angular frequency.  $\theta$  in equation 2.20 is the angle between  $\mathbf{B}$  and  $\mathbf{k}$ . If  $\nabla \cdot \mathbf{V} = 0$  then,  $V_z = \delta\rho = 0$  and equation 2.16 may be written as

$$\frac{\partial^2 V}{\partial t^2} = V_A^2 \frac{\partial V^2}{\partial z^2}, \quad (2.21)$$

corresponding to shear waves that propagate along the magnetic field lines. Considering disturbance variables as for the compressible case then this reduces to

$$\omega^2 - V_A^2 k^2 \cos^2 \theta = 0. \quad (2.22)$$

Combining equations 2.22 and 2.20 provides the complete dispersion relation for warm

plasma waves and may be written for convenience as

$$[\omega^2 - V_A^2 k^2 \cos^2 \theta][\omega^4 - (V_A^2 + S^2)k^2 \omega^2 + V_A^2 S^2 k^4 \cos^2 \theta] = 0. \quad (2.23)$$

The solutions to equation 2.23 are presented as

$$\omega^2 = V_A^2 k^2 \cos^2 \theta \quad (2.24)$$

and

$$\omega^2 = \frac{k^2}{2} [S^2 + V_A^2 \pm [(S^2 + V_A^2)^2 - 4S^2 V_A^2 \cos^2 \theta]^{\frac{1}{2}}] \quad (2.25)$$

(Cowling, 1980). Equation 2.24 is the Alfvén dispersion relation. This dispersion relation depends only on the parallel wavevector and so demonstrates, as was true for the cold plasma wave solution, that Alfvén waves are field guided and that the polarisation is orthogonal to the background magnetic field. The perturbation magnetic field vector,  $\mathbf{b}$ , is always perpendicular to both the background field,  $\mathbf{B}_0$ , and the wavevector,  $\mathbf{k}$ . The electric field vector,  $\mathbf{E}$ , is orthogonal to the background magnetic field,  $\mathbf{B}_0$ , as shown in Figure 2.1.

Equation 2.25 are the fast and slow magnetoacoustic wave modes denoted by the positive and negative solution, respectively, and depend on the sound speed of the plasma gas. As shown in Figure 2.1,  $\mathbf{b}$  is within the plane of  $\mathbf{B}_0$  and  $\mathbf{k}$ . For fast mode waves, in warm plasmas, the pressure and magnetic perturbations are in phase with each other. However, for slow mode waves, the thermal pressure and magnetic perturbations are out of phase. The fast mode is produced when the total pressure of the plasma changes locally. A source of compressional waves, therefore, is this pressure perturbation. Equation 2.7 shows that incorporating the pressure gradient term gives a source of plasma motion. As the waves radiate away from the source they carry the excess pressure with them. The fast wave mode is hence confirmed as being isotropic in propagation. Using  $\omega = uk$ , where  $u$  is the phase velocity, equations 2.24 and 2.25 give solutions perpendicular and parallel to the field ( $\theta = 0$  and  $\theta = \frac{\pi}{2}$ ). For  $\theta = 0$  the slow mode has a phase velocity of  $u = \pm S$ , while

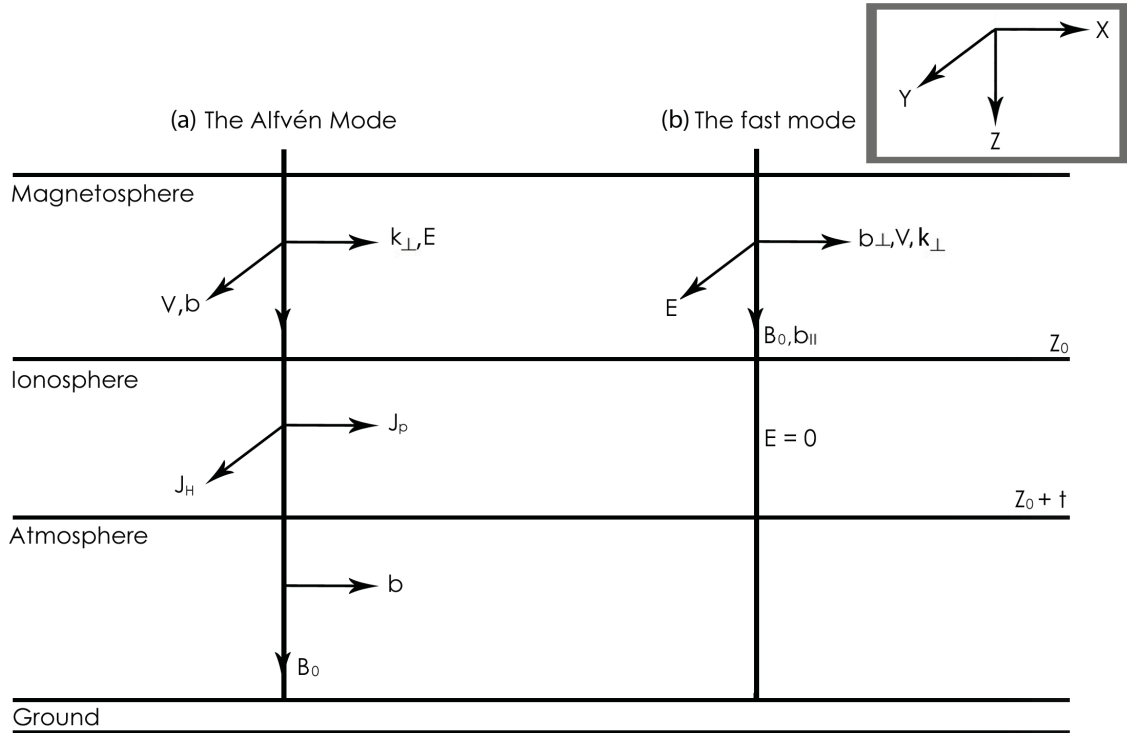


Figure 2.1: **(a and b)** A schematic showing the Alfvén and fast wave mode propagation. Panels (a) and (b) show the Alfvén and fast mode propagation through the magnetosphere, ionosphere and atmosphere to the ground, respectively.

the fast mode has a phase velocity of  $u = \pm V_A$ . However, for  $\theta = \frac{\pi}{2}$  the slow mode has a phase velocity of  $u = 0$ , while the fast mode has a phase velocity of  $u = \pm(S^2 + V_A^2)^{\frac{1}{2}}$ . The three different phase velocities are given as polar plots in Figure 2.2. If the magnetic pressure dominates over the plasma pressure (a cold plasma), the fast mode becomes isotropic and the slow mode disappears revealing the same fast mode dispersion relation as given in equation 2.10. This thesis deals with regions that have a cold plasma regime and so from now on only Alfvén and fast wave modes will be considered.

### 2.3 Ionospheric Boundary Conditions

When an Alfvén wave propagates along a closed magnetospheric field line, then it may result in resonance, like a wave on a string, and the ionospheric boundary conditions are an important consideration in this process, which are also analogous to the string boundary conditions. When an Alfvén wave travels along a geomagnetic field line, the wave energy

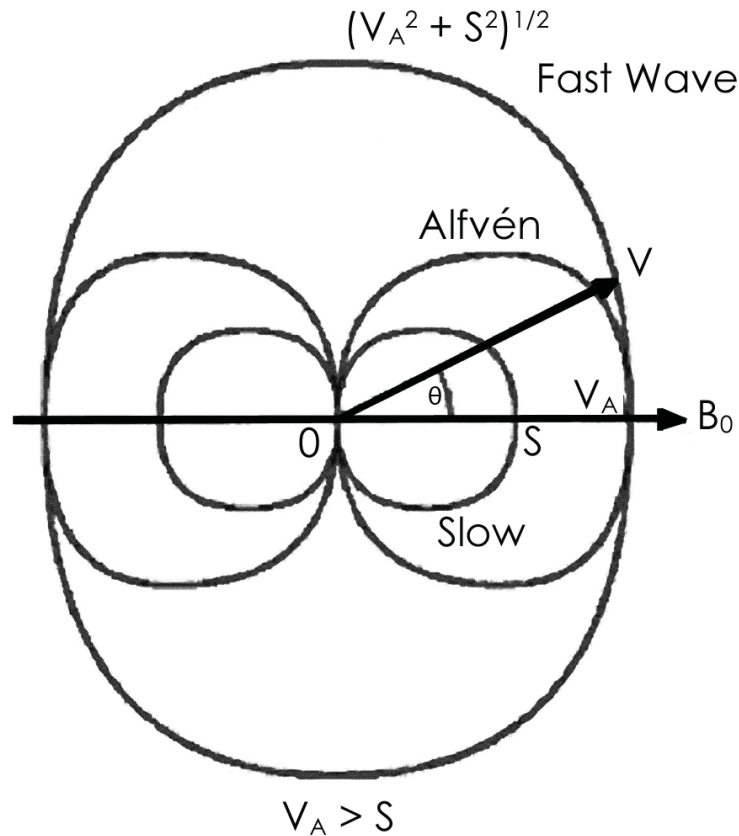


Figure 2.2: A Friedrichs diagram (hodograph), which represents the three phase velocities possible in a magnetised plasma (Kallenrode, 2004).

propagates along the field lines into the ionosphere where it is dissipated by frictional forces. If the wave frequency matches the field line resonant frequency, then the wave energy may couple to standing waves. The driver could be an incoming compressional wave, whose source is external to the magnetosphere, as will be considered in section 2.6.2.

Panels (a) and (b) of Figure 2.3 show the dipole field standing wave oscillations representing the fundamental and second harmonic solutions shown by the dashed lines. Panel (a) shows the odd mode (fundamental) result for  $\mathbf{E}$  and  $\mathbf{b}$ . Panel (b) shows the even mode (second harmonic).

Figure 2.3 corresponds to a model of the magnetosphere/ionosphere system with conjugate ionospheres having large conductivities, which are located at the ends of the field lines. At the boundaries the electric field will therefore tend to zero.

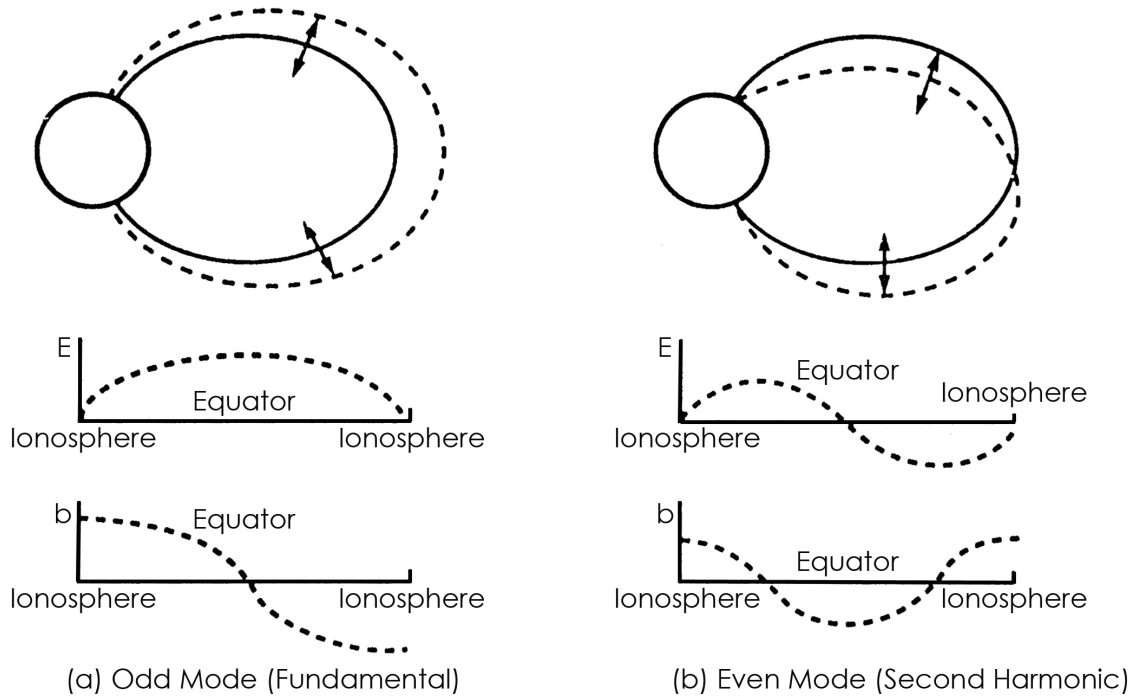


Figure 2.3: **(a and b)** Fundamental and second harmonic FLRs. Panel (a) shows the odd mode (fundamental) while panel (b) shows the even mode (second harmonic) (Southwood and Hughes, 1983).

Using this boundary condition and assuming that the length of the field line between the two ionospheres is  $l$ , then the allowed standing wavelengths in the field direction,  $\lambda_{parallel}$ , are

$$\lambda_{parallel} = \frac{2l}{n}, \quad (2.26)$$

where  $n$  is a positive integer. The corresponding allowed periods of oscillation along the closed magnetic field lines are of the form

$$t = \frac{2}{n} \int \frac{(\mu_0 \rho)^{\frac{1}{2}}}{B} dl, \quad (2.27)$$

where equation 2.11 has been applied.

As already mentioned, FLRs are large-scale toroidal mode waves. By definition toroidal implies that the oscillation is in the east-west direction. Figure 2.1 shows that the perturbation magnetic field,  $b$ , is in the Y direction in the magnetosphere. In the atmosphere

there are no current flows and so assuming an  $\exp^{i(kx-\omega t)}$  dependence, the Z component of the current density may be expressed as

$$J_z = \frac{(\nabla \wedge \mathbf{b})_z}{\mu_0} = \frac{i\mathbf{k}_\perp \wedge \mathbf{b}_{\text{horizontal}}}{\mu_0} = 0. \quad (2.28)$$

To satisfy equation 2.28 either the horizontal component of the perturbation field vector must be zero or perpendicular to  $\mathbf{k}_\perp$ . Figure 2.1 presents the resulting  $90^\circ$  ionospheric rotation of the magnetic perturbation vector indicating that the signature on the ground is in the X component (Hughes, 1983). Since  $J_x = J_P$  from Figure 2.1 and using equations 2.4 and  $\mathbf{J} = \sigma \mathbf{E}$ ,  $\nabla \wedge \mathbf{b} = \mu_0 \mathbf{J} = \frac{\partial b_y}{\partial z} = \mu_0 J_x = \mu_0 \sigma_P E_x$ . The change in the Y component of the perturbation magnetic field vector,  $\Delta b_y$ , may be expressed in terms of the height integrated Pedersen conductivity,  $\Sigma_P = \int_B^A \sigma_P dz$ , and Pedersen conductivity,  $\sigma_P$ , as

$$\Delta b_y = \int_B^A \mu_0 E_x \sigma_P dz = \mu_0 E_x \Sigma_P \quad (2.29)$$

where  $B$  to  $A$  represents the thickness of the ionosphere. Similarly, the change in the X component in terms of the ionospheric integrated Hall conductivity,  $\Sigma_H$ , may be expressed as

$$\Delta b_x = \mu_0 E_x \Sigma_H. \quad (2.30)$$

In the terrestrial ionosphere the height integrated Hall and Pedersen conductivities are roughly equal and therefore,  $\Delta b_y \sim \Delta b_x$ . Equation 2.29 now gives an ionospheric boundary condition:

$$\mathbf{b}_m \wedge \hat{\mathbf{Z}} = \mu_0 \mathbf{E}_m \Sigma_P. \quad (2.31)$$

Equation 2.31 derives from the fact that ionospheric Pedersen currents completely shield each relevant component of the incident magnetic perturbation,  $\mathbf{b}$ . The subscript,  $\mathbf{m}$ , denotes the magnetospheric values. Equation 2.31 also implies that in the ionosphere there is a balance between joule heating and the downwards Poynting flux of the wave.

There are different ionospheric boundary conditions for fast and Alfvén mode waves as first considered by Nishida (1964) and later by Kivelson and Southwood (1988).

Kivelson and Southwood (1988) explained that the rotation of the Alfvén mode wave is due to this mode carrying a parallel current, which gives rise to ionospheric currents. These ionospheric currents imply the Pedersen conductivity mediates the boundary condition for Alfvén mode waves. However, since the ionospheric electric field associated with a fast mode wave is small and the fast mode wave itself carries no parallel current, then the ionospheric boundary condition for the fast mode is not determined by ionospheric conductivity. Instead, the signal associated with the fast mode is determined by matching to a free space signal in the atmosphere.

## 2.4 The Ionospheric Reflection Coefficient

The ionospheric reflection coefficient,  $R$ , is the ratio of the amplitude of the reflected wave to the amplitude of the incident wave. If the incident and reflected electric field vectors are defined as  $\mathbf{E}_i$  and  $\mathbf{E}_r$ , respectively, then the ionospheric reflection coefficient in terms of the Alfvén velocity,  $V_A$ , may be expressed as

$$R = \frac{\mathbf{E}_r}{\mathbf{E}_i} = \frac{1 - \mu_0 \Sigma_P V_A}{1 + \mu_0 \Sigma_P V_A}, \quad (2.32)$$

(Southwood and Hughes, 1983). Equation 2.32 reveals that the Pedersen conductivity determines the reflection coefficient of the ionosphere. If the height integrated Pedersen conductivity tends to infinity, then perfect wave reflection is achieved and the electric field vector within the ionosphere tends to zero. If the height integrated Pedersen conductivity tends to zero, then the perturbation magnetic field vector,  $\mathbf{b}$ , is zero in the ionosphere, again implying perfect reflection. If the condition  $\Sigma_P = \frac{1}{\mu_0 V_A}$  is satisfied then no standing wave will appear since the incident wave,  $\mathbf{E}_i$ , is fully absorbed.

## 2.5 Field Line Resonances

ULF waves are thought to be standing waves in the magnetospheric system with the northern and southern ionosphere being boundaries where the electric field oscillations exhibit a node (Glassmeier et al., 2004). In this process an incoming compressional fast-mode wave couples to an Alfvén mode oscillation on a geomagnetic field line of a matching eigenfrequency and an FLR will occur (Chen and Hasegawa, 1974a; Southwood, 1974). FLRs have large spatial-scale in longitude, but develop small-scale structures in the latitudinal direction.

A simple model to illustrate FLRs is known as the box model.

### 2.5.1 The Box Model of the Magnetosphere

To develop the idea of field line resonance the box model of the magnetosphere by Southwood (1974) is expanded upon here. Figure 2.4 illustrates a cold plasma permeating a region containing a straight, uniform, background magnetic field,  $B\hat{\mathbf{z}}$ , with a density that is a function of the X component alone,  $\rho(x)$ , and contains finite boundaries in the X and Z directions. The non-uniformity is introduced because the density and hence the Alfvén velocity are allowed to vary in the X direction. The perturbed variables are of the form

$$\mathbf{b} = \mathbf{b} \exp^{i(\lambda y + kz - \omega t)}. \quad (2.33)$$

The effective azimuthal wavenumber,  $m$ , corresponds to the parameter  $\lambda$  in the model. If the value of  $l$  in Figure 2.4 is  $\pm 1$ , then  $\mathbf{k}$  is quantised according to  $\mathbf{k} = \pm \frac{n\pi}{2}$ .

For a cold plasma  $-\nabla P$  may be neglected and so equation 2.7 becomes

$$\mu_0 \rho \frac{\partial^2 \xi}{\partial t^2} = (\nabla \wedge \mathbf{b}) \wedge (\mathbf{B} + \mathbf{b}), \quad (2.34)$$

where  $\xi$  is the field line displacement vector and is related to the velocity vector by the following expression

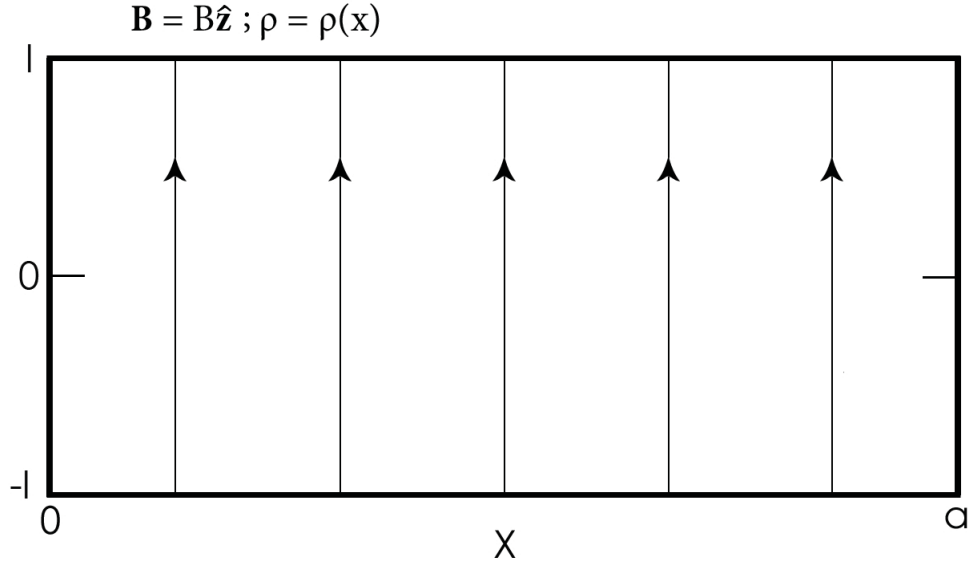


Figure 2.4: A schematic of the box model of the magnetosphere (Southwood and Kivelson, 1986).

$$\xi = \int \mathbf{V} dt. \quad (2.35)$$

Explicitly, the components of the right hand side of equation 2.34 may be expressed as the following determinant

$$\mu_0 \rho \frac{\partial^2 \xi}{\partial t^2} = \begin{vmatrix} \hat{\mathbf{i}} & \hat{\mathbf{j}} & \hat{\mathbf{k}} \\ \left(\frac{\partial b_z}{\partial y} - \frac{\partial b_y}{\partial z}\right) & \left(\frac{\partial b_x}{\partial z} - \frac{\partial b_z}{\partial x}\right) & \left(\frac{\partial b_y}{\partial x} - \frac{\partial b_x}{\partial y}\right) \\ b_x & b_y & b_z + B \end{vmatrix}. \quad (2.36)$$

The  $\hat{\mathbf{i}}$  component of the determinant in equation 2.36, is

$$\mu_0 \rho \frac{\partial^2 \xi_x}{\partial t^2} = B \left( \frac{\partial b_x}{\partial z} - \frac{\partial b_z}{\partial x} \right), \quad (2.37)$$

where the terms with coefficient perturbation magnetic field components have been neglected, since  $B \gg b$ . Using a similar method, the  $\hat{\mathbf{j}}$  component of the determinant is

$$\mu_0 \rho \frac{\partial^2 \xi_y}{\partial t^2} = B \left( \frac{\partial b_y}{\partial z} - \frac{\partial b_z}{\partial y} \right). \quad (2.38)$$

The Faraday equation, equation 2.3, may be expressed in terms of the perturbation magnetic field as

$$\frac{\partial \mathbf{b}}{\partial t} = -\nabla \wedge \mathbf{E}. \quad (2.39)$$

This is because the full current density,  $\mathbf{J}$ , can be expressed as,

$$\mathbf{J} = \sigma(\mathbf{E} + \mathbf{V} \wedge \mathbf{B}). \quad (2.40)$$

Rearranging for the Electric field vector,  $\mathbf{E}$ , this becomes

$$\mathbf{E} = \frac{\mathbf{J}}{\sigma} - \mathbf{V} \wedge \mathbf{B}. \quad (2.41)$$

If the displacement currents are neglected in equation 2.4 and the subsequent equation is substituted into equation 2.41, then the Faraday equation becomes

$$\frac{\partial \mathbf{b}}{\partial t} = \nabla \wedge \mathbf{V} \wedge \mathbf{B} - \frac{\nabla^2 \mathbf{B}}{\mu_0 \sigma}. \quad (2.42)$$

Assuming that the plasma is ideal then the conductivity is assumed to be infinite. If this is the case then the second term, the diffusion term, on the right hand side of equation 2.42 vanishes. This leads to the "frozen-in" flow equation,

$$\frac{\partial \mathbf{b}}{\partial t} = \nabla \wedge \mathbf{V} \wedge \mathbf{B}. \quad (2.43)$$

Incorporating the field line displacement vector into equation 2.43, with the use of equation 2.35, reveals the scalar triple product relation for,  $\mathbf{b}$ , as

$$\mathbf{b} = \nabla \wedge \xi \wedge \mathbf{B}. \quad (2.44)$$

Explicitly, equation 2.44 is

$$\mathbf{b} = \nabla \wedge \xi \wedge \mathbf{B} = \begin{vmatrix} \hat{\mathbf{i}} & \hat{\mathbf{j}} & \hat{\mathbf{k}} \\ (\frac{\partial \xi_z}{\partial y} - \frac{\partial \xi_y}{\partial z}) & (\frac{\partial \xi_x}{\partial z} - \frac{\partial \xi_z}{\partial x}) & (\frac{\partial \xi_y}{\partial x} - \frac{\partial \xi_x}{\partial y}) \\ 0 & 0 & B \end{vmatrix}. \quad (2.45)$$

Hence,  $b_x$  may be expressed as

$$b_x = B \left( \frac{\partial \xi_x}{\partial z} - \frac{\partial \xi_z}{\partial x} \right). \quad (2.46)$$

Therefore the partial derivative of  $b_x$  with respect to  $z$  can be written as,

$$\frac{\partial b_x}{\partial z} = -ik(b_x) = -k^2 B \xi_x. \quad (2.47)$$

Using equation 2.47, equation 2.37 can be expressed as

$$\left( \frac{\mu_0 \rho(x)}{B^2} \frac{\partial^2}{\partial t^2} + k^2 \right) \xi_x = -\frac{1}{B} \frac{\partial b_z}{\partial x}. \quad (2.48)$$

A similar analysis is performed for the perturbation field in the Y component. Using the fact that  $\frac{\partial b_z}{\partial y} = i\lambda b_z$ , the Y component counterpart to equation 2.48 is

$$\left( \frac{\mu_0 \rho(x)}{B^2} \frac{\partial^2}{\partial t^2} + k^2 \right) \xi_y = -\frac{i b_z}{\lambda B}. \quad (2.49)$$

The Z component of the perturbation field can be expressed as

$$b_z = -i\lambda \xi_y B - B \frac{\partial \xi_x}{\partial x}. \quad (2.50)$$

If  $\mathbf{K}$  is defined such that  $K^2 = \frac{\omega^2 \mu_0 \rho(x)}{B^2}$  then the X and Y components of the field line displacement vector may be written as

$$\xi_x = \left( \frac{\partial b_z}{\partial x} \right) \left( \frac{1}{B(K^2 - k^2)} \right) \quad (2.51)$$

and

$$\xi_y = \frac{i\lambda b_z}{B(K^2 - k^2)}, \quad (2.52)$$

respectively. Substituting equations 2.51 and 2.52 into 2.50, simplifying and using the product rule for differentials yields

$$\frac{\partial b_z^2}{\partial x^2} - \frac{\frac{\partial(K^2)}{\partial x}}{(K^2 - k^2)} \left( \frac{\partial b_z}{\partial x} \right) + (K^2 - k^2 - \lambda^2) b_z, \quad (2.53)$$

which is a version of the fast mode equation. If  $K^2 = k^2$  then there is a magnetic shell which resonates with the fast mode. So this condition allows wave energy into the magnetosphere, which drives field line resonances. The maximum amplitude of the Alfvén mode is excited when  $K^2 = k^2$  within equation 2.53.

The sense of polarisation of the wave switches on each side of the maximum in amplitude. In the magnetosphere, a westward propagating wave has an anticlockwise and clockwise polarisation south and north of resonance, respectively. The exact reverse applies for an eastward propagating wave. In the immediate vicinity of the resonance, where the amplitude is largest, the polarisation is linear. The results of the box model have been analysed fully and more detail may be found in Kivelson and Southwood (1986).

## 2.5.2 Illustration of Field Line Resonances

The Super Dual Auroral Radar Network (SuperDARN) have been a useful diagnostic tool of ULF wave research for many years (Chisham et al., 2007). The first SuperDARN radar was located at Goose Bay (Greenwald et al., 1995) and has a temporal resolution of approximately 100 s, which allows the continual observation of many Pc5 FLRs (e.g., Ruohoniemi et al., 1991; Walker et al., 1992). An example FLR event observed by Ruohoniemi et al. (1991) is presented in Figure 2.5. Panel (a) of Figure 2.5 shows the backscatter power recorded along beam 8 of the Goose Bay SuperDARN radar between 00:00 UT - 12:00 UT on 11 January 1989. Panel (b) shows the corresponding Doppler velocity measurements. A shear flow is observed in panel (b) between 01:30 UT - 04:00 UT. The poleward motion of the backscatter is characteristic of a quiet-time contraction of the

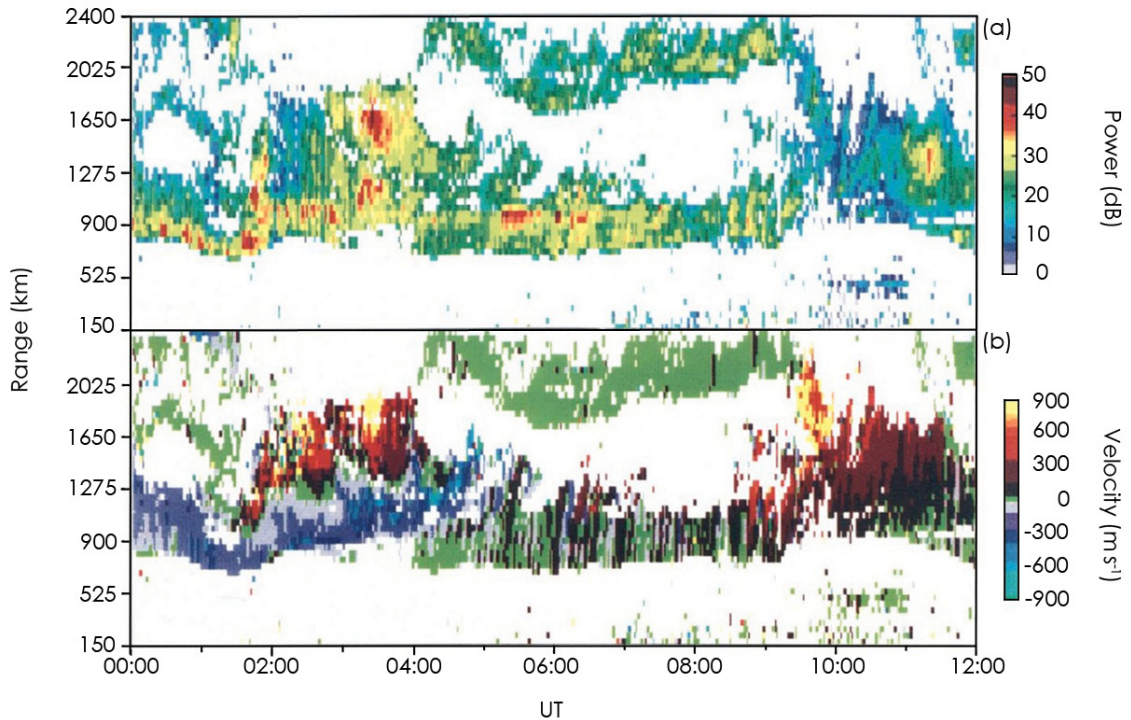


Figure 2.5: **(a and b)** A Range Time Intensity (RTI) Plot recorded along beam 8 of the Goose Bay SuperDARN radar between 00:00 UT - 12:00 UT on 11 January 1989. Panels (a) and (b) show the backscatter power and the line-of-sight velocity measurements, respectively (Ruohoniemi et al., 1991).

auroral zone and polar cap. Panel (b) also shows periodic oscillations in the line-of-sight velocity sign between approximately 04:00 UT - 09:00 UT. The sign change implies there is a geomagnetic pulsation modulating the background convection between eastward and westward flow. Latitudinal power and phase profiles are a useful way of investigating the nature of geomagnetic pulsations. Figure 2.6 presents latitudinal power and phase profiles for a frequency of 2.6 mHz along beam 8 of the Goose Bay SuperDARN radar for 05:01:57 UT - 05:51:33 UT on 11 January 1989. Panel (a) presents the latitudinal power profile and shows a narrow power peak within a latitudinal window of 2°. Panel (b) of Figure 2.6 shows the corresponding phase profile and illustrates a characteristic FLR signature by showing a 180° phase change across resonance. Both the clear peak in the power profile at a single latitude and the 180° phase change were predicted from theoretical work conducted by Southwood (1974) and Chen and Hasegawa (1974a).

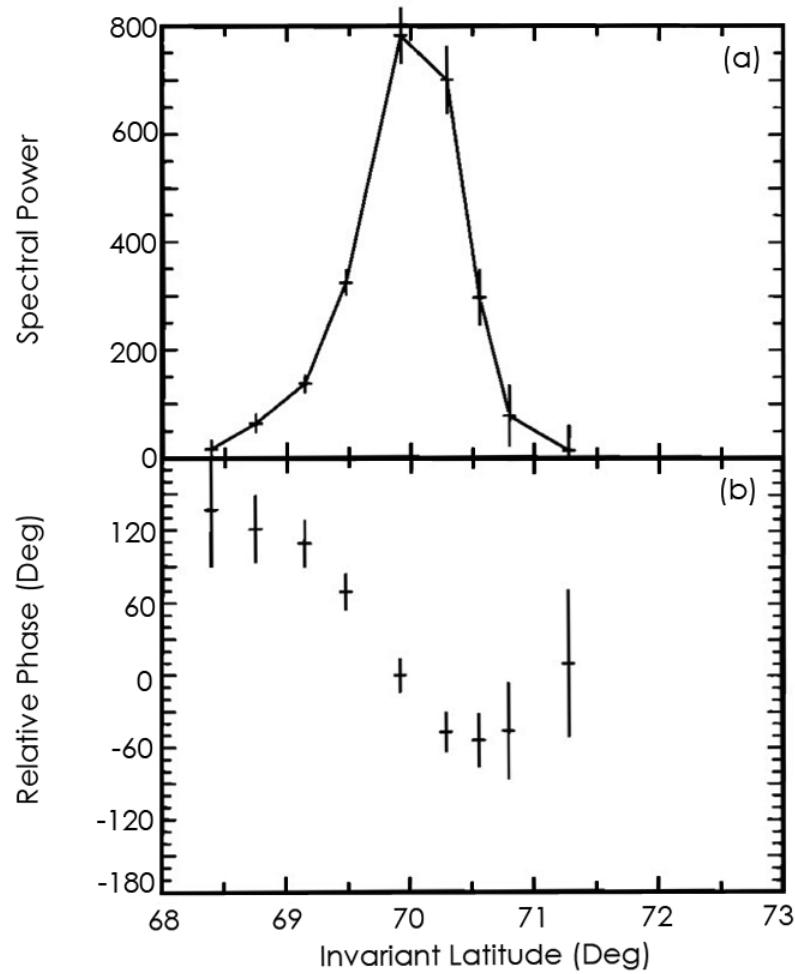


Figure 2.6: **(a and b)** Latitudinal power and phase profiles for 2.6 mHz along beam 8 of the Goose Bay SuperDARN radar for 05:01:57 UT - 05:51:33 UT on 11 January 1989. Panel (a) presents the latitude power profile while panel (b) shows the corresponding phase profile (Ruohoniemi et al., 1991).

## 2.6 Ultra Low Frequency Wave Generation Mechanisms

The Sun is clearly the energy source for all ULF wave activity. However, specific source mechanisms driving the wave activity may be classified into two categories, namely, internal or external magnetospheric drivers.

### 2.6.1 Internal Mechanisms

Internal sources, such as particle driven pulsations, are produced by particles within the terrestrial magnetosphere. In chapter 1, reconnection in the magnetotail was intro-

duced and the injection of highly energetic particles into near-Earth space was explained. Particle-wave interactions within the magnetosphere may clearly drive wave activity (e.g., Southwood, 1973; Glassmeier et al., 1999). Internal drivers are thought to drive small spatial-scale ULF waves whilst external drivers are thought to drive large spatial-scale ULF waves. Small-scale (internal) ULF wave drivers will not be considered further within this thesis. Further information on the internal mechanisms, associated with ULF wave activity, may be found within Baddeley (2003).

### **2.6.2 External Mechanisms**

External sources are those where the solar wind (or IMF) interacts with part of the outer magnetosphere exciting an FLR or cavity mode oscillation (McDiarmid, 1994). A fast mode wave source is Kelvin-Helmholtz (K-H) driven surface waves on the magnetospheric flanks caused by solar wind flow (e.g., Kivelson and Pu, 1984; Engebretson et al., 1998). One prime example of the K-H instability is wind blowing over a water surface, where the wind causes relative motion between the layers. The waves formed on the surface are the direct manifestation of the instability. In a similar manner, the magnetosheath plasma and the magnetopause are analogous to the "wind-flow" and the boundary layer between the water and air, respectively.

Figure 2.7 presents a schematic of the stimulation of an FLR by the K-H instability. The large arrows on Figure 2.7 illustrate the solar wind flowing from the subsolar point, at the "nose" of the magnetosphere, and then around the outside of the magnetospheric cavity. The K-H instability causes surface waves and structures, in the form of vortices, to form on the flanks (Hasegawa et al., 2005) and recent simulations of the instability agree with observation. The resonance condition is that the eigenfrequency of a field line matches the wave frequency of the evanescent surface wave, exciting a resonance (Allan and Poulter, 1992). Anderson et al. (1990) studied toroidal FLRs using AMPTE/CCE magnetic field data from  $L = 5$  to 9 in the equatorial magnetosphere, where  $L$  is the McIlwain  $L$ -parameter. The toroidal resonances were found to be the dominant wave activity in the dawn sector with an occurrence peak at 5 MLT - 7 MLT. Anderson et al. (1990) suggested

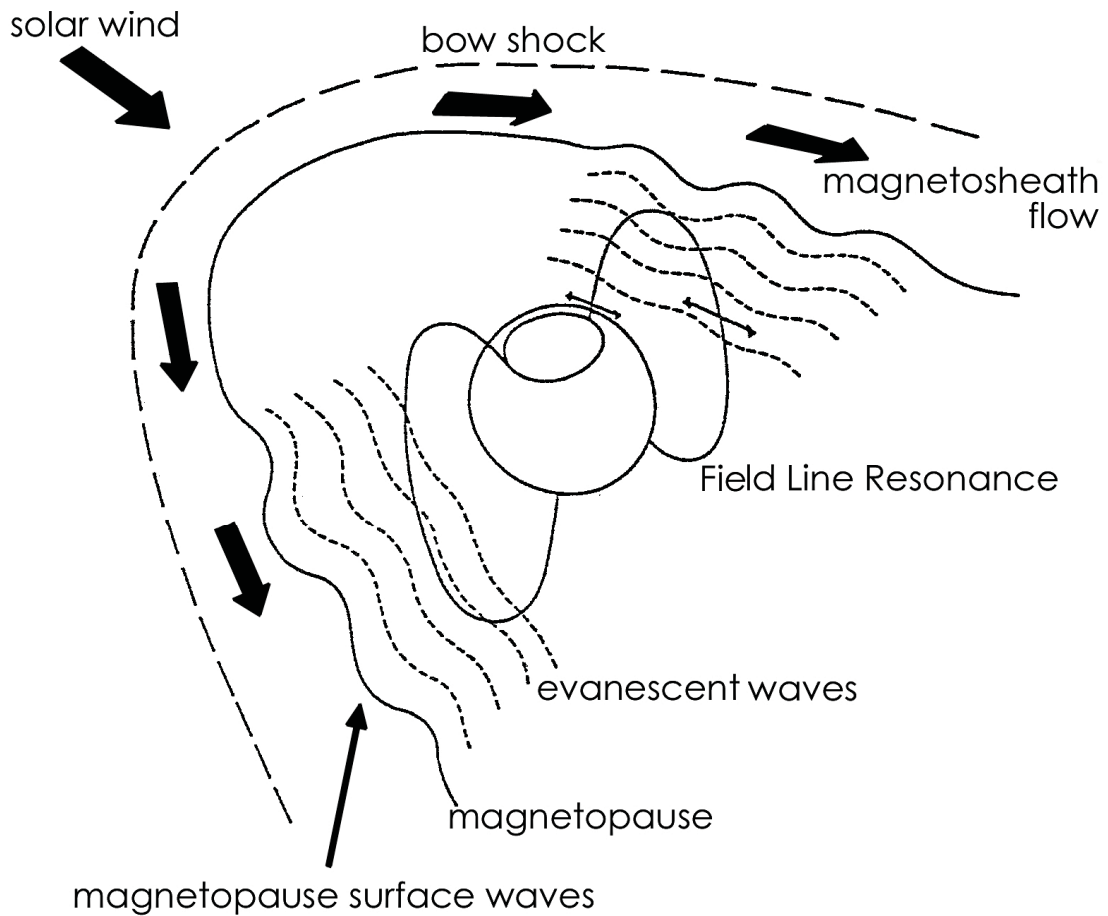


Figure 2.7: The stimulation of an FLR by the Kelvin-Helmholtz (K-H) instability. The evanescent waves on the flanks of the magnetosphere excite a resonance (adapted from Allan and Poulter, 1992).

that the resonances are present continuously at the dawn flanks implying the driver is the K-H instability.

Another mechanism that may generate ULF waves is known as an external impulse. External solar wind impulses, such as those caused by solar wind density fluctuations, may act as wave sources and drive magnetospheric waves (Zhang et al., 2009).

Chapter 5 investigates an impulsively excited pulsation. Such phenomena have been studied over a considerable period both experimentally (e.g., Siebert, 1964; Matsushita and Saito, 1967; Voelker, 1968) and theoretically (Tamao, 1965; Chen and Hasegawa, 1974b). In the case of an impulsively excited wave the source of the compressional mode lies in

the impulse, with this transient compressional mode then coupling to the Alfvén mode oscillation on a geomagnetic field line similarly to the more steady-state picture described previously (Southwood, 1976). An FLR is the result of such an interaction since the coupling allows energy to be transferred into the Alfvén mode. More recent observational, theoretical and modelling studies (e.g., Kivelson et al., 1984; Allan et al., 1986; Kivelson and Southwood, 1986; Allan et al., 1986b; Lee and Lysak, 1989; Samson, 1991) have subsequently developed the idea that following an impulse to, or solar wind buffeting of, the magnetosphere, it is the dimensions of the magnetospheric cavity that determine the eigenfrequencies of cavity or waveguide mode waves. These modes then couple to Alfvén modes, driving FLRs at discrete, harmonically related frequencies. Excitation of FLRs by magnetospheric waveguide modes have been detailed previously (e.g., Walker et al., 1992; Wright, 1994) and Samson et al. (1992) suggested that there are global waveguide modes. Fenrich et al. (1995) observed 12 ULF wave events using the Saskatoon, Kapuskasing, and Goose Bay SuperDARN radars. The 12 events spanned 1988 - 1994 and each event showed discrete-frequency FLRs. Lower frequencies were observed at higher latitudes, which is a characteristic of an Alfvén velocity gradient in the plasmatrough. Of noteworthy importance is a statistical study conducted within Fenrich et al. (1995), which presents the common ULF wave frequencies observed as a histogram. Figure 2.8 presents occurrence statistics for various resonant frequencies. The frequency bins are 0.2 mHz in width centred at 0.1, 0.3, 0.5 mHz e.t.c. For example, the bin centred at 1.3 mHz covers the range  $1.2 < f \leq 1.4$  mHz. Figure 2.8 implies that observations of mHz period geomagnetic pulsations occur at discrete frequencies.

Provan and Yeoman (1997) provided observations of discrete ULF wave frequencies using data provided by the Wick Very High Frequency (VHF) coherent radar. Figure 2.9 presents the latitude dependence of frequency spectra derived from time series of backscattered power from the Wick VHF coherent radar averaged over 16 days, between 01:45 UT - 02:45 UT. The linear colour scale shows the spectral power, which has been normalised to unity for each latitude bin. Also displayed are previous results from the Goose Bay radar (Samson et al., 1992), and the field-line resonance periods for each lat-

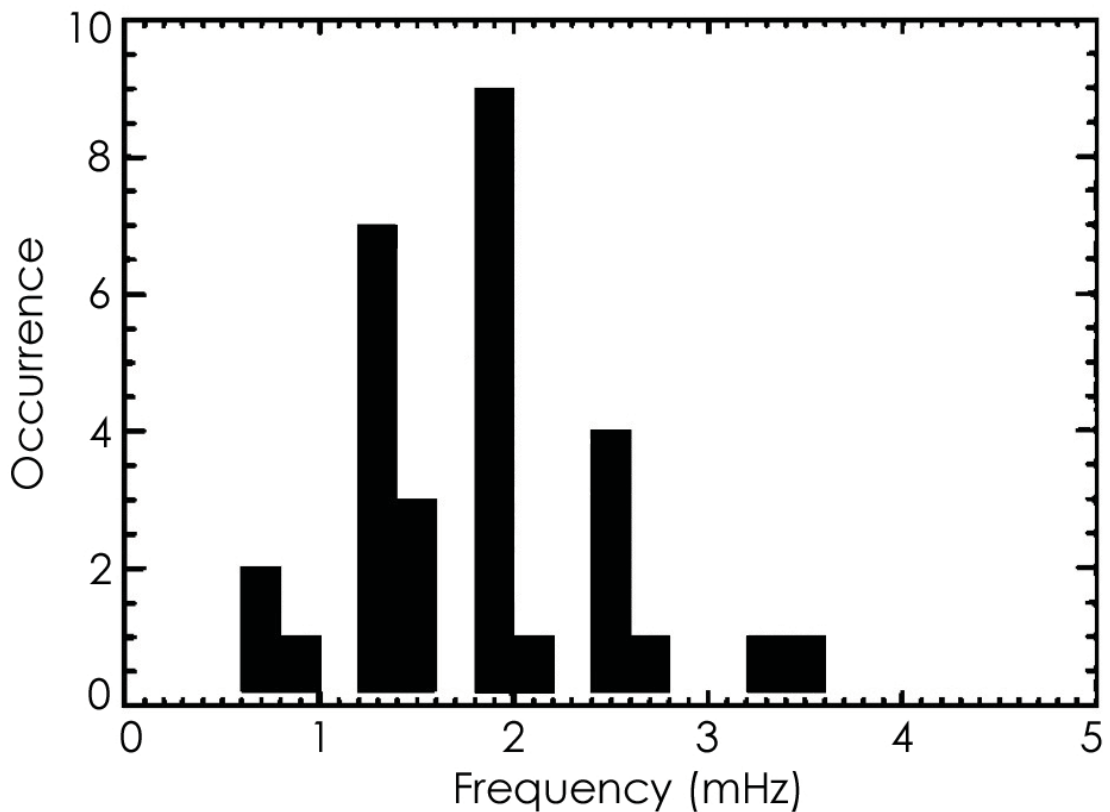


Figure 2.8: Occurrence statistics for various resonant frequencies. The frequency bins are 0.2 mHz in width centred at 0.1, 0.3, 0.5 mHz e.t.c. For example, the bin centred at 1.3 mHz covers the range  $1.2 < f \leq 1.4$  mHz (Fenrich et al., 1995).

itude, which are estimated from the Tsyganenko 89 (T89) model for two plasma-density regimes.

The spectra revealed within Figure 2.9 show three distinct peaks at 1.8 mHz, 2.4 mHz - 2.8 mHz, and 3.2 mHz. The spectral frequencies appear to decrease with increasing latitude, which is consistent with the results seen at Goose Bay shown by the grey shaded region. The solid and dot-dash lines show estimations of the first harmonic eigenfrequencies of magnetic flux tubes that are located within the magnetosphere. A plasma density of  $38 \text{ protons cm}^{-3}$  at  $L = 6$  is required in order to match the results of the Goose Bay SuperDARN radar.

Mann and Wright (1999) suggested that the velocity of the solar wind affects the waveguide modes. The authors also suggested that waves reflected at the "leaky" magnetopause boundary may increase their energy due to energy input from boundary instabilities in a

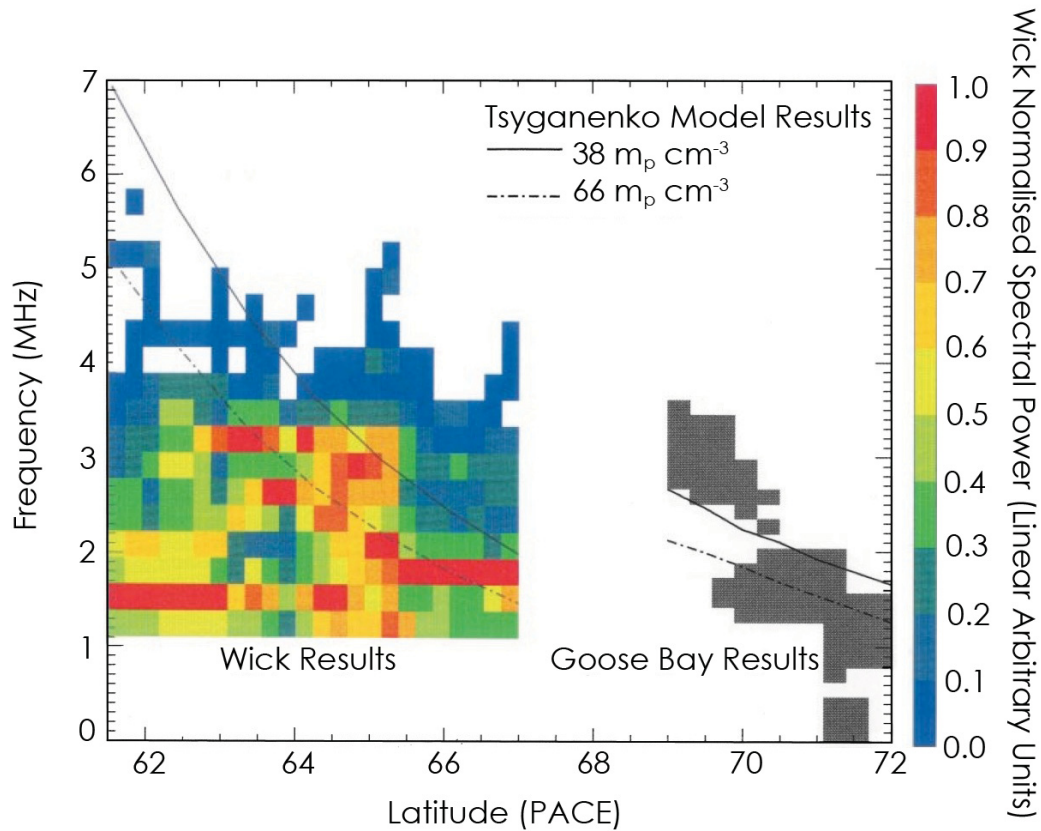


Figure 2.9: The latitude dependence of frequency spectra derived from time series of backscattered power from the Wick VHF coherent radar averaged over 16 days, between 01:45 UT - 02:45 UT. The linear colour scale shows the spectral power, which has been normalised to unity for each latitude bin. Also displayed are previous results from the Goose Bay SuperDARN radar, by the grey shaded region, (Samson et al., 1992), and the field-line resonance periods for each latitude, which are estimated from the Tsyganenko 89 model for two plasma-density regimes. (Provan and Yeoman, 1997).

process known as over-reflection. Figure 2.10 presents a schematic of over-reflection and shows that the conditions at the flanks of the magnetospheric cavity allow for (a) over-reflection and (b) trapped modes. Panel (a) of Figure 2.10 illustrates the magnetospheric waveguide for low-moderate solar wind velocities. The magnetopause near the subsolar point is leaky, which may drive small magnitude Alfvén waves. The magnetospheric flanks allow the excitation of FLRs as the waveguide mode wave passes over the perfectly reflecting magnetopause. Panel (b) of Figure 2.10 demonstrates how over-reflection is achieved at the magnetospheric flanks for a high solar wind velocity ( $> 500 \text{ km s}^{-1}$ ).

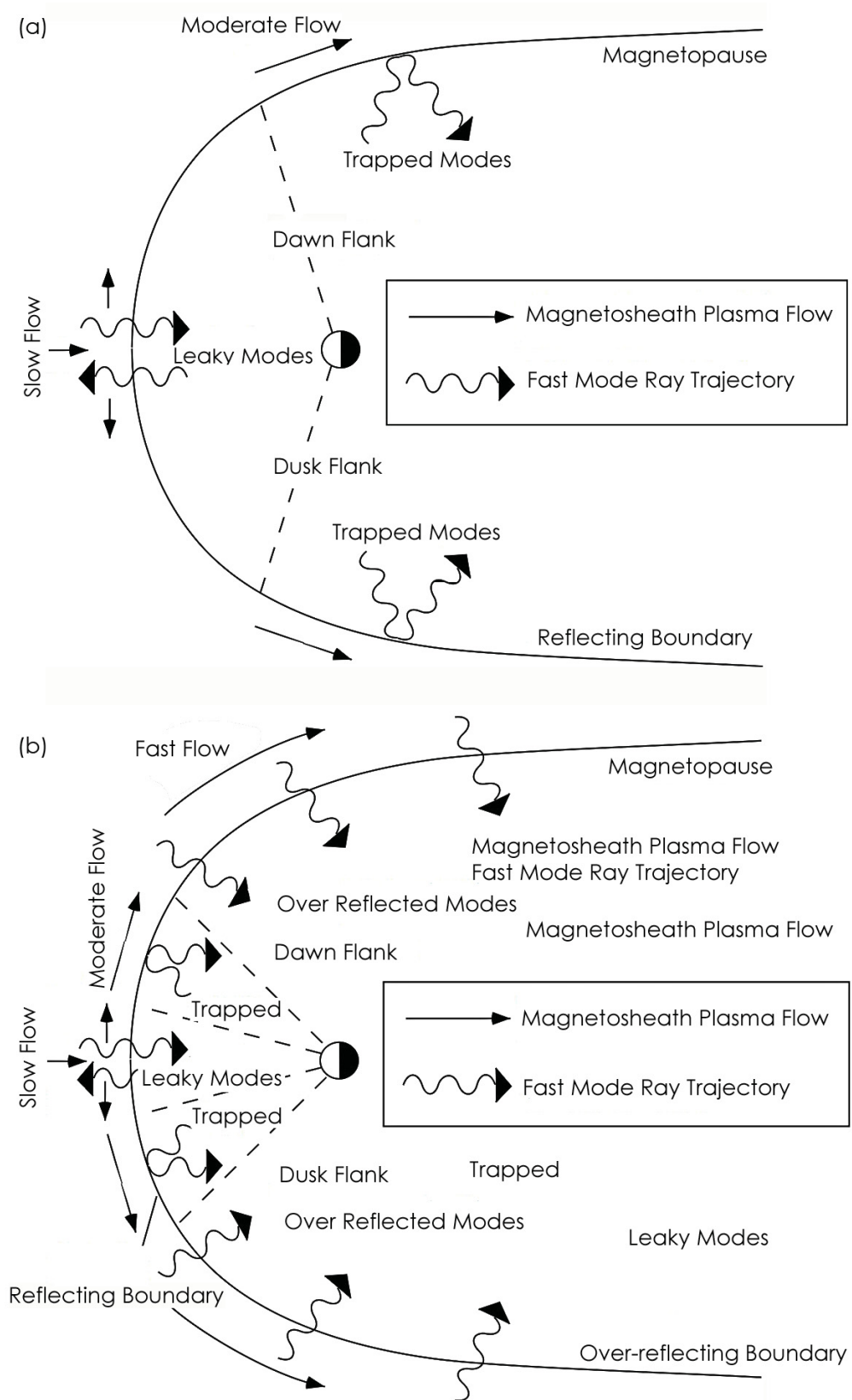


Figure 2.10: **(a and b)** A schematic demonstrating the effects of (a) moderate solar wind, and (b) high speed solar wind on the waveguide mode magnetopause boundary (adapted from Mann and Wright, 1999).

## 2.7 High-Frequency Radio Wave Sounding of the Ionosphere

A correlation between geomagnetic fluctuations and oscillations recorded by fixed-frequency vertically-sounding ionosondes was suggested by Dieminger et al. (1934) and observed later in auroral radar backscatter by Harang (1939). It was to be approximately 21 years later until the earliest example of correlations of magnetic field changes with fluctuations in the frequency of HF transmissions was reported by Fenwick and Villard (1960), which was precipitated by the invention of the continuous-wave (CW) Doppler technique by Watts and Davies (1960). Following the work by Fenwick and Villard (1960), numerous Doppler shift observations of reflected radio waves from the ionosphere have taken place. The purpose of the next section of this thesis is to outline and overview these observations and their contributions to ionospheric physics.

### 2.7.1 The Altar-Appleton-Hartree Equation

To understand the observed ULF wave signatures within, as well as outside, the ionosphere, the refractive index of a magnetoplasma must first be understood. The refractive index influences radio wave propagation and a sound usage of this parameter allows instruments to remote-sense the terrestrial upper atmosphere from the ground.

The refractive index,  $n$ , of a magnetoplasma may be determined from the Altar-Appleton-Hartree (AAH) equation, which may be expressed in its full form as:

$$n^2 = 1 - \frac{\frac{(\frac{n_0 e^2}{\epsilon_0 m})^{\frac{1}{2}})^2}{\omega^2}}{1 - i\frac{\nu}{\omega} - \frac{\frac{(B e)}{m} \sin \theta}{2(1 - \frac{(\frac{n_0 e^2}{\epsilon_0 m})^{\frac{1}{2}})^2}{\omega^2} - i\frac{\nu}{\omega})} \pm \left( \frac{\frac{(B e)}{m} \sin^4 \theta}{4(1 - \frac{(\frac{n_0 e^2}{\epsilon_0 m})^{\frac{1}{2}})^2}{\omega^2} - i\frac{\nu}{\omega})^2} + \frac{(B e)}{m} \cos^2 \theta \right)^{\frac{1}{2}}, \quad (2.54)$$

where  $\omega$  is the radio wave angular frequency,  $B$  is the magnetic field,  $m$  is the electron mass,  $\nu$  is the electron collision frequency,  $\theta$  is the angle between the direction of propagation and the magnetic field (e.g., Hunsucker and Hargreaves, 2003). Equation 2.54

implies that the refractive index of the ionosphere varies with altitude since it depends on the electron density. The refractive index is complex as it contains both real and imaginary parts. Thus,  $n$  may be expressed as  $n = \mu - i\chi$ . Equation 2.54 contains a  $\pm$  sign and hence this equation shows that there are, in fact, two solutions for the refractive index. The minus sign is for the extraordinary (X-mode) wave, while the positive sign represents the ordinary (O-mode) wave. The AAH equation may be simplified by neglecting both the magnetic field and collision frequencies to become

$$n^2 = 1 - \frac{n_0 e^2}{4\pi^2 \epsilon_0 m f^2}, \quad (2.55)$$

where  $f$  is the frequency of the transmitted wave. Equation 2.55 implies that a wave with a plasma frequency equal to the transmitted wave frequency will be reflected, whereas a wave with a frequency greater than the plasma frequency will pass through the ionosphere. Clearly, this is important for spacecraft and satellite communication but it is also important if ionospheric characteristics need to be determined. This thesis is concerned with measuring the ionospheric signature of ULF waves using HF Doppler sounders as a primary diagnostic tool and, therefore, the critical frequency is a very important parameter for this study.

### **2.7.2 HF Doppler Ultra Low Frequency Wave Modelling**

Variations in the ionosphere resulting from ULF waves will change the phase path of a radio wave, and hence result in a frequency shift in the received radio wave detected by an HF Doppler sounder. This section introduces ULF wave modelling using the work conducted in a set of papers by Poole and Sutcliffe (1988); Sutcliffe and Poole (1989, 1990), which presented model results of Doppler shift mechanisms as a function of reflection altitude, based upon the AAH equation. The mathematical foundation of the model will be discussed in detail in section 4.2.

The first study contained within Sutcliffe and Poole (1990) used an electron density profile for sunspot maximum, local midday, and at a mid-latitude (St. Santin 44.1° N, 2.0° E)

location, from the International Reference Ionosphere (IRI 79). Other parameters used in their computations were an inclination angle of  $I = +60^\circ$ , a background field intensity,  $B_0 = 30,000$  nT, a pulsation period of 20 s, a north-south characteristic scale-length of  $L_x = 500$  km and an east-west characteristic scale-length,  $L_y = 6000$  km.

Figure 2.11 presents the corresponding Sutcliffe-Poole model results revealing the Doppler velocity and phase variation with transmit frequency, and hence reflection height.

Panels (a) and (b) show the Doppler velocity and phase variation with reflection height, respectively. The symbols used for the various mechanisms are as follows: total Doppler velocity (+); contributing mechanisms: "magnetic" (o); "advection" (x) and "compressional" ( $\Delta$ ). All parameters are measured relative to a north-south wave magnetic field perturbation,  $b_x$ , of 1 nT and  $0^\circ$  phase.

The absence of data points at  $\sim 120$  km in each panel of Figure 2.11 is due to the valley between the E- and F-regions of the ionosphere in the electron density profile. Panels (a) and (b) of Figure 2.11 show a reduction in the total Doppler shift between approximately 120 km - 280 km. The amplitude reduction is caused by the phase difference between the contributing mechanisms when they are added vectorially. Between 160 km - 240 km, the total Doppler shift amplitude is less than the individually contributing amplitudes of either the advection or the compressional mechanisms.

Panels (c) and (d) of Figure 2.11 present similar data from Sutcliffe and Poole (1990) but now for summer and sunspot maximum conditions at local midnight. A comparison between panel (a) of Figure 2.11 with panel (c) of Figure 2.11 reveals that the Doppler velocity at midnight is much greater than at noon for similar conditions. To sustain the perturbation magnetic fields recorded on the ground, the electric field vector in the E-region must be larger to compensate for the lowered Pedersen and Hall conductivities in the nighttime E-region. Sutcliffe and Poole (1990) explained that the Y component of the electric field vector is 10 - 50 times larger at midnight compared with midday.

Figure 2.12 presents data from Sutcliffe and Poole (1990) but now for winter and sunspot minimum conditions at local noon for the same mid-latitude location. A comparison of panel (a) from Figure 2.11 with panel (a) of Figure 2.12 demonstrates that on average

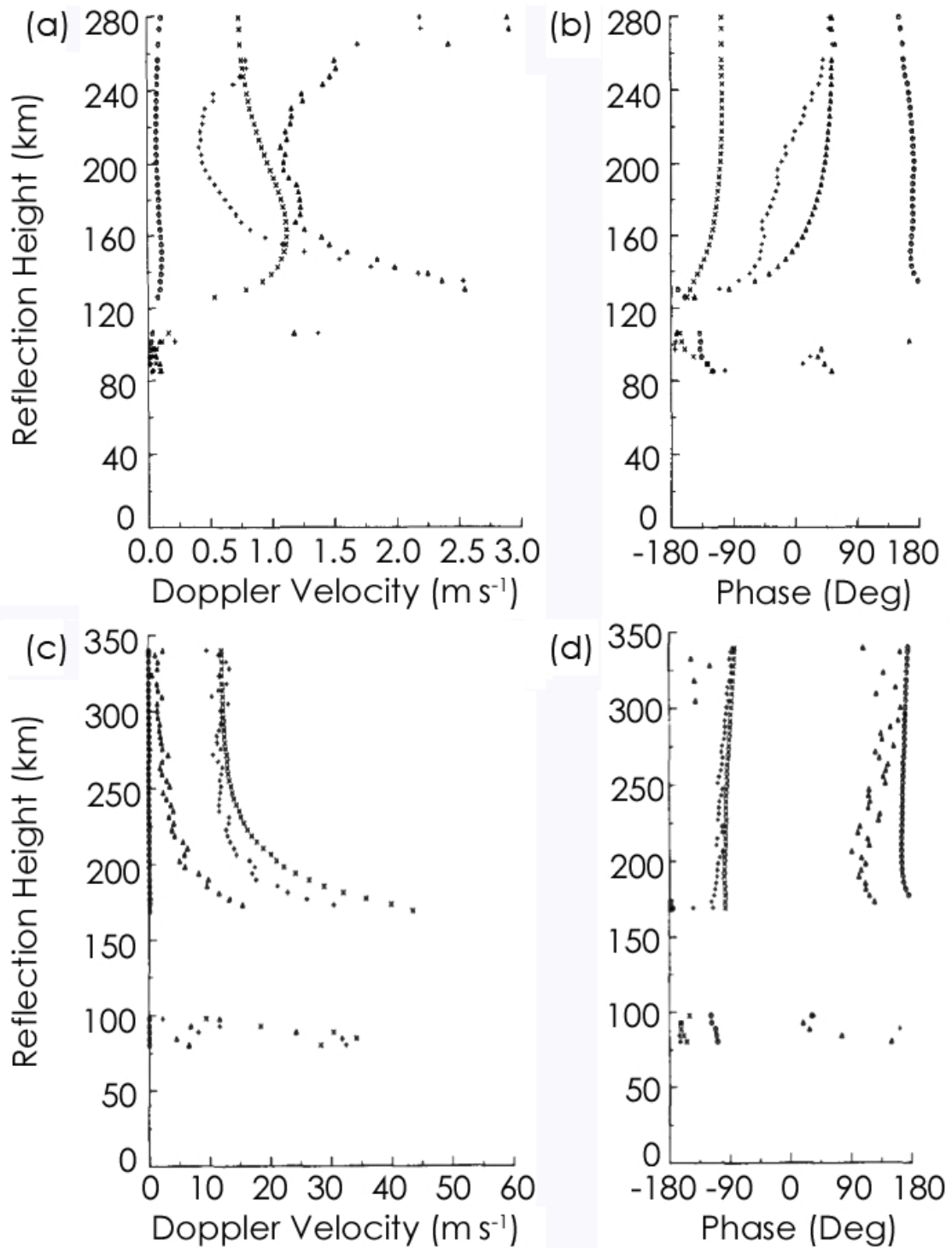


Figure 2.11: **(a – d)** The model results for midday and midnight, sunspot maximum, at a mid-latitude location, presenting the Doppler velocity and phase variation with reflection height. Panels (a) and (b) show the midday results from Sutcliffe and Poole (1990) while panels (c) and (d) show the midnight results. All four panels give the Doppler velocity and phase variation with reflection height. The symbols used for the various mechanisms are as follows: total Doppler velocity (+); contributing mechanisms: "magnetic" (o); "advection" (x) and "compressional" ( $\Delta$ ). All phases are measured relative to a north-south wave magnetic field perturbation,  $b_x$ , of 1 nT.

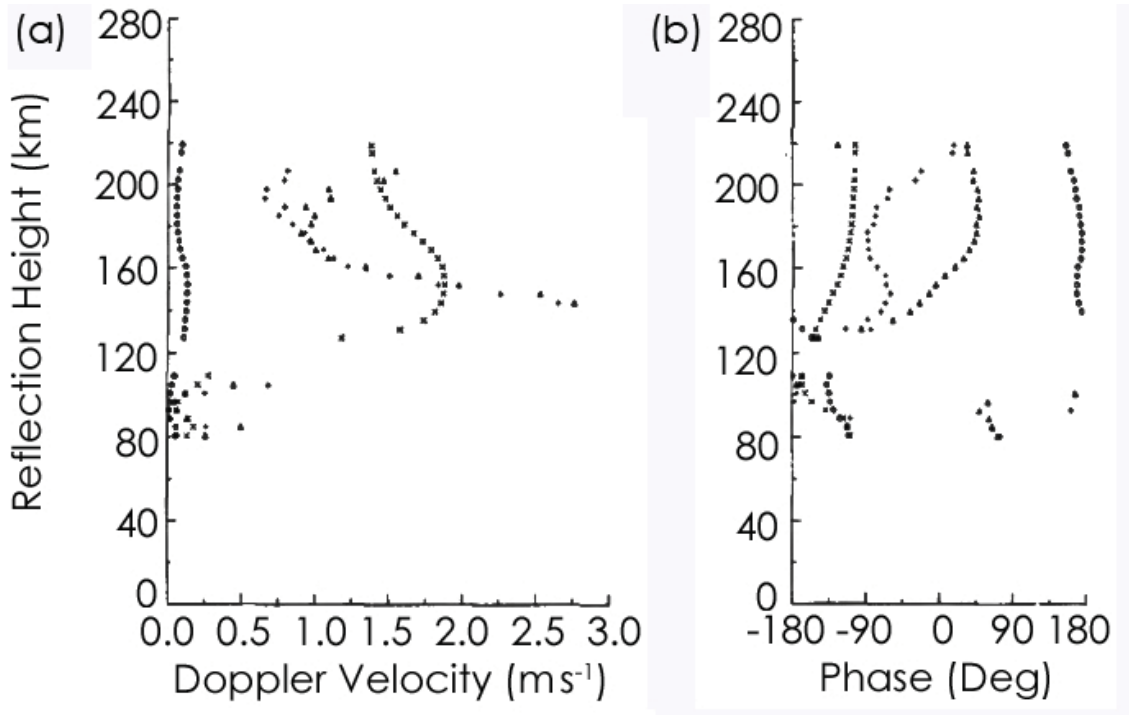


Figure 2.12: **(a and b)** The model results for noon, sunspot minimum, winter, at a mid-latitude location, revealing the Doppler velocity and phase variation with reflection height. Panels (a) and (b) present the results from Sutcliffe and Poole (1990) showing the Doppler velocity and phase variation with reflection height. The symbols used for the various mechanisms are as follows: total Doppler velocity (+); contributing mechanisms: "magnetic" (o); "advection" (x) and "compressional" ( $\Delta$ ). All phases are measured relative to a north-south wave magnetic field perturbation,  $b_x$ , of 1 nT.

advection slightly increases in the winter season and that compression slightly decreases. Sutcliffe and Poole (1990) also show that the phase change is relatively small between summer and winter conditions.

In general, the overall Doppler shift tends to increase slightly with decreasing sunspot number. The opposing relative phase behaviour between the advection and compressional mechanisms explains the weakening of the overall Doppler shift amplitude compared with the larger individual contributing amplitudes. In all comparisons detailed here, the magnetic mechanism appears to provide a negligible contribution to the overall Doppler shift.

### 2.7.3 HF Doppler Ultra Low Frequency Wave Observations

Davies et al. (1962) suggested that changes in the ionospheric morphology produce variations in the frequency of waves emitted from a frequency stable transmitter. Davies et al. (1962) described observations from a radio station located near Washington, D. C., which was designated WWV. The received signal was compared to a local oscillating signal, which had a high frequency stability. When the frequency was "disturbed" upward, a downward motion of the reflection altitude was indicated. Panel (a) of Figure 2.13 presents observations of quiet conditions recorded on 31 January 1961. Strong signals were observed in the data at about 05:30 UT, 08:12 UT and 14:33 UT coinciding with solar flare activity. Panel (b) shows disturbed conditions, recorded on 15 November 1960, where rapid variations in the frequency occurred and the peaks may broaden (Fenwick and Villard, 1960). Davies et al. (1962) concluded that Doppler shifts observed by HF Doppler sounders are correlated with solar flares and magnetic disturbances.

Klostermeyer and Röttger (1976) observed Pi2 pulsations at Lindau, FRG (geographic: 55.6°N, 10.1°E) with a frequency range of between 8.3 mHz - 33 mHz yielding Doppler shifts of order 0.3 Hz. Figure 2.14 presents three examples of Doppler frequency oscillations correlated with ground-based magnetometer measurements. Panels (a) to (c) present data from 16 October 1975 between 18:29 UT - 18:39 UT, 22 October 1975 between 20:32 UT - 20:42 UT, and 22 October 1975 between 21:20 UT - 21:30 UT, respectively. The HF Doppler data,  $\Delta f$ , were recorded using a quasi-vertical incident sounding frequency of 3.57 MHz. The figure displays magnetometer data from the east-west,  $\Delta D$ , and the north-south,  $\Delta H$ , directions. Figure 2.14 shows that the oscillations occurred simultaneously in both the Doppler data and the magnetic field measurements. The Doppler velocity,  $U_{ez}$ , in  $\text{m s}^{-1}$ , may be calculated using  $\Delta f$ . Figure 2.15 presents  $|U_{ez}|$  plotted as a function of  $|\Delta H|$  for plasma critical frequencies of between 2.6 MHz - 3.2 MHz (black circles) and less than 1.5 MHz (open circles). Figure 2.15 clearly demonstrates a strong correlation between geomagnetic pulsations recorded by ground-based magnetometers and oscillations recorded in the ionosphere by HF Doppler sounders.

Klostermeyer and Röttger (1976) went on to show that their results were consistent with

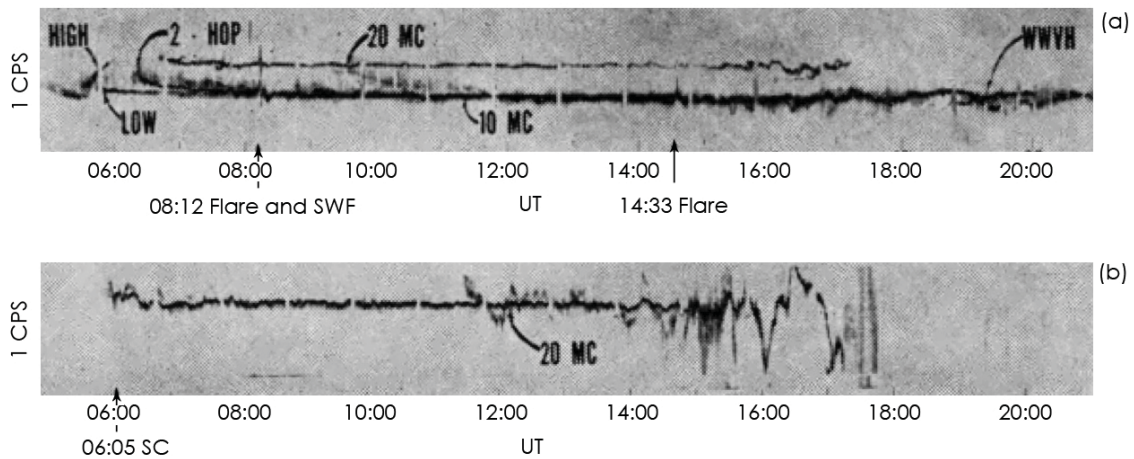


Figure 2.13: **(a and b)** HF Doppler frequency records. Panel (a) shows an example from 31 January 1961 showing quiet conditions. Panel (b) presents an example from 15 November 1960, which shows disturbed conditions (Davies et al., 1962).

an oscillating electric field causing the motor effect within the ionosphere. This was later termed the "advection" mechanism after work by Poole and Sutcliffe (1988), which was discussed in section 2.7.2 of this thesis.

Menk et al. (1983) continued the work of (Klostermeyer and Röttger, 1976) by investigating correlations between ionospheric disturbances and geomagnetic pulsations during sudden storm commencements.

Figure 2.16 presents ionospheric and magnetic oscillations associated with a sudden storm commencement on 20 August 1979 between 16:20 L.T. - 16:29 L.T. Panel (a) shows the change in magnetic intensity with time. Panels (b) and (c) present the Doppler frequency shift time series for sounding frequencies of 5.5 MHz and 8.34 MHz, respectively. Menk et al. (1983) concluded that sudden storm commencements are associated with ionospheric oscillations and simultaneous changes in HF phase path.

Menk (1992) investigated the mechanisms, which affect perturbations in ionospheric signatures of down-going Pc3-4 and Pi2 ULF waves. An example of this study, presented in Figure 2.17, shows a clear Pc3 wave signature at a low-latitude location (geomagnetic 46.7°S, 220.8°E). Figure 2.17 presents ionospheric Doppler and ground magnetic oscillations recorded between 19:37 AEST (Australian Eastern Standard Time) - 19:52 AEST on the 20 August 1979. Panels (a), (b) and (c) show the change in magnetic field

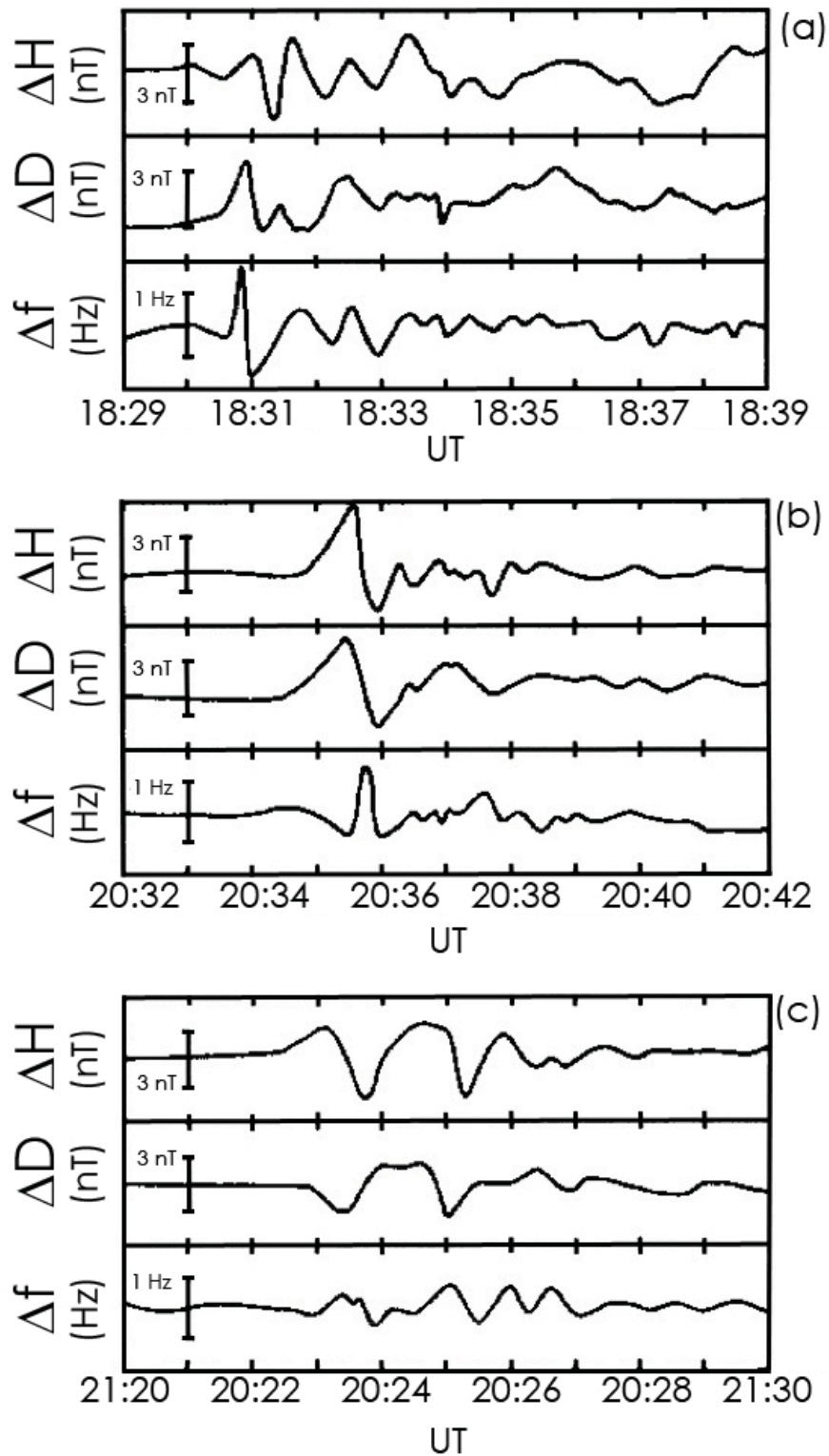


Figure 2.14: (a – c) Three examples of Doppler frequency oscillations correlated with ground-based magnetometer measurements of the terrestrial magnetic field. Panels (a) to (c) present data from 16 October 1975 between 18:29 UT - 18:39 UT, 22 October 1975 between 20:32 UT - 20:42 UT, and 22 October 1975 between 21:20 UT - 21:30 UT, respectively. The HF Doppler data are recorded using a quasi-vertical incident sounding frequency of 3.57 MHz (Klostermeyer and Röttger, 1976).

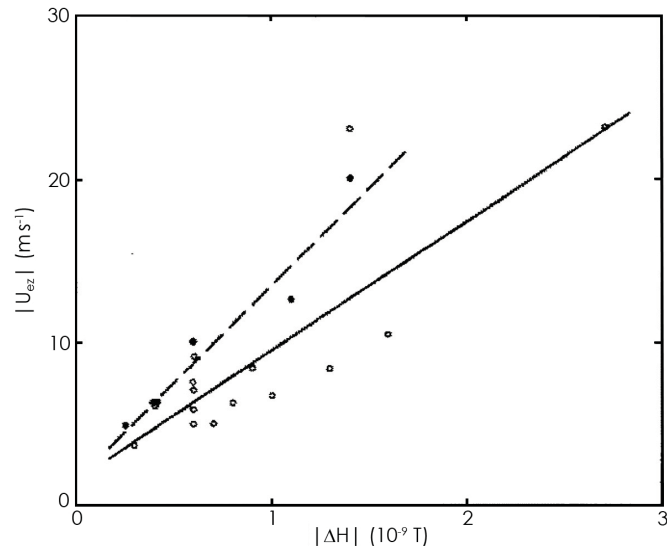


Figure 2.15:  $\Delta H$  as a function of  $|U_{ez}|$  for plasma critical frequencies of between 2.6 MHz - 3.2 MHz (black circles) and less than 1.5 MHz (open circles) (Klostermeyer and Röttger, 1976).

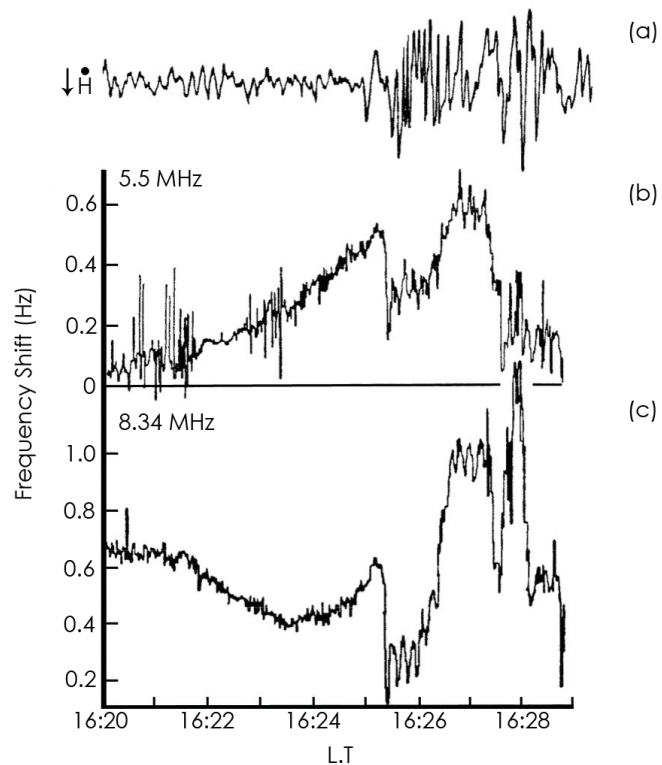


Figure 2.16: (a – c) Ionospheric and magnetic oscillations associated with a sudden storm commencement recorded on 20 August 1979 between 16:20 L.T. - 16:29 L.T. Panel (a) shows the change in magnetic intensity with time. Panels (b) and (c) present the Doppler frequency shift time series for sounding frequencies of 5.5 MHz and 8.34 MHz, respectively (Menk et al., 1983).

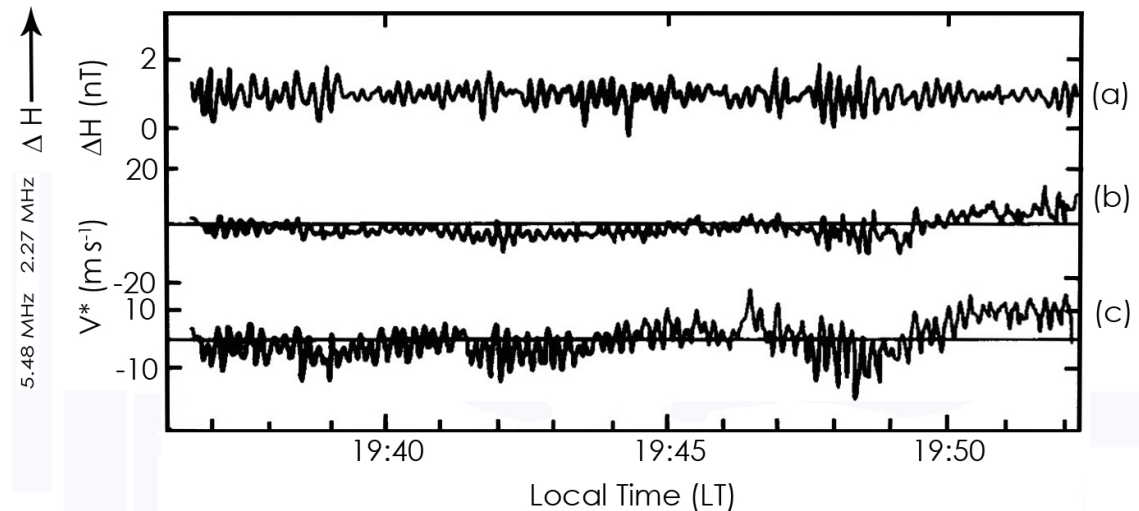


Figure 2.17: (a – c) Ionospheric Doppler and ground magnetic oscillations recorded between 19:37 AEST (Australian Eastern Standard Time) - 19:52 AEST on the 20 August 1979. Panels (a), (b) and (c) show the change in magnetic field intensity,  $\Delta H$ , in nT, the vertical-incidence Doppler shift,  $V^*$  at 2.27 MHz and the vertical-incidence Doppler shift at 5.48 MHz (Menk, 1992).

intensity,  $\Delta H$ , in nT, the vertical-incidence Doppler shift,  $V^*$ , at 2.27 MHz and the vertical-incidence Doppler shift at 5.48 MHz, respectively. Panels (a) - (c) show that the majority of the Doppler oscillations are in phase with the ground magnetic field signatures. Panels (b) and (c) use data from different sounding frequencies such that panel (b) corresponds with a reflection altitude of approximately 270 km while panel (c) corresponds to an altitude of roughly 330 km. Menk (1992) used an ionogram to determine these values.

Menk (1992) used the modelling work of Sutcliffe and Poole (1990) to analyse their observational results. The specific model used for comparison was detailed in panels (a) and (b) of Figure 2.11 for midday summer at solar maximum.

Thus, Menk (1992) concluded that during the day the advection mechanism was contributing the most to the overall Doppler shift amplitude. Of importance, Menk (1992) realised that the modelling work of Sutcliffe and Poole (1990) assumed only shear Alfvén waves were incident on the ionosphere. Menk (1992) suggested that the plasmasphere contains global cavity resonance modes and coupling between the fast and transverse modes will occur (Kivelson and Southwood, 1988). Menk (1992) concluded that while the Pi pulsa-

tions yield model Doppler shifts that were different from reality, there were similarities between the observations and modelling of Pc3-4 waves.

Wright et al. (1997) used an HF Doppler sounder for observations and showed that their ULF wave events exhibited relative phases in the range  $90^\circ$  -  $150^\circ$  with  $b_y$  leading. Figure 2.18 presents a histogram of these 10 results. Using the model developed by Poole and Sutcliffe (1988), Wright et al. (1997) made some tentative conclusions for the mechanisms generating the observed Doppler shift signatures at high-latitude. Comparing Figure 2.18 with modelling studies conducted by Sutcliffe and Poole, Wright et al. (1997) concluded that 60% of their observed ULF wave signatures were a result of the advection mechanism. The observations contained within Wright et al. (1997) also suggested that the Alfvénic signatures at high-latitude dominated over an extensive latitudinal region.

Another example of HF Doppler shift observations of ULF wave activity was reported by Wright et al. (1998) where the authors compared European Incoherent Scatter (EISCAT) and Doppler Pulsation Experiment (DOPE) observations of ULF wave activity.

Figure 2.19 presents HF Doppler, International Monitor for Geomagnetic Effects (IMAGE) magnetometer and EISCAT UHF data for a ULF signature recorded on 13 February 1996 between 11:00 UT - 11:40 UT.

Panel (a) shows the Doppler peak traces for the O- and X-modes. A clear wave signature can be seen within the Doppler data between 11:00 UT - 11:40 UT. Panel (b) shows the TRO-X (Tromsø-X) and TRO-Y magnetic field measurements. The relative phase of TRO-Y and the Doppler O-mode signature was determined to be approximately  $160^\circ$  with  $b_y$  leading. Fourier analysis reveals a Pc5 wave of frequency 4 mHz. Using IMAGE Y component data the effective azimuthal wavenumber was determined to be approximately -3 where the negative sign indicated a westwards propagating wave. All data in panels (a) and (b) were filtered to exclude waves with periods outside of the range 60 s - 300 s.

Wright et al. (1998) then compared their observational results with those from the model developed by Poole and Sutcliffe (1988) and deduced that the ionospheric signature was most likely caused by the vertical motion of the ionosphere being driven by  $\mathbf{E} \wedge \mathbf{B}$  drift. The wave, therefore, was assumed to have Alfvénic behaviour and the signature in the

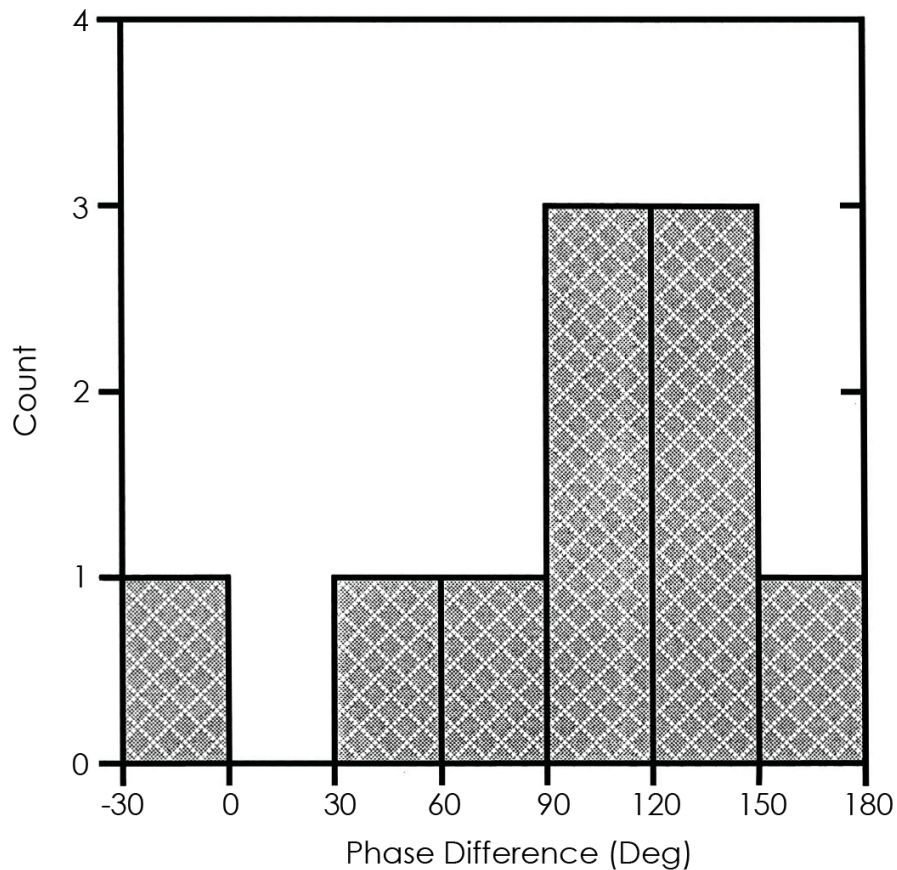


Figure 2.18: The phase difference occurrence between TRO-Y and the Doppler O-mode signature recorded by the DOPE instrument. A leading TRO-Y component is indicated by a positive phase difference (Wright et al., 1997).

ionosphere was deduced to be the result of the Poole and Sutcliffe (1988) "advection mechanism."

This interpretation was confirmed with data from the EISCAT radar, which provided a direct measurement of the electric field. Panel (c) of Figure 2.19 shows the northward,  $V_n$ , and eastward,  $V_e$ , components of the field perpendicular velocity recorded by the EISCAT UHF radar filtered to exclude waves with periods outside of the range 120 s-400 s. The vertical component of the northward field perpendicular velocity provided by measurements from EISCAT yields a value of the Z component of the  $\mathbf{E} \wedge \mathbf{B}$  drift velocity, which is effectively the advection mechanism provided by Poole and Sutcliffe (1988).

Waters et al. (2007) investigated the amplitudes of two ULF wave events recorded at high-latitude (geographic: 69.6°N, 19.2°E) with an HF Doppler sounder, ground-based

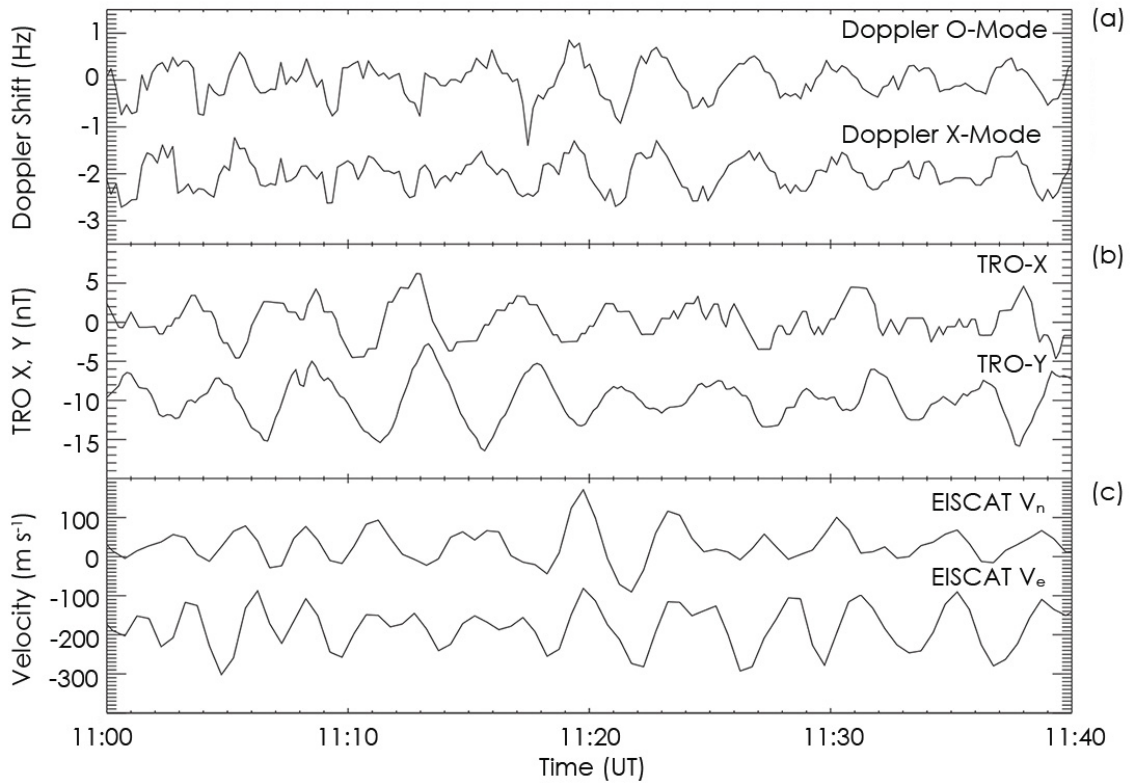


Figure 2.19: **(a – c)** HF Doppler, IMAGE magnetometer and EISCAT (European Incoherent Scatter) data for a ULF signature recorded on 13 February 1996 between 11:00 UT - 11:40 UT. Panel (a) shows the Doppler peak traces for the O- and X-modes. Panel (b) shows the TRO-X and TRO-Y magnetic field measurements. Panel (c) shows the northward and eastward components of the field perpendicular velocity recorded by the EISCAT UHF radar. Data are filtered to exclude waves with periods outside of the range 60 s - 300 s, in panels (a) to (b) and 120 s- 400 s, in panel (c) (Wright et al., 1998).

magnetometers, and a numerical model developed by Sciffer et al. (2005). The authors showed that the model could correctly determine the amplitudes of ULF waves. This numerical model will be detailed in chapter 4 but it is worth mentioning here that the model allows for a mixture of incident wave modes unlike the modelling work conducted by Poole and Sutcliffe (1988); Sutcliffe and Poole (1990), which assumed a purely Alfvénic incident mode.

Describing the first comparisons of observed changes in radio frequency with predictions of the Poole and Sutcliffe (1988); Sutcliffe and Poole (1989, 1990) model Waters et al. (2007) used parameters relevant for two specific ULF wave events. The experimental constraints were the radio frequency, the observed Doppler shifts, and the ground

magnetic field perturbations. The ground magnetic field measurements and the east-west wavenumber,  $k_y$ , were determined from ground-based magnetometers and the value of the north-south wavenumber,  $k_x$ , was inferred from the work by Hughes (1974). Figure 2.20 presents data from Waters et al. (2007) showing magnetic field, electric field, and the corresponding Doppler shift modelling results for two ULF wave events recorded by an HF Doppler sounder. Panels (a) to (c) show the first event, which occurred on 25 March 2002 between 16:00 UT - 18:00 UT where a purely Alfvénic incident wave mode was assumed while panels (d) to (f) show the second event recorded on 24 March 2001 between 04:30 UT - 05:30 UT when a 90% Alfvénic (10% fast compressional) incident wave mode was used. Panels (a) and (d) show the ULF wave magnetic fields with  $b_x$ ,  $b_y$  and  $b_z$  shown by the solid, dotted, and dashed lines, respectively. Panels (b) and (e) present the ULF wave electric field amplitudes with  $e_x$ ,  $e_y$  and  $e_z$  shown by the solid, dotted, and dashed lines, respectively. Panels (c) and (f) show the resulting model Doppler shifts after applying the Poole and Sutcliffe (1988) model where  $V_I$  (X),  $V_{II}$  (+),  $V_{III}$  (squares) and  $V^*$  (\*). Panels (c) and (f) both indicate that advection is the dominant process affecting the Doppler shift for these two ULF wave events. Waters et al. (2007), therefore, showed that the Poole and Sutcliffe (1988) model predicts the correct magnitudes for the Doppler shifts and identifies advection as the dominant mechanism.

## 2.8 Summary

This chapter reviews the underpinning theoretical concepts and exemplary observations, which have allowed scientists to explore near-Earth ULF wave phenomena in unprecedented detail. Principal ground data sources for this scientific endeavour were provided by magnetometer arrays, HF Doppler sounders, and SuperDARN. The chapter firstly outlined basic theory surrounding ULF waves, considering both cold and warm plasma waves before focussing on the ionospheric boundary conditions and the ionospheric reflection coefficient. The basic theory surrounding field line resonances was detailed with the box model developed by Southwood (1974).

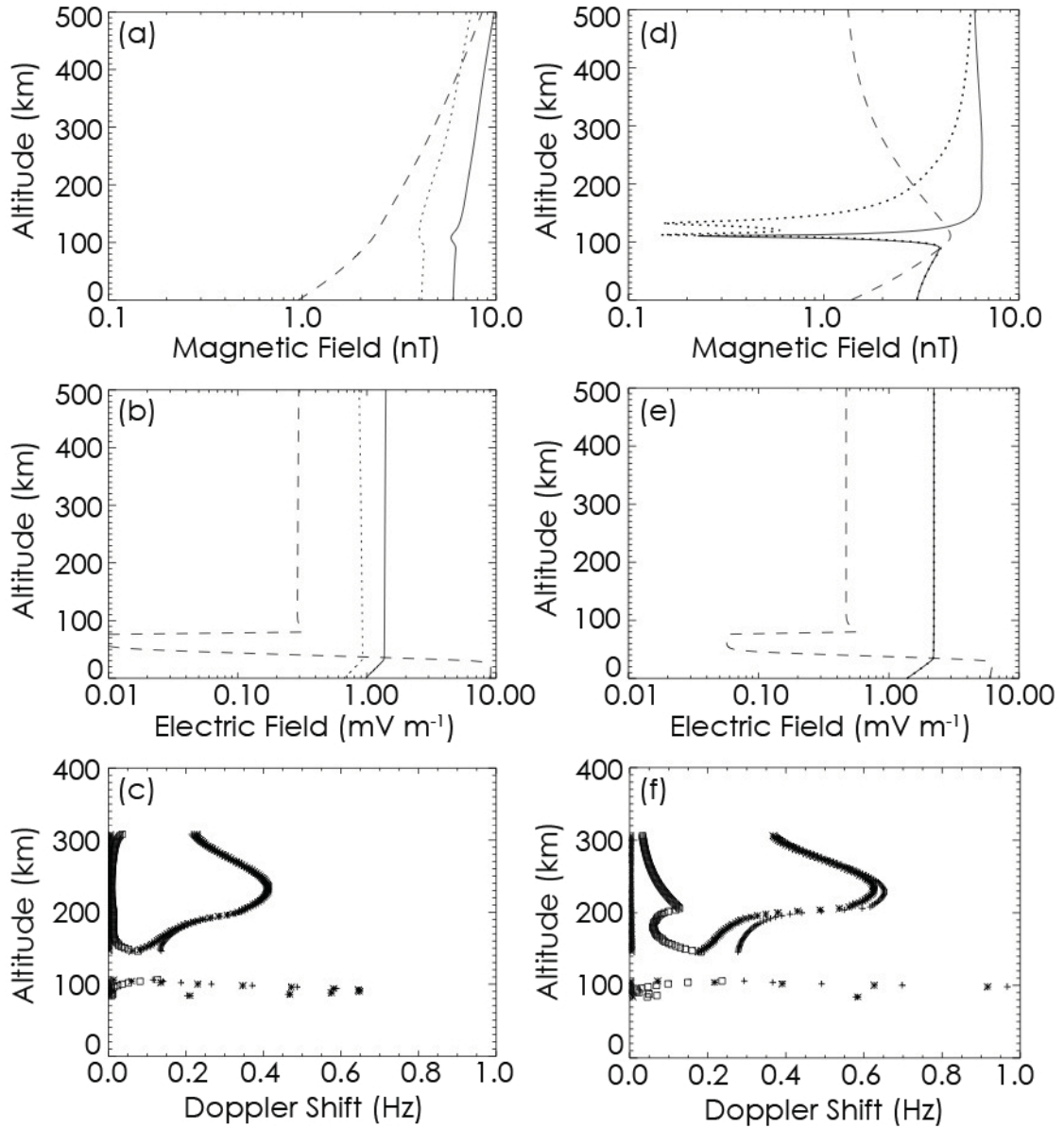


Figure 2.20: (a – f) A figure showing magnetic field, electric field, and corresponding Doppler shift modelling results for two ULF wave events recorded by an HF Doppler sounder. Panels (a) to (c) show the first event which occurred on 25 March 2002 between 16:00 UT - 18:00 UT while panels (d) to (f) show the second event recorded on 24 March 2001 between 04:30 UT - 05:30 UT. Panels (a) and (d) show the ULF wave magnetic fields with  $b_x$ ,  $b_y$  and  $b_z$  shown by the solid, dotted and dashed lines, respectively. Panels (b) and (e) present the ULF wave electric field amplitudes with  $e_x$ ,  $e_y$  and  $e_z$  shown by the solid, dotted and dashed lines, respectively. Panels (c) and (f) show the model Doppler shifts where  $V_I$  (X),  $V_{II}$  (+),  $V_{III}$  (squares) and  $V^*$  (\*) (Waters et al., 2007).

ULF wave observations have been detailed here and have highlighted the importance of SuperDARN as an analysis tool of ULF waves (e.g., Ruohoniemi et al., 1991). Ionospheric observations provided by HF Doppler sounders, combined with the vast abundance of ground magnetometer data provided by magnetometer chains, yield large statistical data sets recording geomagnetic pulsations. The chapter then considered HF Doppler sounders and their role in understanding ULF wave activity. The modelling of ULF waves, with a particular focus on the work by Poole and Sutcliffe (1988), Sutcliffe and Poole (1989) and Sutcliffe and Poole (1990), complements the vast array of observational data. Example studies provided by Wright et al. (1997) and Menk (1992) showed that there are necessities for more advanced models to understand the vast abundance of wave activity that propagate within the terrestrial space environment such as that introduced with the work by Waters et al. (2007). The Sutcliffe-Poole model used in this work demonstrates that although the velocity observed by an HF Doppler sounder varies with altitude, the greatest change occurs over a very narrow region, which corresponds to peak FoF2. The Sutcliffe-Poole model is not a high-latitude model but instead operated at mid-latitudes. In section 4.3.2 of this thesis, the results of the model developed by Sciffer et al. (2005), which may be run at any geographic location, will be used to analyse the conclusions and extrapolations made by Wright et al. (1997).

# Chapter 3

## Instrumentation

### 3.1 Introduction

This section outlines the instrumentation used in chapters 4, 5, 6 and 7 of this thesis. In order to provide a full understanding of the dynamic processes, which take place in the near-Earth space environment, a vast array of instrumentation must be employed. The use of HF radar, HF Doppler sounders, ground-based magnetometers, and ionosondes in conjunction with space-based instrumentation all provide necessary information about both the terrestrial magnetosphere and ionosphere. Ground-based observations have the advantage that they can monitor large ionospheric regions at the same time, unlike in-situ spacecraft, and will be detailed first.

### 3.2 The Super Dual Auroral Radar Network

#### 3.2.1 Introduction

The Super Dual Auroral Radar Network (SuperDARN) was created after years of experimentation with VHF radars such as STARE (Scandinavian Twin Auroral Radar Experiment) (Greenwald et al., 1978). SuperDARN (Greenwald et al., 1995) routinely measures coherent scatter from plasma waves produced by plasma instabilities.

SuperDARN provides an almost global coverage of the ionosphere with fields-of-view

over both the northern and southern polar regions. The northern hemisphere SuperDARN radar fields-of-view are presented in Figure 3.1 and the HF radar data included in this thesis are from a pair of SuperDARN radars, Hankasalmi, Finland and Þykkvibær, Iceland, which are labelled "han" and "pyk" in the figure, respectively. These two radars are collectively called the Co-operative UK Twin Located Auroral Sounding System (CUTLASS). CUTLASS, therefore, is a twin-station HF radar optimised to study the high-latitude ionosphere and measure the ionospheric plasma convection velocity (Milan et al., 1997). Independent plasma drift measurements may be obtained in two directions from the overlapping fields-of-view that pairs of SuperDARN radars, such as CUTLASS, provide.

The operating frequency of the SuperDARN radar,  $f_{rad}$ , lies between 8 MHz - 20 MHz, and is constrained to several frequency bands. Each SuperDARN radar has 16 horizontally polarised log periodic antennae that are used for both the transmission and retrieval of signals (Lester et al., 2004).

### **3.2.2 Standard Super Dual Auroral Radar Network Operations**

In the Standard Radar Mode (SRM) SuperDARN transmits an unequally spaced seven-pulse sequence. The sequence is presented in Figure 3.2 and shows that the duration is approximately 65 ms. The pulse length (SMSEP) is 300  $\mu s$  long, which provides the standard 45 km range gates, and the pulses are separated by integral multiples of the multi-pulse increment (MPINC), which is normally set at 2400  $\mu s$ . The lag to first range (LAGFR) is 1200  $\mu s$ , which corresponds to a distance of 180 km. As the pulse propagates away from the radar, some of the energy is backscattered by irregularities that are aligned with the background magnetic field, and are referred to as Field-Aligned Irregularities (FAIs). After each pulse is transmitted, and the first range is reached, the radar then switches over to receiver mode. The backscatter signals are sampled and processed to produce multi-lag complex Auto-Correlation Functions (ACFs).

To take a full scan over the 16 beams, the standard mode consisted of originally two modes of operation, which had 2- and 1-minute integration times. The 2-minute version

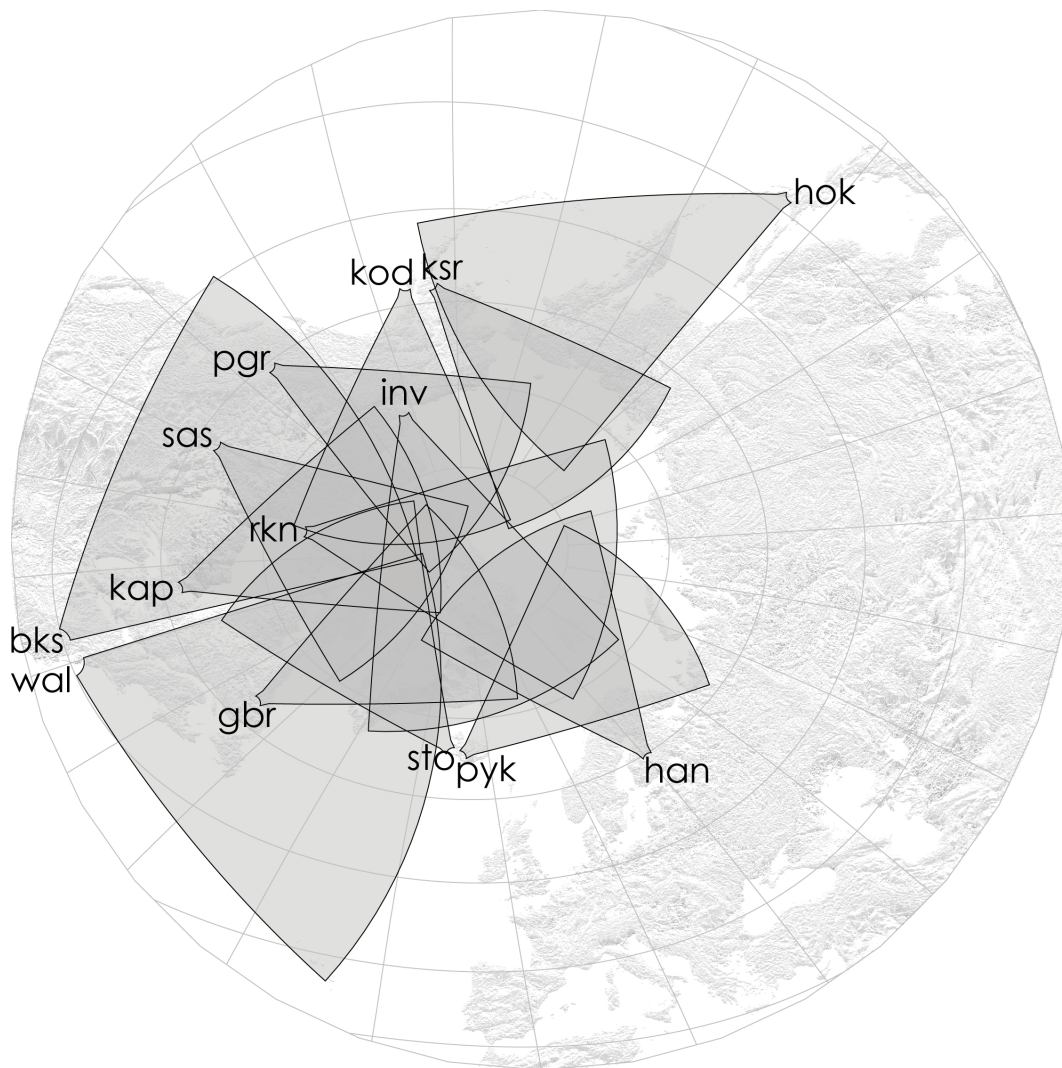


Figure 3.1: The northern hemisphere SuperDARN radar fields-of-view during the common mode of operation. The three-letter identifier codes for each of the radar are presented in the figure (adapted from JHUAPL, 2009).

had an integration period of 7 seconds per beam, implying 2 minutes for a full scan. The other standard mode is the 1-minute full scan, where the integration and scan times are 1-minute and 3 s, respectively. The 1-minute full scan mode is currently still in use and there are 66 pulse sequences, which are integrated over a single integration period.

To provide a full global ionospheric convection map, the SuperDARN radars must be synchronised. To achieve this synchronisation, roughly 8 s must be lost at the end of each scan, with each new scan beginning on a 1- or 2-minute boundary. Global-scale convection velocities may be found using the map potential model. In this model, equipotential

contours are calculated from a series of spherical harmonic functions and are fitted to the measured velocity components (Ruohoniemi and Baker, 1998).

### 3.2.3 Ionospheric Sounding by Pulsed Radars

The method of Bragg scattering in crystals is analogous to the process that SuperDARN uses to receive backscatter from plasma irregularities. Bragg scatter occurs when the wavelength of an incoming electromagnetic wave is comparable to the atomic spacing of a crystalline sample (Tanner, 1995). If the interplanar distance is  $d$ , then the scattered waves from two crystal planes may interfere constructively due to the path length difference of each wave equalling an integer number of wavelengths,  $n$ . The path difference in terms of the scattering angle,  $\theta$ , of the two interfering waves, may be expressed as

$$n\lambda = 2d \sin(\theta). \quad (3.1)$$

The analogous system for radar backscatter implies that the Bragg scattering is no longer off planes of atoms but instead off plasma irregularities within the terrestrial ionosphere. In the analogous radar system,  $n$  defines the order of the backscatter and  $\lambda$ , in equation 3.1, is now the wavelength of the incident electromagnetic wave,  $\lambda_I$ . The radar is sensitive to Fourier components of the electron density fluctuations with a wavevector,  $k$ , corresponding to a wavelength,  $\lambda_{irregularity}$ . In terms of the scattering angle,  $\theta$ , the Bragg scattering condition for HF radar may then be written as

$$n\lambda_I = 2\lambda_{irregularity} \sin(\theta), \quad (3.2)$$

where  $\theta$  is twice the angle between the transmitted and scattered wavevectors. For a backscatter radar, with transmitting and receiving antennae at the same location (such as the SuperDARN radars),  $2\theta = 180^\circ$ . Thus, the scattering condition becomes

$$\lambda_{irregularity} = \frac{\lambda_I}{2}. \quad (3.3)$$

If  $k_I$  is the incident wavevector, equation 3.3 may be expressed as

$$k = 2k_I. \quad (3.4)$$

Equation 3.3 and, therefore, equation 3.4 imply that backscatter will only be detected if the incident electromagnetic wave, governed by  $k_I$ , is orthogonal to the FAIs. The process by which radar wave backscatter occurs from FAIs is well understood (Milan et al., 1997). FAIs are locally depleted regions in the local ionospheric plasma density. These depleted regions are the result of anisotropic electron transport. FAIs may be natural, such as standard radar ionospheric scatter, or artificial, such as heater-induced backscatter. Both types of scatter will be discussed in chapter 7 of this thesis.

### 3.2.4 The Standard SuperDARN pulse sequence

The standard SuperDARN pulse sequence yields the echo power, range, line-of-sight Doppler velocity, and spectral width of ionospheric irregularities. The pulse sequence shown in Figure 3.2 implies a set of "lags" may be determined and that some of these lags will be missing. The lag table for the standard seven-pulse sequence is presented in Figure 3.3. The "missing lags" in Figure 3.3 are clearly inherent to the pulse sequence as shown in Figure 3.2.

However, even when the transmission may theoretically be received, as shown in Figure 3.3, there are still a few possible problems associated with transmission recovery. These problems are either due to (a) the fact that the radar cannot receive and transmit at the same time or (b) cross-range noise. The magenta, orange and green lines on Figure 3.2 illustrate these issues. The magenta line represents the second transmitted pulse of the sequence while the orange line shows the backscattered return signal. The green line represents the third transmitted pulse, which occurs at the same time as the backscattered "orange" second pulse is received. The coloured lines on Figure 3.2 also present an example of cross-range noise. The transmission associated with pulses 2 and 3 are shown by the magenta and green lines, respectively. The red line illustrates that backscatter pulses

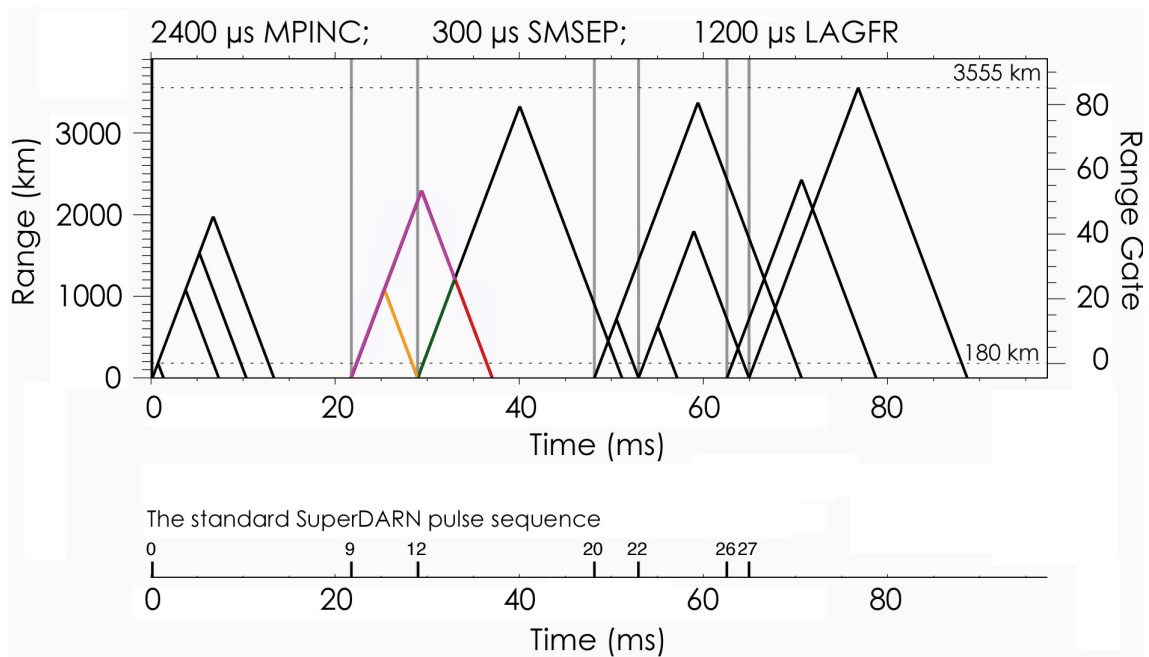


Figure 3.2: The space-time diagram for the SuperDARN standard radar mode (SRM). The magenta and green lines present the transmission associated with pulses 2 and 3, respectively. The orange line shows a possible received transmission from pulse 2 and the red line shows possible backscatter signals from pulses 2 and 3.

originating from two different range gates may be received at the same time, implying that the receiver cannot necessarily identify each individual signal. Cross-range noise is most clearly illustrated in panel (f) of Figure 3.5, which will be discussed later in this chapter. Lags missing for any of the 2 reasons are termed "bad lags", others are called "good lags."

Figure 3.4 presents a complex ACF, which was measured along beam 9 at range gate 54, at 10:45:03 UT on 25 February 2007 by the SuperDARN radar at Hankasalmi, Finland. Panel (a) of Figure 3.4 shows the complex auto-correlation function. The solid blue and red lines are fits to the imaginary and real components of the ACF, respectively. The real component power maximises at lag zero, as expected. Panel (b) presents the phase of the complex ACF (plotted as stars and squares for good and bad lags, respectively). The phase is calculated from the real,  $Re$ , and imaginary,  $Im$ , components of the ACF and may be written in terms of these parameters as

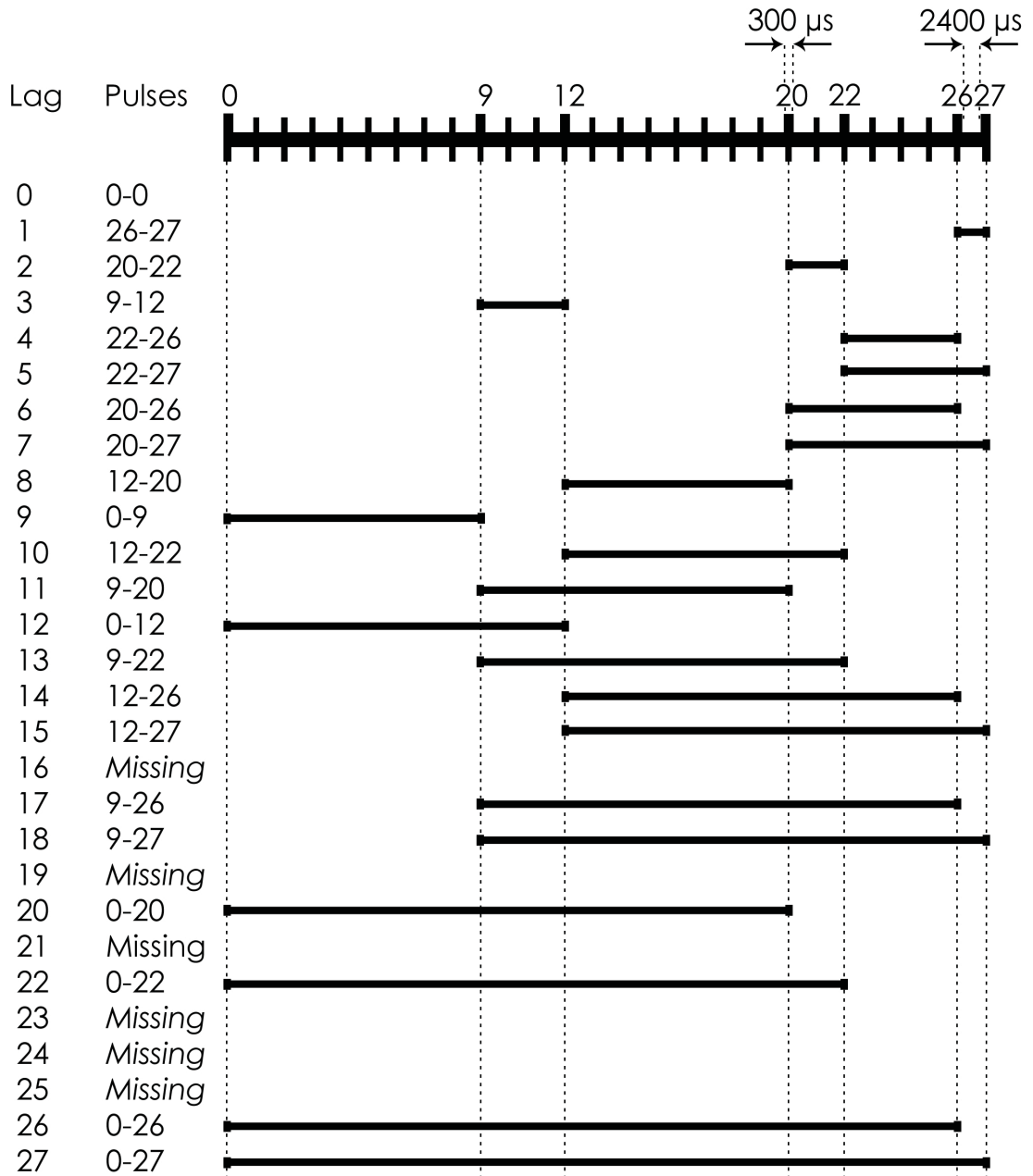


Figure 3.3: The standard seven-pulse sequence transmitted by the SuperDARN radars. Each pulse is 300 μs long and the pulses are separated by integral multiples of the multi-pulse increment (MPINC), 2400 μs (adapted from McWilliams, 2001).

$$\phi = \tan^{-1}\left(\frac{Im}{Re}\right). \quad (3.5)$$

The fitted phase, determined by SuperDARN ACF routines, is represented by the dashed red line. The Doppler shift, and hence the line-of-sight velocity of the plasma irregularities, is determined from the phase fitting procedure. If the plasma irregularity under consideration has a single velocity component then the phase increases and decreases for velocities towards and away from the radar, respectively. A least-squares fit to the ACF phase yields a straight line, which passes through zero at lag zero as shown in panel (b) of Figure 3.4.

The gradient of the red dashed line provides a measure of the mean Doppler frequency,  $\omega_{Doppler}$ . At certain lags, the fitted phase in panel (b) of Figure 3.4 exceeds the range of  $\pm\pi$  over the entire ACF, and aliases. In order to solve this issue, a first guess of the Doppler frequency using close pairs of phases is attempted. The Doppler frequency is then adjusted until the Doppler frequency with the minimum error is revealed. If the radar transmission frequency,  $f_{rad}$ , is known, then in terms of the Doppler frequency,  $\omega_{Doppler}$ , the line-of-sight velocity,  $V_{Doppler}$ , may be written as

$$V_{Doppler} = \frac{c\omega_{Doppler}}{4\pi f_{rad}} = \frac{c}{4\pi f_{rad}} \frac{d\phi}{dt}, \quad (3.6)$$

where the Doppler frequency has been expressed in terms of the phase change with time as  $\omega_{Doppler} = \frac{d\phi}{dt}$ . Once the Doppler velocity is determined, the spectral width and backscatter power may be calculated from the ACF. The Fourier transform of the complex ACF presented in panel (a) of Figure 3.4 yields a velocity distribution with a peak centred on the ionospheric convection velocity. Panel (c) of Figure 3.4 presents the velocity distribution as a normalised power spectrum plotted in black and labelled "Fourier." The power spectrum that is calculated from the velocity, power and spectral width parameters (from the ACF fitting routines) is plotted as the solid red line and labelled as "Fitacf." Fitacf is, therefore, a very powerful and useful tool designed to efficiently determine the Doppler line-of-sight velocity.

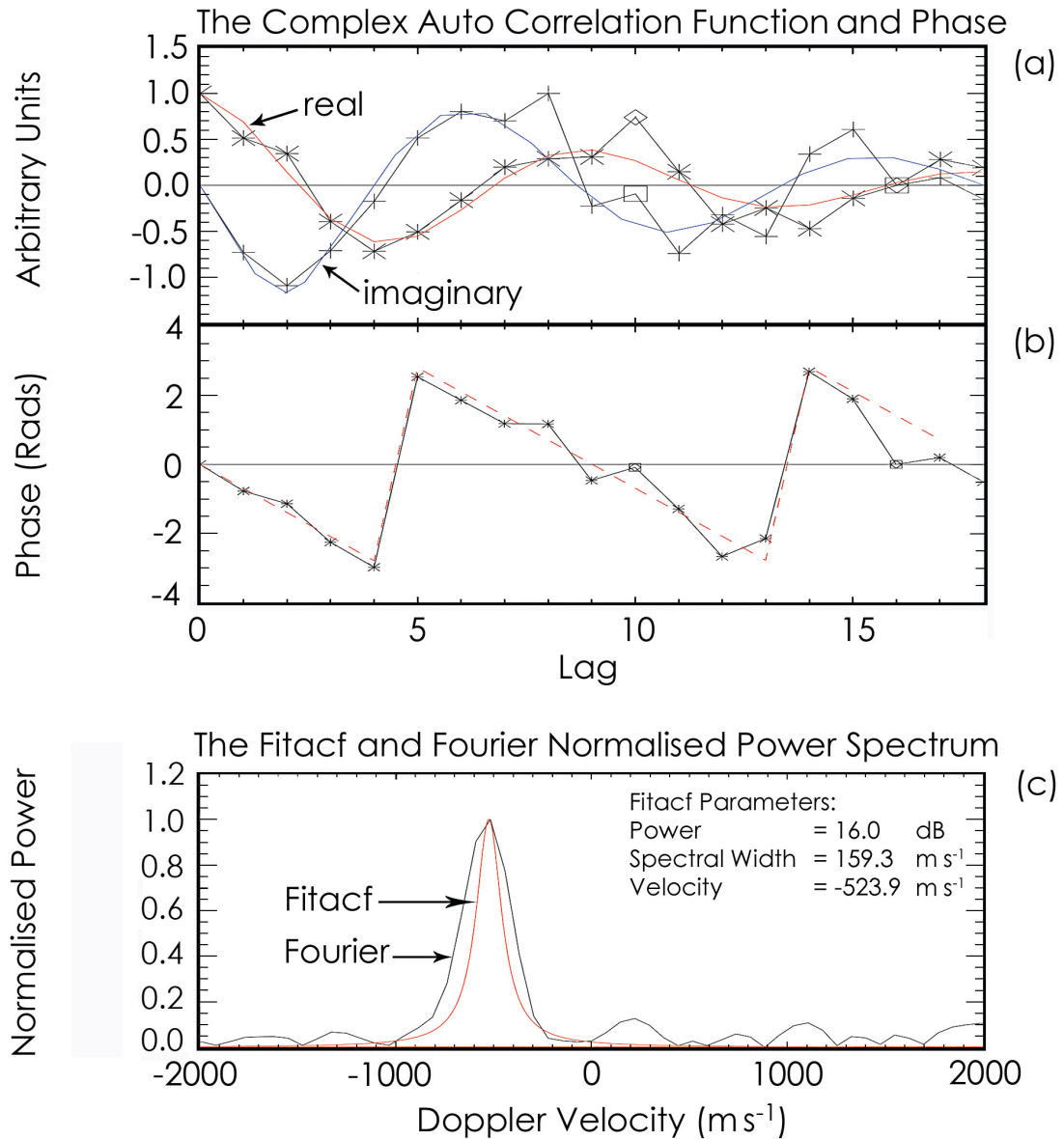


Figure 3.4: **(a – c)** A figure illustrating the complex auto-correlation function (ACF) that is used routinely by SuperDARN to determine the power, velocity and spectral width of ionospheric plasma. Panel (a) presents the complex auto-correlation function measured along beam 9 at range gate 54, at 10:45:03 UT on 25 February 2007 by the SuperDARN radar at Hankasalmi, Finland. The solid blue and red lines show fits to the imaginary and real components of the ACF, respectively, and are labelled accordingly. Panel (b) shows the phase of the ACF (plotted as stars and squares for good and bad lags, respectively), which aliases at  $\pm\pi$ . The fitted phase, as determined by the SuperDARN ACF routines, is represented by the dashed red line. Panel (c) presents the normalised power spectrum (plotted in black and labelled "Fourier") obtained from the Fourier transform of the ACF, and the power spectrum calculated from the velocity, power and spectral width parameters from the ACF fitting routines (plotted in red and labelled "Fitacf").

Long decorrelation times are normally associated with slow moving ground scatter. Conversely, short decorrelation times are usually a characteristic of fast-moving ionospheric scatter, such as that presented here in Figure 3.4. The spectral width is determined by the decorrelation time of the ACF, which is also fitted during the Fitacf procedure. Gaussian and exponential fits are done and both stored, and are usually very similar (e.g., Hanuise et al., 1993; Villain et al., 1996).

### 3.2.5 TMS Super Dual Auroral Radar Network Operations

The standard seven unequally spaced multi-pulse transmission is clearly highly optimised to provide as many usable lags as possible. However, under certain circumstances, it may be advantageous to change the standard pulse sequence for a newly modified version. The new sequence may not be able to form ACFs, using the standard method, and so novel methods may be required in order to recover and analyse backscatter from the SuperDARN radar. In order to allow the largest choice of post-processing it is advantageous to recover as many radar samples as possible. TMS is one possible technique, which allows this recovery (Yukimatu and Tsutsumi, 2002). The TMS mode operates in a very different manner to the standard SuperDARN mode, which was explained in the previous section. TMS is a new Raw Time Series Analysis (RTSA) technique, which was originally devised to analyse meteor backscatter echoes at near ranges. TMS involves saving all of the In-phase and Quadrature (I&Q) samples from the receiver. For standard SuperDARN operations, the raw samples are deleted once the Radar Operating System (ROS) has integrated over a number of pulse sequences and completed the ACF fitting procedure. Thus, the TMS process involves a huge data rate of approximately  $\frac{1}{2}$  GB for each hour of transmission in addition to the standard Fitacf and rawacf datafiles.

Figure 3.5 summarises the data samples that may be used for TMS analysis recorded on 25 February 2007 at 10:40:00 UT. The data presented in Figure 3.5 is from channel A (cp-id -6401) from the Hankasalmi Finland SuperDARN radar, showing 1 s of radar operations. This type of figure is referred to colloquially as a Sessaiogram after A. Sessai Yukimatu. Panel (a) of Figure 3.5 presents the possible sample times within a pulse se-

quence. The vertical black lines show the pulse transmission times. Panel (b) shows the sample power found from  $I^2 + Q^2$ . The panel shows the power from each pulse sequence over the 1 s beam integration period overlaid on top of each other. The noise level acts as a discriminator between good and bad samples and is shown by the horizontal black line. Panel (c) presents the mean power profile averaged over the 1 s beam integration time using the data from panel (b). The horizontal dashed line again shows the noise level. Panel (d) shows the mean lag zero power profile. The dotted lines show the mean power profile shifted by the pulse time delays, which are just integral multiples of MP-INC. Panel (e) presents the reconstructed power profile for a single pulse sequence and is calculated by superimposing all the shifted power profiles on top of each other. Panel (f) shows the same reconstructed mean power profile as given in panel (e) but contains crosses and circles, which show unusable and usable samples for RTSA for analysing range gate 58, respectively. The process must be repeated for each range gate under analysis. For this particular example, at 10:40:00 UT on 25 February 2007, there are three samples out of the possible seven that are not contaminated and may be analysed. The contamination that is mentioned here is the cross-range noise issue that was mentioned in section 3.2.4. Here, it can be seen that backscatter from the first three transmissions of the pulse sequence do not contaminate each other and the signal may be recovered. However, from the fourth transmission of the sequence the return samples are contaminated with backscatter returns from other pulses. Panel (g) presents a summary of all the samples that are available for RTSA and are marked with a +. Panels (h) to (j) present the main results of the RTSA. Panels (h), (i) and (j) show the time evolution at gate 58 over 10 pulse sequences throughout the 1 s integration for power, phase and cross-phase, respectively. The processes outlined in Figure 3.5 occur for every beam and range available for TMS analysis and is necessary to find usable I&Q samples. The TMS method outlined here forms the basis of the implementation of a double-pulse sequence on the SuperDARN radar described in chapter 7.

## Sessaiogram: SuperDARN Raw Time Series Plot 25 February 2007

Hankasalmi Finland, 10:40:00 UT, Channel A: cpid -6401, beam 9, Frequency 11560 kHz, Integration time 1 s, xcf 1, mppul 7, MPINC 2400  $\mu$ s, TXPL 100  $\mu$ s (rsep 15 km), SMSEP 100  $\mu$ s (15 km), number of range gates 240, maximum range 3600 km, nsmp 888, seqtime 88.8, mssofs -400  $\mu$ s, pulse sequence = {0, 9, 12, 20, 22, 26, 27}, noise 1182 (fclr 2573), att 0 (0 -> 0), DCofs 11:3, Q1 = -10 (removed), ercod 0x0000, Maximum Bad Range 105 km, Power threshold 6.0 dB (20.0 dB, finechk)

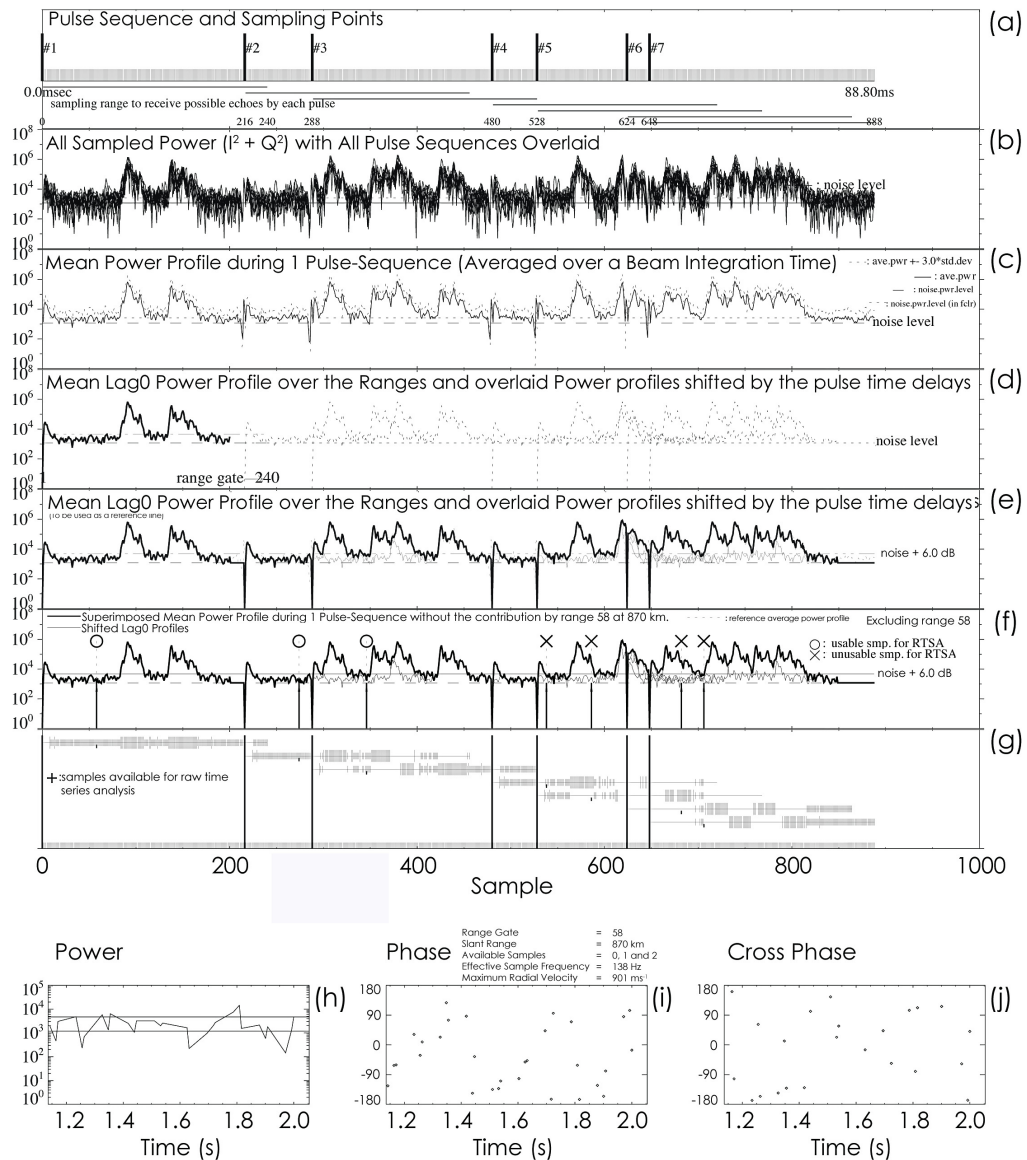


Figure 3.5: (a – j) Data samples that are available for TMS analysis for 25 February 2007 at 10:40:00 UT on beam 9 and channel A using the standard SuperDARN pulse sequence. This type of figure is colloquially referred to as a Sessaiogram after A. Sessai Yukimatu.

### 3.3 The Doppler Pulsation Experiment

In section 1.6 the ordinary (O-) and extraordinary (X-) modes were introduced with regards to ionospheric sounding. One such instrument designed to probe the high-latitude ionosphere and specifically detect ULF wave signatures using O- and X-modes is the Doppler Pulsation Experiment (DOPE) (e.g., Wright et al., 1997, 1998; Wright and Yeoman, 1999a; Yeoman et al., 2000). Figure 3.6 shows when an HF radio signal from DOPE is transmitted, the O-mode wave deviates poleward and the X-mode deviates equatorward. Consequently, the reflection points of the two modes are separated horizontally as well as vertically. The O-mode path consistently provided higher clarity ULF wave signatures than the X-mode throughout chapters 5 and 6, and consequently, only O-mode propagation paths are considered.

DOPE was deployed in May 1995 near Tromsø, Norway (geographic: 69.6° N 19.2° E; geomagnetic: 67.0° N 117.0° E; L = 6.3). The Doppler sounder records the HF radio signal reflected from the F-region of the ionosphere. Small shifts in the received radio wave frequency can be interpreted as signatures of ionospheric perturbations caused by changes in the phase path of the radio wave in the ionosphere (Baddeley et al., 2005). Figure 3.7 presents a schematic of the DOPE system after the substantial upgrade in 1998. The four transmitters radiated fixed-frequency CW signals and a four-channel receiver system resulted in ground separations of between 40 km and 90 km. The upgraded system incorporated two altitude-separated paths at 4.16 MHz and 5.25 MHz, between Ramfjordmoen and Seljelvnes, that were used to eliminate possible infrasonic modes, and two paths that were azimuthally separated from these at 5.73 MHz and 5.26 MHz (Ramfjordmoen-Skibotn and Ramfjordmoen-Kilpisjärvi, respectively). These phase stable CW signals may be reflected from the ionosphere and mixed with a reference signal to calculate a frequency shift,  $\Delta f$ , along the ray path (Wright et al., 1997). The frequency shift, in terms of the free space wavelength,  $\lambda$ , and the phase path of the signal,  $P$ , may be expressed as

$$\Delta f = -\frac{1}{\lambda} \frac{dP}{dt} \quad (3.7)$$

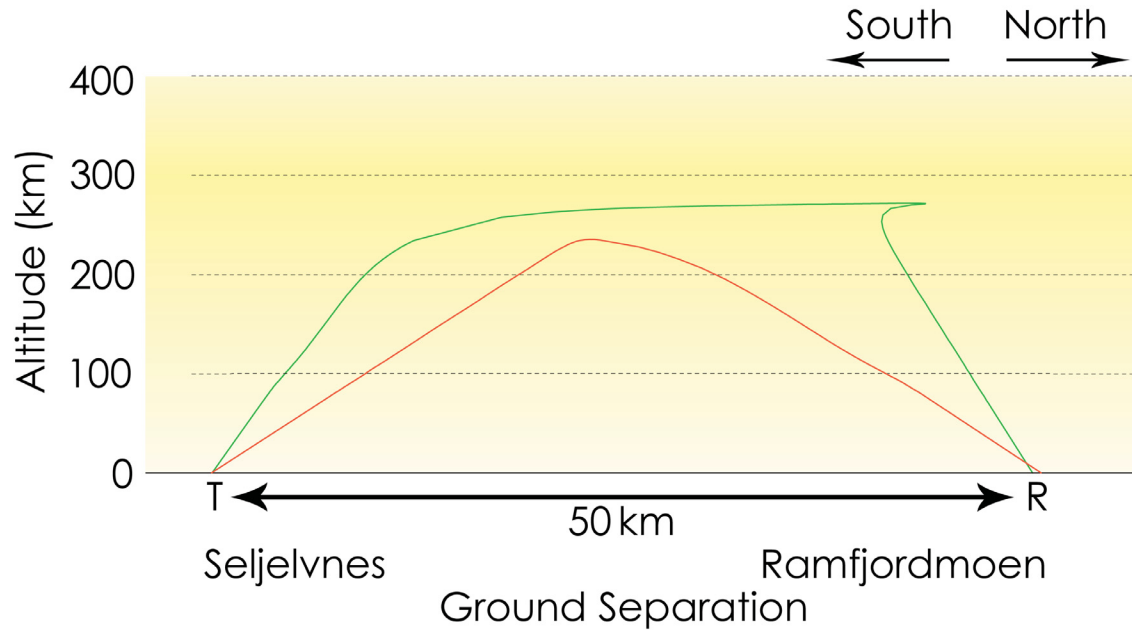


Figure 3.6: A schematic showing the ray-traced modes of propagation for the DOPE instrument. The solid red and green lines show the X- and O-modes, respectively (Yeoman et al., 2000).

(Davies, 1962). Figure 3.8 presents a schematic of a down-going Alfvén wave and shows how, through the motor effect, the vertical motion of the reflection height of an HF radio wave might be affected. The notation used in the figure is identical to that used in Figure 2.1.

The magnetic field lines at high-latitude are not orthogonal to the ground but are tilted slightly to the vertical and so results in a vertical component of the  $\mathbf{E} \wedge \mathbf{B}$  drift velocity. If the change in phase path results purely from the motion of the reflection point in the ionosphere with a velocity,  $v$ , the frequency shift,  $\Delta f$ , may be written as

$$\Delta f = -\frac{2vf}{c} \quad (3.8)$$

(Georges, 1967).

For an electromagnetic wave, the phase velocity,  $V_{phase}$ , may be related to the group velocity,  $V_{group}$ , and the speed of light,  $c$ , by

$$c = (V_{group}V_{phase})^{\frac{1}{2}}. \quad (3.9)$$

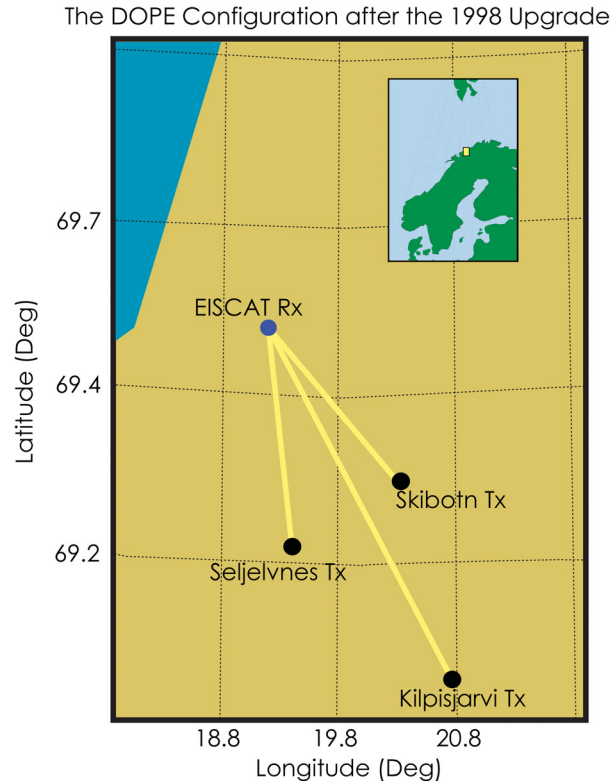


Figure 3.7: A schematic of the HF radio paths of the DOPE (Doppler Pulsation Experiment) sounder located in northern Scandinavia.

The Doppler shift is a measure of the changing phase path and provides a measure of the phase velocity. For a sounding frequency close to the peak FoF2 frequency there is a large group delay on the transmitted wave. Peaks at the E and F1 layers are points where the group velocity,  $V_{group}$ , tends to zero. Since equation 3.9 applies, then consequently,  $V_{phase} \rightarrow \infty$ . Therefore, as the sounding frequency approaches peak FoF2 the observed wave signature appears to increase in magnitude, this is known as magnification.

In the DOPE system, the reflected signal, after mixing with a reference signal, is sampled at the receiver, at 40 Hz, and processing through a Fast Fourier Transform (FFT) algorithm (512 points per FFT) provides a Doppler trace with a time resolution of 12.8 s. In this thesis, the Doppler trace is resampled from 12.8 s to 10.0 s. This resampling was conducted in order to make direct phase and amplitude comparisons between the DOPE and IMAGE magnetometer instruments and will be explained further in chapter 5. The case study presented in chapter 5 uses data from the DOPE system before the upgrade while

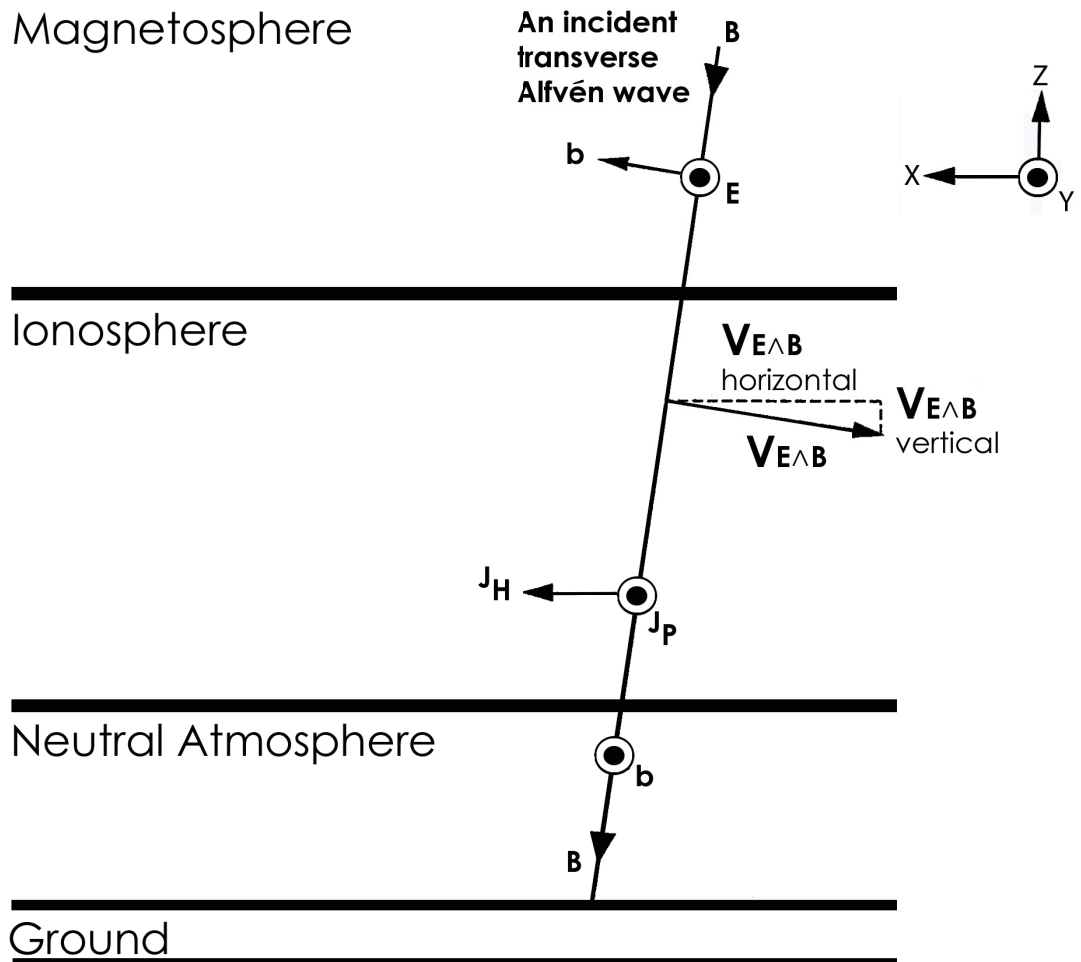


Figure 3.8: A schematic illustrating the vertical motion of the reflection height of an HF radio wave caused by the interaction of the electric field vector,  $E$ , and the perturbation magnetic field vector,  $b$ , associated with a down-going Alfvén wave (adapted from Wright, 1996).

the statistical investigation, which follows subsequently in chapter 6, uses data from before and after the upgrade. Before the upgrade, a fixed-frequency 4.45 MHz CW signal with a dual-channel receiver was used. The two channels provided the O- and the X-mode data.

Panels (a) and (b) of Figure 3.9 show an example Doppler trace from the O-mode recording 60 minutes of data from 09:45 UT to 10:45 UT on 16 April 1998. A clear ULF wave signature is visible in the data. Panel (a) presents the unfiltered Doppler O-mode frequency shift representing spectral components above the threshold value (50% of the peak value) overlaid with a solid black line showing the Doppler O-mode peak trace. The peak trace is essentially the spectral maxima of each integration interval joined together. The peak trace is useful as subsequent Fourier analysis may be performed to reveal the spectral power as a function of frequency, which provides a measure of the wave frequency. Panel (b) shows the filtered Doppler O-mode bandpass filtered to exclude waves with periods outside of the range 250 s - 500 s.

## 3.4 Ground Magnetic Measurements

### 3.4.1 Fluxgate Magnetometers

Magnetic fields are measured using fluxgate magnetometers (FGMs) (Primdahl, 1979), and therefore, these instruments are the primary tool for providing ground- and space-based measurements of the terrestrial and interplanetary magnetic fields, respectively. Typically, FGMs are composed of ring-cores made from a magnetically permeable alloy. Figure 3.10 presents a schematic of the ring-cores wrapped within two coil windings, which are called the drive and sense windings and are shown in panels (a) and (b) as black and blue, respectively. Introducing a current into the drive winding makes one half-core generate a field in the same direction as  $H_{external}$  and the other half-core generate a field in the opposite direction.

If the FGM is situated within a region free of an external magnetic field ( $H_{external} = 0$ ), then each half-core of the system will saturate and desaturate at the same time. Con-

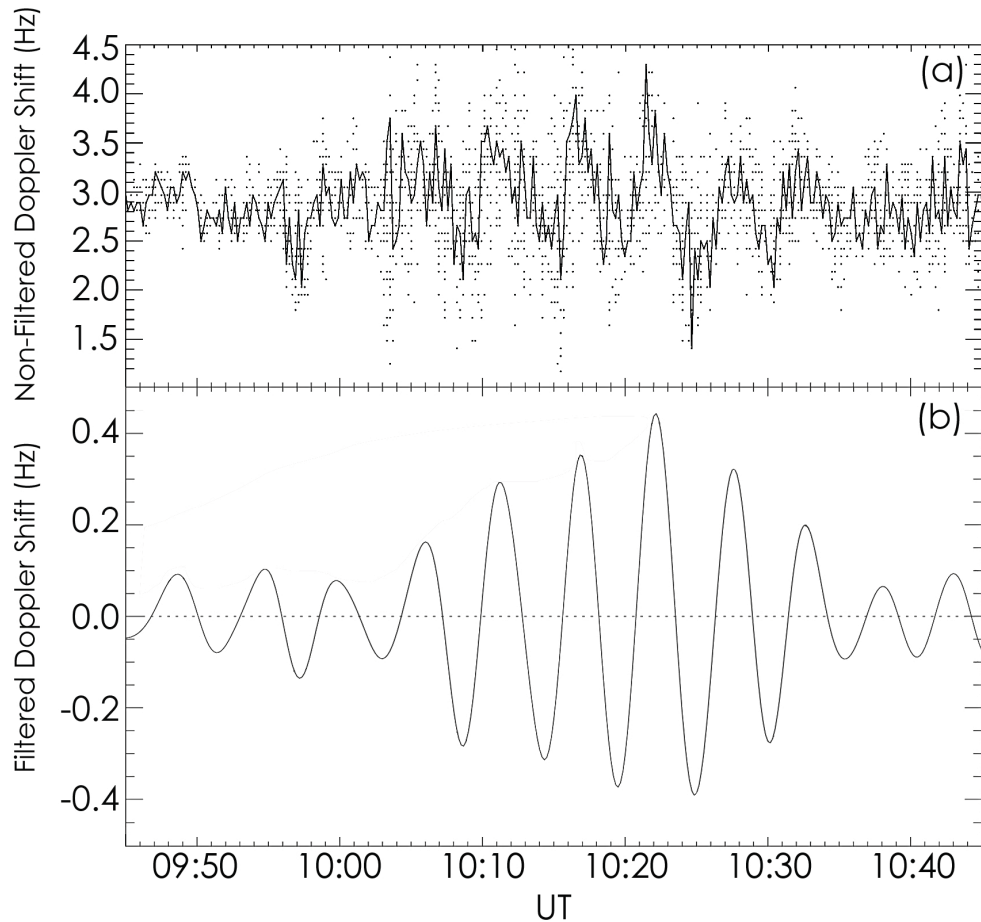


Figure 3.9: **(a and b)** DOPE data for a ULF wave event on 16 April 1998. Panel (a) shows an HF unfiltered Doppler O-mode frequency shift representing spectral components above a threshold value (50% of the peak value) overlaid with a solid black line showing the Doppler O-mode peak trace found from the data in panel (a), resampled at 10 s. Panel (b) presents the filtered DOPE peak trace data excluding variations with time periods outside of the range 250 s to 500 s.

sequently, the generated fields cancel out, the sense winding has no net change of flux, and no voltage is induced. If, however, the FGM is located in a region permeated by an external magnetic field the half-core generating a field in the opposite direction to the external field,  $H_{external}$ , will come out of saturation earlier than the half-core generating a field in the same sense as the external field. Contrary to the field free case, there is now a net change of flux in the sense winding, which is shown in blue in panel (b) of Figure 3.10. The Faraday equation, equation 2.3, implies that a net change of flux will induce a voltage. The phase and size of the induced voltage spikes reveal both the direction and magnitude of the external magnetic field,  $H_{external}$ . A triaxial FGM has three of the cores,

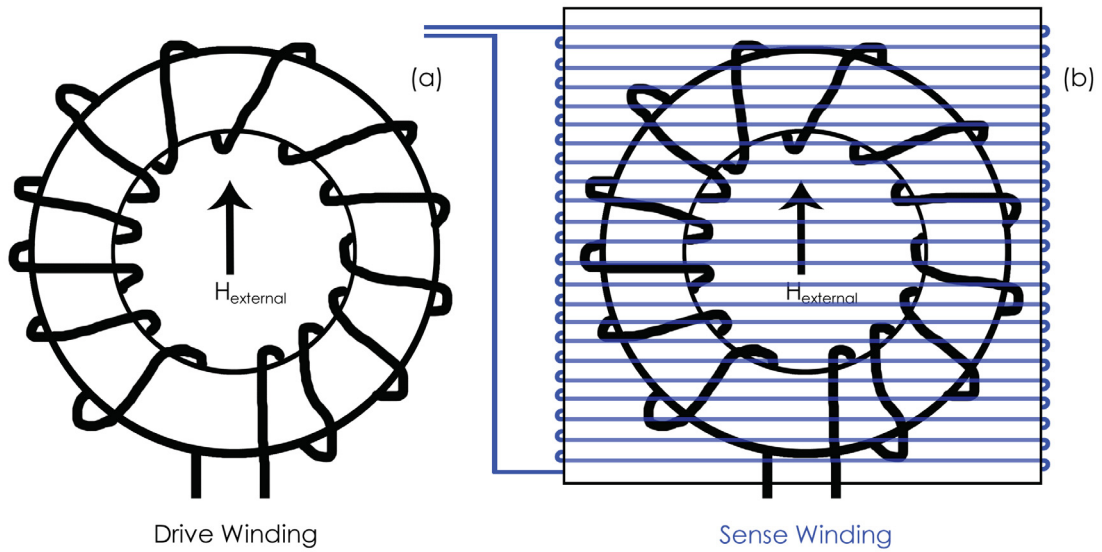


Figure 3.10: **(a and b)** A schematic of a typical fluxgate magnetometer. Panel (a) displays the driving coil in black and panel (b) shows the sensing coil in blue.

described previously, aligned orthogonally with each other in order to measure each component of the magnetic field vector,  $\mathbf{B}$ , namely,  $B_x$  (positive north),  $B_y$  (positive east), and  $B_z$  (vertically downwards).

### 3.4.2 The International Monitor for Auroral Geomagnetic Effects

The International Monitor for Auroral Geomagnetic Effects (IMAGE) magnetometer array comprises a chain of triaxial FGMs that are located across northern Scandinavia and provide important measurements of ULF variations in the magnetic field throughout this study (Luhr, 1994). Figure 3.11 presents the locations of the 31 stations that presently form the array. The magnetometer data are sampled at 10 s intervals and have a resolution of 0.01 nT. The IMAGE data throughout this thesis are presented in geographic coordinates and are used to provide conjugate ground signatures with ionospheric measurements made by the HF Doppler sounder.

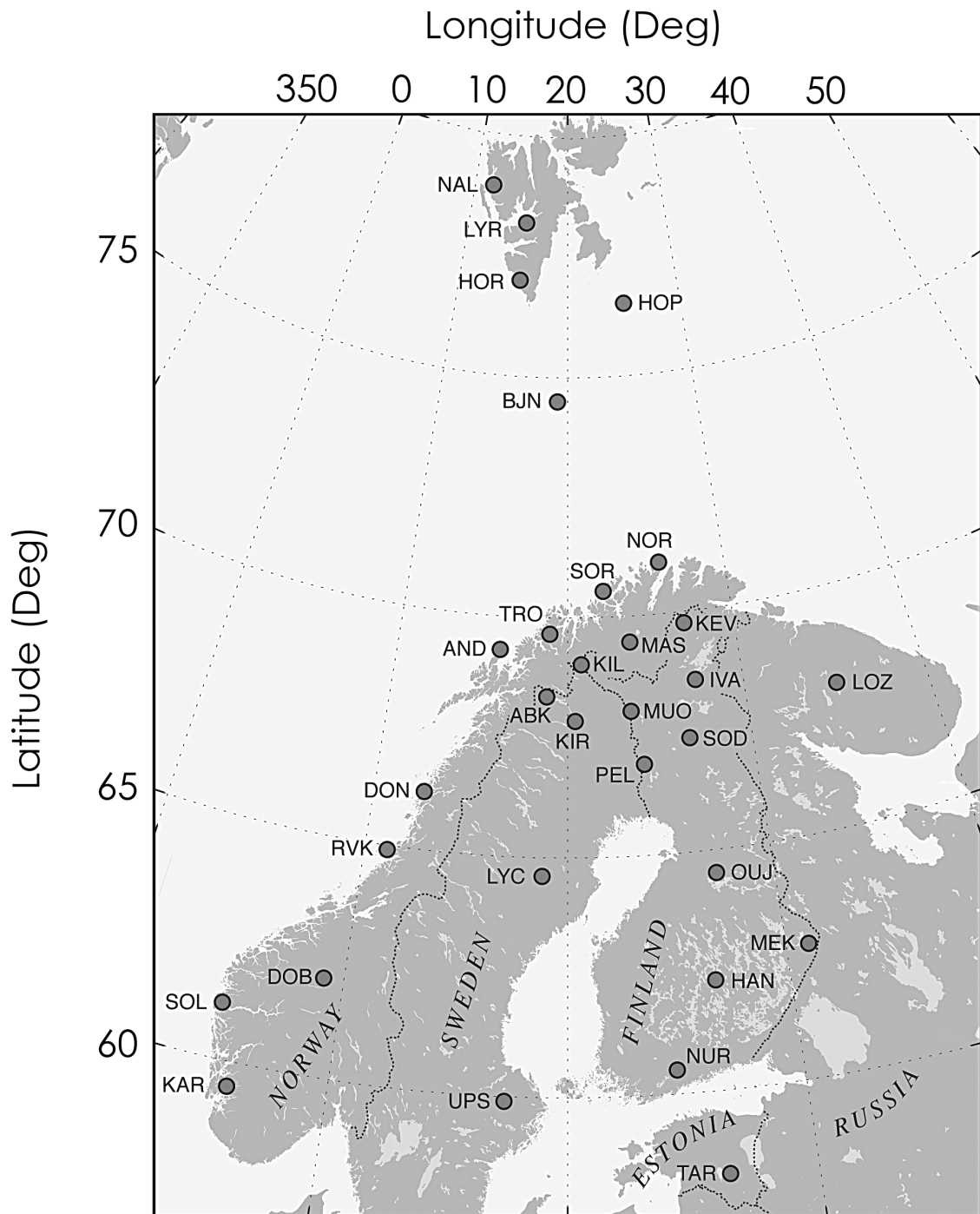


Figure 3.11: The locations of the magnetometer stations that comprise the IMAGE array (after Institute, 2009).

### 3.5 The Tromsø Dynasonde

In this thesis, ionospheric electron density inputs to a numerical model (detailed in chapter 4) are determined from local ionosonde measurements using the Tromsø dynasonde (Rietveld et al., 2008). The dynasonde is a modern-day, digital ionosonde utilising sounding frequencies of 1 MHz to 30 MHz. The dynasonde may be operated like an ionosonde or in other modes such as fixed-frequency sounding. An ionosonde is a very useful tool for ionospheric research as sounding the ionosphere at different frequencies until no reflected signal is received, yields the entire bottom-side electron density variation with virtual height up to peak FoF2. The time of flight for the radio wave to reach the reflection altitude and return to the ground may be expressed as

$$t = \frac{2}{c} \int_0^h \frac{dz}{n}, \quad (3.10)$$

where  $z$  is the altitude,  $h$  is the reflection altitude,  $n$  is the refractive index of the local medium, and  $c$  is the speed of light. The incident transmitted wave will slow down before the reflection point is reached due to an increase in the electron density with altitude. At a certain point, known as the reflection point, the group velocity of the incident wave becomes zero and the plasma,  $f_p$ , and wave,  $f$ , frequencies are equal. Using a simplified form of the AAH equation, equation 2.55, the virtual height,  $h'$ , of a vertically incident radio wave on the ionosphere may be written as

$$h' = \int_0^h \frac{dz}{[1 - (\frac{f_p}{f})^2]^{\frac{1}{2}}}. \quad (3.11)$$

Numerical solutions are required to solve equation 3.11 since there are no analytical solutions. The virtual height always has a higher altitude than the true height. The true height may be determined by inverting the virtual height variation to give an electron density profile using the POLynomial ANALysis (POLAN) algorithm. The use of the algorithm will be detailed in section 4.2.5.

## 3.6 The Tromsø Heater

The high-power HF heating facility at Tromsø generates artificial field aligned ionospheric density striations, at the upper-hybrid height, that may enhance the visibility of ionospheric plasma to HF radars. The artificial generation of backscatter targets is shown in Figure 3.12, which presents an illustration of the heater and its operation. The green lines in Figure 3.12 show the artificially generated FAIs and the near-vertical solid black lines show the terrestrial magnetic field,  $\mathbf{B}$ .

The heater transmits in the frequency range of 3.9 MHz - 5.6 MHz and consists of twelve transmitters feeding a six-by-six array of crossed dipole antennae. The heater itself is capable of radiating over 1 MW of CW power. Further technical details about the heater may be found within Rietveld et al. (1993). Artificial backscatter has many useful attributes, It has a well-defined spatial position, allows short radar integration times and produces a narrow spectral width, yielding SuperDARN backscatter with a well-defined spatial position, and an increased velocity resolution (Wright and Yeoman, 1999c).

Figure 3.13 presents fields-of-view of the CUTLASS radars relative to the location of the Tromsø heater. The heater is marked by the black square and beam 5, which overlays the heater, is identified by the black shaded region. Experiments using these instruments have been undertaken previously in a number of studies such as that by Wright and Yeoman (1999b) when a coordinated experiment, designated OUCH (Observations of ULF waves with CUTLASS and the Heater) was performed. Artificial backscatter generated by the HF heating facility at Tromsø will be detailed in chapter 7 of this thesis.

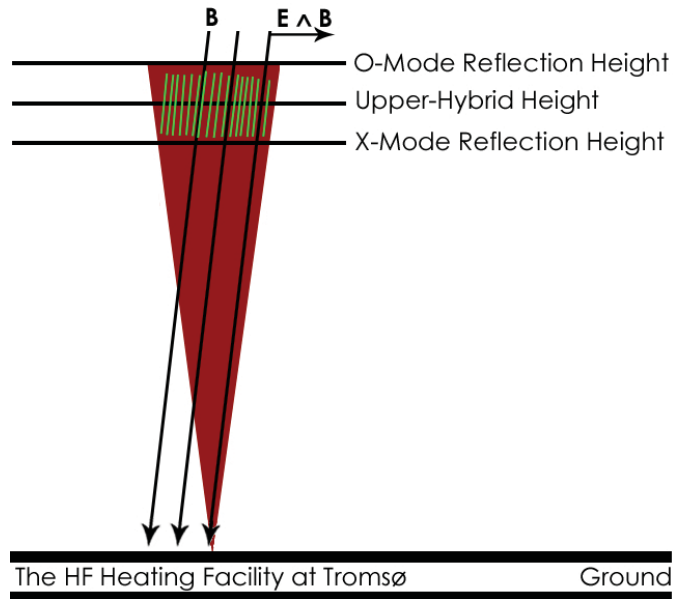


Figure 3.12: An illustration showing the generation of artificial field aligned irregularities. The red shaded region shows the transmitted radio wave. The green lines show the artificially generated field aligned irregularities and the near-vertical solid black lines show the terrestrial magnetic field,  $B$ .

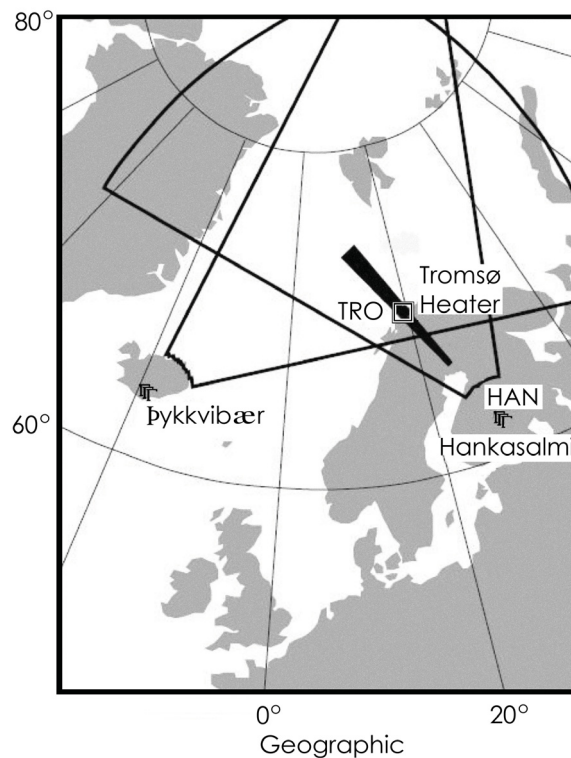


Figure 3.13: The CUTLASS HF radar fields-of-view during the common mode of operation. The overlaid black line shows beam 5 and the black square highlights the position of the heater (adapted from Wright et al., 2004).

### 3.7 The Advanced Composition Explorer

The National Aeronautics and Space Administration (NASA) Advanced Composition Explorer (ACE) spacecraft was launched on 25 August 1997 (Stone et al., 1998). ACE is presently orbiting the Lagrangian (L)-1 point, which is a location approximately  $235 R_E$  upstream of the Earth where the solar and terrestrial gravitational fields are balanced. ACE provides continuous coverage of important solar wind parameters such as the magnetic field components,  $B_x$ ,  $B_y$  and  $B_z$ , the solar wind velocity,  $V_{SW}$ , the dynamic pressure,  $P_{dyn}$ , and the proton number density,  $N_p$ . The location implies that the solar wind passes ACE roughly 60 minutes before it reaches the terrestrial magnetosphere.

### 3.8 The Interplanetary Monitoring Platform -8

The Interplanetary Monitoring Platform (IMP)-8 spacecraft was a NASA mission, which was launched on 26 October 1973 (Armstrong et al., 1978). The primary mission of the spacecraft was to measure the near-Earth solar wind. IMP-8 measured energetic particles but most important to this study was the spacecraft's capability to provide in-situ measurements of the IMF for comparisons with measurements from the ACE spacecraft. IMP-8 was originally inserted into an elliptical orbit with perigee and apogee distances of approximately  $25 R_E$  and  $45 R_E$ , respectively. The spacecraft took roughly 12.5 days to orbit around the Earth and almost 60% of this time was spent in the solar wind. IMP-8 was ideally located, therefore, to provide comparable measurements of IMF structures as monitored by the ACE spacecraft approximately 60 minutes earlier.

# Chapter 4

## An Introduction to the Numerical Model and Example Results

### 4.1 The 1-D Ultra Low Frequency Wave Numerical Model

#### 4.1.1 Introduction

ULF wave properties may be examined with the aid of models. The complexity of ULF wave modelling has increased dramatically with variants considering vertical (or near-vertical) and horizontal orientations of the background magnetic field (e.g., Southwood, 1976; Zhang and Cole, 1995). In the earliest example, Hughes (1974) examined ULF wave propagation from the magnetosphere through the ionosphere to the ground using the Maxwell equations (equations 2.1 to 2.4). Hughes (1974) concluded that the reflection coefficient of the ionosphere (equation 2.32) is approximately unity, indicating that the wave reflection at the top of the ionosphere is almost perfectly efficient. The ionosphere, atmosphere and ground introduce important effects that alter the amplitude and polarisation of the waves. These effects lead to rotation and attenuation of the wave magnetic signatures detected on the ground (Hughes and Southwood, 1976b). Remote sensing of the magnetosphere is, therefore, only possible if the effects of the ionosphere and atmosphere are included. It is important to develop theoretical models explaining the interaction of such atmospheric layers. The ionospheric signature of ULF waves is thus

an important research area.

High-latitude analytical solutions for a non-vertical background field were not determined until much later (e.g., Sciffer and Waters, 2002). The results of this later analytical model were developed and enhanced in a 1-D numerical model developed by Sciffer et al. (2005), which is used in this thesis. This numerical model solves for an oblique magnetic field and contains a resistive MHD upper boundary. The model includes a mixture of Alfvén and fast wave modes incident at the top of the model. A boundary value approach is adapted similar to work by Zhang and Cole (1995) allowing the polarisation and wave mode of the incident wave to be specified. The ground is the lower boundary and is assumed to have a finite isotropic conductivity. The incident wave is assumed to vary as  $\exp^{i(\omega t - k_x x - k_y y)}$  where the east-west,  $k_y$ , and north-south,  $k_x$ , wavenumbers may be determined from observation. The resultant electric and magnetic ULF wave fields in the ionosphere are calculated. The 1-D model used here is a corrected version of that presented by Sciffer et al. (2005). The correction will be detailed later.

There have been a number of papers detailing aspects of the Doppler oscillations of vertically incident radio waves correlated with ULF geomagnetic pulsations (e.g., Poole and Sutcliffe, 1988; Wright et al., 1997). Section 2.7.2 of this thesis outlines early approaches to ULF modelling, from Rishbeth and Garriott (1964) to "modern" methods using the Sutcliffe-Poole model (Poole and Sutcliffe, 1988; Sutcliffe and Poole, 1990). In the simplest case, Rishbeth and Garriott (1964) suggested that down-going ULF waves drive  $\mathbf{E} \wedge \mathbf{B}$  drifts in the ionosphere. However, the effects of the ionosphere and atmosphere on the ULF wave also require consideration. Section 2.7.2 also introduced the Sutcliffe-Poole model, which presents three separate mechanisms that may lead to Doppler shifts in HF signals. These mechanisms will be detailed in section 4.2. Poole and Sutcliffe (1988) described a model that predicts the Doppler shift, using realistic values for electron density and other relevant parameters. A limitation of the Sutcliffe-Poole model is that it only considers Alfvén waves incident on the ionosphere. If the ULF wave fields and modes are determined as a function of altitude from the 1-D numerical ULF wave model, developed by Sciffer et al. (2005), then more realistic HF Doppler shifts may be calculated. The

Doppler shift contributions for the three mechanisms outlined in the model of Poole and Sutcliffe (1988) are determined by an implementation of the Sutcliffe-Poole model.

It should be noted that all previous work, with the exception of Waters et al. (2007), have restricted themselves to examining the behaviour of the models without detailed reference to observations (e.g., Sciffer et al., 2005) or to comparing observations with the generic runs presented by Sutcliffe and Poole (1990), rather than model runs under the appropriate ULF wave and ionospheric conditions.

The implementation of the Sutcliffe-Poole model is that presented in Waters et al. (2007). Both these models were developed at the University of Newcastle, New South Wales, Australia. Here the mathematical foundation of the model and the numerical scheme used to find a solution are described. Example runs will then be given to verify the implementation of the model under Linux at the University of Leicester. A comparison of the Sutcliffe-Poole model results with the latest implementation of the model with identical input parameters is then presented, along with runs under these conditions but moved to auroral latitudes. Model runs are shown with some key input parameters varied over the ranges typically observed in the auroral zone, in order to gain insight into the behaviour of the model under these conditions.

### 4.1.2 The 1-D Numerical Model - A Mathematical Description

The 1-D numerical model used here is that described in Sciffer et al. (2005), which develops the existing work of Hughes (1974); Hughes and Southwood (1976b) and Zhang and Cole (1995). The new 1-D model formulates the altitude variation of the ULF wave electric and magnetic fields, allows for an oblique geomagnetic background field,  $B_0$ , and includes both Alfvénic and fast mode waves incident from the magnetosphere.

As described in Waters et al. (2007), the ULF wave energy, which is incident from the magnetosphere, is described as an electromagnetic disturbance. The two Maxwell equations required are

$$\nabla \wedge \mathbf{E} = -\frac{\partial \mathbf{B}}{\partial t} \quad (4.1)$$

and

$$\nabla \wedge \mathbf{H} = \mathbf{J} + \frac{\partial \mathbf{D}}{\partial t}, \quad (4.2)$$

where  $\mathbf{H}$  is the magnetic intensity and  $\mathbf{D}$  is the electric displacement. The current density,  $\mathbf{J}$ , and the magnetic flux density,  $\mathbf{B}$  may be expressed as

$$\mathbf{J} = \vec{\sigma} \mathbf{E} \quad (4.3)$$

and

$$\mathbf{B} = \mu \mathbf{H}, \quad (4.4)$$

respectively, where  $\vec{\sigma}$  is the conductivity tensor. The same coordinate system as described in Sciffer and Waters (2002) is used here, where  $X$  is northward,  $Y$  is westward and  $Z$  is radially outward from the surface of the Earth.  $B_0$  lies in the  $XZ$  plane at an angle  $I$  to the horizontal. If there is no background electric field ( $E_0 = 0$ ) then  $\mathbf{B}$  and  $\mathbf{E}$  may be expressed as

$$\mathbf{B} = (B_0 \cos(I), 0, B_0 \sin(I)) + (b_x, b_y, b_z), \quad (4.5)$$

and

$$\mathbf{E} = (e_x, e_y, e_z), \quad (4.6)$$

respectively. If the ionospheric medium varies only in the vertical direction, then the horizontal spatial and temporal dependence is

$$\exp^{i(k_x x + k_y y - \omega t)} \quad (4.7)$$

and the governing equations in their full component form may be written as

$$i\left[\frac{k_y^2}{\omega} - \frac{\omega}{c^2}\left(\varepsilon_{11} - \frac{\varepsilon_{13}\varepsilon_{31}}{\varepsilon_{33}}\right)\right]e_x - i\left[\frac{k_x k_y}{\omega} + \frac{\omega}{c^2}\left(\varepsilon_{12} - \frac{\varepsilon_{13}\varepsilon_{32}}{\varepsilon_{33}}\right)\right]e_y - ik_y \frac{\varepsilon_{13}}{\varepsilon_{33}} b_x + \frac{\partial b_y}{\partial z} + i \frac{k_x \varepsilon_{13}}{\varepsilon_{33}} b_y = 0, \quad (4.8)$$

$$i\left[\frac{k_x k_y}{\omega} + \frac{\omega}{c^2}\left(\varepsilon_{21} - \frac{\varepsilon_{23}\varepsilon_{31}}{\varepsilon_{33}}\right)\right]e_x - i\left[\frac{k_x^2}{\omega} - \frac{\omega}{c^2}\left(\varepsilon_{22} - \frac{\varepsilon_{23}\varepsilon_{32}}{\varepsilon_{33}}\right)\right]e_y + ik_y \frac{\varepsilon_{23}}{\varepsilon_{33}} b_x + \frac{\partial b_x}{\partial z} - i \frac{k_x \varepsilon_{23}}{\varepsilon_{33}} b_y = 0, \quad (4.9)$$

$$ik_y \frac{\varepsilon_{31}}{\varepsilon_{33}} e_x + \frac{\partial e_y}{\partial z} + ik_y \frac{\varepsilon_{32}}{\varepsilon_{33}} e_y + i\left(\omega - \frac{c^2 k_y^2}{\omega \varepsilon_{33}}\right) b_x + ik_x k_y \frac{c^2}{\omega \varepsilon_{33}} b_y = 0, \quad (4.10)$$

and

$$\frac{\partial e_x}{\partial z} + ik_x \frac{\varepsilon_{31}}{\varepsilon_{33}} e_x + ik_x \frac{\varepsilon_{32}}{\varepsilon_{33}} e_y - ik_x k_y \frac{c^2}{\omega \varepsilon_{33}} b_x - i\left(\omega - \frac{c^2 k_x^2}{\omega \varepsilon_{33}}\right) b_y = 0, \quad (4.11)$$

where  $\varepsilon_{ij}$  are the elements of the dielectric tensor,  $\varepsilon$  (Waters, 2006). It should be explained that there are typographical errors within both Sciffer et al. (2005) and Waters et al. (2007) regarding the four 1-D differential equations, which have been corrected here after personal communication with the first author of Waters et al. (2007). These corrections may be found at Waters (2006). The conductivity tensor,  $\vec{\sigma}$ , may be expressed in terms of the dielectric tensor,  $\vec{\varepsilon}$ , as

$$\vec{\varepsilon} = \vec{\mathbf{I}} - \frac{i}{\varepsilon_0 \omega} \vec{\sigma}, \quad (4.12)$$

where  $\vec{\mathbf{I}}$  is the identity tensor (Zhang and Cole, 1995). Equations 4.8, 4.9, 4.10 and 4.11 are four first order differential equations that only consider derivatives in the vertical direction,  $Z$ . To complete the set, the  $e_z$  and  $b_z$  ULF wave field components are

$$e_z = -\frac{\varepsilon_{31}}{\varepsilon_{33}} e_x - \frac{\varepsilon_{32}}{\varepsilon_{33}} e_y - k_y \frac{c^2}{\omega \varepsilon_{33}} b_x + k_x \frac{c^2}{\omega \varepsilon_{33}} b_y \quad (4.13)$$

and

$$b_z = -\frac{k_y}{\omega}e_x + \frac{k_x}{\omega}e_y. \quad (4.14)$$

A total of four boundary conditions are required to solve the system. The ground specifies two of these. The Earth is assumed to be a uniform, homogenous conductor of finite conductivity. The ULF waves decay in amplitude in the medium due to the small frequency and are described by

$$\frac{\partial e_x}{\partial z} - \gamma(\sigma_g, k_x, k_y, \omega)e_x = 0 \quad (4.15)$$

and

$$\frac{\partial e_y}{\partial z} - \gamma(\sigma_g, k_x, k_y, \omega)e_y = 0, \quad (4.16)$$

where  $\gamma$  specifies the ground to be a uniform medium with a conductivity of  $\sigma_g = 10^{-2}$  Mho  $m^{-1}$ .

The top boundary is set at 1000 km where resistive MHD plasma conditions are assumed. The model allows for the existence of both the shear Alfvén and fast mode waves up to the top boundary. For more information on the mathematical foundation of the numerical model see Sciffer et al. (2005).

## 4.2 The Sutcliffe and Poole Model

### 4.2.1 Introduction

Oscillations in radio waves reflected from the ionosphere (Doppler frequency oscillations) are correlated with oscillations recorded by ground-based magnetometers. A long-standing theory to describe the relationship between these oscillations was proposed by Rishbeth and Garriott (1964). The early analytical models do not consider the effect of a non-vertical background field and, consequently, these theoretical models required improvement. Serious progression in the field of ULF modelling occurred due to the pub-

lication of a set of papers that analyse the effect of ULF waves on transmitted HF Doppler signals (Poole and Sutcliffe, 1987, 1988; Sutcliffe and Poole, 1989, 1990).

For vertical incidence, the relationship between the overall total Doppler velocity,  $\mathbf{V}^*$  and the Doppler frequency shift,  $\Delta f$  may be expressed as

$$\Delta f = \frac{2f_R \mathbf{V}^*}{c}, \quad (4.17)$$

where  $f_R$  is the radio transmission frequency and  $c$  is the speed of light in a vacuum. The total Doppler shift,  $\mathbf{V}^*$ , from the Sutcliffe-Poole model, may be expressed as

$$\mathbf{V}^* = \mathbf{V}_I + \mathbf{V}_{II} + \mathbf{V}_{III}, \quad (4.18)$$

which is the vector sum of the three contributing components. These three components are known as the magnetic,  $\mathbf{V}_I$ , advection,  $\mathbf{V}_{II}$ , and compression,  $\mathbf{V}_{III}$ , mechanisms.

#### 4.2.2 The Magnetic Mechanism ( $\mathbf{V}_I$ )

The magnetic mechanism results from the changes in refractive index due solely to the ULF magnetic field intensity. Hence, this mechanism requires no bodily movement of electrons. The magnetic mechanism may be expressed as

$$\mathbf{V}_I = - \int_0^{z_R} \left[ \frac{\partial \mu}{\partial B_L} \frac{\partial B_L}{\partial t} + \frac{\partial \mu}{\partial B_T} \frac{\partial B_T}{\partial t} \right] dz, \quad (4.19)$$

where  $\mu$  is the real part of the refractive index in the AAH equation,  $z_R = z_R(t)$  is the real height of reflection and  $B_T$  and  $B_L$  are the components of the terrestrial magnetic induction transverse and parallel to the radio wave direction, respectively. If the perturbation field is assumed to vary as  $\mathbf{b} = \mathbf{b}_0 \exp^{-i\omega t}$ , then the magnetic mechanism may be simplified to

$$\mathbf{V}_I \cong -i\omega \int_0^{z_R} \left[ \frac{\partial \mu}{\partial B_L} b_z + \frac{\partial \mu}{\partial B_T} b_x \right] dz, \quad (4.20)$$

where  $b_x$  and  $b_z$  are the magnetic field perturbations in the X and Z components, respec-

tively. Equation 4.20 describes a contributing mechanism to the overall Doppler shift,  $V^*$ , that is produced solely from changes in the magnetic field intensity.

### 4.2.3 The Advection Mechanism ( $V_{II}$ )

The early theory developed by Rishbeth and Garriott (1964) explained that the Doppler frequency oscillations were due to the ULF electric field, causing a vertical bulk motion of electrons in the ionosphere. Figure 3.8 presented a schematic of a down-going Alfvén wave and shows how, through the motor effect, the vertical motion of the reflection height of an HF radio wave might be affected.

The vertical motion is the vertical component of the  $\mathbf{E} \wedge \mathbf{B}$  plasma drift velocity as shown in Figure 3.8. This vertical motion is now known as the advection mechanism. The electron drift velocity was originally inferred by Rishbeth and Garriott (1964) as

$$v = \frac{(\mathbf{E} \wedge \mathbf{B})_Z}{B^2}. \quad (4.21)$$

Using equation 4.21 with the perturbation electric field vector varying as  $\mathbf{E} = \mathbf{E}_0 \exp^{-i\omega t}$ , in conjunction with the knowledge that (a) the vertical component of  $\nabla \mathbf{B}$  is relatively far greater than the horizontal component and (b) that the refractive index is far more sensitive to changes in electron density than magnetic field intensity, the advection mechanism may be expressed as

$$\mathbf{V}_{II} \cong - \int_0^{z_R} \left[ \frac{\partial \mu}{\partial z} V_z \right] dz. \quad (4.22)$$

### 4.2.4 The Compressional Mechanism ( $V_{III}$ )

The compressional mechanism results from changes in the refractive index brought about by variations in the local plasma density. The redistribution of electrons caused by the compression and/or rarefaction induced by the ULF energy, as the plasma is "frozen-into" the background field, causes this change. The compressional mechanism may be expressed as

$$\mathbf{V}_{\text{III}} = - \int_0^{z_R} \left[ \frac{\partial \mu}{\partial N} N (\nabla \cdot \mathbf{V}) \right] dz, \quad (4.23)$$

where  $N$  is the electron number density. After rewriting  $\nabla \cdot \mathbf{V}$  as three components and simplifying by considering the relative magnitude of these terms 4.23 may be expressed as

$$\mathbf{V}_{\text{III}} = - \int_0^{z_R} \left[ -i\omega \frac{\partial \mu}{\partial N} \frac{N}{\mathbf{B}_0} b_p - \frac{\partial \mu}{\partial N} \frac{6N f(\Lambda)}{\mathbf{B}_0 r} E_y \right] dz, \quad (4.24)$$

where  $f(\Lambda) = \frac{\cos(\Lambda)[\cos^2(\Lambda)+1]}{[3 \sin^2(\Lambda)+1]^{\frac{3}{2}}}$ ,  $\Lambda$  is the dipole latitude,  $r$  is the geocentric distance and  $b_p$  is the field-aligned component of the pulsation field and is defined as,  $b_p = b_x \cos(I) + b_z \sin(I)$ .

#### 4.2.5 The 1-D Numerical Model - Running the Model

The numerical system used in this thesis (Sciffer et al., 2005) solves one dimensional differential equations utilising inputs of atmospheric, ionospheric and ULF wave parameters. The model comprises 500 points in the  $Z$  (vertical) direction, as the upper boundary and grid spacing are set at 1000 km and 2 km, respectively. The top boundary at 1000 km is where resistive MHD conditions are assumed. The four one-dimensional differential equations are solved using the Numerical Algorithms Group (NAG) package, F04ADF. The electrical properties of the ionosphere are described by height integrated Pedersen, Hall and parallel (or direct) conductivities. In the model the atmospheric composition is found from a thermosphere model based on satellite mass spectrometer and ground-based incoherent scatter data (MSISE90) (Hedin et al., 1991). The ionospheric composition is found from the IRI model with the exception of the electron density profile, which is determined using the POLAN algorithm (Titheridge, 1985), which will be detailed later in this section. The final step in the process is to calculate the Doppler shift contributions for the three mechanisms outlined in the model of Poole and Sutcliffe (1988) and the Altar-Appleton-Hartree equation is used for this purpose.

Experimental inputs to the model are required from observation and comprise the: date, electron density profile, Ap index, F10.7 index, incident wave mode, east-west wavenumber and north-south wavenumber. The numerical model then solves the four 1-D differential equations, equations 4.8, 4.9, 4.10 and 4.11, with the use of the relevant boundary conditions.

### **F10.7 cm Flux**

Radio energy is emitted from the Sun with an intensity that varies periodically. The radio flux originating from the solar chromosphere is highly sunspot number dependent. Figure 4.1 presents the solar flux at 2800 MHz, corresponding to a 10.7 cm wavelength, over the entire solar disk between 1940 - 2005. The periodic variation in intensity is highlighted by the grey shaded regions that show the years of maximum flux. This parameter is called F10.7 (Bougher and Roble, 1991).

### **Ap Index**

The Ap index is another input to the model and is a measure of geomagnetic activity over the Earth.

### **Electron Density Profile**

Another required input to the model is the electron density variation with altitude and is either provided from the IRI, or when ionosonde data are available inverting the ionosonde trace with the POLAN algorithm (Titheridge, 1985).

The POLynomial ANalysis program (POLAN) algorithm (Titheridge, 1985) provides a means of determining the real height of the lower slope of the electron density profile by inverting the virtual height determined from the Tromsø dynasonde. The real and virtual heights for a vertically incident radio wave on the ionosphere are related by equation 3.11. A simple procedure to verify that the numerical solution has been calculated correctly is to invert the electron density profile and convert this to a plasma frequency variation with height. A determination of the decrease in propagation speed at each point along the

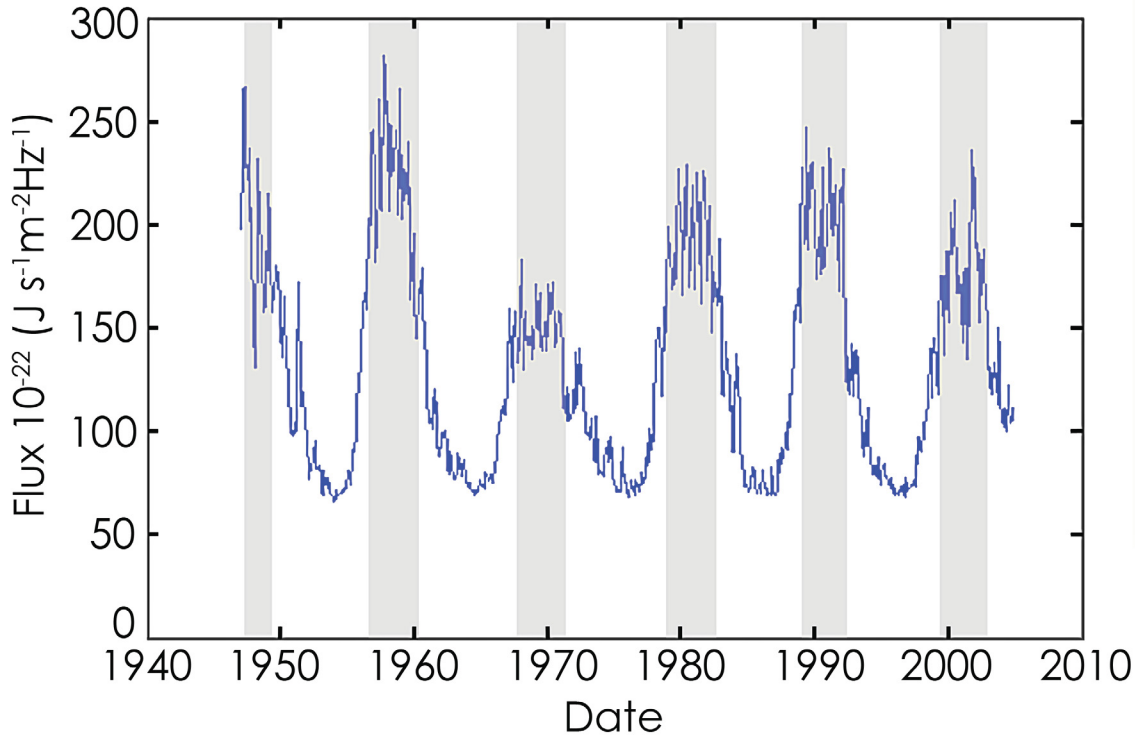


Figure 4.1: The F10.7 cm flux from 1940 to 2005. The periodic variation in intensity is highlighted with the grey shaded regions that show the years of maximum flux.

bottom side of the electron density profile reveals the time taken to propagate upwards, be reflected in the ionosphere, and propagate to the ground. This process yields a virtual height, which can be compared with the virtual height found by the ionosonde.

Figure 4.2 presents an example plasma frequency profile as a function of altitude for 16 April 1998 10:04 UT. The green dots represent the O-mode ionogram trace and the red dots represent the X-mode. The overplotted  $F$  and  $E$  characters show the location of the assumed F- and E- regions, respectively, which are used to generate the POLAN inversion (shown in blue). A dual-Chapman function (shown in black) may be fitted to the output from POLAN in order to generate an electron density profile that more closely matches observations from the Tromsø dynasonde than using the IRI. The red vertical line on Figure 4.2 shows the DOPE transmission frequency and the corresponding horizontal red line highlights the reflection altitude. The reflection altitude is found to be approximately 184 km in this example. The peak FoF2 is shown by the vertical purple line.

While the IRI seems reasonable for long-term variations of ionospheric trends, on a

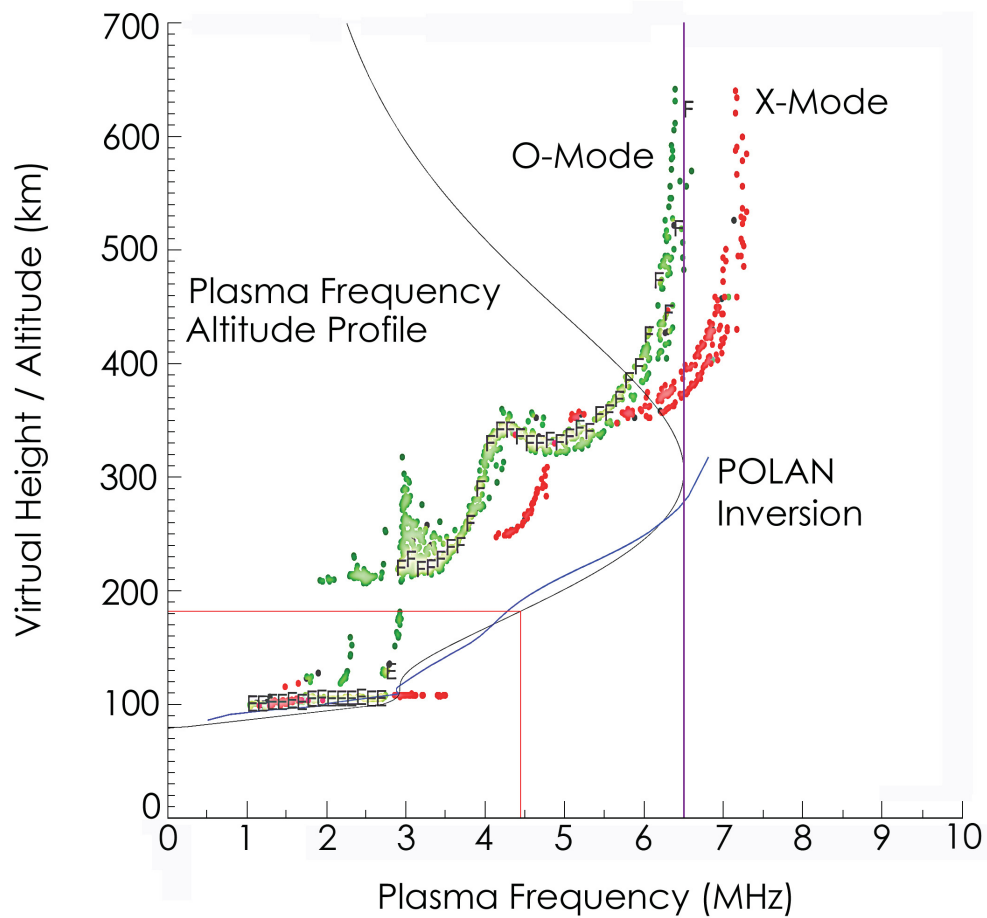


Figure 4.2: Plasma frequency as a function of altitude for 16 April 1998 10:04 UT. The green dots represent the O-mode ionogram trace and the red dots represent the X-mode. The curved black line presents the dual-Chapman function fit to the POLAN inversion, which is highlighted by the solid blue line. The red vertical line on the panel shows the DOPE transmission frequency. The reflection altitude is determined to be 184 km. Peak FofF2 is shown by the vertical purple line.

day-to-day basis using ionosonde data is a more accurate approach. Since this thesis is concerned with high-latitude observations of ULF waves using the DOPE HF Doppler sounder, located at Tromsø, the Tromsø dynasonde is the logical instrument of choice. Once the inversion is accomplished, a dual-Chapman function profile is fitted to the POLAN output to generate the electron density profile employed in the model. Fitted values, evenly sampled, are used to ensure a smooth function is used in the subsequent numerical calculation.

## The Wavenumbers

Since the east-west component of the wavevector,  $k_y$  is related to  $m$  by

$$k_y = \frac{m}{R_E \cos(\Lambda)}, \quad (4.25)$$

an estimate of  $k_y$  may be determined for the ULF wave signature. Typically,  $k_y$  is of order  $-1.0 \times 10^{-6} \text{ m}^{-1}$  ( $1.0 \times 10^{-6} \text{ m}^{-1}$  due to the sign convention of the 1-D numerical model, which is defined as westwards being positive). A negative effective azimuthal wavenumber,  $m$ , implies a westwards propagating wave. There are a number of measurements of  $m$  available and averaging the values, from a variety of station pairs of the IMAGE magnetometer chain and applying equation 4.25, produces a value of  $k_y$ . However, the choice for  $k_x$  is more challenging to obtain. The difficulty lies in measuring the phase difference at latitudinally spaced magnetometer sites close to resonance, where the phase varies rapidly. One method of determining a value of  $k_x$  is to find the change in the phase change of the wave with latitude at the geographical coordinates of Tromsø. Another method for determining the north-south wavenumber is to consider that since  $\nabla \wedge \mathbf{b} = 0$  in the atmosphere, the north-south wavenumber may be determined from the ratio of the X to Y components of the magnetic field recorded on the ground, together with the calculated value of  $k_y$ , using equation 4.25 (Hughes, 1974).

The first method proved to give a highly variable value of  $k_x$ , depending on the choice of magnetometer stations and so is not considered further. The second method based on Hughes (1974) is used here, as was also the case in Waters et al. (2007).

The Sutcliffe-Poole model is implemented after the 1-D numerical ULF wave model has produced vertical profiles of the electric and magnetic field. The Doppler shift mechanisms are calculated using equations 4.20, 4.22 and 4.24 and the aforementioned profiles, using a range of sounding frequencies up to peak FoF2.

## 4.3 Testing the 1-D Ultra Low Frequency Wave Numerical Model

### 4.3.1 Introduction

The results of the Leicester implementation of the 1-D numerical model are not completely consistent with those found within Waters et al. (2007) or Sciffer et al. (2005) for two reasons. Firstly, an issue was found with model wave phase after plotting the north-south wavenumber as a function of incident wave mode and altitude. This process identified a critical value of  $k_x$ , which yielded a discontinuity in the model phase profile. These findings revealed that the original model implementation contained an error in the mode eigensolver which could misidentify the fast mode top boundary condition (up and down) for certain values of  $k_x$  and  $k_y$ . The model implemented within this thesis is a corrected version, which has a correctly working eigensolver. In order to validate the new model the wave fields located within Hughes (1974) are reproduced using the corrected model and the correct structures of the electric and magnetic fields are determined.

Secondly, after personal communication with the author, the electric field within Waters et al. (2007) was not correctly scaled according to a horizontal magnetic field on the ground, resulting in a factor of two discrepancy between the ULF wave electric fields. The current implementation of the model thus represents the best such model available to date. Comparing the model Doppler shifts with those from Waters et al. (2007) has confirmed that the Sutcliffe-Poole model has been implemented correctly. Sutcliffe and Poole (1989) present the underlying electric and magnetic wave field profiles, which will be investigated now in order to see how the corrected Sciffer et al. (2005) model determines these two parameters.

### 4.3.2 The Sutcliffe-Poole Model Results

Section 2.7.2 detailed the original Sutcliffe-Poole model results from Sutcliffe and Poole (1990). Using the numerical model (Sciffer et al., 2005) it is possible to determine new

results using the original inputs from Sutcliffe and Poole (1990). The amplitudes and phases of the pulsation electric and magnetic field for the summer sunspot maximum case described by Sutcliffe and Poole (1990) are shown in Figure 4.3. Panel (a) shows the original electric field while panel (b) shows the associated phase. Panel (c) shows the original magnetic field while panel (d) shows the associated phase. Panel (e) shows the 1-D numerical model electric field while panel (f) shows the associated phase. Comparing panel (e) with panel (a) shows that the electric field amplitudes are very similar while comparing panels (b) and (f) shows that the phases are not reproduced exactly. Panel (g) shows the 1-D numerical model magnetic field while panel (h) shows the associated phase. Comparing panel (g) with panel (c) shows that once again the amplitudes are reproduced very well using the 1-D numerical model but similarly comparing panels (d) and (h) reveals that the phases are not reproduced exactly. These differences may arise from differences in the models or the ionospheric and atmospheric input conditions.

Panels (c) and (d) of Figure 4.4 present the Sutcliffe-Poole amplitude and phase model results when using inputs similar to those used in Sutcliffe and Poole (1990). An exact match of these conditions is not possible, as they are not specified precisely in the original publication. The east-west and north-south wavenumbers are matched exactly to the values used in Sutcliffe and Poole (1990). Panels (a) and (b) of Figure 4.4 are the same as those contained within panels (a) and (b) of Figure 2.11 but with coloured symbols for clarity when comparing with panels (c) and (d) of Figure 4.4.

The results are coloured such that the contributing mechanisms are: total Doppler velocity,  $V^*$ , (blue); contributing mechanisms: "magnetic",  $V_I$ , (black); "advection",  $V_{II}$ , (red) and "compressional",  $V_{III}$ , (green). The results are quite different from those seen by Sutcliffe and Poole (1990). From approximately 160 km - 240 km, panel (c) of Figure 4.4 shows that the advection mechanism is greater than either the magnetic or compressional mechanisms and that the compressional mechanism between these altitudes actually matches the total Doppler shift better than any other mechanism. At altitudes from roughly 240 km - 280 km, a regime change is noted whereby the advection term weakens. However, for all altitudes, it is clear that the phases in panels (d) and (b) are

similar but have some differences. In Sutcliffe and Poole (1990) it is apparent that the advective phase held steady for reflection altitudes of between 130 km - 280 km with a relative phase of approximately  $-90^\circ$  -  $-135^\circ$ . The model by Sciffer et al. (2005) agrees with this. However, the overall Doppler shift phase is slightly different when using the newer model.

Figure 4.5 is of an identical format to Figure 4.4, but now presents the 1-D numerical amplitude and phase model results when using inputs similar to those used in Sutcliffe and Poole (1990) for summer, sunspot maximum, midnight at a mid-latitude location.

The results have quite a different form from those modelled by Sutcliffe and Poole (1990). The study using the model by Sciffer et al. (2005) reveals that there are overall bigger Doppler shifts. In addition, while the advective mechanism contributes most to the total Doppler shift agreeing with Sutcliffe and Poole (1990), an increase in the overall Doppler shift with altitude from roughly 200 km - 300 km is seen. Over the same altitude range, panel (c) of Figure 4.5 shows that the total Doppler shift only varies between  $2 \text{ m s}^{-1}$  -  $15 \text{ m s}^{-1}$ . Magnification effects, as first described in section 3.3, seen within the results shown by Sutcliffe and Poole (1990), are not seen within the new Sciffer et al. (2005) model, possibly because peak FoF2 is approximately 0.6 MHz higher than the transmission frequency. The phase comparisons may be considered by looking at panels (b) and (d) of Figure 4.5. Panel (b) shows that the advective phase is most similar to the overall Doppler shift. While the same dominance is observed for the newer 1-D numerical model in panel (d), the difference lies in the relative phases. Panel (d) shows that the total Doppler shift phase varies from approximately  $50^\circ$  at 350 km and becomes roughly  $-30^\circ$  at 180 km.

Finally, Figure 4.6 presents the 1-D numerical amplitude and phase model results when using inputs similar to those used in Sutcliffe and Poole (1990) for winter, sunspot minimum, noon at a mid-latitude location.

The results for winter using the new numerical model reveal that compression and advection have almost equal importance, between reflection altitudes of 160 km - 240 km. The lowering of the overall Doppler shift is caused by the difference in phase between the

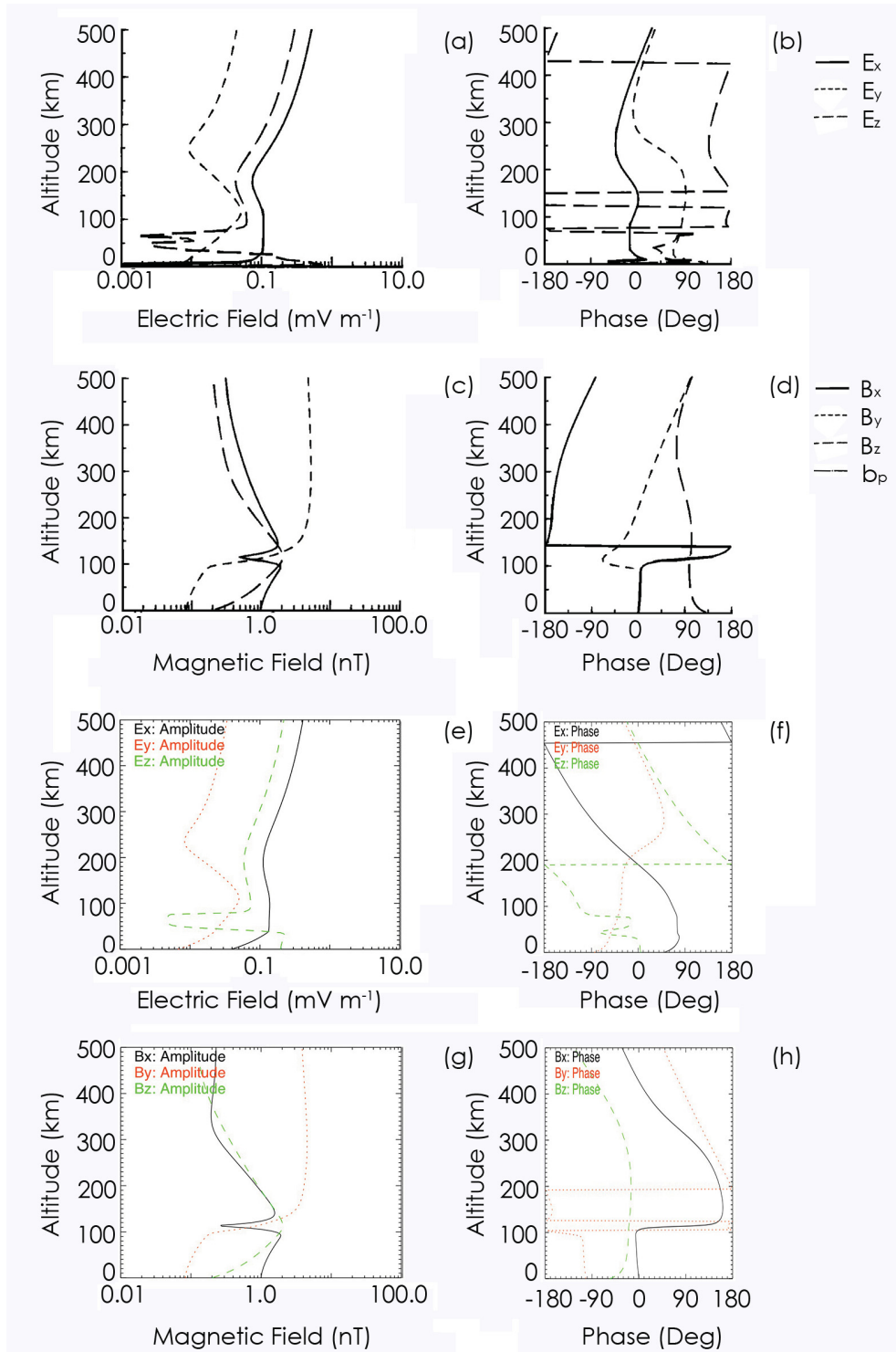


Figure 4.3: **(a – h)** The amplitudes and phases of the pulsation electric and magnetic field for summer and sunspot maximum as described by Sutcliffe and Poole (1989). Panel (a) shows the original electric field while panel (b) shows the associated phase. Panel (c) shows the original magnetic field while panel (d) shows the associated phase. Panel (e) shows the 1-D numerical model electric field while panel (f) shows the associated phase. Panel (g) shows the 1-D numerical model magnetic field while panel (h) shows the associated phase.

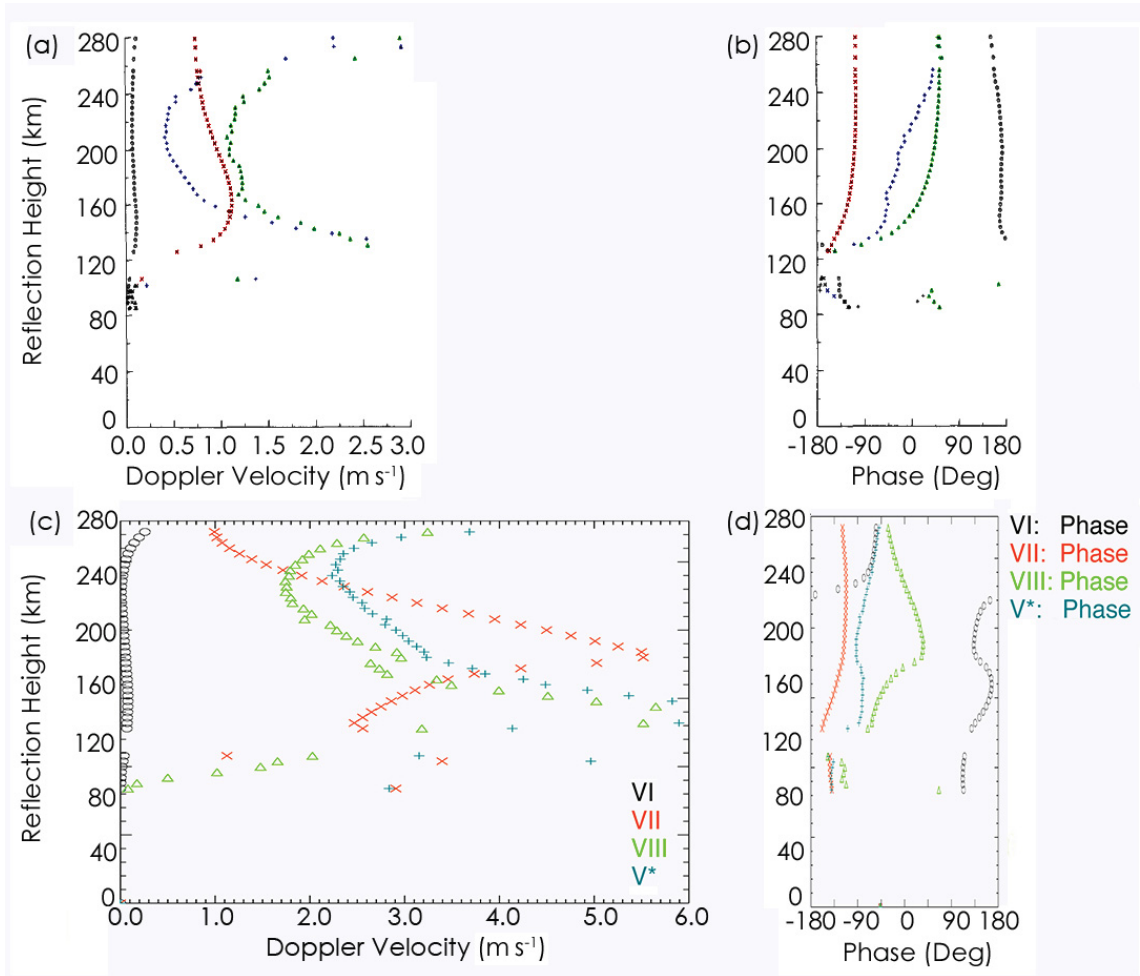


Figure 4.4: **(a – d)** The model results for midday, sunspot maximum, at a mid-latitude location, presenting the Doppler velocity and phase variation with reflection height. Panels (a) and (b) show the results from Sutcliffe and Poole (1990) and give the Doppler velocity and phase variation with reflection height. Panels (c) and (d) show the results from a study using the resistive MHD upper boundary model, developed by Sciffer et al. (2005). The colours and symbols used for the various mechanisms are as follows: total Doppler velocity (+),  $V^*$ , (blue); contributing mechanisms: "magnetic" (o),  $V_I$ , (black); "advection" (x),  $V_{II}$ , (red) and "compressional" ( $\Delta$ ),  $V_{III}$ , (green). All phases are measured relative to a north-south wave magnetic field perturbation,  $b_x$ , of 1 nT.

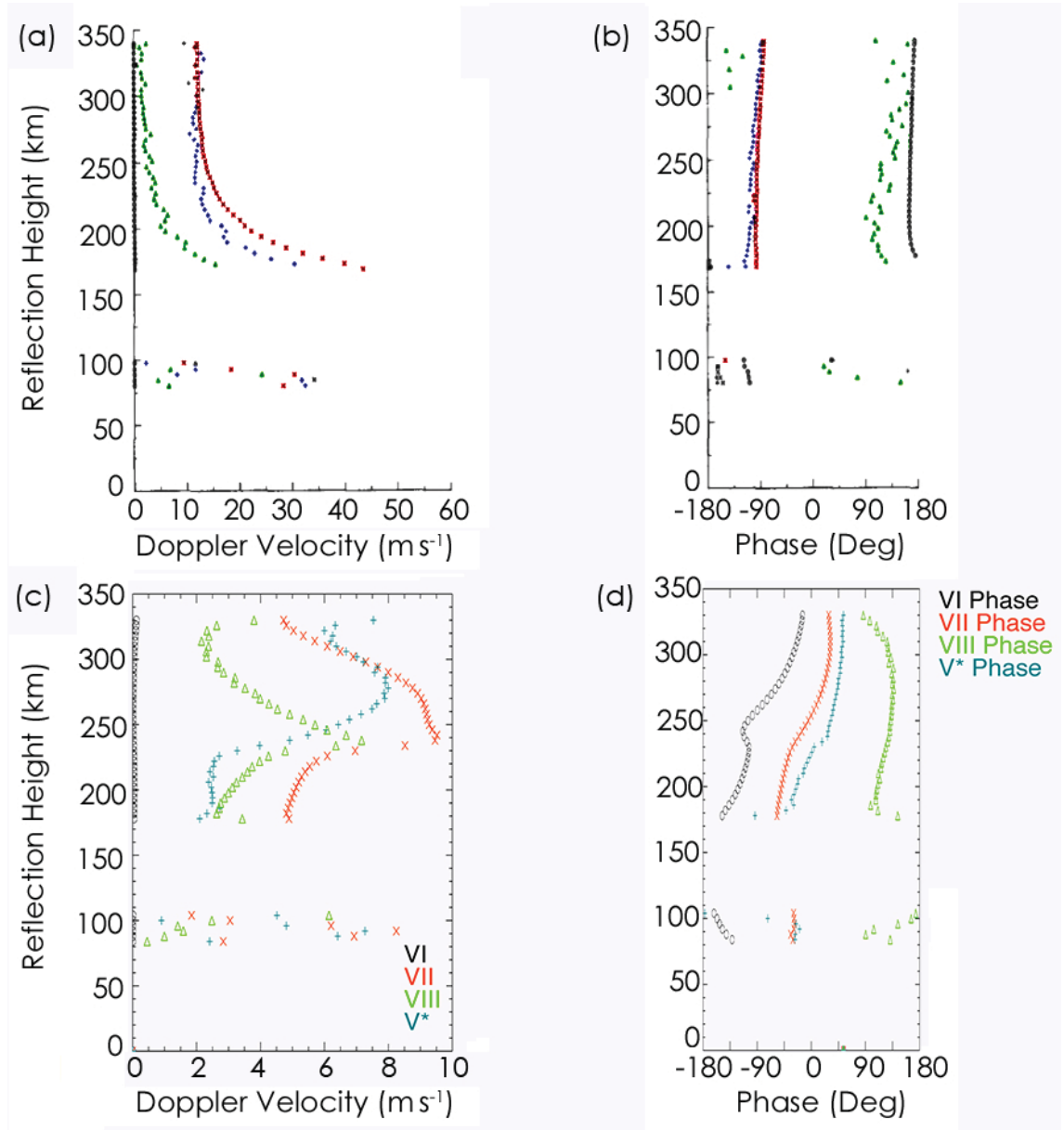


Figure 4.5: **(a – d)** The model results for midnight, sunspot maximum, at a mid-latitude location, revealing the Doppler velocity and phase variation with reflection height. Panels (a) and (b) show the results from Sutcliffe and Poole (1990) presenting the Doppler velocity and phase variation with reflection height. Panels (c) and (d) show the results from a study using the resistive MHD upper boundary model, developed by Sciffer et al. (2005). The panels present the Doppler velocity and phase variation with reflection height. The colours and symbols used for the various mechanisms are as follows: total Doppler velocity (+),  $V^*$ , (blue); contributing mechanisms: "magnetic" (o),  $V_I$ , (black); "advection" (x),  $V_{II}$ , (red) and "compressional" ( $\Delta$ ),  $V_{III}$ , (green). All phases are measured relative to a north-south wave magnetic field perturbation,  $b_x$ , of 1 nT.

compressional and advection mechanisms and Panel (b) of Figure 4.6 shows this phase behaviour is true for Sutcliffe and Poole (1990) as well. Comparing panels (b) and (d) of 4.6 shows that both the advection and compressional mechanism phase are reproduced reasonably well.

There are clearly similarities and differences between the models. These differences could be due to the increased sophistication of the Sciffer et al. (2005) model and or input parameter differences. The results presented here certainly indicate that the Sciffer et al. (2005) model is highly sensitive to input parameters. Indeed, Sutcliffe and Poole (1989) suggested sensitivities of the model to geophysical conditions such as the electron density profile or inclination, which have made verifying their original model difficult. Another restriction of the original Sutcliffe-Poole model, explained in section 2.7.2, is that the model assumes a mid-latitude location. The Sciffer et al. (2005) model does not have such restrictions, and can be run at any geographic location, including high-latitude.

### **4.3.3 The Sutcliffe-Poole Model Results at High-Latitude**

To make ionospheric measurements of the Doppler shift a ground-based HF Doppler sounder is used throughout this thesis. The numerical model input for geographical position must be identical to the position of the DOPE sounder for comparison purposes. Panels (a) and (b) of Figure 4.7 present the 1-D numerical amplitude and phase model results when using the same inputs as those used in panels (c) and (d) of Figure 4.4 apart from the geographical location, which is now at Tromsø, Norway. Panel (a) shows a larger overall Doppler shift at all altitudes for the high-latitude location. The compressional and advection mechanisms contribute the most to give an overall Doppler shift that is (1) less than the individual contributing mechanisms between 200 km - 230 km but (2) larger than the individual components between altitudes of 250 km - 280 km.

However, panel (b) reveals that the advective phase at high-latitude does not match the advective phase from panel (b) of Figure 4.4 showing a relative phase difference of between  $90^\circ$  and  $-10^\circ$ . Panels (c) and (d) of Figure 4.7 present the 1-D numerical amplitude and phase model results when using the same inputs as those used in panels (c) and (d)

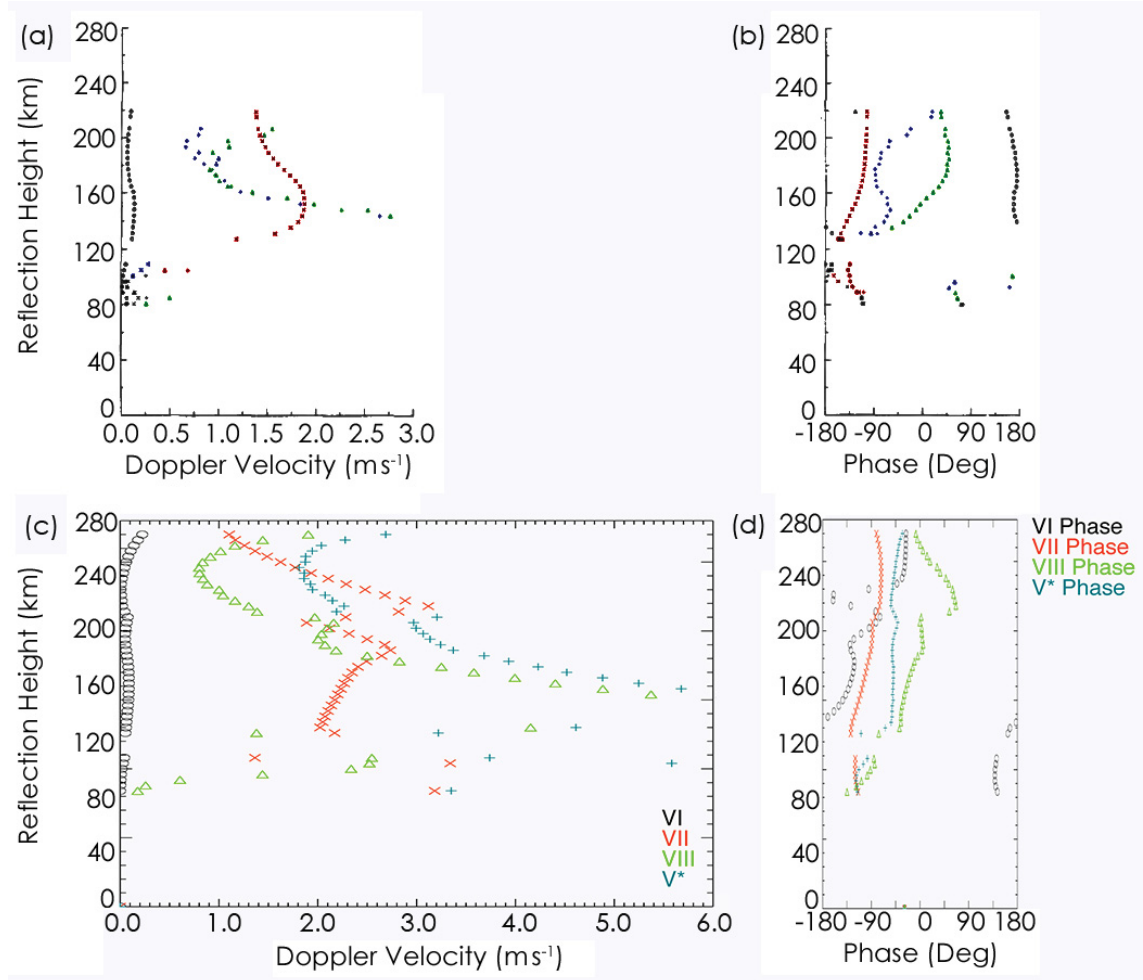


Figure 4.6: **(a – d)** The model results for noon, sunspot minimum, winter, at a mid-latitude location, revealing the Doppler velocity and phase variation with reflection height. Panels (a) and (b) present the results from Sutcliffe and Poole (1990) showing the Doppler velocity and phase variation with reflection height. Panels (c) and (d) show the results from a study using the resistive MHD upper boundary model, developed by Sciffer et al. (2005). The panels present the Doppler velocity and phase variation with reflection height. The colours and symbols used for the various mechanisms are as follows: total Doppler velocity (+),  $V^*$ , (blue); contributing mechanisms: "magnetic" (o),  $V_I$ , (black); "advection" (x),  $V_{II}$ , (red) and "compressional" ( $\Delta$ ),  $V_{III}$ , (green). All phases are measured relative to a north-south wave magnetic field perturbation,  $b_x$ , of 1 nT.

of Figure 4.5, apart from the geographical location. Panel (c) shows that at midnight the overall Doppler shift has a similar form at high-latitude and mid-latitude. The compressional and advection mechanisms contribute out of phase to yield an overall Doppler shift that is less than the sum of these two components between 230 - 300 km. Panel (d) of Figure 4.7 reveals that the advective relative phase at high-latitude remains roughly constant between phases of  $90^\circ$  to  $120^\circ$ . In both cases, once again, the magnetic mechanism provides a negligible contribution to the overall Doppler shift.

Comparing the histogram of Figure 2.18 with panel (b) of Figure 4.4, Wright et al. (1997) concluded that 60% of their ULF signatures, which had relative phases in the range  $90^\circ$  -  $150^\circ$  with  $b_y$  leading, were a result of the advection mechanism. Wright et al. (1997) made a tentative extrapolation of the Sutcliffe-Poole model in order to apply it to a high-latitude location. Panel (d) of Figure 4.4 reveals that advection would have been suggested as the explanation for the relative phase change had the 1-D numerical model been available for mid-latitudes since the mid-latitude results are consistent in the new and old model runs. However, as panel (b) of Figure 4.7 shows the phases are different when the new numerical model is run at high-latitude. This is an example of the dangers of using the results from Sutcliffe and Poole (1990) to extrapolate results to a high-latitude location. Therefore, the explanation of the relative phase change due to the "advective" contribution in Wright et al. (1997) is not entirely valid.

The question as to what the phase and Doppler shift amplitude will be at high-latitudes when the wave characteristics are typical of actual FLRs in that locality will be answered in detail in chapters 5 and 6. A sample event, in the next section, will show one such example.

It should be pointed out that the 1-D numerical ULF wave model results, which were required to be run at the geographical location of Tromsø, were, in error, run in the conjugate hemisphere at a latitude of  $-69.0^\circ$ .

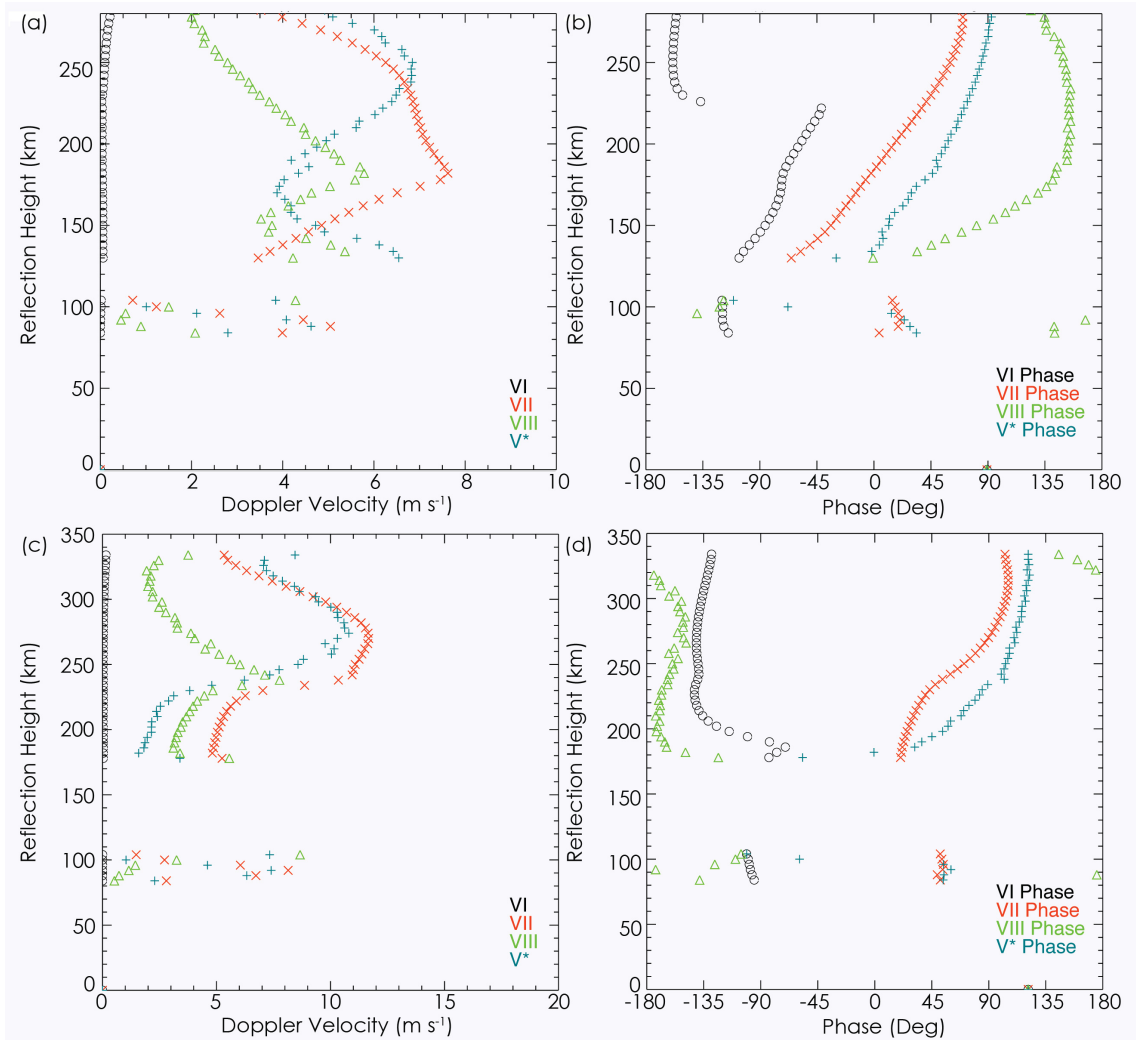


Figure 4.7: **(a – d)** The 1-D Numerical model results for the first two cases considered in Sutcliffe and Poole (1990) run at high-latitude. Panels (a) and (b) show the Doppler velocity and phase variation with reflection height, for local midday, sunspot maximum, at a high-latitude location. Panels (c) and (d) show the Doppler velocity and phase variation with reflection height, for local midnight, sunspot maximum, at a high-latitude location. The colours used for the various mechanisms are as follows: total Doppler velocity,  $V^*$ , (blue); contributing mechanisms: "magnetic,"  $V_I$ , (black); "advection",  $V_{II}$ , (red) and "compressional",  $V_{III}$ , (green). All phases are measured relative to a north-south wave magnetic field perturbation,  $b_x$ , of 1 nT.

### 4.3.4 A Sample Event

Figure 4.8 presents a ULF wave event typical of the ensemble of waves presented in chapter 6 that occurred on 29 December 2001 between 04:00 UT - 05:00 UT. A ULF wave is clearly visible in the SuperDARN CUTLASS (panels (a) and (b)), HF Doppler (panels (c) and (d)) and the IMAGE magnetometer data (panels (e) to (j)). The HF Doppler data are from channel 1, operating at 4.16 MHz. The ULF wave has a clear periodic signature of period approximately 450 s (2.22 mHz) revealed by Fourier analysis. The effective azimuthal wavenumber is calculated as  $m = +4$  from suitable pairs of IMAGE magnetometers indicating an eastward propagating wave. The east-west and north-south wavenumbers are found to be  $1.45 \times 10^{-6} \text{ m}^{-1}$  ( $-1.45 \times 10^{-6} \text{ m}^{-1}$  in the model) and  $1.52 \times 10^{-6} \text{ m}^{-1}$ , respectively. The F10.7 and Ap indices are 264.4 and 11, respectively. The peak FoF2 is determined, by the Tromsø dynasonde, to be 6.2 MHz. Figure 4.9 presents data from the Tromsø dynasonde. The green and red dots signify the X- and O-modes, respectively, while the overplotted solid black curve shows the dual-Chapman fit to the solid blue POLAN line (Titheridge, 1985). The dashed red line shows the original IRI profile and the dashed blue line shows the IRI when a multiplying factor is applied to make the peak match the O-mode peak of the ionosonde data. The electron density profile used in the modelling is the dual-Chapman POLAN fit.

Panels (a) to (d) of Figure 4.10 present results of one run of the 1-D numerical model for a purely shear Alfvénic incident wave mode. The magnetic and electric fields are scaled such that the total ground magnetic field matches observation (roughly 8 nT at 04:30 UT). Panel (a) presents the variation of the three magnetic field components with altitude. Panel (b) shows the magnetic phase variation for the same three components. Panel (c) shows the electric field variation for the three field components as a function of altitude. Panel (d) shows the electric field phase for the same three components. Panels (e) and (f) show the Doppler shift mechanism amplitude and phase, respectively. Black shows the magnetic variation ( $\mathbf{V}_I$ ), red shows the advection mechanism contribution ( $\mathbf{V}_{II}$ ), green is the compressional mechanism ( $\mathbf{V}_{III}$ ) and blue is the overall Doppler shift ( $\mathbf{V}^* = \mathbf{V}_I + \mathbf{V}_{II} + \mathbf{V}_{III}$ ). Finally, panel (f) shows the phase variation for the same mechanisms as in panel (e) and

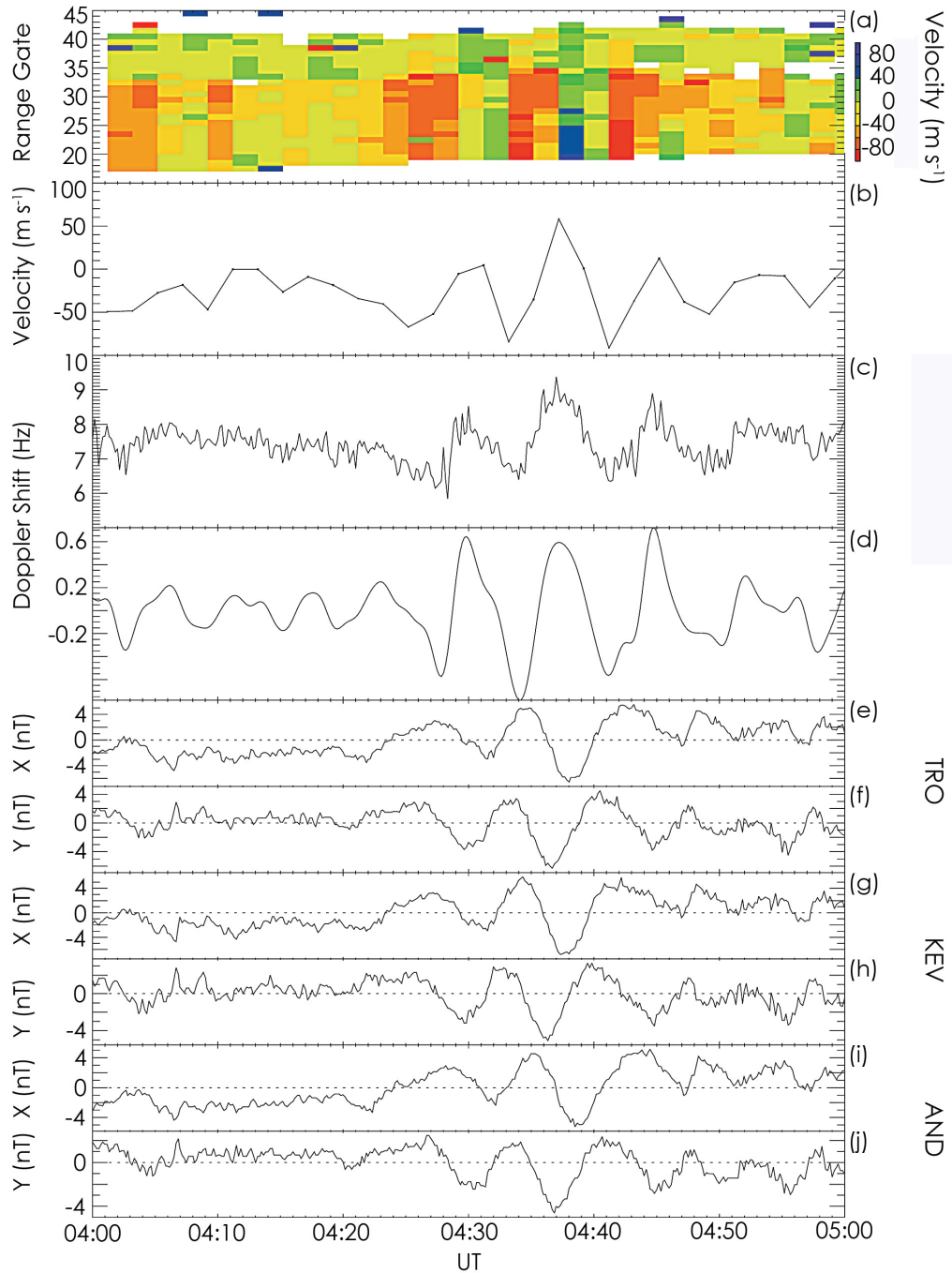


Figure 4.8: **(a – j)** CUTLASS, DOPE and IMAGE magnetometer data for the ULF wave recorded on 29 December 2001 between 04:00 UT - 05:00 UT. Panel (a) presents the CUTLASS Hankasalmi Doppler velocity recorded along beam 5. The dynamical velocity scale is such that red and blue indicate a plasma flow away and towards the radar, respectively. Panel (b) shows range cell 20 of the CUTLASS Hankasalmi radar data presented in panel (a). Panel (c) presents the Doppler O-mode peak trace from channel 1 operating at 4.16 MHz. Panel (d) shows filtered DOPE data excluding waves with periods outside of the range 200 s - 500 s. Panels (e) - (j) present IMAGE magnetometer data from three stations in the array. Panels (e) - (f) show unfiltered TRO-X and TRO-Y data. Panels (g) - (h) show unfiltered KEV-X and KEV-Y data. Panels (i) - (j) show unfiltered AND-X and AND-Y data.

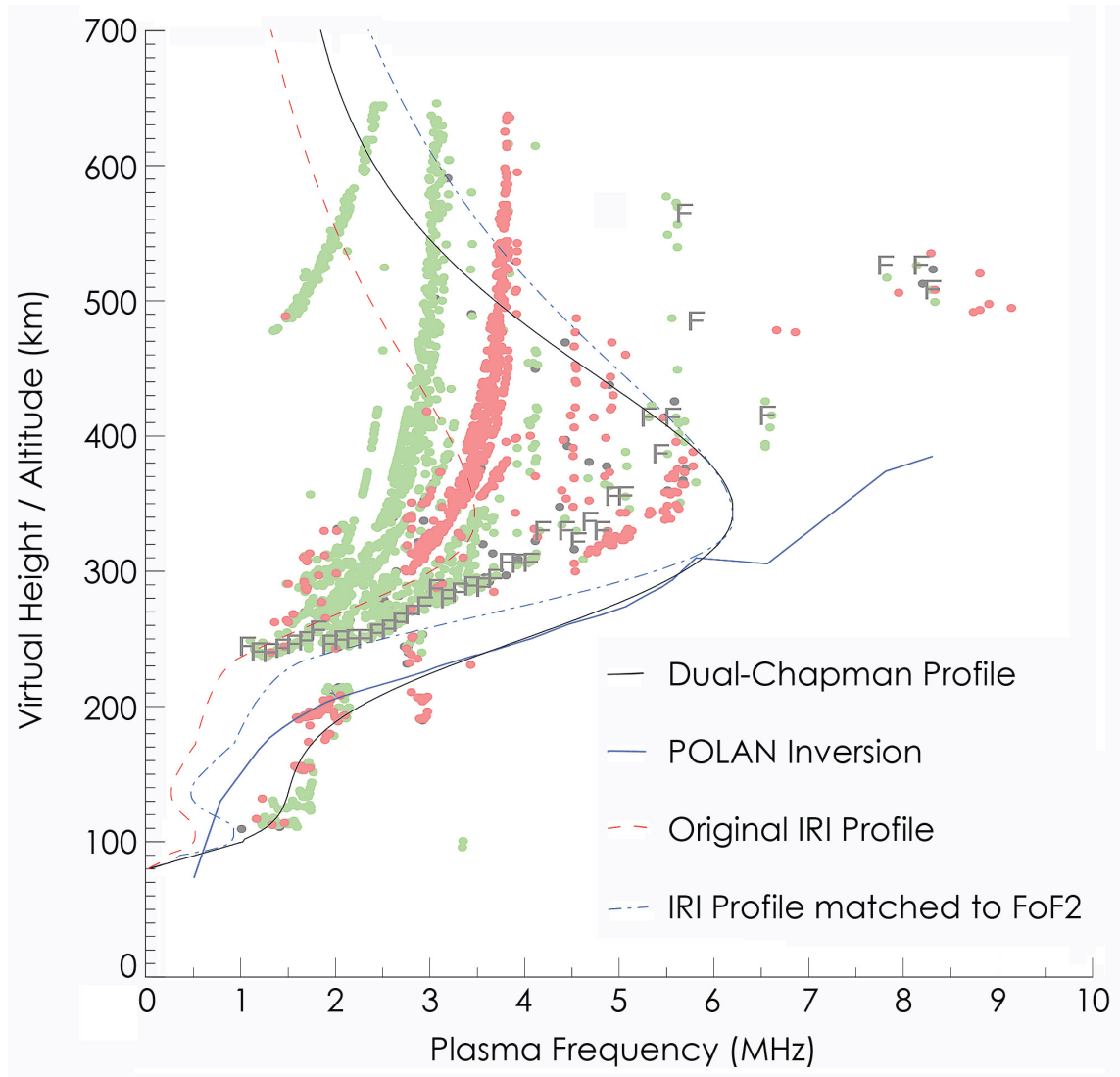


Figure 4.9: Plasma frequency as a function of altitude for the ULF wave event recorded on 29 December 2001 at 04:29 UT. The green and red dots represent the O- and X-mode ionogram traces, respectively. The curved black line presents the dual-Chapman function fit to the POLAN inversion, which is shown by the solid blue line. The dashed red line shows the original IRI profile and the dashed blue line shows the IRI when a multiplying factor is applied to make FoF2 match the ionosonde data. The reflection altitude for this event was 256 km.

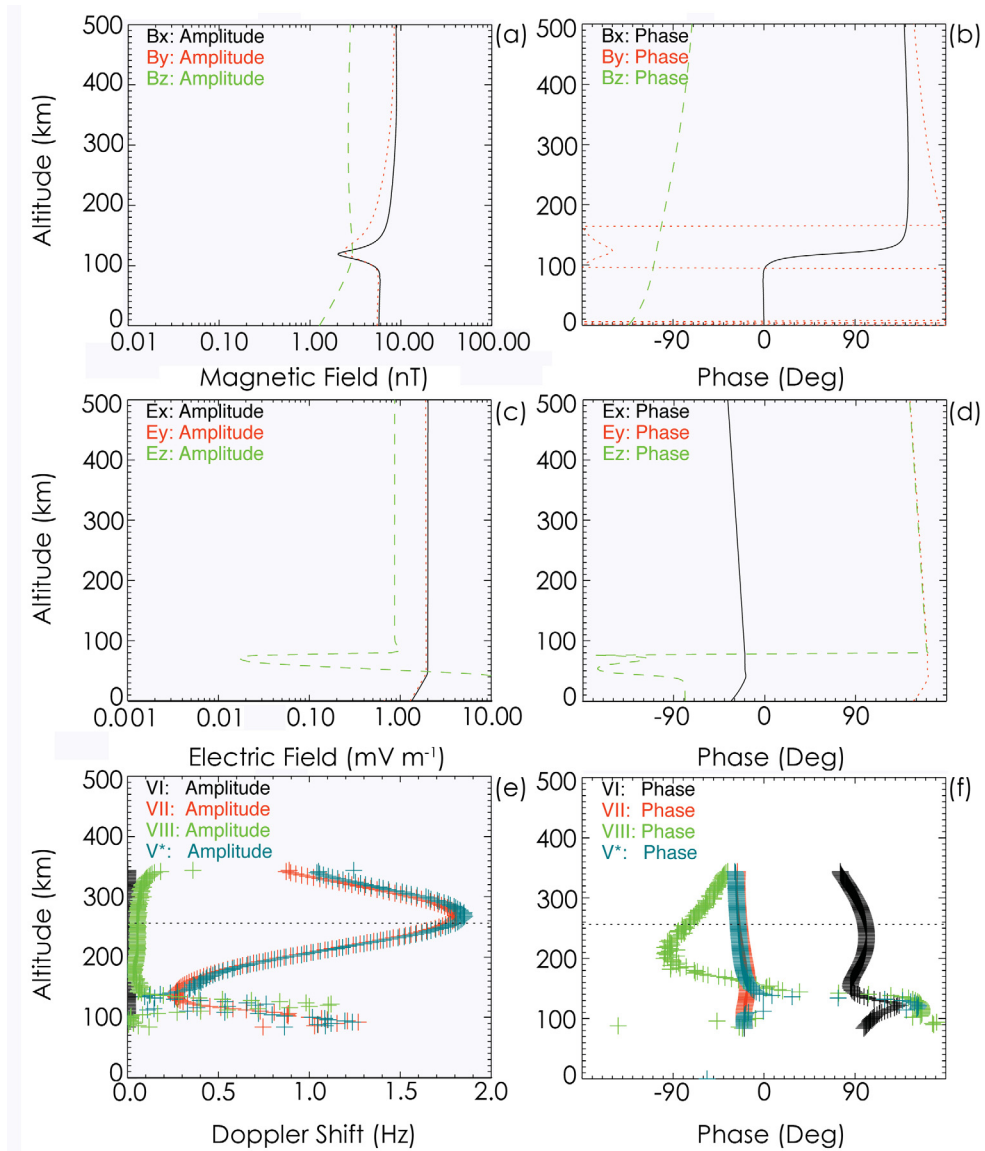


Figure 4.10: (a – f) Results of one run of the 1-D Numerical Model for a purely shear Alfvénic incident wave mode for an altitude range from the ground to 500 km. Panel (a) presents the variation of the three magnetic field components with altitude. Panel (b) shows the magnetic field phase variation for the same three components. Panel (c) shows the electric field variation for the three field components as a function of altitude. Panel (d) shows the electric field phase for the same three components. Panel (e) shows the Doppler shift mechanism contributions as a function of altitude. Black shows the magnetic variation ( $V_I$ ), red is the advection mechanism contribution ( $V_{II}$ ), green is the compression mechanism ( $V_{III}$ ) and blue is the overall Doppler shift given by the vector addition of the three Doppler shift components ( $V^* = V_I + V_{II} + V_{III}$ ). Panel (f) shows the phase variation for the same mechanisms as given in panel (e) and is colour coded in an identical fashion. All phases are plotted relative to a ground magnetic  $B_x$  of zero phase. The overplotted black dot-dashed line highlights the DOPE reflection altitude, at roughly 256 km.

is colour coded identically. All phases are plotted relative to a ground magnetic  $B_x$  of zero phase. The black dot-dashed line shows the DOPE reflection altitude, at roughly 256 km. The overall Doppler shift for a purely shear Alfvénic incident mode wave has most contributions from the advection mechanism ( $V_{II}$ ) as there are very small contributions from the other two mechanisms. There are also very large Doppler shifts recorded in the E-region, which are a characteristic of these plots. The large Doppler shift results from the "knee" in the electron density profile corresponding to a transmission frequency of approximately 1.5 MHz. The X component magnetic field phase illustrates a characteristic phase rotation at approximately 110 km as detailed by Hughes (1974). Compared to the high-latitude Sutcliffe-Poole result (Figure 4.7) it is clear that the advection mechanism is dominant in this FLR example and the model Doppler phase is more closely matched to both the "advective" phase and the X component of the magnetic field recorded on the ground.

### Wave Mode Variation

Figure 4.10 shows that the overall model Doppler amplitude at the DOPE reflection altitude for a purely shear Alfvénic incident wave is approximately 1.8 Hz when using a ground horizontal magnetic wave amplitude of 8 nT. The amplitude is quite comparable with the observed Doppler shift of roughly 1.50 Hz. One factor which strongly influences the predicted Doppler shift, and may account for the marginal discrepancy in the Doppler amplitude, is the wave mode mix of the incoming ULF wave between fast compressional and Alfvénic wave power. Figure 4.11 presents the electric and magnetic field model results for a magnetic field magnitude of 8 nT on the ground. The plots present the electric and magnetic field variation with altitude for various wave mixes. Panels (a) and (c) show the X and Y components of the electric field, while panels (b) and (d) show their respective phases. Panels (e) and (g) show the X and Y components of the magnetic field and panels (f) and (h) show their respective phases. All phases are plotted relative to a ground magnetic  $B_x$  of zero phase. Referring to panels (a) and (e) of Figure 4.11, the fast mode is important as this wave mode gives a smaller electric field within the ionosphere.

A plot of wave mix variation as a function of both altitude and Doppler shift is required to determine the predicted Doppler shift that best matches observation and, hence, the corresponding wave mix. Figure 4.12 presents the Doppler shift amplitude and phase variation as a function of wave mix and altitude. These plots show how a variation in the Alfvénic wave mix affects the Doppler Shift. The wave mix and altitude ( $X$  and  $Y$ ) are scaled identically to Figure 4.11. Panels (a) and (b) show the magnetic mechanism amplitude and phase. Panels (c) and (d) show the advection mechanism amplitude and phase. Panels (e) and (f) show the compressional mechanism amplitude and phase. Finally, panels (g) and (h) show the overall Doppler shift amplitude and phase. Once again all phases are plotted relative to a ground magnetic  $B_x$  of zero phase. As the wave mix tends towards a purely shear Alfvénic mode the Doppler shift increases across all mechanisms. The advection mechanism is the dominating mechanism for a purely shear Alfvénic incident wave mix at the DOPE reflection altitude. The phase contributions from the different mechanisms, panels (b), (d), (f) and (h) of Figure 4.12 highlight that at the DOPE reflection altitude of 256 km the overall Doppler shift phase looks similar to the "advective" phase.

Figure 4.13 presents the Doppler shift variation as a function of wave mix at the DOPE reflection altitude (256 km). The observed Doppler amplitude is approximately 1.5 Hz as recorded by the HF Doppler sounder and is shown via Figure 4.13 to correspond with a wave mix of roughly 0.99. The wave mix value of 0.99 implies that the wave measured on 29 December 2001 at 04:30 UT in the ionosphere and on the ground using an HF Doppler sounder and IMAGE magnetometers, is essentially a pure shear Alfvén wave. The analysis technique outlined here is repeated in chapters 5 and 6 of this thesis.

### 4.3.5 Model Dependence on Key Parameters

Before comparing the model results to observed HF Doppler data, the dependence of the results on the variation of a number of key wave characteristics will be investigated to determine the sensitivity of the modelling on these parameters. To investigate the dependence of the model Doppler shift on the east-west and north-south wavenumbers,  $k_y$  and  $k_x$ , the electron density gradient, the height integrated Pedersen and Hall conductiv-

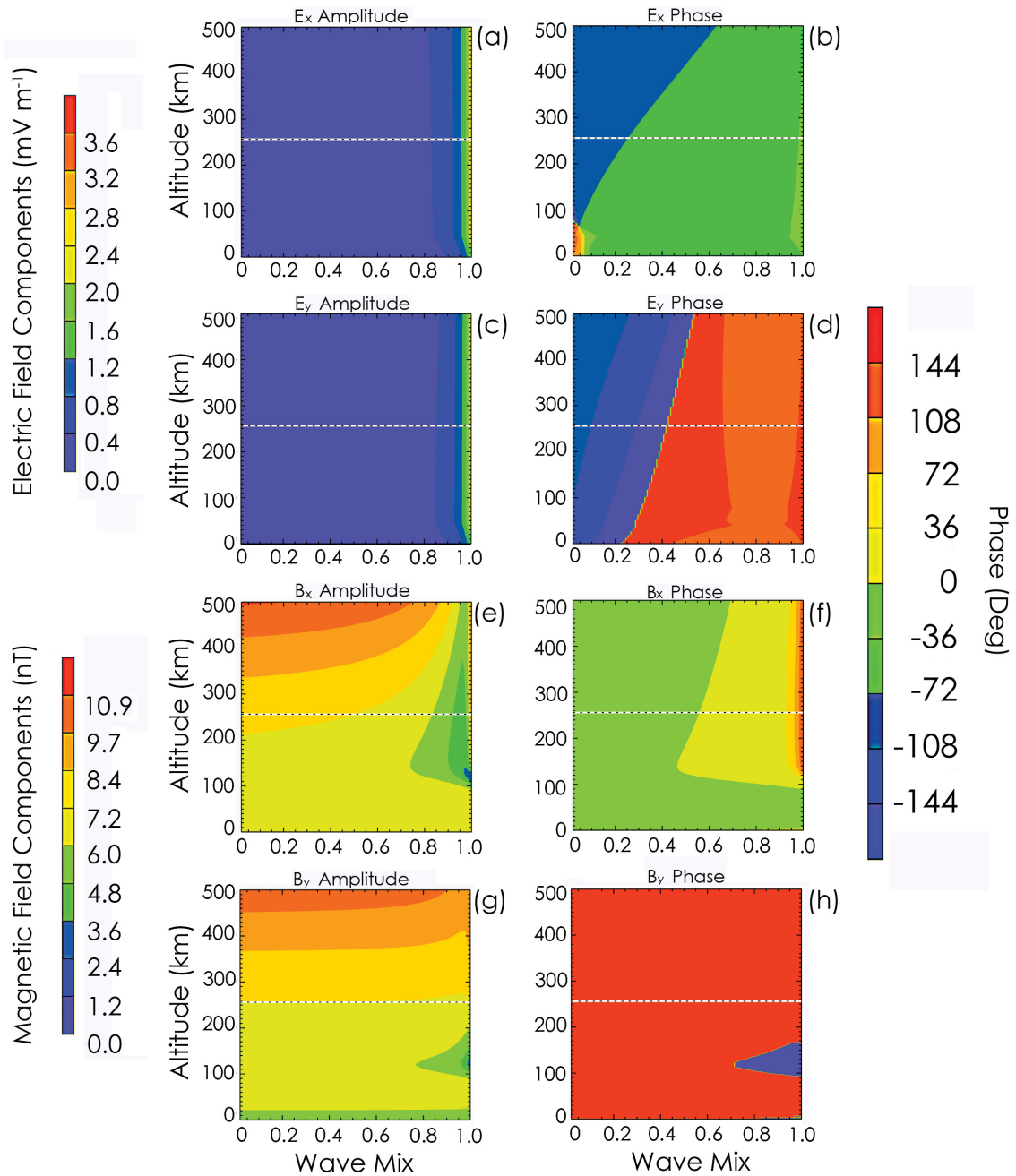


Figure 4.11: **(a – h)** Electric and magnetic field model results of the ULF wave event on 29 December 2001, at 04:30 UT, as a function of altitude and wave mix scaled to make the magnetic field magnitude 8 nT on the ground. Panel (a)  $E_x$ . (b)  $E_x$  phase. (c)  $E_y$ . (d)  $E_y$  phase. (e)  $B_x$ . (f)  $B_x$  phase. (g)  $B_y$ . (h)  $B_y$  phase. All phases are plotted relative to a ground magnetic  $B_x$  of zero phase. The overlaid dot-dashed line shows the reflection height of the HF Doppler sounder.

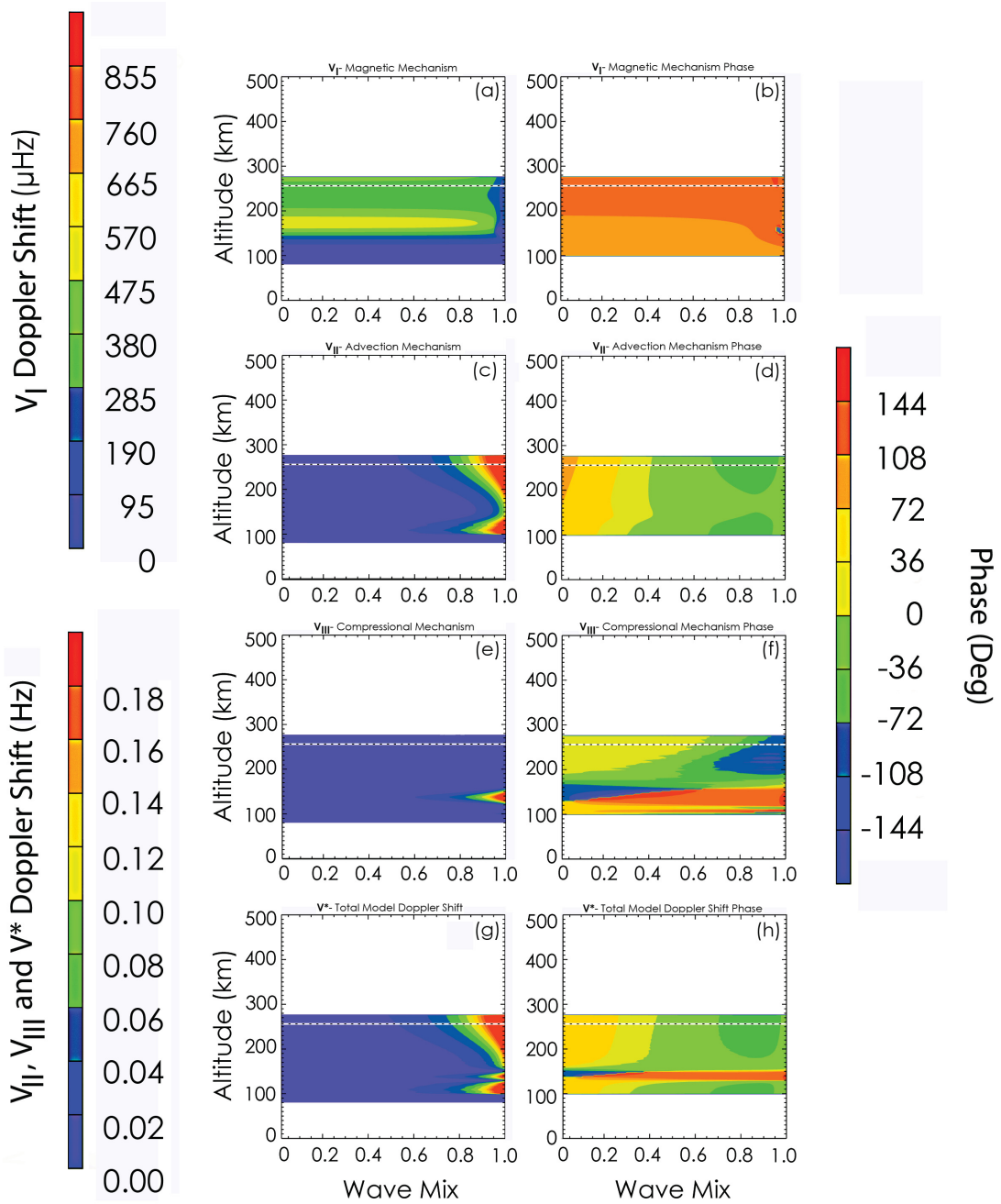


Figure 4.12: (a – h) Doppler shift mechanism model results for the ULF wave event on 29 December 2001, at 04:30 UT. All contour plot panels show data as functions of both altitude and wave mix. Panel (a)  $V_I$ . (b)  $V_I$  phase. (c)  $V_{II}$ . (d)  $V_{II}$  phase. (e)  $V_{III}$ . (f)  $V_{III}$  phase. (g)  $V^*$ . (h)  $V^*$  phase. All phases are plotted relative to a ground magnetic  $B_x$  of zero phase. The overlaid dot-dashed line shows the reflection height of the HF Doppler sounder.

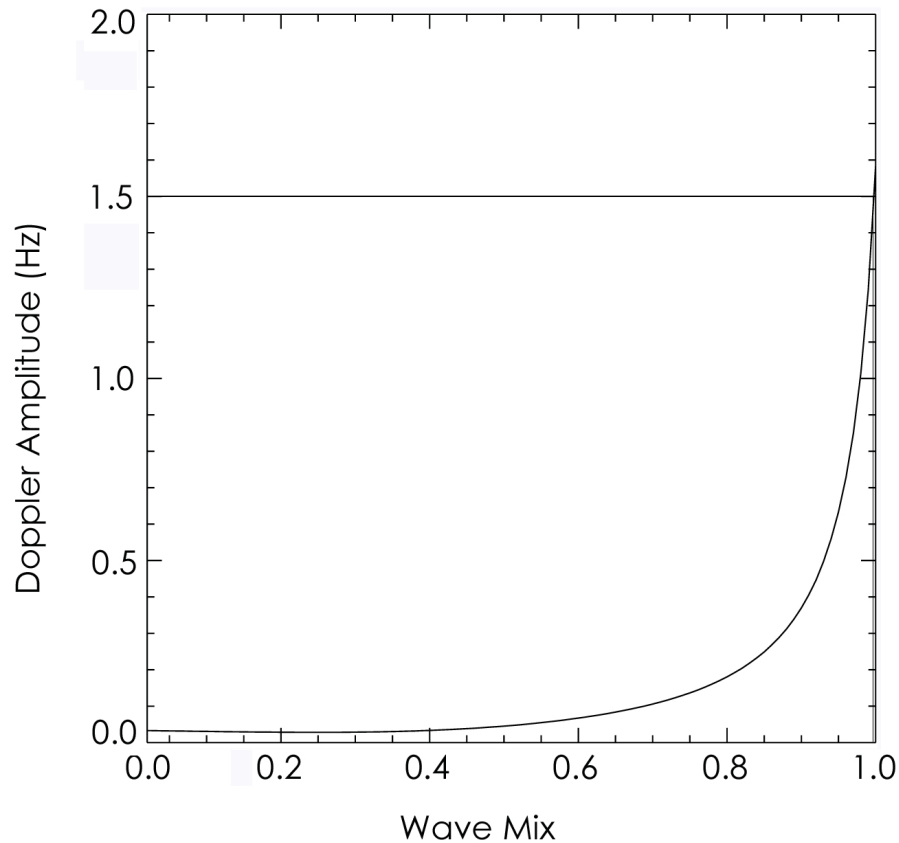


Figure 4.13: Overall Doppler shift model results of the ULF wave event recorded on 29 December 2001 at 04:30 UT for wave mixes ranging between zero and unity. The figure shows the variation of total Doppler shift with wave mix at the DOPE reflection altitude of 256 km when the ground magnetic field has been scaled by the horizontal magnetic field perturbation recorded on the ground. The over-plotted solid black line shows the wave mix corresponding to the observed Doppler amplitude.

ities and the ionospheric reflection coefficient, the example ULF wave event as detailed in Figure 4.8, which occurred on 29 December 2001, will be used. Each of these model parameters will be varied one-by-one while every other parameter will be kept the same as for the original ULF wave event.

### The East-West Wavenumber Dependence

Assuming an incident wave mode of unity (for a purely shear Alfvénic incident mode) the east-west wavenumber may be varied through a range of values to see what effect this parameter has upon the determined model Doppler shift. Figure 4.14 presents the

electric and magnetic field model results. The panels present the electric and magnetic field variation with altitude for east-west wavenumber values of between  $1.0 \times 10^{-6} \text{ m}^{-1}$  and  $1.1 \times 10^{-5} \text{ m}^{-1}$  corresponding to  $m = 2 - 12$  and azimuthal scale lengths of between 630 km - 6300 km. Each of the panels have been scaled for a horizontal magnetic field perturbation of 1 nT recorded on the ground by magnetometers. Panels (a) and (c) show the X and Y components of the electric field, while panels (b) and (d) show their respective phases. Panels (e) and (g) show the X and Y components of the magnetic field and panels (f) and (h) show their respective phases. All phases are plotted relative to a ground magnetic  $B_x$  of zero phase. Referring to panels (c) and (e) of Figure 4.14, an increase in  $k_y$  increases the Y component of the electric field and the X component of the magnetic field for a given magnetic field perturbation on the ground. Thus, it seems likely that as  $k_y$  increases the associated Doppler shift will increase accordingly.

Figure 4.15 presents the Doppler shift amplitude and phase variation as a function of  $k_y$  and altitude. These plots show how a variation in the east-west wavenumber affects the Doppler Shift. The plots are scaled identically to Figure 4.14. Panels (a) and (b) show the magnetic mechanism amplitude and phase. Panels (c) and (d) show the advection mechanism amplitude and phase. Panels (e) and (f) show the compressional mechanism amplitude and phase. Finally, panels (g) and (h) show the overall Doppler shift amplitude and phase. As the east-west wavenumber increases in magnitude the Doppler shift increases across all mechanisms. The advection mechanism is the dominating mechanism for a purely shear Alfvénic incident wave at the DOPE reflection altitude as can be seen by comparing panels (c) and (g) of Figure 4.15. The phase contributions from the different mechanisms, panels (b), (d), (f) and (h) of Figure 4.15 highlight that at the DOPE reflection altitude of 256 km the overall Doppler shift phase looks similar to the "advective" phase.

It should be noted that if the model Doppler shifts are normalised for a horizontal magnetic field perturbation of 1 nT on the ground, as is conducted here, then the normalised model Doppler shift increases as the wave attenuates for small-scales. Therefore, a normalised magnetic field measured on the ground gives a bigger HF Doppler signature.

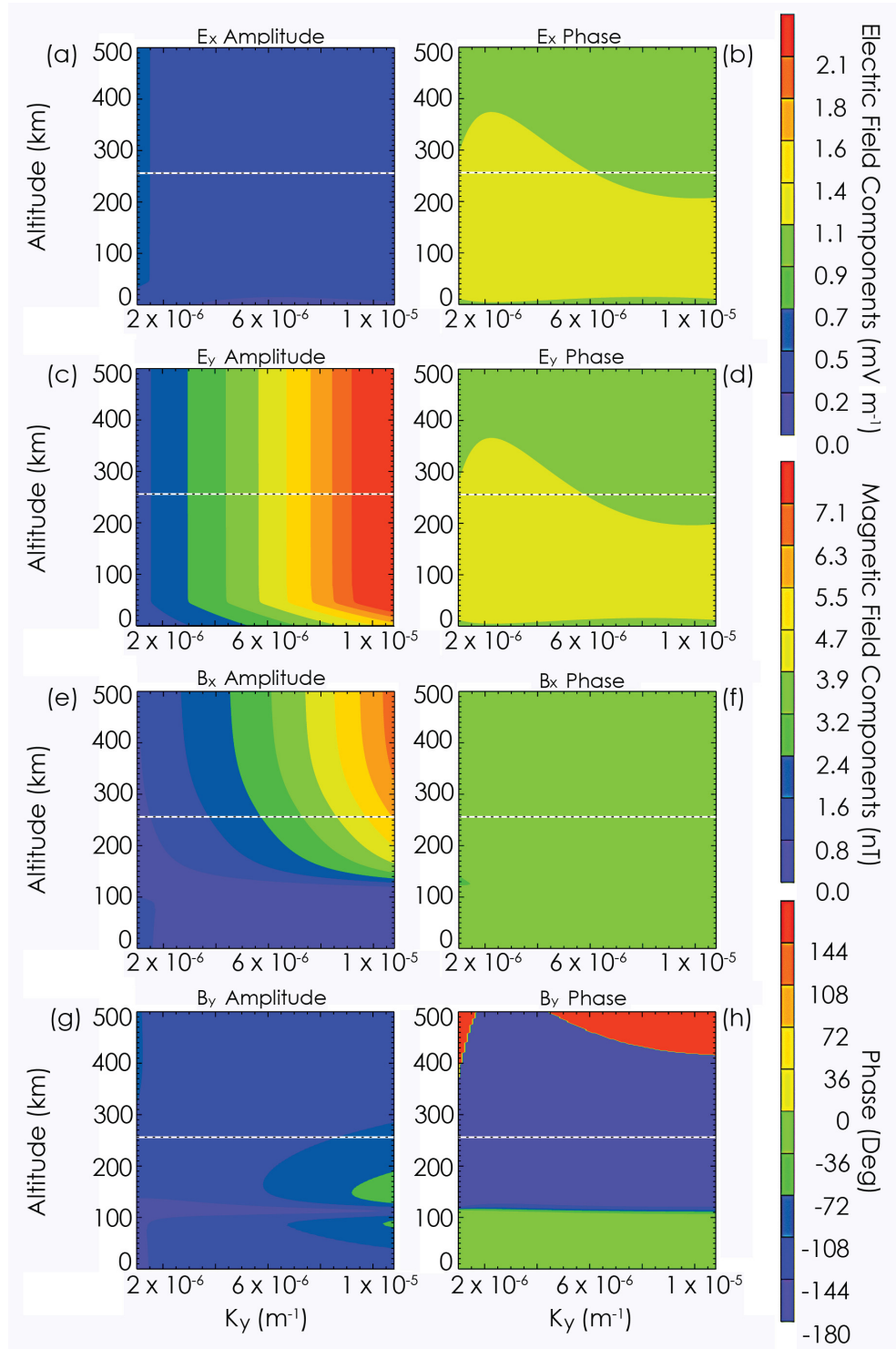


Figure 4.14: (a – h) Electric and magnetic field model results for the ULF wave event recorded on 29 December 2001 at 04:30 UT as a function of altitude and the east-west wavenumber. Each panel has been normalised for a horizontal ground magnetic field perturbation of 1 nT. Panel (a)  $E_x$ . (b)  $E_x$  phase. (c)  $E_y$ . (d)  $E_y$  phase. (e)  $B_x$ . (f)  $B_x$  phase. (g)  $B_y$ . (h)  $B_y$  phase. All phases are plotted relative to a ground magnetic  $B_x$  of zero phase. The overlaid dot-dash line shows the DOPE reflection altitude for this ULF wave event.

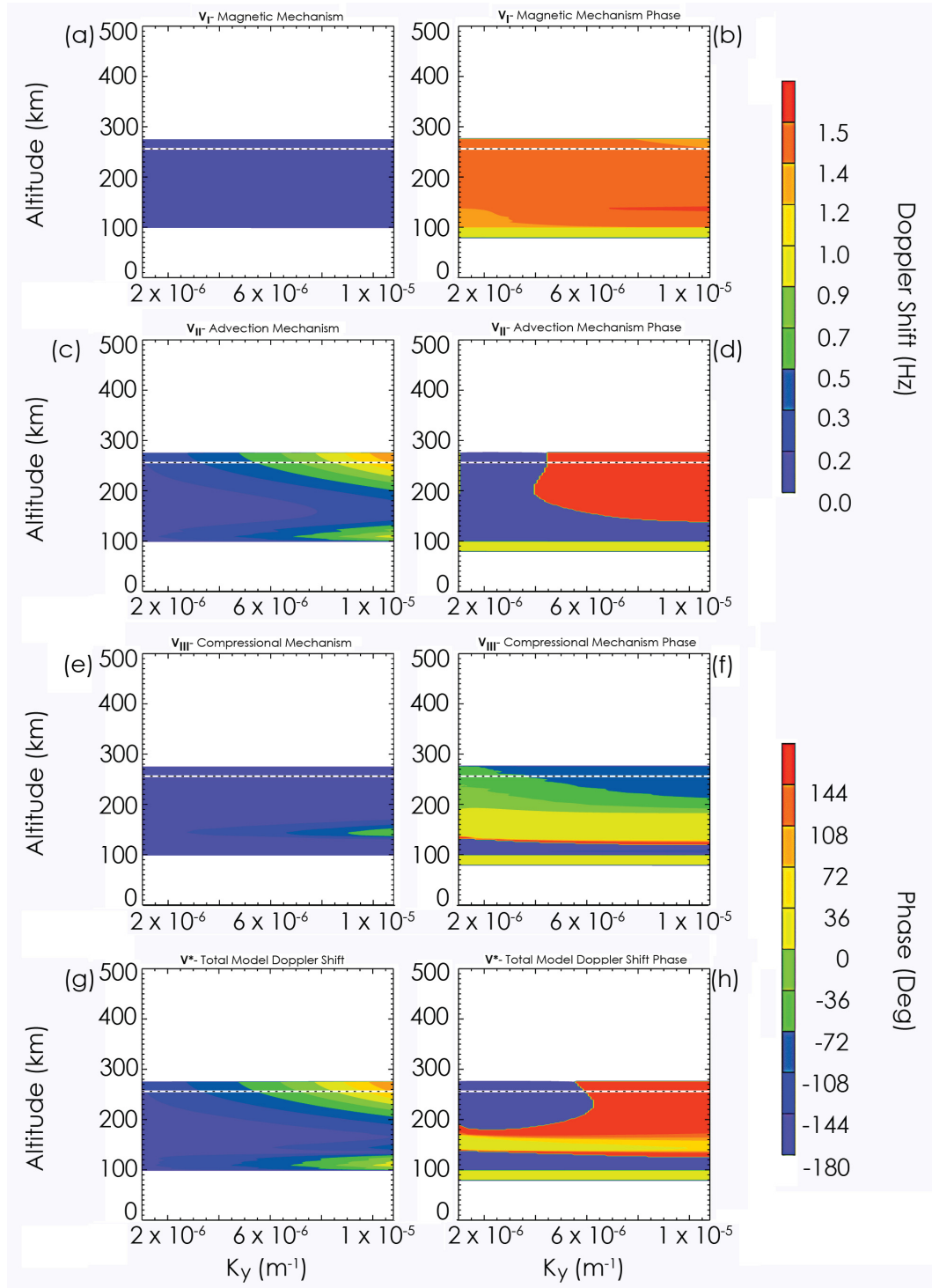


Figure 4.15: (a – h) Doppler shift mechanism model results for the ULF wave event recorded on 29 December 2001 at 04:30 UT scaled to a horizontal ground magnetic field perturbation of 1 nT. All contour plot panels show data as functions of both altitude and the east-west wavenumber. Panel (a)  $V_I$ . (b)  $V_I$  phase. (c)  $V_{II}$ . (d)  $V_{II}$  phase. (e)  $V_{III}$ . (f)  $V_{III}$  phase. (g)  $V^*$ . (h)  $V^*$  phase. All phases are plotted relative to a ground magnetic  $B_x$  of zero phase. The overlaid dot-dash line shows the DOPE reflection altitude for this ULF wave event.

### The North-South Wavenumber Dependence

Assuming an incident wave mode of unity (for a purely shear Alfvénic incident mode) in the same way as for investigating the east-west wavenumber dependence, the north-south wavenumber may be varied through a range of values to see what effect this parameter has upon the determined model Doppler shift. Figure 4.16 presents the electric and magnetic field model results. The panels present the electric and magnetic field variation with altitude for north-south wavenumber values of between  $1.0 \times 10^{-6} \text{ m}^{-1}$  and  $1.1 \times 10^{-5} \text{ m}^{-1}$  (the same as used when investigating  $k_y$  previously) corresponding to meridional scale lengths of between 630 km - 6300 km. Each panel has been normalised for a ground horizontal magnetic field perturbation of 1 nT. Panels (a) and (c) show the X and Y components of the electric field, while panels (b) and (d) show their respective phases. Panels (e) and (g) show the X and Y components of the magnetic field and panels (f) and (h) show their respective phases. All phases are plotted relative to a ground magnetic  $B_x$  of zero phase. Referring to panels (a) and (g) of Figure 4.16, an increase in  $k_x$  increases the X component of the electric field and the Y component of the magnetic field for a given magnetic field perturbation on the ground. Since  $E_y$  seems to be unaffected by a changing  $k_x$  it seems unlikely that an increasing  $k_x$  will increase the Doppler shift.

Figure 4.17 presents the Doppler shift amplitude and phase variation as a function of  $k_x$  and altitude. These plots show how a variation in the north-south wavenumber affects the Doppler Shift. The plots are scaled identically to Figure 4.16. Panels (a) and (b) show the magnetic mechanism amplitude and phase. Panels (c) and (d) show the advection mechanism amplitude and phase. Panels (e) and (f) show the compressional mechanism amplitude and phase. Finally, panels (g) and (h) show the overall Doppler shift amplitude and phase.

There is a range of  $k_x$  between approximately  $4.0 \times 10^{-6} \text{ m}^{-1}$  and  $8.0 \times 10^{-6} \text{ m}^{-1}$  where the advection mechanism gives roughly constant Doppler shift amplitudes resulting in the overall Doppler shift amplitude being a constant over this range too. As the north-south wavenumber increases to greater values, above  $8.0 \times 10^{-6} \text{ m}^{-1}$ , the Doppler shift increases across all mechanisms. The advection mechanism is the dominating mechanism

for a purely shear Alfvénic wave mix at the DOPE reflection altitude as can be seen by comparing panels (c) and (g) of Figure 4.17. At E-region heights the compressional mechanism appears to be contributing the most to the overall Doppler shift as can be seen by comparing panels (e) and (g). The phase contributions from the different mechanisms, panels (b), (d), (f) and (h) of Figure 4.17, highlight that at the DOPE reflection altitude of 256 km the overall Doppler shift phase looks similar to the "advective" phase. In summary, it would appear that the results are similar for  $k_x$  and  $k_y$ , although there are differences as the polarisation of the wave is affected differently. Importantly, the Doppler shift appears to be almost unaffected by a changing meridional scale-size whereas an increasing azimuthal scale-size clearly increases the corresponding Doppler shift as panel (g) of Figure 4.15 showed. The reason for this is principally due to the mathematical form of the advection mechanism given in equation 4.22.  $V_z$  within this equation combines  $E_y$  and  $B_x$ , thus, an increase of  $E_x$  and  $B_y$  with increasing meridional scale-size is unlikely to have a great effect on the advection contribution to the overall Doppler shift.

### Scale Height and Electron Density Gradient Effects on Model Doppler Shifts

This section examines scale height effects on Doppler shifts at high-latitude. To see how the scale height, and hence the electron density gradient, may affect the Doppler shift, the Doppler mechanisms are considered here. A more general form of equation 4.22 may be expressed as

$$\mathbf{V}_{\text{II}} = - \int_0^{z_R} \left[ \frac{\partial \mu}{\partial N} (\mathbf{v} \cdot \nabla N) \right] dz. \quad (4.26)$$

Equation 4.26 shows it is the gradient of the electron density,  $N$ , which is directly proportional to the advection mechanism,  $\mathbf{V}_{\text{II}}$ . The easiest way to investigate,  $\nabla N$ , is by altering the scale height.

The Chapman ionospheric scale height (e.g., Rishbeth and Garriott, 1964) may be described as a measure of the effective thickness of an atmospheric layer. The scale height may be expressed in terms of the Boltzmann constant,  $k$ , the plasma temperature,  $T$ , the

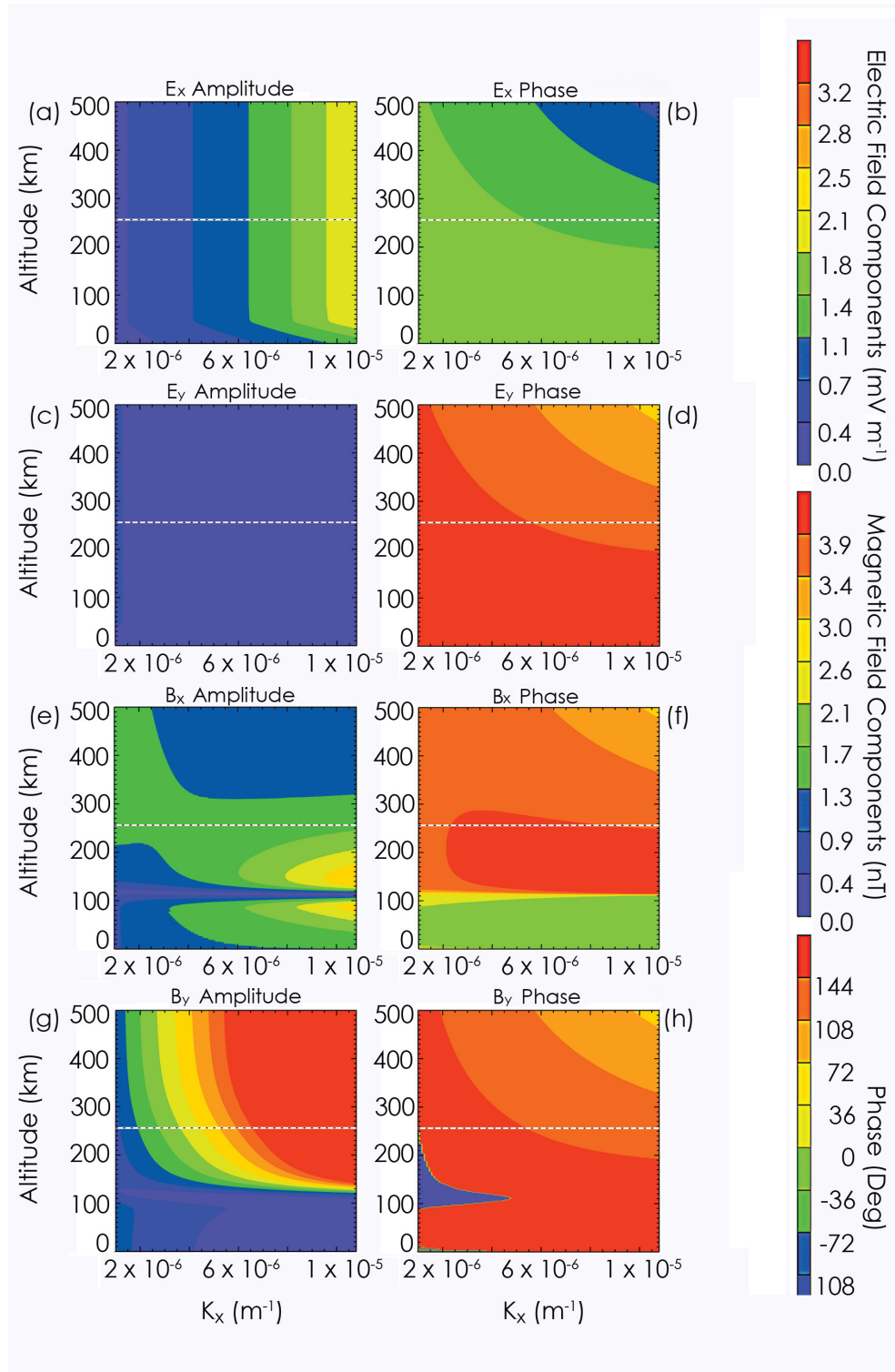


Figure 4.16: (a – h) Electric and magnetic field model results for the ULF wave event recorded on 29 December 2001 at 04:30 UT as a function of altitude and the north-south wavenumber. Each panel has been normalised for a ground horizontal magnetic field perturbation of 1 nT. Panel (a)  $E_x$ . (b)  $E_x$  phase. (c)  $E_y$ . (d)  $E_y$  phase. (e)  $B_x$ . (f)  $B_x$  phase. (g)  $B_y$ . (h)  $B_y$  phase. All phases are plotted relative to a ground magnetic  $B_x$  of zero phase. The overlaid dot-dash line shows the DOPE reflection altitude for this ULF wave event.

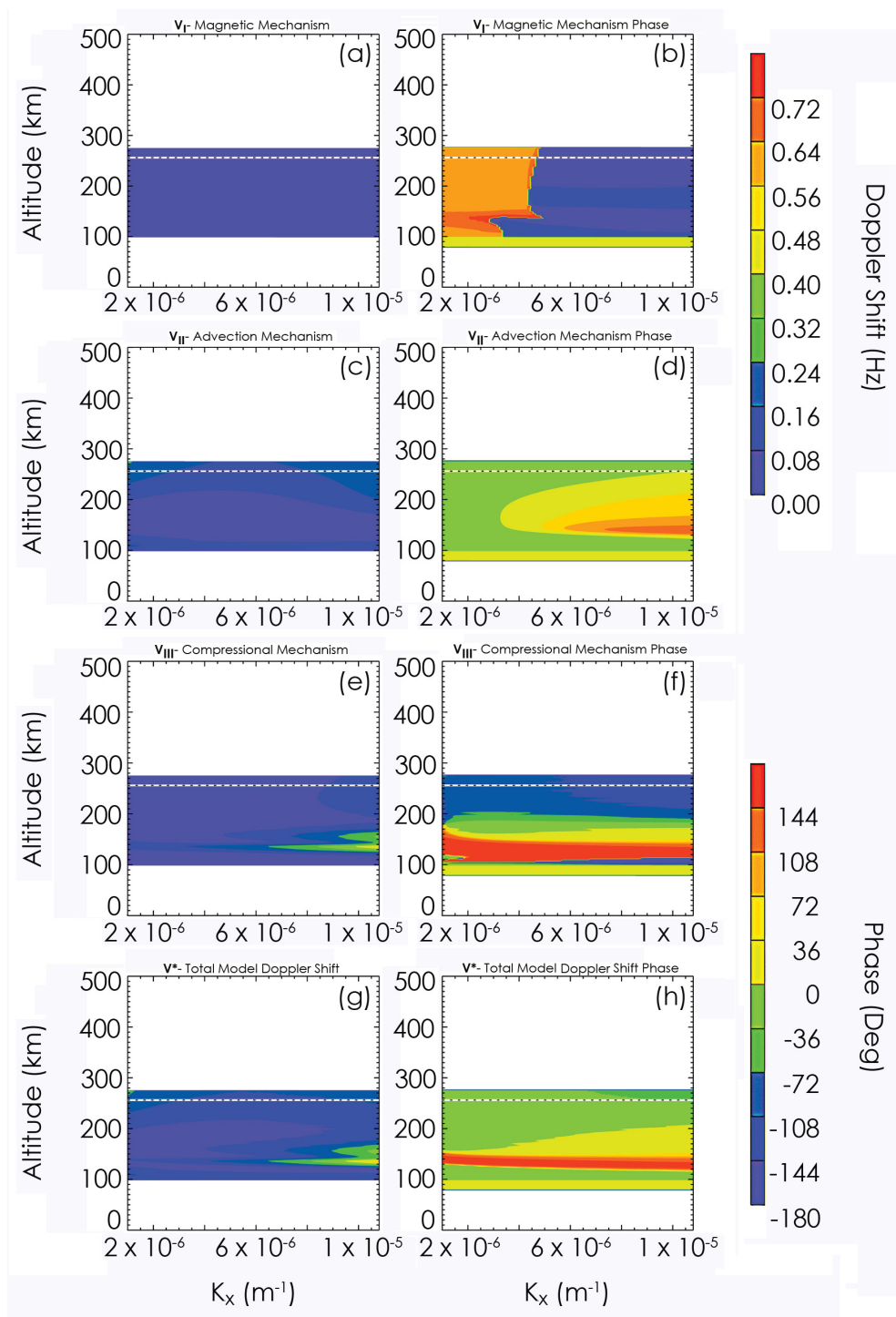


Figure 4.17: (a – h) Doppler shift mechanism model results for the ULF wave event recorded on 29 December 2001 at 04:30 UT scaled for a horizontal ground magnetic field perturbation of 1 nT. All contour plot panels show data as functions of both altitude and the north-south wavenumber. Panel (a)  $V_I$ . (b)  $V_I$  phase. (c)  $V_{II}$ . (d)  $V_{II}$  phase. (e)  $V_{III}$ . (f)  $V_{III}$  phase. (g)  $V^*$ . (h)  $V^*$  phase. All phases are plotted relative to a ground magnetic  $B_x$  of zero phase. The overlaid dot-dash line shows the DOPE reflection altitude for this ULF wave event.

mass of the constituent element(s) in the layer,  $m$ , and the acceleration due to gravity,  $g$ , as

$$H = \frac{kT}{mg}. \quad (4.27)$$

For the purposes of chapters 5 and 6, where the bottom-side profile is critical in determining the reflection altitude of the transmitted wave, the electron density profile is fitted to the POLAN output using dual-Chapman functions. Each panel of Figure 4.18 presents altitude variations of the electron density profile (upper) and resulting normalised Doppler shift (lower) for ionospheric scale heights between 30 km - 80 km from modelling the ULF wave event. In each panel, the Doppler shift has been normalised for a horizontal ground magnetic field perturbation of 1 nT. The scale height is only varied in the Sutcliffe-Poole model, using the same electric and magnetic field profiles. Each panel displays results as follows: panel (a)  $H = 30$  km, panel (b)  $H = 40$  km, panel (c)  $H = 50$  km, panel (d)  $H = 60$  km, panel (e)  $H = 70$  km and panel (f)  $H = 80$  km. The DOPE reflection altitude is marked by the red dot-dashed line in the upper panels for each scale height and is marked by the black dot-dashed line in the lower Doppler shift panels. The reflection altitude and scale height are labelled as parameters  $Z$  and  $H$ , respectively.

The scale height of the ionosphere at the assumed reflection altitude is varied and the corresponding normalised model Doppler shift profiles are plotted. The advection mechanism closely matches the overall normalised model Doppler shift at the DOPE reflection altitude for all scale heights. This implies that the advection mechanism is contributing the most to the total normalised Doppler shift compared with the magnetic and compressional mechanisms. Figure 4.18 shows, as the scale height increases, the overall normalised Doppler shift and the DOPE reflection altitude decrease. Panel (a) of Figure 4.18 shows for a scale height of 30 km the reflection altitude is 254 km and the theoretical normalised Doppler shift is approximately 0.7 Hz. Panel (f) of the same figure shows that for a scale height of 80 km, the reflection altitude is 212 km and the normalised Doppler shift is 0.3 Hz. To investigate electron density gradient effects upon HF Doppler sounders, the gradi-

ent is calculated at the DOPE reflection altitude for each of the panels of Figure 4.18. The results are presented in Figure 4.19, which show the overall normalised model Doppler shift,  $V^*$ , as a function of electron density gradient. The greatest change in electron density occurs for small-scale heights,  $H$ . These small-scale heights coincide with the greatest normalised model Doppler shift amplitudes,  $V^*$ . The results of this scale height study suggests that the electron density gradient greatly affects the Doppler shift. The study also highlights that care must be taken when calculating the electron density profile and indicates the necessity of using ionosonde data to determine the electron density profile. The accuracy of the inverted electron density profile, via POLAN, is far greater on a case-by-case basis than the IRI model. The investigation here illustrates that larger gradients yield correspondingly larger Doppler shifts as suspected from the mathematical form of the advection mechanism as given in equation 4.26. The wave propagation is also clearly affected by the conductivity profiles and the reflection coefficient, so these two parameters will be investigated next.

### **The Height Integrated Pedersen Conductivity Dependence**

Figure 4.20 presents the results of an investigation where the peak FoF2 of the ionosphere is varied in linear steps from 3.0 MHz - 12.0 MHz for the event detailed previously. The resulting electron density profile is used by the 1-D numerical model for each of the 10 test model runs. Importantly, the electron density profile is kept constant (using the original POLAN determined profile) when the normalised model Doppler shift is calculated. A constant electron density profile implies the electron density gradient is not changing when the model Doppler shifts are calculated by the Sutcliffe-Poole model, allowing the effects of a changing conductivity profile on the reflection coefficient and model Doppler shift amplitude to be observed.

Panel (a) of Figure 4.20 shows the model Doppler shift, normalised for a horizontal magnetic field of 1 nT on the ground, as a function of the height integrated Hall and Pedersen Conductivities. Panel (a) clearly shows that the dependence of normalised Doppler shift on both the height integrated Pedersen and Hall conductivities is non-linear.

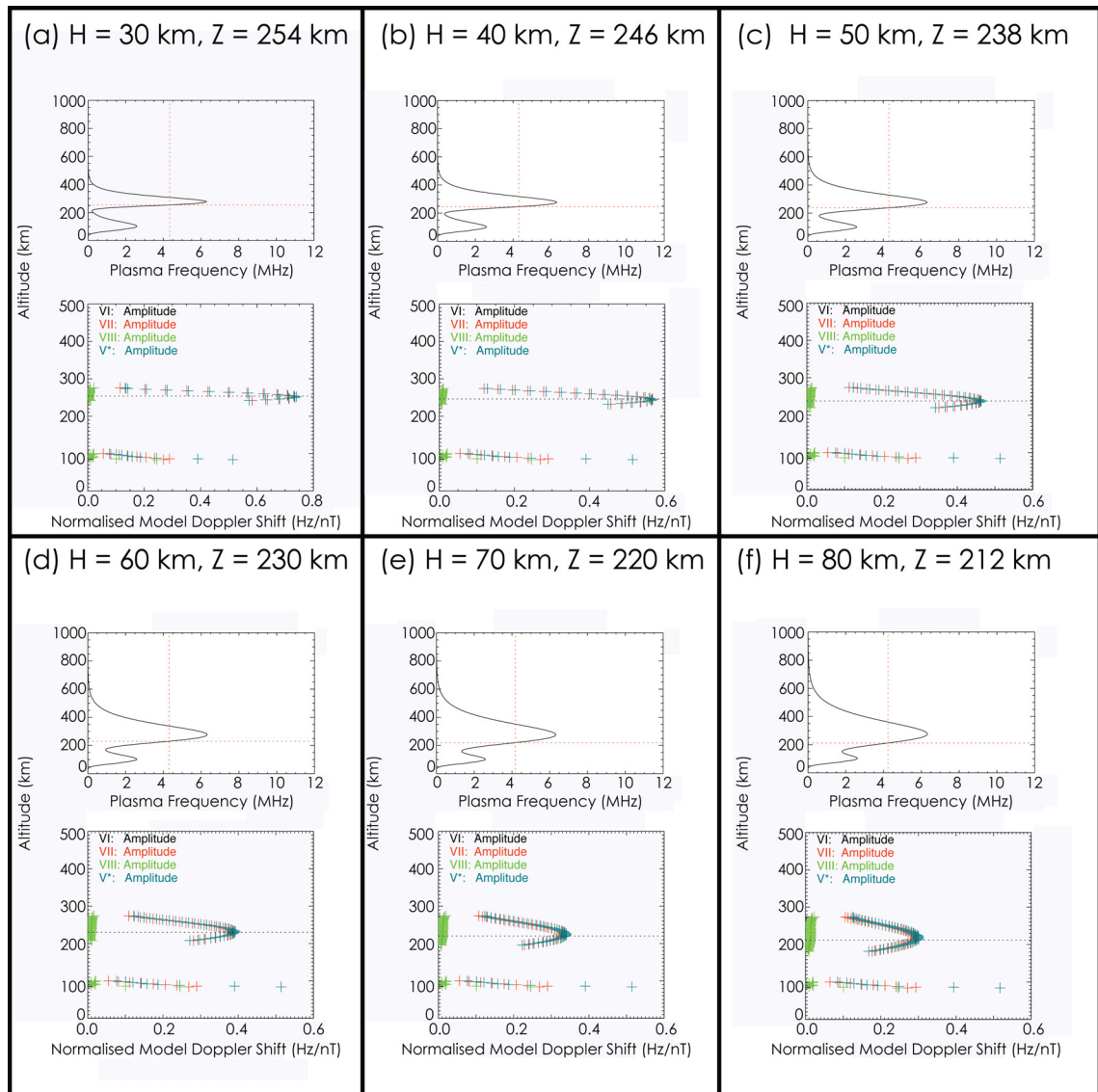


Figure 4.18: **(a – f)** Model results for the ULF wave event, which occurred on 29 December 2001 at approximately 04:30 UT. Each panel presents the electron density profile (upper) and resulting Doppler shift (lower) for ionospheric scale heights between 30 km - 80 km. The Doppler shift in each panel has been normalised for a horizontal ground magnetic field perturbation of 1 nT. Each panel displays results as follows: panel (a)  $H = 30$  km, panel (b)  $H = 40$  km, panel (c)  $H = 50$  km, panel (d)  $H = 60$  km, panel (e)  $H = 70$  km and panel (f)  $H = 80$  km. The HF Doppler reflection altitude is marked by a red dot-dashed line in the upper panels for each scale height and is marked as a black dot-dashed line on the lower normalised Doppler shift panels. The reflection height is also labelled as parameter  $Z$ . The scale height for each panel is specified by  $H$ .

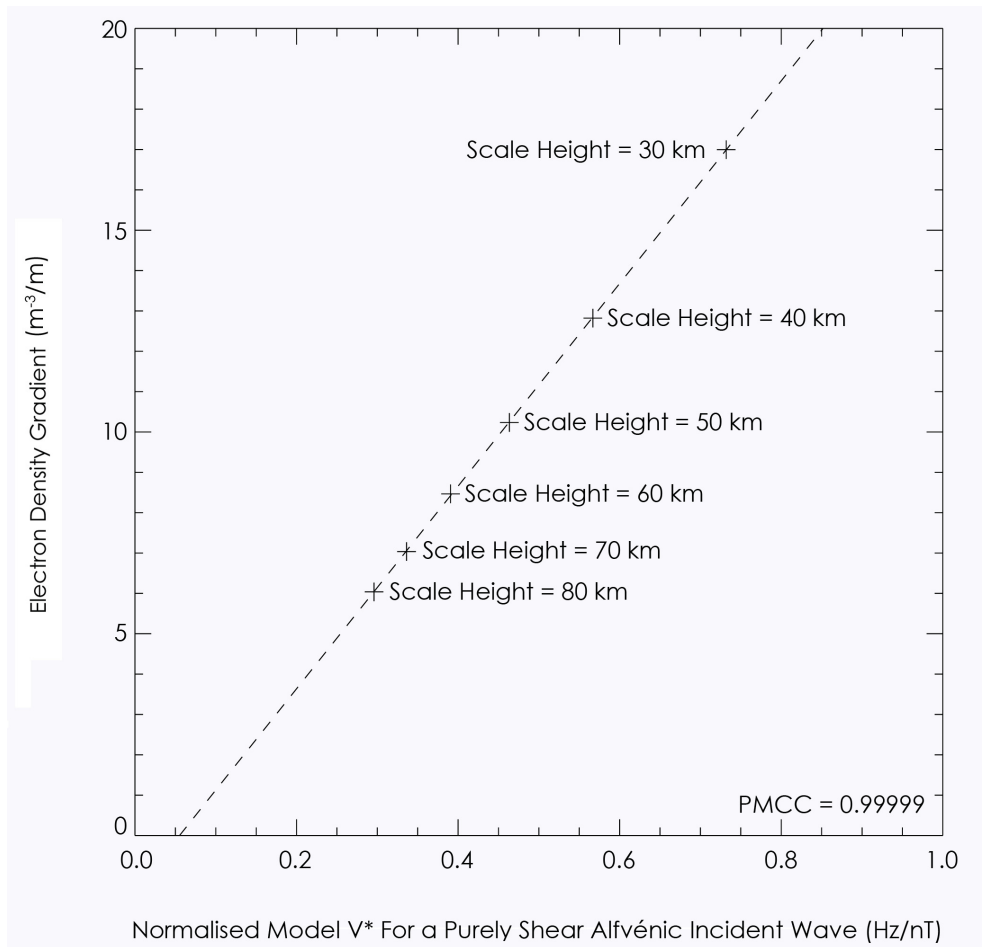


Figure 4.19: The electron density gradient is calculated at the DOPE reflection altitude for each of the panels in Figure 4.18. The results show the overall model Doppler shift,  $V^*$ , as a function of the electron density gradient at the HF Doppler reflection altitude. The model Doppler shift has been normalised for a horizontal ground magnetic field perturbation of 1 nT.

Panel (b) shows the peak FoF2 used by the numerical model. Panel (c) shows the reflection coefficient calculated after each run of the 1-D numerical wave model as a function of the normalised model Doppler shift. The high correlation between the reflection coefficient and the normalised model Doppler shift shows the importance of the reflection coefficient, peak FoF2, and hence the model ionosphere, in determining the correct model Doppler shifts.

It would seem from these model test runs that the electron density gradient and peak FoF2, of the inputted ionosphere, greatly affect the model Doppler shift amplitude. Naively, for a fixed sounding frequency, increasing peak FoF2 enhances the ionosphere, which increases

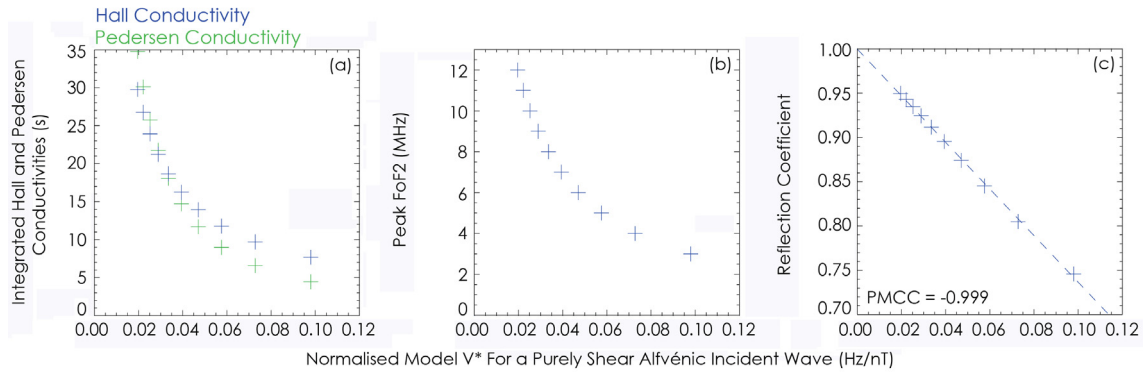


Figure 4.20: **(a – c)** The results of an investigation where the peak FoF2 of the ionosphere is varied in linear steps from 3.0 MHz - 12.0 MHz and the resulting electron density profile is subsequently used by the 1-D numerical model for each of the 10 test model runs. The electron density profile is then kept constant (using the original POLAN determined profile) when the normalised model Doppler shift is calculated. Panel (a) shows the height integrated Hall and Pedersen conductivities as a function of the model Doppler shift, which has been normalised for a horizontal ground magnetic field perturbation of 1 nT. Panel (b) shows the peak FoF2 used by the numerical model. Panel (c) shows the ionospheric reflection coefficient calculated after each run of the 1-D numerical wave model as a function of the normalised model Doppler shift.

the height integrated Hall and Pedersen conductivities.

## 4.4 Summary

This chapter has introduced the 1-D numerical ULF wave model (Sciffer et al., 2005), and the Sutcliffe-Poole model (Poole and Sutcliffe, 1988; Sutcliffe and Poole, 1989, 1990), which will be used in chapters 5 and 6 of this thesis. The testing of these models have been detailed. In order to investigate the effects that key parameters have on the Doppler shift a suitable range of each of these parameters must be selected for high-latitude FLR ULF wave events. Chapter 6 of this thesis provides a statistical study of 25 high-latitude FLR driven ULF wave events and will provide these ranges.

The height integrated Pedersen and Hall conductivities clearly affect the Doppler shift. Panel (a) of Figure 4.20 shows that, for a suitable range of the height integrated Hall conductivity parameter (2 S - 16 S), provided by the 25 ULF wave events recorded at high-latitude in chapter 6, as the integrated Hall conductivity increases, the normalised

model Doppler shift increases non-linearly. Panel (a) of Figure 4.20 also provides an estimation of the height integrated Pedersen conductivity effect on the normalised model Doppler shift. A suitable range of the height integrated Pedersen conductivity parameter provided by the 25 ULF wave events recorded at high-latitude in chapter 6 is 1.8 S - 12.3 S. Using this range and Figure 4.20 shows that, like the integrated Hall conductivity, as the integrated Pedersen conductivity decreases the normalised model Doppler shift also increases non-linearly.

Peak FoF2 is another parameter that affects the model Doppler shift. Panel (b) of Figure 4.20 shows the impact that a changing peak FoF2 has on the normalised model Doppler shift. A suitable range of peak FoF2 provided by the 25 ULF wave events recorded at high-latitude reveals a range of between 4.6 MHz - 9.0 MHz. Using this range and panel (b) of Figure 4.20 shows a halving in the normalised model Doppler shift from approximately 0.06 Hz/nT to 0.03 Hz/nT.

As has already explained, the reflection coefficient modifies the electric field within the ionosphere and is, therefore, an important parameter affecting the recorded Doppler shift. A suitable range for the reflection coefficient provided by the 25 ULF wave events recorded at high-latitude is 0.6 - 0.9. Using this range and panel (c) of Figure 4.20 yields a decrease in the normalised model Doppler shift from 0.2 Hz/nT to 0.05 Hz/nT. The corresponding gradient in the normalised Doppler shift with the ionospheric reflection coefficient is  $-0.5 \text{ Hz nT}^{-1}$ .

The electron density gradient provides a large contribution to the advection mechanism as can be seen from equation 4.22. Figure 4.19 clearly shows that doubling the electron density gradient increases the normalised model Doppler shift by a factor of approximately 2. A suitable range of the electron density gradient, provided by the 25 high-latitude ULF wave events recorded in chapter 6, is  $2 \text{ m}^{-3}/\text{m}$  to  $6 \text{ m}^{-3}/\text{m}$ . Using this range and Figure 4.19 shows a corresponding increase in the normalised model Doppler shift from approximately 0.1 Hz/nT to 0.3 Hz/nT, (an increase by a factor of approximately 3). The corresponding gradient in the normalised Doppler shift with the electron density gradient is  $0.04 \text{ Hz nT}^{-1}/\text{m}^{-3}/\text{m}$ .

The contributions of the east-west and north-south wavenumber will now be investigated. The statistical study contained within chapter 6 of this thesis provides an approximate range of  $k_x$  and  $k_y$  as  $1 - 3 \times 10^{-6} \text{ m}^{-1}$  and  $-5 - +3 \times 10^{-6} \text{ m}^{-1}$ , respectively. Investigating  $k_y$  first and using the determined range of  $1 - 5 \times 10^{-6} \text{ m}^{-1}$  when considering panel (g) of Figure 4.15 shows that as  $k_y$  increases over this range the corresponding Doppler shift increases from 0.18 Hz/nT to 0.53 Hz/nT (approximately a 3-factor increase).

For  $k_x$  the determined range is approximately  $1 - 3 \times 10^{-6} \text{ m}^{-1}$ . Figure 4.17 shows that as  $k_x$  decreases over this range the corresponding normalised model Doppler shift decreases from 0.25 Hz to 0.18 Hz. Therefore, over the range of scale-sizes given by chapter 6, the meridional scale-size does not change sufficiently for FLR driven ULF wave events.

A prediction, using the study contained within section 4.3.5, can be made as to the relative importance of the parameters affecting the normalised model Doppler shift at high-latitude and is summarised here (with 1 expected to provide the greatest change in the normalised Doppler shift):

- (1) The height integrated Hall conductivity,
- (2) the height integrated Pedersen conductivity,
- (3) the electron density gradient,
- (4) the ionospheric reflection coefficient,
- (5) the peak FoF2,
- (6) the east-west wavenumber, and finally,
- (7) the north-south wavenumber.

The relative importance of each of these parameters will be considered in more detail in chapter 6 of this thesis when a statistical study of 25 FLR driven ULF wave events will be undertaken.

# Chapter 5

## Observations and Modelling of the Wave Mode Evolution of an Impulse-Driven 3 mHz Ultra Low Frequency Wave

### 5.1 Introduction

A combination of an HF Doppler sounder, a network of ground magnetometers, upstream solar wind monitors and a numerical model is used to examine the temporal evolution of a ULF wave. The event occurred on 16 April 1998 and followed a solar wind density and pressure increase seen in the upstream ACE spacecraft data. The magnetometer and HF Doppler sounder data show that the event develops into a low- $m$  ( $-6$ ) field line resonance. HF signals that propagate via the ionosphere exhibit Doppler shifts due to a number of processes that give rise to a time-dependent phase path. The ULF electric and magnetic fields are calculated by a one-dimensional model, which calculates the wave propagation from the magnetosphere, through the ionosphere to the ground with an oblique magnetic field. These values are then used to determine a model HF Doppler shift, which is subsequently compared to HF Doppler observations. The ULF magnetic field at the ground and

Doppler observations are then used to provide model inputs at various points throughout the event. This chapter shows that the incident wave mode evolved from a mixture of fast and Alfvén modes at the beginning of the event to an almost purely shear Alfvénic mode after 6 wavecycles (33 minutes).

## 5.2 Observations

This section presents data associated with a ULF wave, which occurred on 16 April 1998 between the hours of 09:45 UT and 10:45 UT and was detected simultaneously in the ionosphere by the DOPE sounder and on the ground by the IMAGE magnetometer array. An impulsive increase in solar wind dynamic pressure was detected by the ACE spacecraft preceding the onset of FLR activity and this upstream data is presented first.

### 5.2.1 Interplanetary Magnetic Field Analysis

The origin of the ULF wave may be revealed by an examination of upstream IMF and solar wind data. Upstream solar wind and IMF conditions during the interval discussed here are measured using the Solar Wind, Electron, Proton, and Alpha Monitor (SWEPAM) and (Magnetometer instrument) MAG, respectively, on the ACE spacecraft (Stone et al., 1998).

Figure 5.1 presents the lagged ACE and IMP-8 data sets for the ULF wave event on 16 April 1998 between 09:00 UT - 11:00 UT. The ACE data, lagged by 57 minutes as predicted by the OMNI data set (King and Papitashvili, 2005) are shown by the solid black lines and reveal a rise in dynamic pressure from 2 nPa to 7 nPa occurring at approximately 10:03 UT. This increase in dynamic pressure coincides with a rotation of the IMF, and a drop in magnetic field magnitude (and hence pressure). The plasma thermal pressure rises at this time (not shown), although the total pressure drops slightly. The IMF and solar wind data are thus consistent with the arrival of a tangential discontinuity at this time. In order to confirm the validity and accuracy of this applied lag, magnetic field data from the IMP-8 spacecraft are also examined (no plasma data are available from IMP-8). The solar

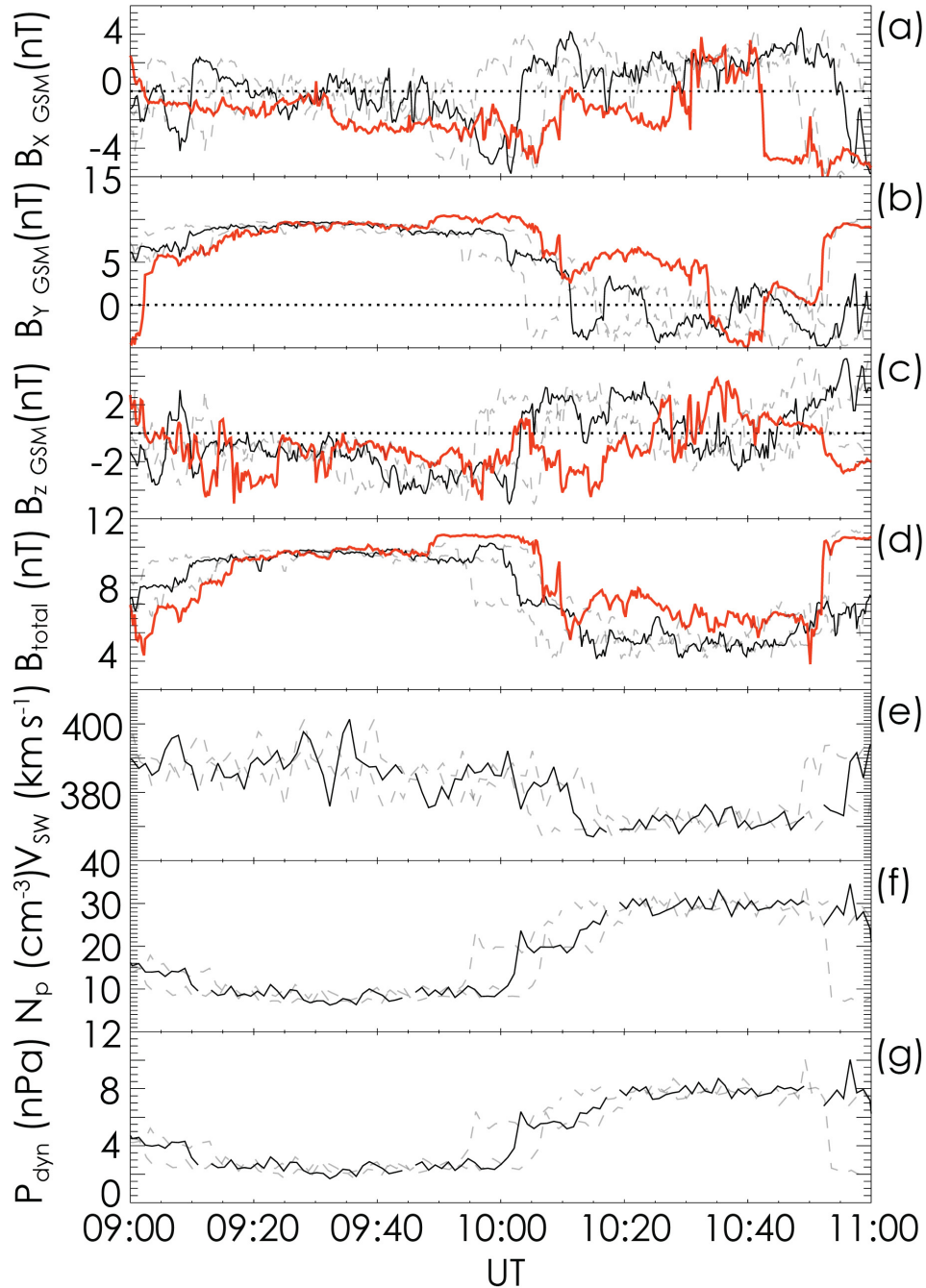


Figure 5.1: (a – g) ACE and IMP-8 spacecraft observations during the ULF wave event on 16 April 1998 between 09:00 UT - 11:00 UT. Magnetic field data are displayed in the GSM (Geocentric Solar Magnetic) coordinate system. Panels (a) to (d) show the three magnetic field components recorded by the ACE and IMP-8 spacecraft, ( $B_x$ ,  $B_y$ ,  $B_z$ ) and the magnetic field magnitude,  $B_{total}$ , respectively. Panels (e), (f) and (g) show the solar wind velocity, the solar wind proton number density, and the solar wind dynamic pressure as recorded by ACE. The ACE data, with a 57 minute lag are shown by the solid black lines, whereas the IMP-8 data, lagged by 14 minutes, are shown by the solid red lines. The dashed grey lines show a range of lag times (50 minutes - 61 minutes) for the IMF and solar wind data as observed by ACE (see text for details).

wind propagation time from IMP-8 was found using the method of Khan and Cowley (1999). This technique for determining the lag time comprises three parts: the solar wind advection time, the magnetosheath transit time, and the Alfvén transit time along the geomagnetic field lines from the subsolar magnetopause to the ionosphere. The subsolar bow shock location is found using a model (Peredo et al., 1995). The transit time from the subsolar magnetopause to the ionosphere was approximated as 2 minutes. The transit time from IMP-8 to the terrestrial ionosphere, using the solar wind velocity recorded by ACE as a guide, was determined to be  $14.1 \pm 2$  minutes. IMP-8 data at this lag are shown in Figure 5.1 by the solid red lines. The IMP-8 data have been used to compare structures within the IMF at IMP-8 with those recorded by the ACE spacecraft. Cross-correlating the ACE data with the IMP-8 data for the total magnetic field and for each component of the IMF over a variety of time series lengths centred between 09:00 UT and 11:00 UT provided a range of time delays for the ACE data between 50 minutes and 61 minutes. The limits of these calculated lags on the ACE upstream data are presented in Figure 5.1 as dashed grey lines, and indicate that the effect of the increase in solar wind dynamic pressure is expected to arrive in the ionosphere between 09:56 UT and 10:07 UT. This time interval is marked as a grey box on the time series of the ground-based measurements of the wave activity under investigation presented in Figure 5.3. The interval is consistent with the arrival of the effects of the solar wind impulse being coincident with the start of the wave event recorded in the ground magnetometer data, indicative of a wave source originating from the solar wind dynamic pressure impulse. An alternative source of wave power on the ground is direct driving by oscillatory activity at a suitable frequency within the IMF or solar wind. An FFT analysis of the lagged ACE IMF and solar wind data reveals that between 09:45 UT - 10:45 UT (and over the longer interval 07:00 UT - 12:00 UT) the peak spectral power occurs at a frequency of approximately 2.0 mHz. There is a little spectral power close to 3 mHz (the dominant frequency of the ground-based magnetometer data) at a steady level from 09:20 UT - 11:00 UT in the lagged solar wind data, which might result in weak steady state driving at 3 mHz, but the main wave source is consistent with the pressure impulse.

## 5.2.2 Ionospheric and Ground Data Observations

Figure 5.2 presents the locations of the ground-based instrumentation used during this chapter. The red crosses represent the locations of the DOPE sounder and the black crosses represent the locations of the ten IMAGE magnetometer stations used in this study. The grey shaded square shows a zoomed in view of the DOPE site highlighting both the location of the transmitter (Tx) and Receiver (Rx) sites relative to the IMAGE magnetometer at Tromsø (TRO).

The top panels in Figure 5.3 display HF Doppler data from DOPE, bandpass filtered between 250 s to 500 s (2 mHz - 4 mHz), along with identically filtered X and Y component magnetic field data from nine IMAGE magnetometer stations, covering geomagnetic latitudes from 75.12° (Longyearbyen, LYR), to 60.99° (Oulujarvi, OUI). The IMAGE data are presented with latitude decreasing from top to bottom. A series of wave cycles are clearly visible in the data, which started at 09:45 UT and continued until about 10:45 UT. A coherent wave packet can be seen across the magnetometer chain, with maximum amplitude of 15 nT, at 10:08 UT, observed in the X component magnetic field between the latitudes of TRO, and Abisko, (ABK). The wave signature in the magnetometer data was strongest in the interval 09:55 UT - 10:30 UT.

The time development of the amplitudes in the Doppler and magnetometer traces is different, with peak amplitude seen early on in the wave packet in the magnetometer data (10:04 UT), but later in the Doppler trace (10:22 UT). The grey shaded region on both panels of Figure 5.3 shows the possible range of arrival times of the effects of the solar wind dynamic pressure increase as measured by the ACE spacecraft, as determined in Figure 5.1.

Figure 5.4 presents Fourier power spectral analysis of the DOPE instrument and the X and Y components of the field data from the IMAGE magnetometer at Tromsø, respectively. Fourier power spectral analysis of the DOPE instrument and the X and Y components of the data from the IMAGE magnetometer array reveal a consistent wave period of 330 s (3 mHz).

Figure 5.5 panels (a) and (b) show the latitudinal Fourier power and phase profiles for

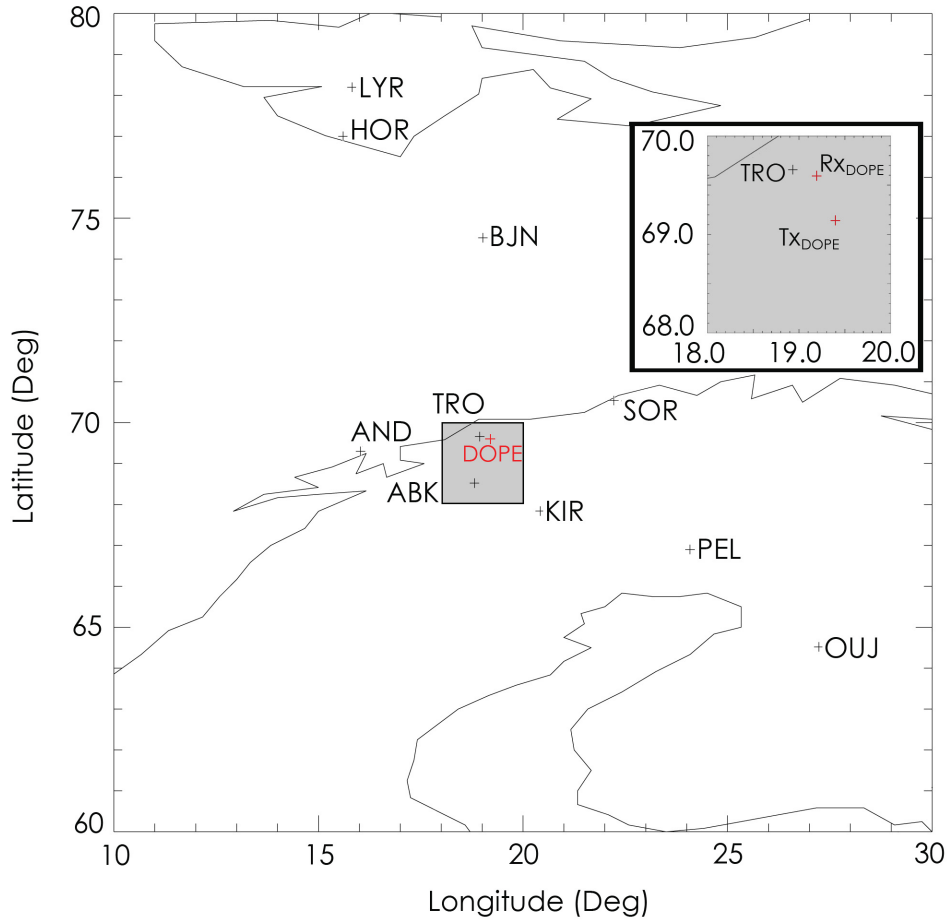


Figure 5.2: The locations of the ground-based instrumentation used during this study. The red crosses represent the locations of the DOPE sounder and the black crosses represent the locations of the ten IMAGE magnetometer stations used in this chapter. The grey shaded square shows a zoomed in view of the DOPE site highlighting both the location of the transmitter (Tx) and Receiver (Rx) sites relative to the IMAGE magnetometer at Tromsø (TRO).

the X component of the magnetic field, at a frequency of 3 mHz, for the IMAGE magnetometer data displayed in Figure 5.3. The overlaid dot-dash line shows the location of the DOPE instrument. A clear phase change with latitude centred across the resonant peak can be seen in panel (b) of Figure 5.5. These plots confirm that there is an FLR close to the latitude of Andenes (AND). The azimuthal phase variation was also examined for this wave, using the Y component data from a number of longitudinally separated IMAGE magnetometers. The azimuthal wave number was found to be -6, where the negative sign here indicates westward propagation. The Ap and Kp indices were 6 and 2+ during the event, respectively. The Ap index is used as an input to the numerical model detailed in

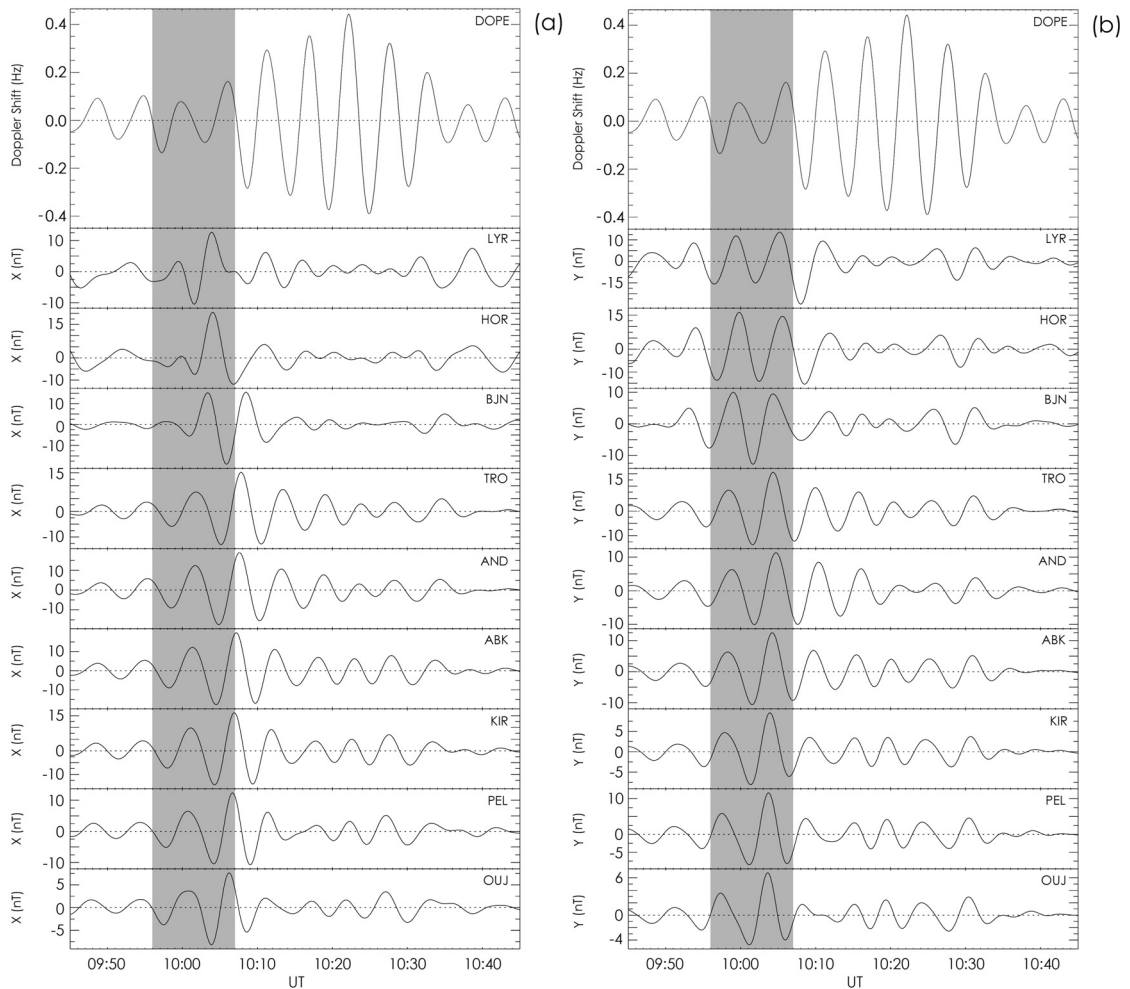


Figure 5.3: **(a and b)** DOPE and IMAGE magnetometer data for the ULF wave event on 16 April 1998. Panels (a) and (b) display data from the X and Y components of nine stations of the IMAGE magnetometer array bandpass filtered between 250 s and 500 s. The upper panel in both (a) and (b) show the bandpass filtered DOPE data also excluding variations with time periods outside of the range 250 s to 500 s, resampled from 12.8 s to 10.0 s. The grey shaded region shows the possible range of arrival times of the effects of the solar wind dynamic pressure increase as measured by the ACE spacecraft. The time series plots have been scaled individually to provide the highest clarity of the wave signature.

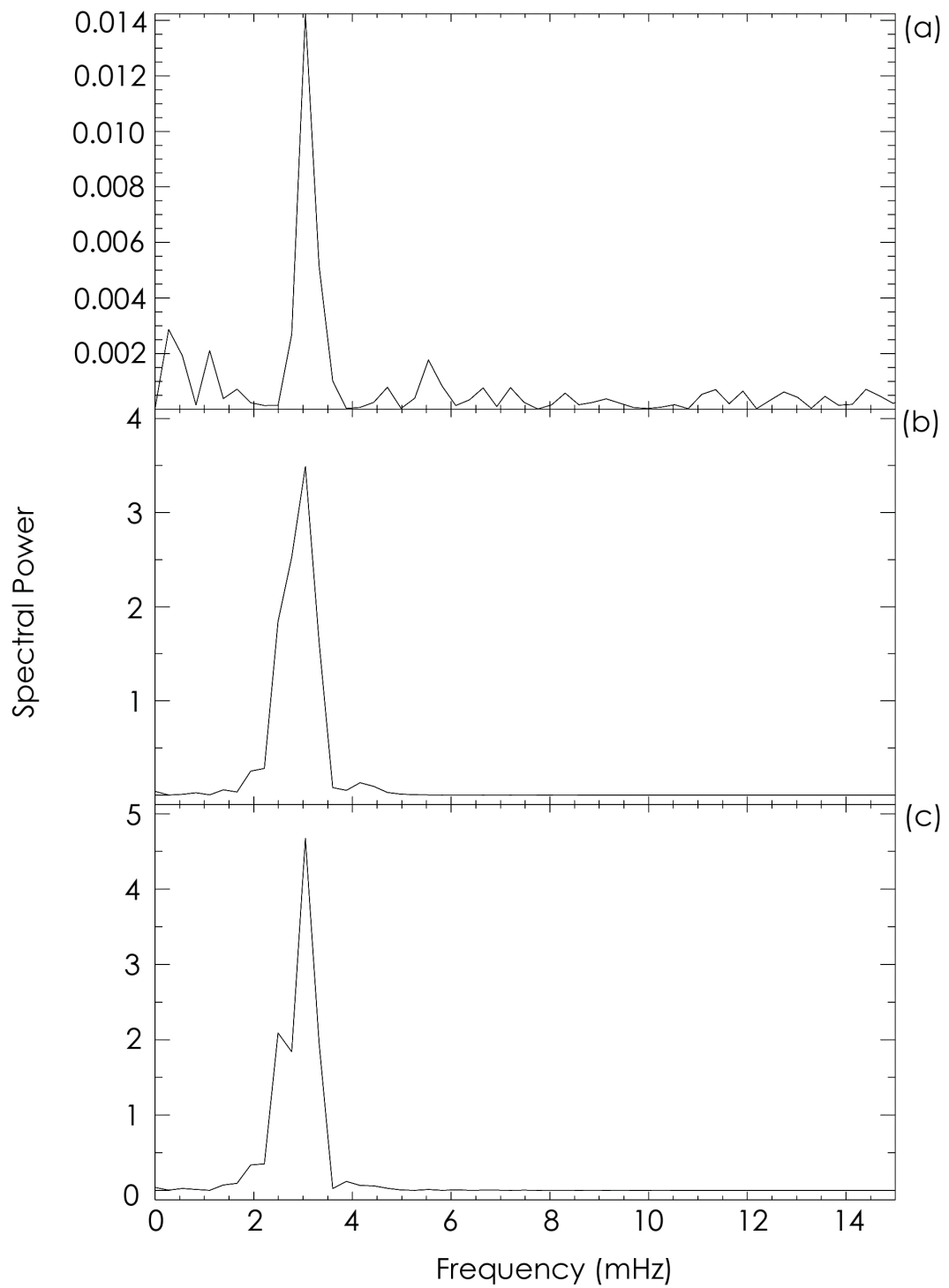


Figure 5.4: (a – c) An FFT analysis of the filtered data presented in Figure 5.3 (a) the 10 second DOPE data. (b) the X component at TRO. (c) the Y component at TRO.

section 4.2.5.

### 5.2.3 Wave Evolution

As mentioned earlier in section 5.2.2, the different temporal development observed in the amplitudes of the combined Doppler sounder and magnetometer data sets indicate an evolution in the incident wave mode, azimuthal or meridional scale-size of the wave. This evolution is investigated further here, through a dynamic Fourier analysis of the wave phase and amplitude. Fourier amplitude rather than power is used in order to provide a more direct relationship with the time-domain variation of the wave amplitude presented in Figure 5.3. Here, a 100-point (1000 s) sliding window FFT with a slip of 30 points (5 minutes) is used. Using this shorter FFT a frequency resolution of 1 mHz is available, and the peak wave power occurs at 3 mHz. Panel (a) of Figure 5.6 presents the HF Doppler amplitude variation calculated from an integrated Fourier amplitude over a frequency range of 1.7 mHz - 5.1 mHz. The HF Doppler amplitude rises from 0.1 Hz at approximately 10:00 UT to a peak of 0.4 Hz at roughly 10:20 UT. Panels (b) and (c) show the TRO-X and TRO-Y amplitudes found using the same technique as panel (a). Panel (b) shows TRO-X peaks with an amplitude of 15.0 nT at roughly 10:10 UT while panel (c) shows TRO-Y attaining a peak amplitude of 16.0 nT at approximately 10:05 UT. Panel (d) of Figure 5.6 shows the cross-phase between the X component of IMAGE stations TRO and Pello (PEL), at the peak frequency of 3 mHz.

This cross-phase calculation allows an examination of the time evolution of the relative phase between the wave signatures measured at the two stations. At the beginning of the wave event PEL leads TRO by approximately  $60^\circ$ . As the wave progresses, this phase lead increases, maximising at approximately  $140^\circ$  between 10:15 UT and 10:25 UT. After this time the wave amplitudes start to decrease. The phase difference between the stations thus starts with a small phase lead at the lower latitude station, evolving towards the  $180^\circ$  phase lead expected between stations equatorward of and poleward of a field line resonance. This suggests a wave with an impulsive origin, which then exhibits a time-dependent phase evolution as an FLR develops.

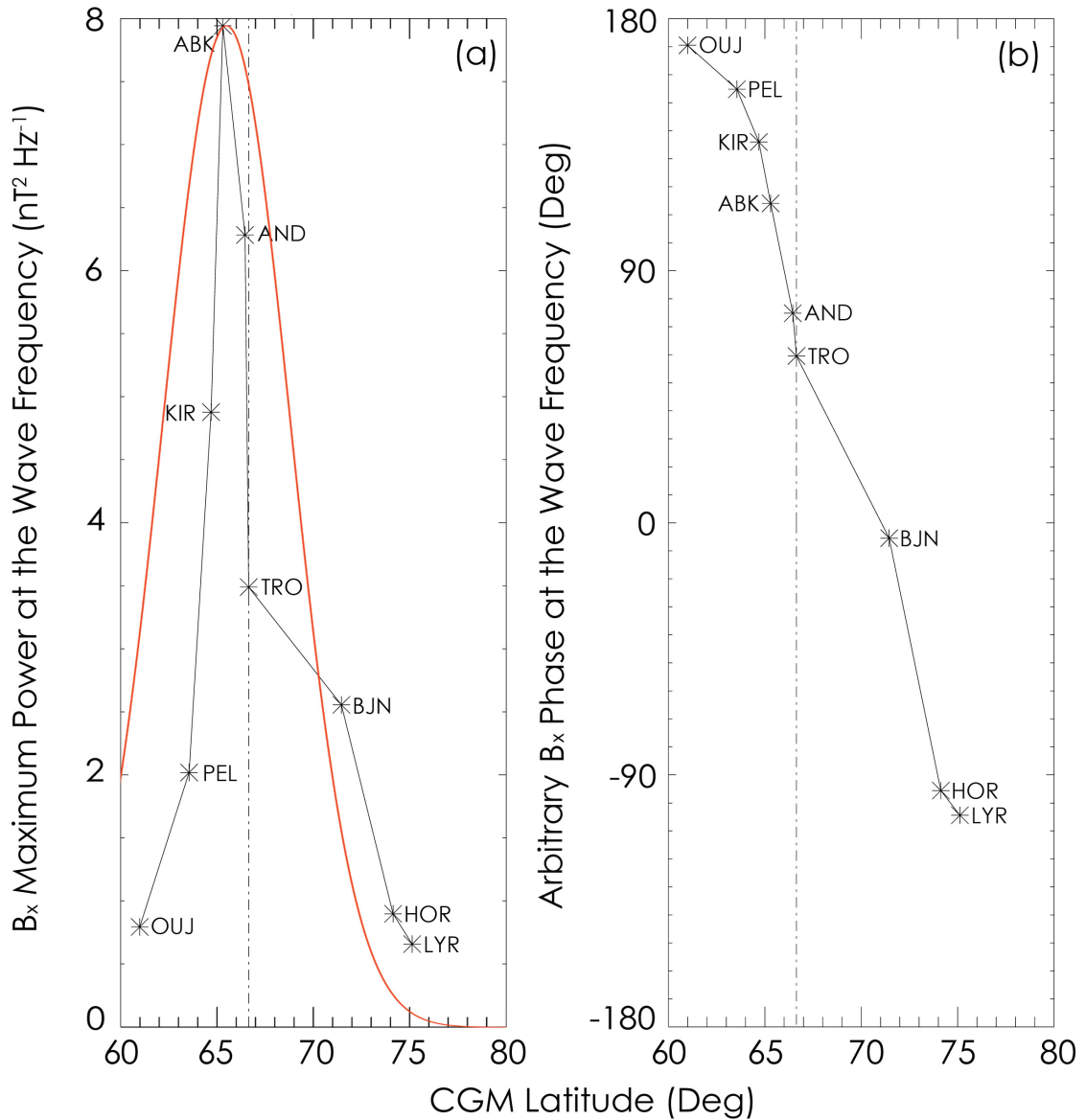


Figure 5.5: **(a and b)** IMAGE magnetometer data for the ULF wave event on 16 April 1998. Panels (a) and (b) show the latitudinal Fourier power and phase profiles for the X component of the magnetic field, respectively. A fitted Gaussian to the latitudinal power recorded at each IMAGE station is shown by the overlaid solid red line on panel (a). In both panels the overlaid dot-dash line shows the location of the DOPE instrument.

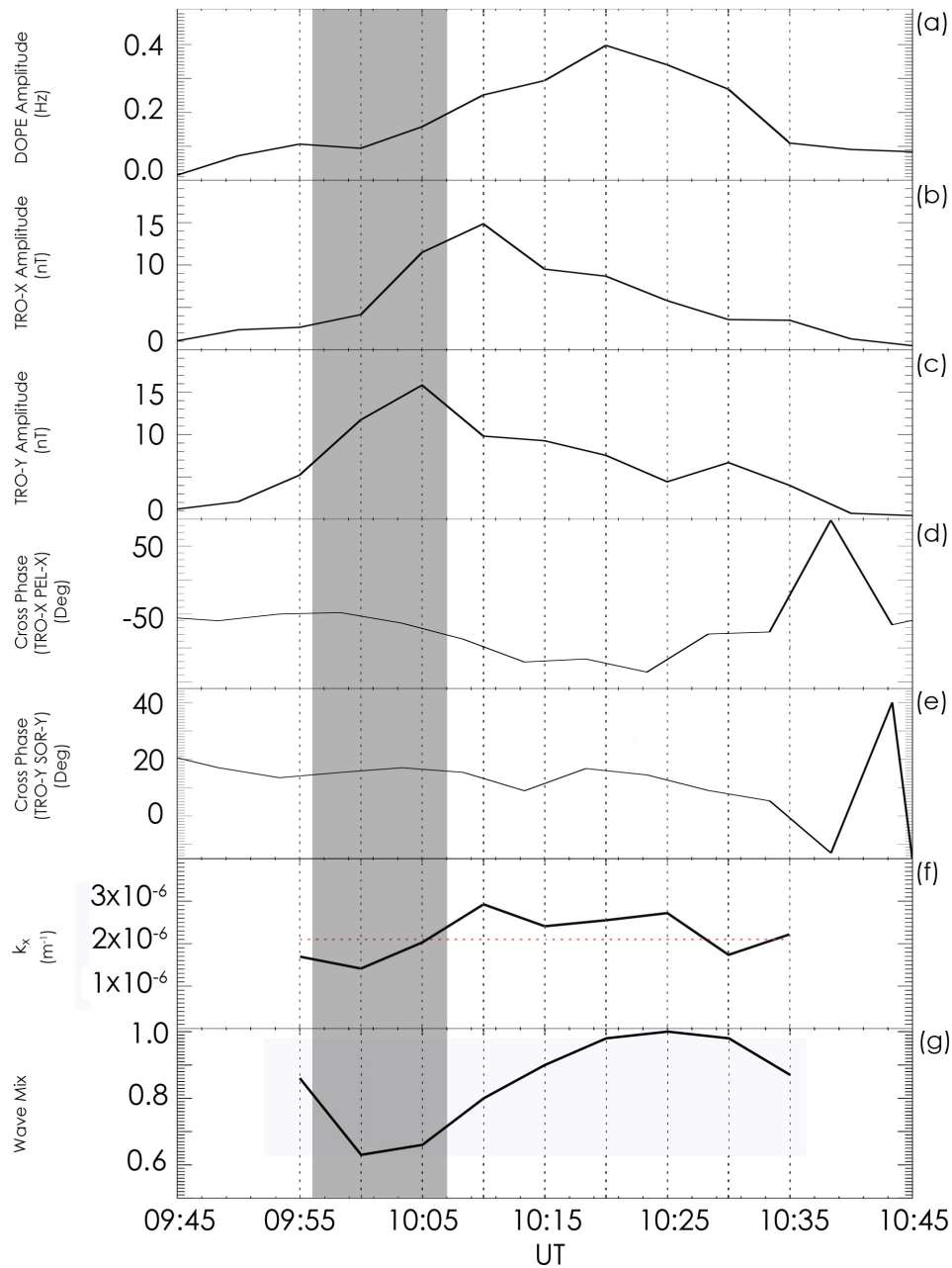


Figure 5.6: **(a – g)** Panel (a) presents the HF Doppler amplitude variation calculated from an integrated Fourier amplitude over a frequency range of between 1.7 mHz - 5.1 mHz using a slip of 5 minutes. Panels (b) and (c) show the TRO-X and TRO-Y amplitudes found using the same technique as for panel (a). Panel (d) shows the X component cross-phase between IMAGE stations TRO and PEL. Panel (e) shows the Y component cross-phase between the azimuthally separated IMAGE stations TRO and SOR. Panel (f) shows the  $k_x$  time evolution determined from the ratio of the amplitudes of TRO-X and TRO-Y. The overplotted horizontal red dotted line shows the constant value of  $k_x$  assumed during the study. Panel (g) shows the implied ULF wave mix evolution. The overplotted dot-dash lines show the 5-minute intervals when the wave mix is calculated. The grey shaded region shows the possible range of arrival times of the effects of the solar wind dynamic pressure increase as measured by the ACE spacecraft.

Panel (e) of Figure 5.6 shows a comparable analysis of the Y component of the magnetic field data from two azimuthally separated stations of TRO and Sørøya (SOR) and shows an approximately constant phase difference, indicating a steady value of the effective azimuthal wavenumber,  $m$ . The value of azimuthal wavenumber deduced from this phase difference is consistent with that derived from a number of IMAGE stations in section 5.2.2, namely  $m \sim -6$ . The grey shaded region shows the possible range of arrival times of the effects of the solar wind dynamic pressure increase as measured by the ACE spacecraft as shown in figures 5.1 and 5.3. Panels (f) and (g) will be discussed in section 5.4.

## 5.3 The Numerical Model

### 5.3.1 Observational Inputs

The characteristics of the observed ULF wave are used as input parameters to the Sciffer et al. (2005) model, which computes the propagation of ULF waves from the magnetosphere, through the ionosphere to the ground for oblique magnetic fields, as was detailed in chapter 4. Using the  $m$  number determined from the IMAGE magnetometer data recorded on 16 April 1998, the east-west wave number was  $k_y = -2.4 \times 10^{-6} \text{ m}^{-1}$  ( $2.4 \times 10^{-6} \text{ m}^{-1}$  in the 1-D model since positive is defined as westwards).

Since  $\nabla \wedge \mathbf{b} = 0$  in the atmosphere the north-south wavenumber may be calculated from the ratio of the X to Y components of the magnetic field recorded on the ground (Hughes, 1974) and here was set at,  $k_x = 2.1 \times 10^{-6} \text{ m}^{-1}$  (a poleward propagating wave).

In the model the atmospheric composition is found from a thermosphere model based on satellite mass spectrometer and ground-based incoherent scatter data (MSISE90) (Hedin et al., 1991). The ionospheric composition is found from the IRI model with the exception of the electron density profile, which is determined using the POLynomial ANalysis (POLAN) algorithm (Titheridge, 1985) and was detailed in section 4.2.5. The final step in the process is to calculate the Doppler shift contributions for the three mechanisms outlined in the model of Poole and Sutcliffe (1988) and the Altar-Appleton-Hartree equation is used for this purpose.

The computation of observed Doppler shifts from the ULF wave model is highly sensitive to the electron density profile, so care must be taken in accurately measuring this parameter. Here ionospheric electron density inputs for the model were determined from local ionosonde measurements. Figure 4.2 presented Tromsø dynasonde data for 16 April 1998 recorded at 10:04 UT. The peak FoF2 was found for the O-mode data (green circles) using the overplotted purple line as a guide and was determined to be 6.5 MHz. The ionospheric inputs to the model were provided by inverting the ionosonde trace with the POLAN algorithm (Titheridge, 1985). POLAN determines the real height by inverting the virtual height as found from ionosonde measurements.

Finally, a dual-Chapman function profile is fitted to the output from POLAN, which is shown by the blue line, to generate an electron density profile. The plasma frequency profile is represented in Figure 4.2 by the black line. The vertical and horizontal red lines on Figure 4.2 show the DOPE transmission frequency and reflection altitude, respectively. The reflection altitude for this event was approximately 184 km.

### 5.3.2 The Model Output

Observations are used to generate input parameters for the ULF event recorded on the 16 April 1998 09:45 UT - 10:45 UT. The model magnetic amplitude on the ground was matched to observed ground values using the IMAGE magnetometer array. At TRO typical magnetic field amplitudes, in the centre of the wave event at 10:14 UT, were roughly 10.0 nT and 9.0 nT for the X and Y components, respectively, yielding a total ground field of approximately 13.5 nT.

Panels (a) to (d) of Figure 5.7 present the results of one run of the model for a purely shear Alfvénic incident wave mode. The magnetic and electric fields are scaled such that the total ground magnetic field matched that from observation (roughly 13.5 nT). Panel (a) presents the variation of the three magnetic field components with altitude. Panel (b) shows the magnetic field phase variation for the same three components. Panel (c) shows the electric field variation for the three field components as a function of altitude. Panel (d) shows the electric field phase for the same three components.

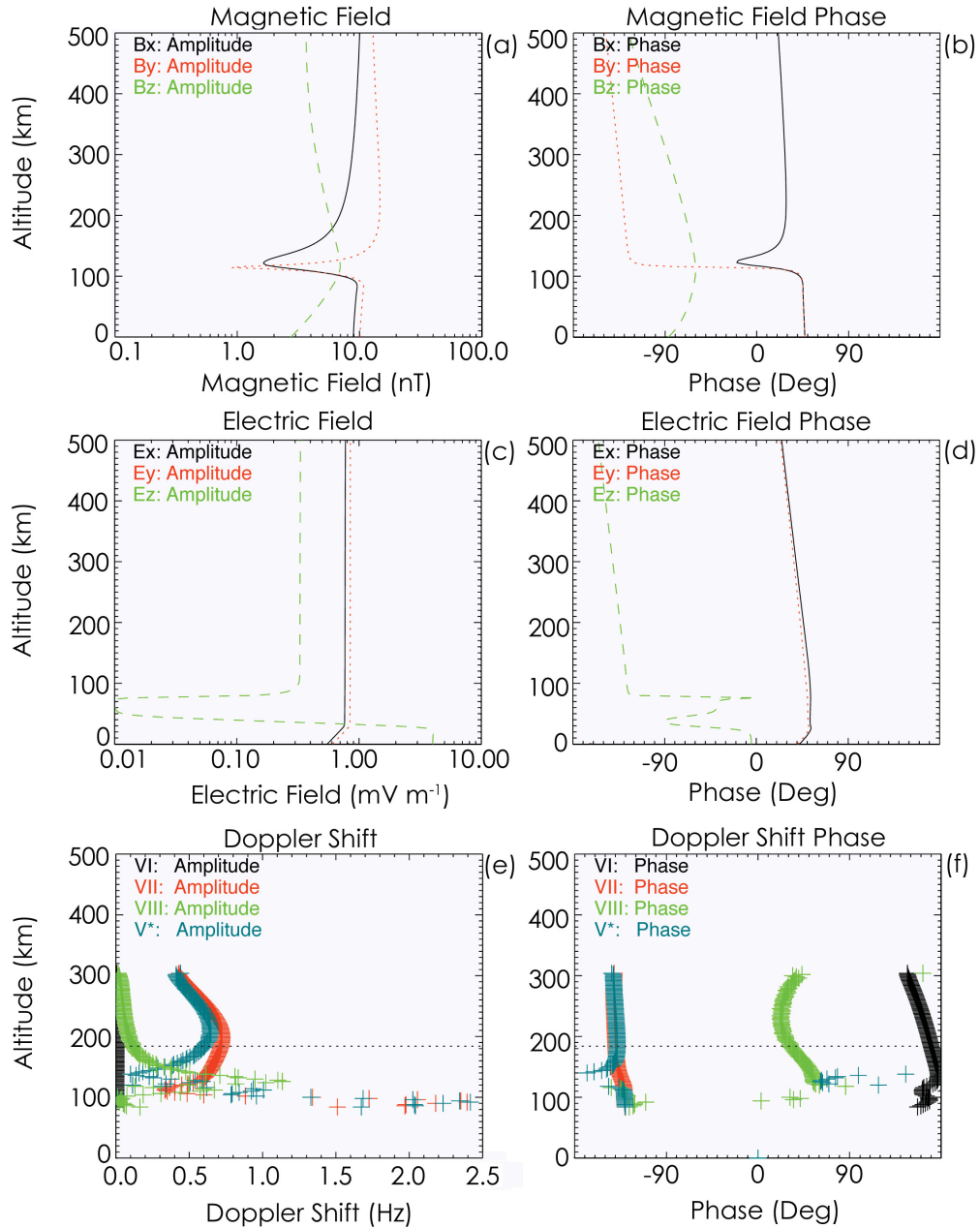


Figure 5.7: **(a – f)** Results of one run of the 1-D Numerical Model for a purely shear Alfvénic incident wave with an altitude range from the ground to 500 km. Panel (a) presents the variation of the three magnetic field components with altitude. Panel (b) shows the magnetic field phase variation for the same three components. Panel (c) shows the electric field variation for the three field components as a function of altitude. Panel (d) shows the electric field phase for the same three components. Panel (e) shows the Doppler shift mechanism contributions as a function of altitude. Black is the magnetic mechanism contribution ( $V_I$ ), red is the advection mechanism contribution ( $V_{II}$ ), green is the compressional mechanism contribution ( $V_{III}$ ) and blue is the overall Doppler shift given by the vector addition of the three Doppler shift components ( $V^*=V_I+V_{II}+V_{III}$ ). Panel (f) shows the phase variation for the same mechanisms as given in panel (e) and is colour coded in an identical fashion. The overplotted black dotted line highlights the DOPE reflection altitude, at roughly 184 km.

The effect that the ULF wave has upon the DOPE radio waves can be calculated using a model (Poole and Sutcliffe, 1988), as described in subsequent work by Waters et al. (2007). Panel (e) shows the Doppler shift mechanism amplitude, as a function of altitude. Black is the magnetic mechanism contribution ( $V_I$ ). Red is the advection mechanism contribution ( $V_{II}$ ), green is the compressional mechanism contribution ( $V_{III}$ ) and blue is the overall Doppler shift ( $V^*=V_I+V_{II}+V_{III}$ ). Panel (f) shows the phase variation for the same mechanisms as in panel (e) and is colour coded in an identical fashion. The overplotted black dotted line highlights the DOPE reflection altitude, at roughly 184 km. The overall Doppler shift for a purely shear Alfvénic incident wave is dominated by the advection mechanism ( $V_{II}$ ) as there are very small contributions from the other two mechanisms. There are also very large E-region values of Doppler shift, which is a characteristic of these calculations. The large Doppler shift results from the "knee" in the electron density profile corresponding to a transmission frequency of approximately 3 MHz at 100 km, as seen in Figure 4.2.

As is clear from Figures 5.5 and 5.6, the wave event under study here has a complicated spatial and temporal structure in amplitude and phase. The 1-D model is suggested to be too simplistic to reproduce accurately the details of the phase relationships between the various magnetic and electric field components, but Waters et al. (2007) demonstrated that Doppler amplitudes are predicted well. Accordingly, only model amplitude information is considered in this chapter. Chapter 6 will investigate these phase relationships.

For magnetic field amplitudes recorded on the ground by TRO of 10.0 nT and 9.0 nT, in the X and Y components of the field, respectively, the overall Doppler amplitude at the DOPE reflection altitude for a purely shear Alfvénic incident wave determined by the model is roughly 0.5 Hz. This is quite comparable with the typical Doppler Shift as found by the DOPE instrument in the centre of the wave event, of approximately 0.3 Hz at 10:14 UT. However, the ULF wave does not show steady state behaviour throughout the event. The amplitudes in DOPE appear to increase as the wave evolves towards an FLR and the relative phase between magnetometer stations evolves also (see Figure 5.6). One factor, which strongly influences the predicted Doppler shift, is the wave mix of the

incoming ULF wave between fast compressional and Alfvénic wave power. Therefore, an investigation of the effect of wave mix is required in order to determine the predicted Doppler shift that best matches observation throughout the evolution of the wave. Figure 5.8 presents the electric field, magnetic field, and Doppler shift mechanism results as functions of altitude for different wave mixes normalised such that there is a total magnetic field magnitude of 1 nT on the ground. A wave mix of 1.00 is a purely shear Alfvénic incident wave mode whereas a wave mix of 0.0 is a purely fast/compressional incident wave mode. Panels (a) and (b) show the X and Y components of the electric field respectively. Panels (c) and (d) show the X and Y components of the magnetic field respectively. The electric field in the ionosphere is clearly a strong function of incident wave mode for a given ground magnetic field signature, and hence so will be the Doppler signature.

Figure 5.8 also presents the corresponding Doppler shift amplitude variation as a function of incoming wave mix and altitude. These plots show how a variation in the incoming Alfvénic wave mix affects the Doppler Shift amplitude. Panel (e) shows the magnetic mechanism. Panel (f) shows the advection mechanism. Panel (g) shows the compressional mechanism. Finally, panel (h) shows the overall Doppler shift. As the wave mix tends towards a purely shear Alfvénic mode the Doppler shift amplitude increases across all mechanisms. The advection mechanism is the dominating mechanism for a purely shear Alfvénic incident wave mix. The phase contributions from the different mechanisms, although not presented here, highlight that although significant differences occur at lower altitudes, at the DOPE reflection altitude of 184 km, the overall Doppler shift phase looks similar to the "advective" phase.

Panel (a) of Figure 5.9 presents the overall Doppler shift variation as a function of wave mix at the DOPE reflection altitude (184 km), scaled for 1 nT measured on the ground. The scaling allows the determination of the predicted Doppler shift for a given wave mix at different times throughout the event. Matching the observed magnitude of the Doppler amplitudes at various times during the wave event allows the actual incident wave mode to be determined assuming  $k_y$  and  $k_x$  are constant.

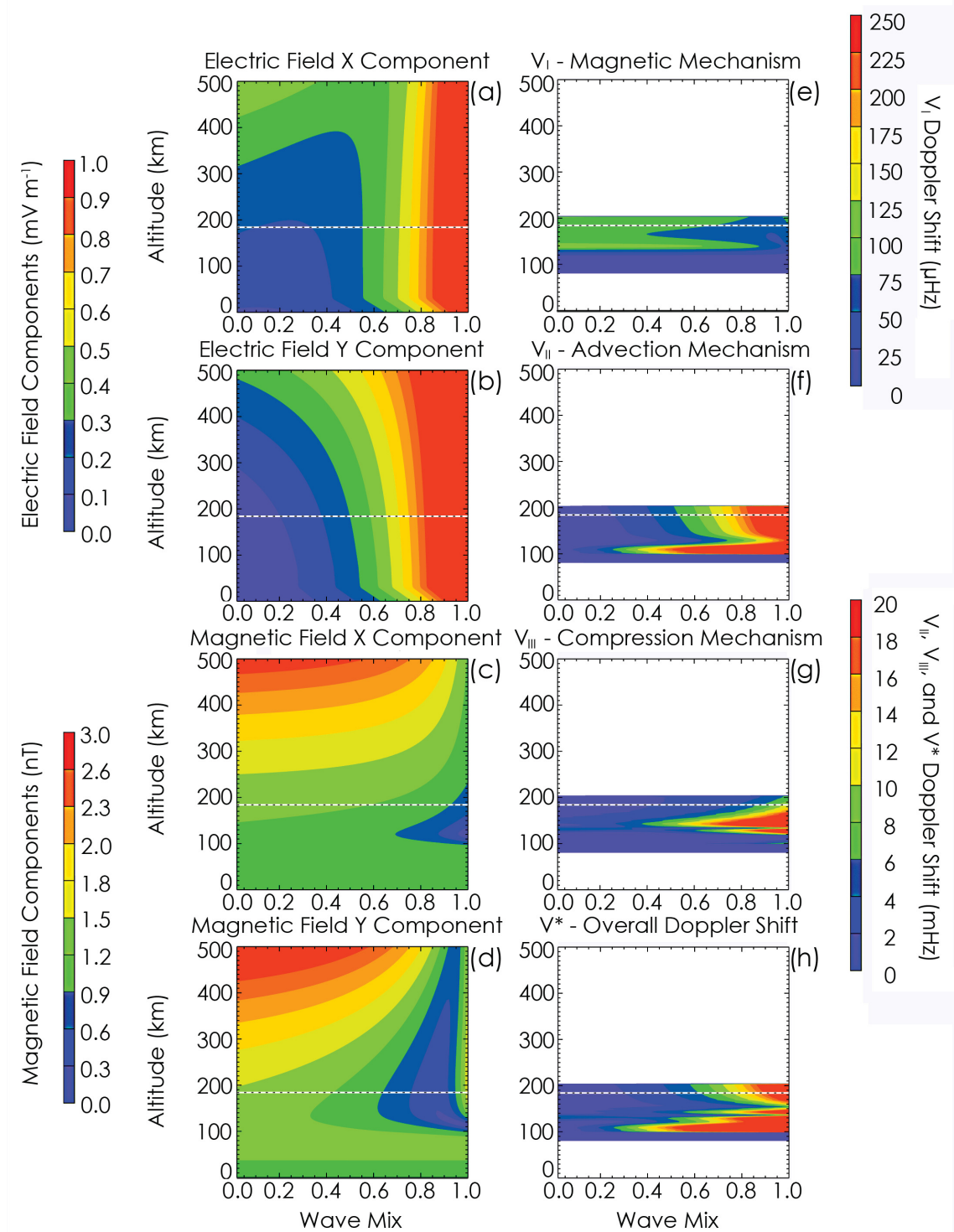


Figure 5.8: Electric field, magnetic field and Doppler shift mechanism results for the ULF wave event on 16 April 1998 between 09:45 UT - 10:45 UT as a function of altitude and wave mix scaled to make the magnetic field magnitude 1 nT on the ground. Panel (a)  $E_x$ . (b)  $E_y$ . (c)  $B_x$ . (d)  $B_y$ . (e)  $V_I$ . (f)  $V_{II}$ . (g)  $V_{III}$ . (h)  $V^*$ .

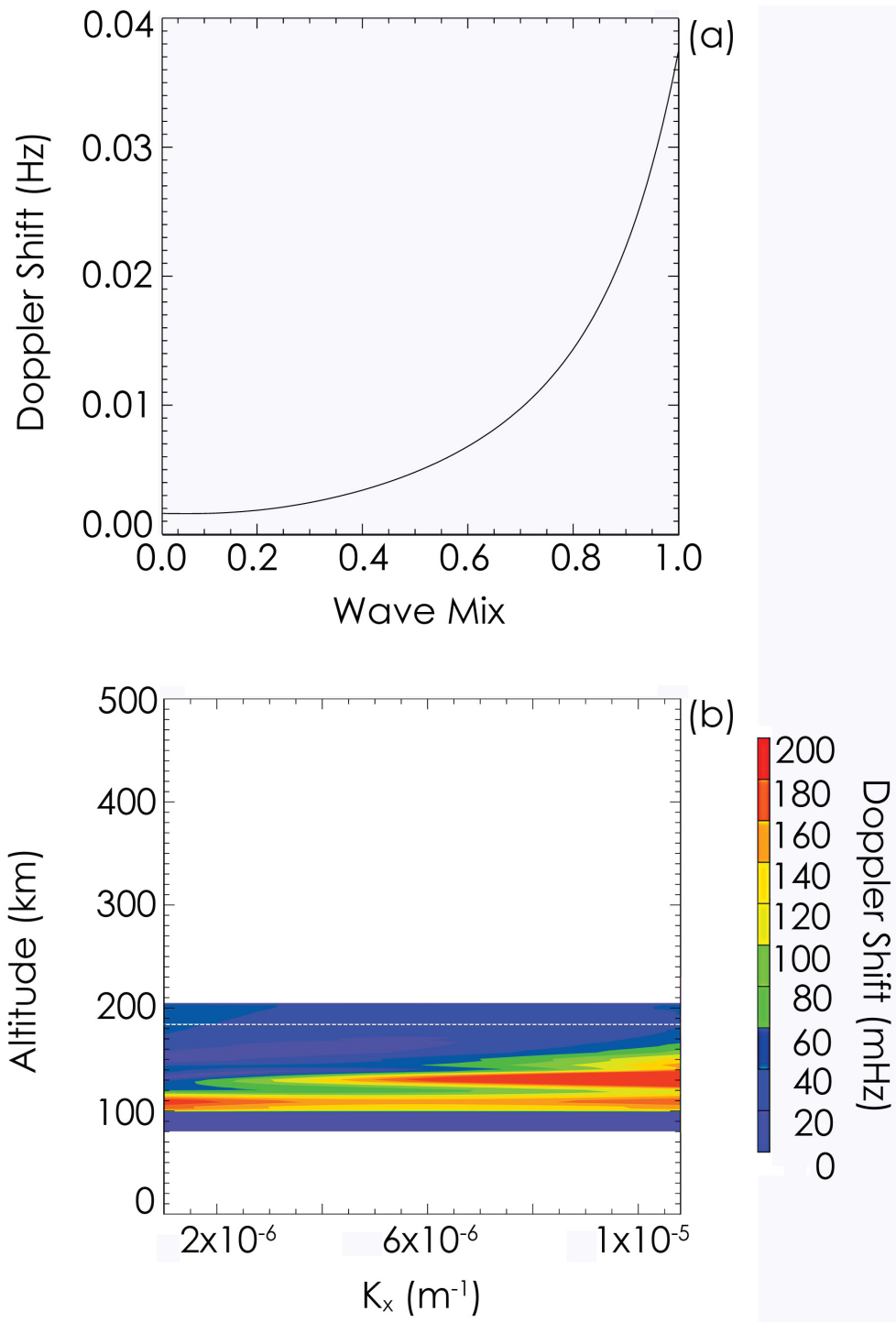


Figure 5.9: **(a and b)** Overall Doppler shift model results of the ULF wave event on 16 April 1998 between 09:45 UT - 10:45 UT for wave mixes ranging between zero and unity. Panel (a) shows the variation of total Doppler shift with wave mix at the DOPE reflection altitude of 184 km. Panel (b) presents the variation in the total Doppler shift contributions as a function of altitude and  $k_x$ . The overplotted white dashed line shows the DOPE reflection altitude at approximately 184 km. The ground magnetic field in both panels has been scaled to 1 nT.

The values of  $k_y$ ,  $k_x$  and the incident wave mode all affect the overall Doppler magnitude. Eliminating these variables one by one provides an explanation for the model Doppler shifts presented in Figure 5.9. Section 5.2.3 presented a cross-phase analysis of the Y components of two azimuthally separated IMAGE stations (TRO and SOR). A constant effective azimuthal wavenumber was determined, implying a constant east-west wavenumber.  $k_y$ , therefore, may be neglected as the cause of variations in the Doppler signature. Thus, the parameter responsible for the nature of Figure 5.6 must be either a changing incident wave mode, or the north-south wavenumber,  $k_x$ , or a combination of the two. Panel (b) of Figure 5.9 presents the variation in the total Doppler shift contributions similarly to Figure 5.8 but now as a function of altitude and  $k_x$  for a ground magnetic field magnitude scaled to 1 nT on the ground. Larger Doppler shifts are expected at larger  $k_x$  (smaller-scale) values for a given ground magnetic field magnitude due to attenuation effects (Hughes and Southwood, 1976a). One would expect an evolving  $k_x$ , and an increase in the X component of the field, as the system tends towards FLR, and this will also affect the total Doppler shift. An analysis of the relative importance of  $k_x$  and incoming wave mode mix will be discussed in the next section.

## 5.4 Discussion

Employing the DOPE HF Doppler sounder in conjunction with the IMAGE network of ground magnetometers, the Tromsø dynasonde, the ACE and IMP-8 spacecraft, and a numerical model, it is possible to fully characterise the nature of a magnetospheric ULF wave both in the ionosphere and at the ground. The event, which occurred on 16 April 1998, is the result of a low- $m$  (-6) FLR with a large characteristic scale-size. Figure 5.3 presented the filtered HF Doppler and TRO magnetometer data for the event. The time development of the amplitudes in the Doppler and magnetometer traces was different, with the peak amplitude seen early on in the wave packet in the magnetometer data (10:10 UT), but later in the Doppler trace (10:20 UT). This implies some evolution of the wave characteristics (wave mode, azimuthal or meridional scale-size) during the wave. Panel

(d) of Figure 5.6 showed a phase difference of approximately  $-60^\circ$  between stations TRO and PEL at 10:00 UT evolving to approximately  $-140^\circ$  at 10:15 UT. The increasing cross-phase suggests a more FLR-like perturbation as time progresses. Panel (g) of Figure 5.1 showed an impulsive disturbance in the solar wind, the effects of which are expected to arrive at the ionosphere between 09:56 UT and 10:07 UT. This impulse is interpreted as the source of the observed wave event.

### 5.4.1 Wave Evolution

Section 5.3.2 presented evidence of the model Doppler amplitude being a result of either variations in  $k_x$  and/or the incident wave mode since  $k_y$  remained approximately constant throughout the event. To determine the relative importance of the incident wave mode and/or the meridional scale-size on the Doppler amplitude, ground magnetic field and Doppler observations are used to find inputs to the numerical model at various times throughout the event. The north-south wavenumber may be calculated from the east-west wavenumber and the ratio of the X and Y components of the magnetic field recorded on the ground (Hughes, 1974), which are presented in panels (b) and (c) of Figure 5.6. Panel (f) of Figure 5.6 presents the north-south wavenumber variation calculated from these data. The calculated range of  $k_x$  shows a variation from  $k_x = 1.5 \times 10^{-6} \text{ m}^{-1}$  to  $k_x = 3.0 \times 10^{-6} \text{ m}^{-1}$ . Referring to panel (b) of Figure 5.9 it can be seen that such a range of  $k_x$  variation has a negligible effect on the derived total Doppler shift, which also agrees with section 4.3.5. Therefore, the incoming wave mode mix must be the dominant factor affecting the Doppler amplitude and a constant  $k_x$  value of  $2.1 \times 10^{-6} \text{ m}^{-1}$  is used in subsequent calculations, in the chapter, indicated in panel (f) of Figure 5.6 by a horizontal red dotted line.

The wave mix variation is calculated by matching the observed Doppler shift to the model Doppler shift at 5-minute intervals throughout the event, which are marked by the vertical dotted lines on Figure 5.6. At each 5-minute interval, the time-evolving Doppler shift,  $B_x$  and  $B_y$  are found by using the DOPE,  $B_x$ , and  $B_y$  amplitudes presented in panels (a) to (c) of Figure 5.6, respectively. The magnetic field components, therefore, are used to scale

the predicted Doppler shift using a constant scale-size. Panel (g) of Figure 5.6 presents the wave mix evolution derived from such an analysis throughout the event. The first point of the Alfvénic wave mix, at 09:55 UT, has a value of 0.86 (implying contributions from both fast mode compressional and Alfvén modes) although at this time the amplitudes of Doppler shift,  $B_x$  and  $B_y$  are small so this point is probably not significant. Once the event is established, at roughly 10:00 UT, the wave mix becomes 0.63 and subsequently rises to unity (a purely shear Alfvén wave) by approximately 10:25 UT. The implied wave mix value of unity occurs just after the peak observed Doppler amplitude as shown in panel (a) of Figure 5.6.

#### 5.4.2 The Advection Mechanism

The early theory developed by Rishbeth and Garriott (1964) considered that the Doppler frequency oscillations were due to the ULF electric field, causing a vertical bulk motion of electrons in the ionosphere. The vertical motion is the vertical component of the plasma drift velocity as given by equation 4.21. This vertical motion is now known as the advection mechanism, as was detailed in section 4.2.3. Equation 4.22 suggests that  $V_z$  and the vertical gradient of the refractive index contribute to the observed Doppler shift. The contribution of these two mechanisms may be separated within the model employed here. If  $V_z$  is plotted as a function of both incident wave mode and altitude, assuming the constant value of  $k_x$ , and using a magnetic field magnitude of 1 nT recorded on the ground, Figure 5.10 is the result. The very high similarity with the Doppler variation illustrated in panel (c) of Figure 5.8 establishes that the  $V_z$  parameter contained within the advection mechanism is contributing the most to the overall Doppler shift at high-latitude for this impulse-driven large spatial-scale ULF wave. This conclusion, that the signature observed here is well described by a simple advection mechanism as proposed by Rishbeth and Garriott (1964), agrees with the overall results of previous ULF wave studies (e.g., Wright et al., 1997, 1998; Waters et al., 2007) that the advection mechanism dominates the overall Doppler shift observed at high-latitudes.

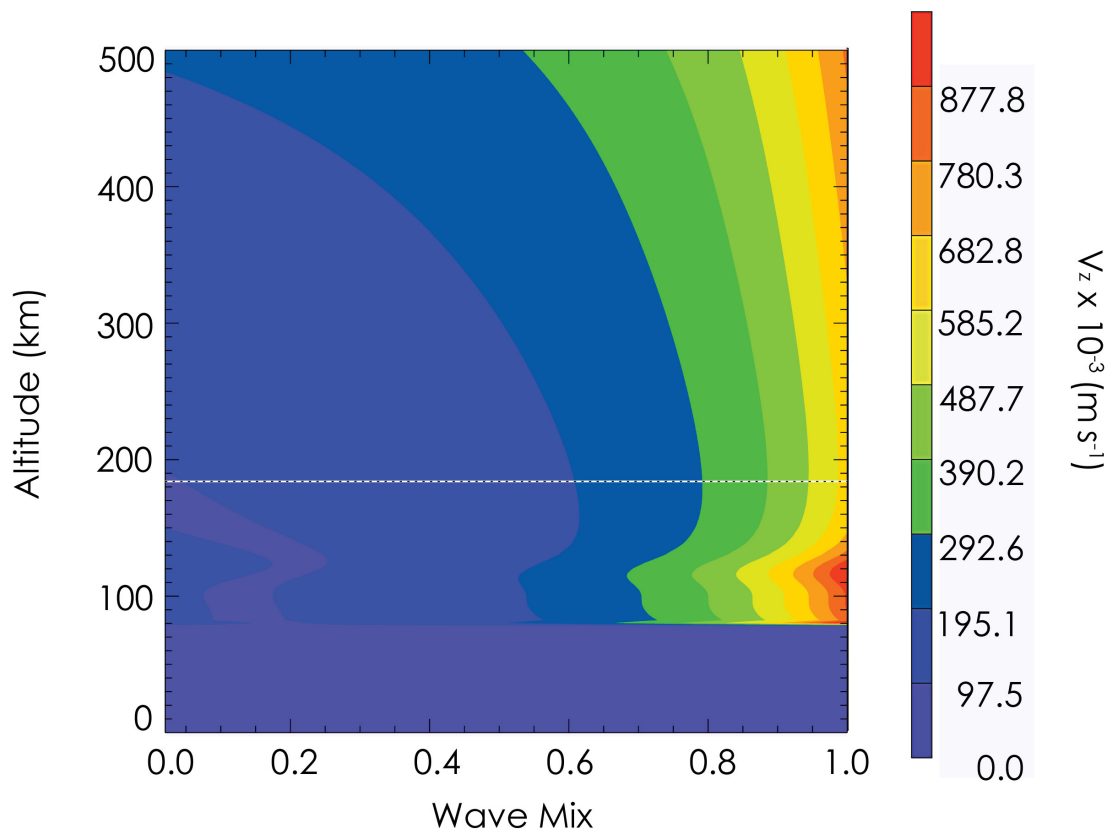


Figure 5.10: The plot shows  $V_z$  as a function of both altitude and wave mode mix. The overplotted white dot-dashed line highlights the DOPE reflection altitude at roughly 184 km.

## 5.5 Summary

In this chapter, a numerical one-dimensional model developed by Sciffer et al. (2005) has been employed to account for the observed relationship between the Doppler velocity oscillations of reflected radio waves from the ionosphere and geomagnetic pulsations. The event that occurred on 16 April 1998 is the result of a low- $m$  (-6) FLR with a large characteristic scale-size. An impulsive disturbance is seen in the ACE upstream spacecraft data and the IMF dynamic pressure increased at about the same time as the wave onset as recorded on the ground by magnetometers. Here, the effect of the modelled incident wave field on an HF radio path is calculated, and compared to observation. Ground magnetic field and Doppler observations are used to find model inputs at various points throughout

the event. The model, on average, correctly predicts the Doppler amplitudes for this impulse-driven ULF wave event. Presented here, for the first time, are measurements of the incident wave mode evolution. The model demonstrates that the incident wave mode evolves from a partially shear Alfvénic wave to a purely shear Alfvén wave. The advection mechanism is contributing the most to the overall Doppler shift at high-latitudes in this instance, agreeing with previous statistical studies of large spatial-scale ULF waves (e.g., Wright et al., 1997, 1998; Waters et al., 2007). For this event, it is also confirmed that the vertical velocity dominates the advection mechanism, rather than refractive index effects. 25 ULF wave events with measurements from a high-latitude Doppler sounder and the IMAGE magnetometer array have been analysed. A statistical analysis of more large spatial-scale ULF waves will follow in the next chapter of this thesis.

# Chapter 6

## Observations and Modelling of High-Latitude HF Doppler Measurements of Large-Scale Ultra Low Frequency Waves

### 6.1 Introduction

This chapter focuses on 25 geomagnetic pulsation events measured by the DOPE system, the IMAGE magnetometer array, and the Tromsø dynasonde, between January 1998 and September 2003. During this period the DOPE system measured approximately 300 geomagnetic pulsation events in total. The 25 included in this study were extracted because they fulfilled three simple selection criteria that (a) after passing the wave data through an FFT routine to obtain the dominant frequency of the wave, the wave signature had an identical frequency in both the DOPE instrument and the IMAGE magnetometer array, (b) the effective azimuthal wavenumber,  $m$ , was less than 10 and (c) there are data available from the Tromsø dynasonde that provide a satisfactory electron density profile using the POLAN algorithm (Titheridge, 1985).

## 6.2 Basic Event Statistics

The basic wave parameters measured for each event were used as inputs to the 1-D ULF wave model of Sciffer et al. (2005), and the output of this model was employed as an input to the implementation of the Sutcliffe-Poole model for Doppler shifts, as described in section 4.2.

Figure 6.1 presents an overview of the 25 events found during this study. The distributions shown in each panel of Figure 6.1 are presented as occurrence histograms apart from panels (e) and (f), which are presented as scatter plots. The overplotted vertical dashed lines on panels (c) and (g) show the location of zero. The overplotted lines on panels (e) and (f) show  $y = x$  and  $y = -x$  lines where appropriate. Panel (a) shows the distribution of wave frequencies, in mHz, and highlights that the most commonly observed frequency range is between 2 mHz - 4 mHz. The frequency range is typical for FLR activity within the vicinity of Tromsø (e.g., Wright et al., 1997; Borderick et al., 2010). Panel (b) presents the MLT location of the 25 wave events showing occurrence predominantly in the 5 MLT - 12 MLT range with a few events located between 15 MLT - 20 MLT. Most events occurred within the daytime, which was probably due to the Peak FoF2 at these times being high enough to allow a reflection of the DOPE HF radio wave from the ionosphere. Panel (c) shows the east-west wavenumber distribution and highlights that most events are between  $k_y = -5 \times 10^{-6} \text{ m}^{-1} - +3 \times 10^{-6} \text{ m}^{-1}$ , with corresponding effective azimuthal wavenumbers,  $m$ , of between -6 and 4, where the negative sign indicates westward propagation. The north-south wavenumber,  $k_x$ , can be inferred from the east-west wavenumber,  $k_y$ , and the ratio of the  $B_x$  to the  $B_y$  component of the magnetic field recorded on the ground by

$$k_y B_x \approx k_x B_y \quad (6.1)$$

(Hughes, 1974). Panel (d) shows the north-south wavenumber distribution for the events with most events lying in the region of  $k_x = 0 - 3 \times 10^{-6} \text{ m}^{-1}$ . Here the positive value of  $k_x$  implies a poleward propagating wave. Panel (e) presents the north-south wavenumber

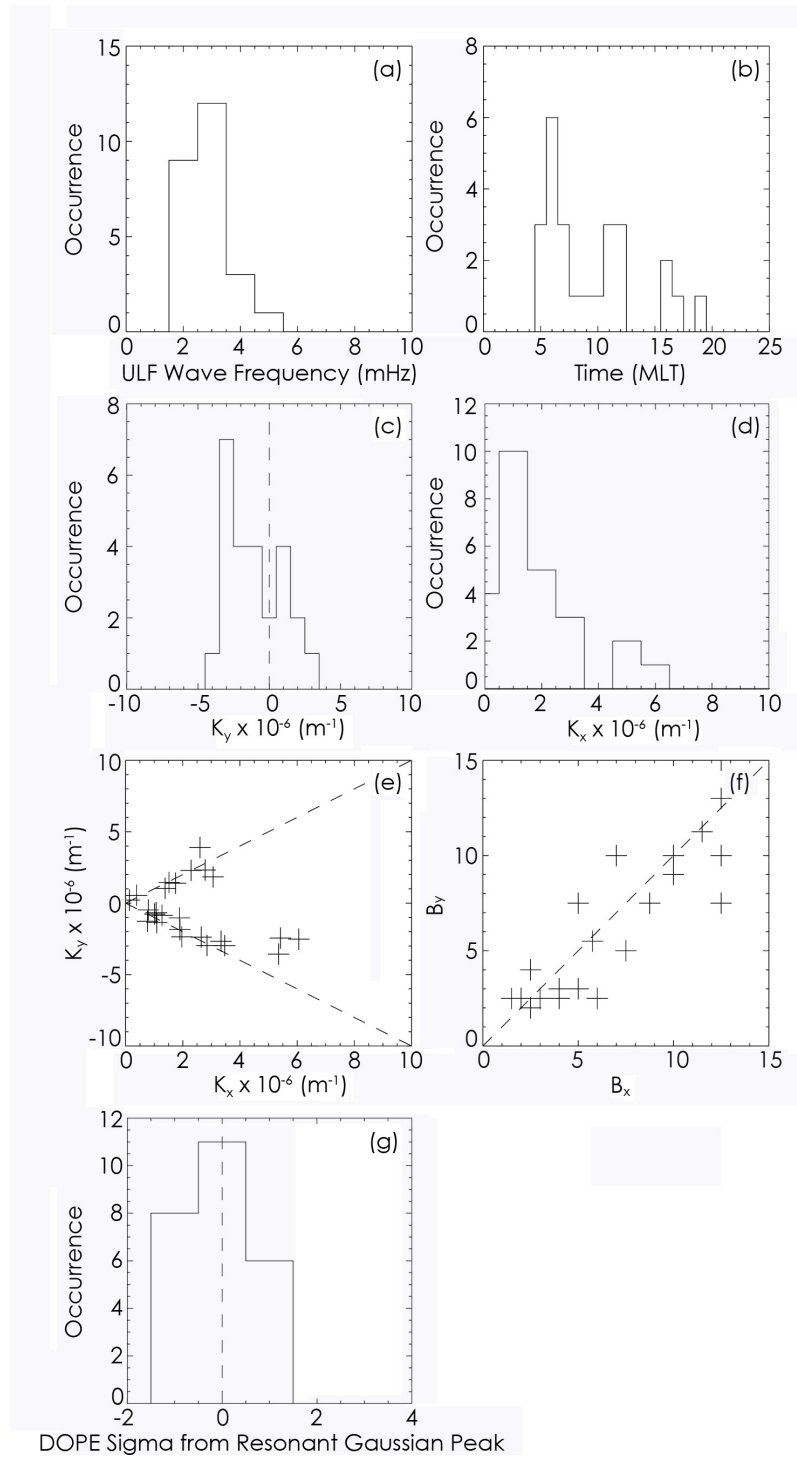


Figure 6.1: **(a – g)** ULF wave statistics for the 25 events recorded throughout this study. Panels show distributions of (a) the wave frequency (b) the time of day in MLT (c) the east-west wavenumber (d) the north-south wavenumber (e) the north-south wavenumber as a function of the east-west wavenumber (f) the X component amplitude of the magnetic field recorded at Tromsø (TRO) as a function of the Y component of the magnetic field amplitude and (g) the DOPE sigma distance from the resonant Gaussian peak, which will be detailed in section 6.6. The overplotted vertical dashed lines on panels (c) and (g) show the location of 0. The overplotted lines on panels (e) and (f) show  $y = x$  and  $y = -x$  lines where appropriate.

as a function of the east-west wavenumber and shows that for most events  $k_x > k_y$ . This implies slightly smaller scale-sizes in X than Y, and the corresponding the azimuthal scale ranges from 30,000 km,  $m \sim 1$  (small  $k_y$ ), to 2000 km,  $m \sim 9$  (large  $k_y$ ). The meridional scale ranges from 20,000 km (small  $k_x$ ), to 1,000 km (large  $k_x$ ). Panel (f) shows the X component amplitude of the magnetic field recorded at Tromsø (TRO) as a function of the Y component of the magnetic field amplitude and indicates that for most of the events  $B_x > B_y$ , as dictated by equation 6.1, and as expected for FLR driven events, detailed in chapter 2. Panel (g) of Figure 6.1 will be discussed later.

Figure 6.2 presents additional ULF wave parameter statistics for the 25 events recorded throughout this study now considering ionospheric as well as ground magnetic measurements. Panel (a) presents the peak FoF2 measured by the Tromsø dynasonde for each event and shows that predominantly the critical frequency of the ionosphere is approximately 6 MHz with all events lying in a range of between 3 MHz - 10 MHz, which agrees with typical daytime peak FoF2 as modelled by the IRI. Panel (b) presents the DOPE reflection altitude in km as a function of occurrence for the 25 ULF wave events and shows a reflection altitude fairly uniformly distributed between the lower F-region to peak F-region (180 km - 310 km). Panel (c) shows the phase difference of the ULF signature between TRO-X and the Doppler instrument, calculated by Fourier analysis at the peak frequency of the wave event. Panel (c) shows a fairly uniform distribution of phase differences and will be discussed later. Panel (d) shows the same analysis as for panel (c) but uses TRO-Y instead of TRO-X. In both panels (c) and (d), the positive and negative phase differences indicate TRO leading and lagging the Doppler signature, respectively. Panel (d) shows that the majority of events exhibit phase differences of between  $90^\circ$  -  $150^\circ$  with  $B_y$  leading as highlighted by the overplotted dashed lines.

### 6.3 Doppler Shift Amplitude Dependence on Mechanisms

Section 4.3.4 outlined an analysis technique using the Sciffer et al. (2005) implementation of the Sutcliffe and Poole numerical model, which calculated the possible Doppler

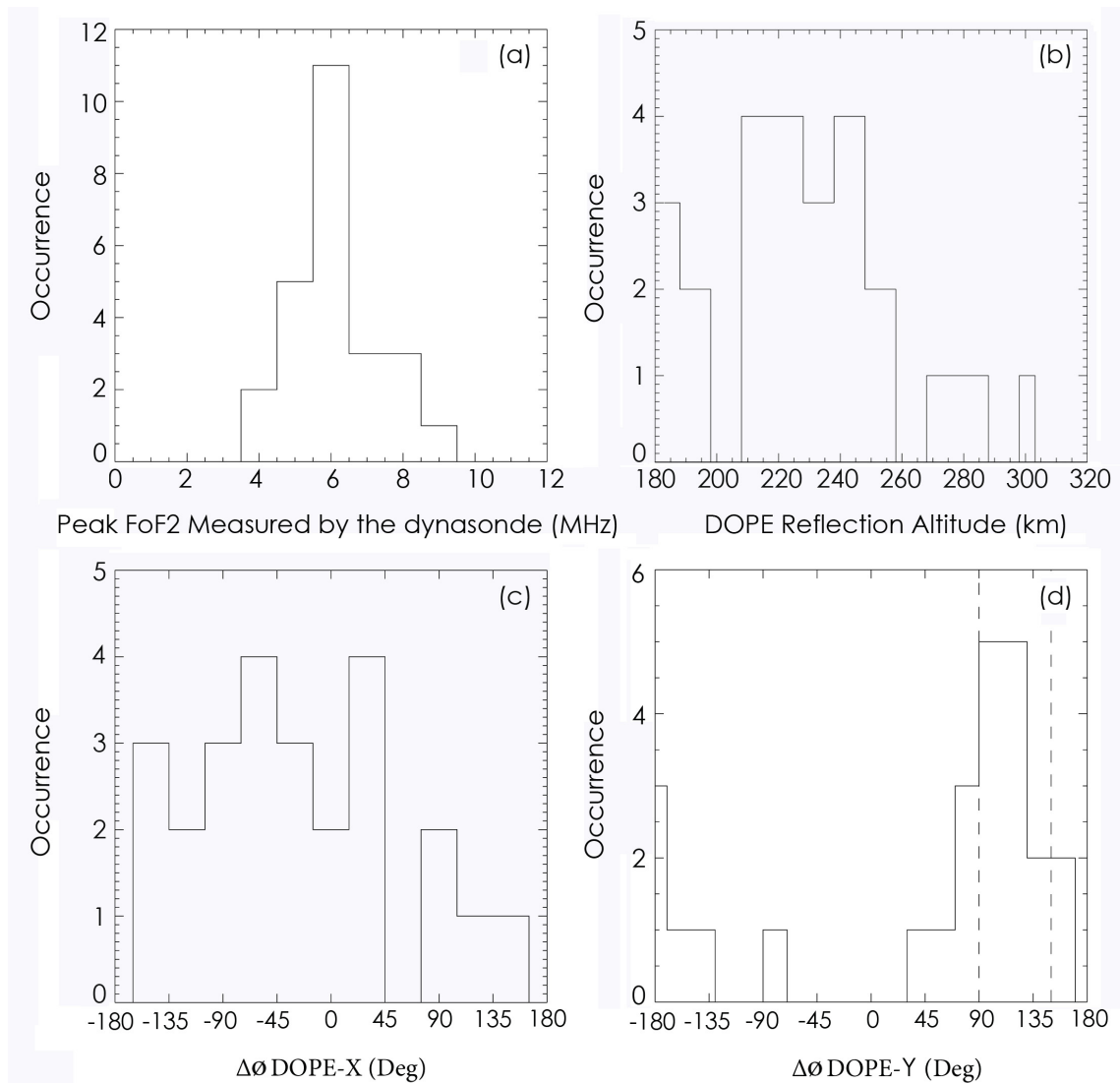


Figure 6.2: **(a – d)** More ULF wave statistics for the 25 events recorded throughout this study. Panels show distributions of (a) the peak FoF2 measured by the Tromsø dynasonde (b) the DOPE reflection altitude (c) the phase difference at the peak power of the ULF signature between the TRO-X and the Doppler instrument (d) the phase difference at the peak power of the ULF signature between the TRO-Y and the Doppler instrument. Each panel is expressed as a histogram and are a function of occurrence. The overplotted vertical dashed lines on panel (d) show the region enclosed between phase differences of  $90^\circ$  and  $120^\circ$ .

shift mechanisms contributing to the signatures recorded in the DOPE sounder. Figure 4.13 presented the overall Doppler shift model results for an example ULF wave event, recorded on 29 December 2001, at the DOPE reflection altitude. Here this analysis technique is applied to all 25 ULF wave events assuming a purely shear Alfvénic incident wave, with the models driven by the measured wave characteristics and ionospheric profiles chosen appropriately for each event. At an incident wave mode of unity, the amplitude of the contributing Doppler shift mechanism is recorded and displayed as a scatter plot. Figure 6.3 presents the results of such an investigation. Panels (a) to (c) of Figure 6.3 present the total model Doppler shift as a function of the magnetic mechanism,  $V_I$ , the advection mechanism,  $V_{II}$  and the compressional mechanism,  $V_{III}$ , respectively. All panels have units of Hz apart from panel (a), which depicts the very small magnetic mechanism contributions in mHz.

Figure 6.3 shows that for all 25 ULF wave events the model predicts that advection is the dominant mechanism contributing to the overall Doppler shift for a purely shear Alfvénic incident wave. Furthermore, Figure 6.3 highlights that the magnetic and compressional mechanisms provide negligible contributions.

Panel (a) of Figure 6.4 shows the model Doppler shift for a purely shear Alfvénic incident wave as a function of the observed Doppler shift recorded by the HF Doppler sounder. The Product Moment Correlation Coefficient (PMCC) of 0.53 shows that for many events good agreement between the model and the observations is found when a purely Alfvénic incident wave is assumed. The panel shows that there are a few events which lie above the  $y = x$  line. These events may have their associated Doppler shift reduced by including a compressional component in the model incident wave mode, which was introduced in section 4.3.4.

Panel (b) of Figure 6.4 shows the same plot as in panel (a) except that the model Doppler shift is modified by the incident wave mode (ranging from 0.2 - 1.0) until the model and observed Doppler shifts match as closely as possible. Choosing a suitable value of this free parameter allows an excellent agreement between model and observation. This process will be discussed further in section 6.6. Panels (a) and (b) of Figure 6.4 also

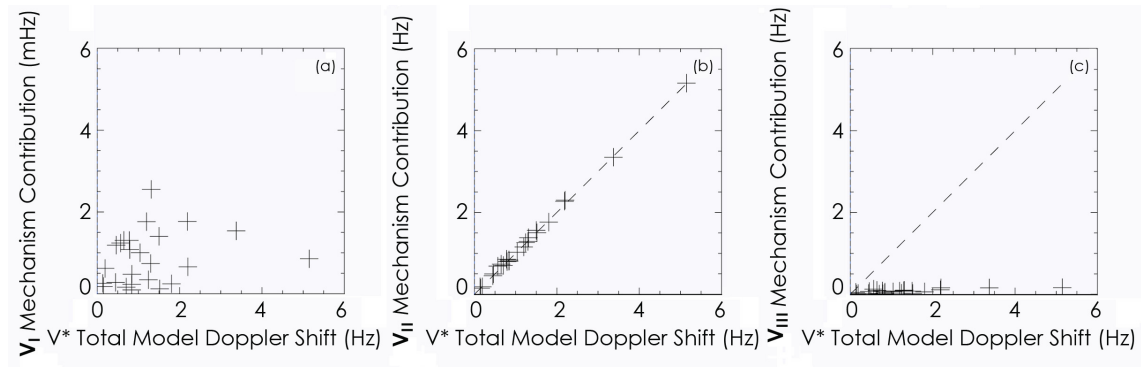


Figure 6.3: **(a – c)** Model output statistics showing the individual Doppler shift mechanism contributions to the overall Doppler shift. Panel (a) presents the total model Doppler shift, in Hz, as a function of the magnetic mechanism,  $V_I$ , in mHz. Panel (b) presents the total model Doppler shift, in Hz, as a function of the advection mechanism,  $V_{II}$ , in Hz. Panel (c) presents the total model Doppler shift, in Hz, as a function of the compressional mechanism,  $V_{III}$ , in Hz.

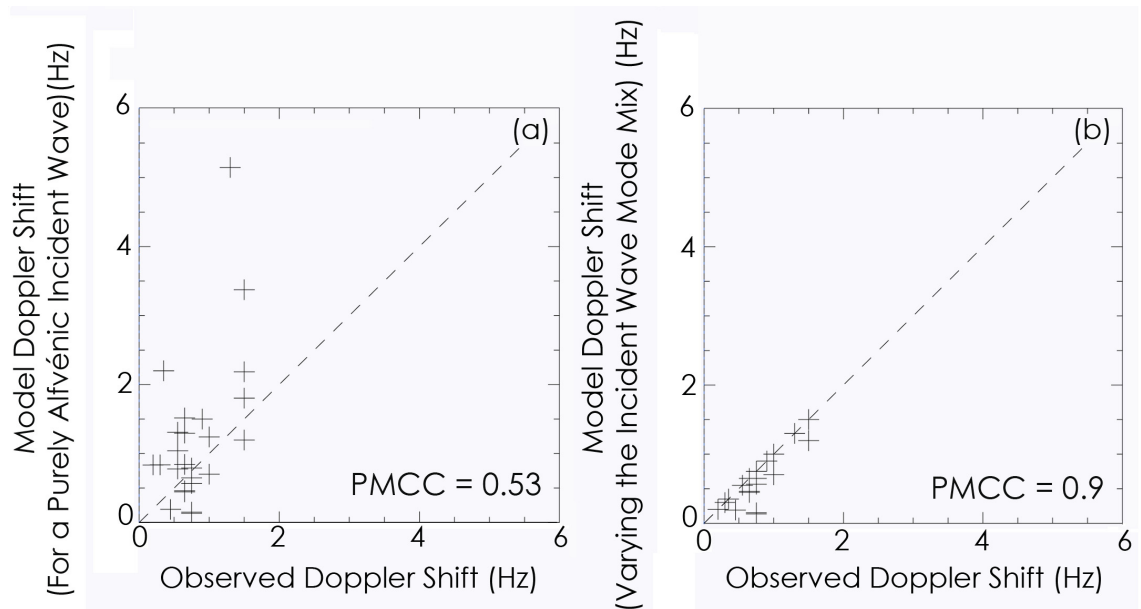


Figure 6.4: **(a and b)** Model output statistics showing the model Doppler shift as a function of the observed Doppler shift. Panel (a) shows model results when a purely Alfvénic incident wave is assumed and panel (b) shows when the model Doppler shift is modified by the incident wave mode until the model and observed Doppler shifts match.

show that there are events which lie below the  $y = x$  line. These events cannot match observation as changing the incident wave mode does not match the resulting model Doppler shift. Two of these events, within this population, are not close to the  $y = x$  line, however, the remainder appear to be within experimental error of the line, and follow a linear relationship.

Figure 6.5 presents the dependence of horizontal ground magnetic field perturbation for each event as a function of the total electric field. Figure 6.5 shows that the electric field is strongly correlated with the ground magnetic field, as expected, although the considerable scatter indicates that other parameters strongly influence the ratio of electric to magnetic fields. To investigate the dependencies of the Doppler shift on other parameters, it will subsequently be normalised relative to a horizontal ground magnetic field perturbation of 1 nT.

## 6.4 Normalised Doppler Amplitude

### 6.4.1 Normalised Model Doppler Shift

The dependency of the Doppler shift on the key parameters considered previously in section 4.3.5 is important when the 1-D numerical ULF wave model, and the subsequent Sutcliffe-Poole model, is applied to observed FLRs. However, in order to investigate the effects that these key parameters have on the Doppler shift a suitable range of each of these parameters must be selected for high-latitude FLR ULF wave events.

This chapter has provided occurrence histograms of various parameters for 25 high-latitude FLR driven ULF wave events and will provide these ranges. Therefore, a prediction using the study contained within section 4.3.5 can be made as to the relative importance of the parameters affecting the normalised model Doppler shift at high-latitude. Figure 6.6 presents the dependence of the normalised model output for the 25 ULF wave events on these seven parameters. Two-tailed t-tests are performed for the data contained within each plot, and printed on the panels for convenience, to test the statistical significance of the PMCC's.

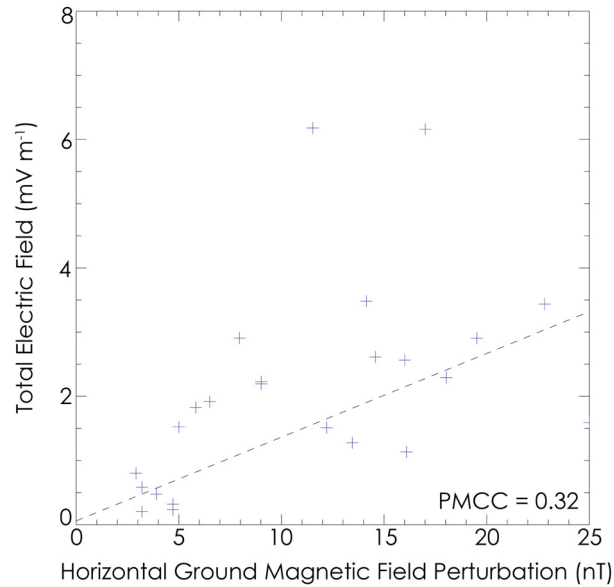
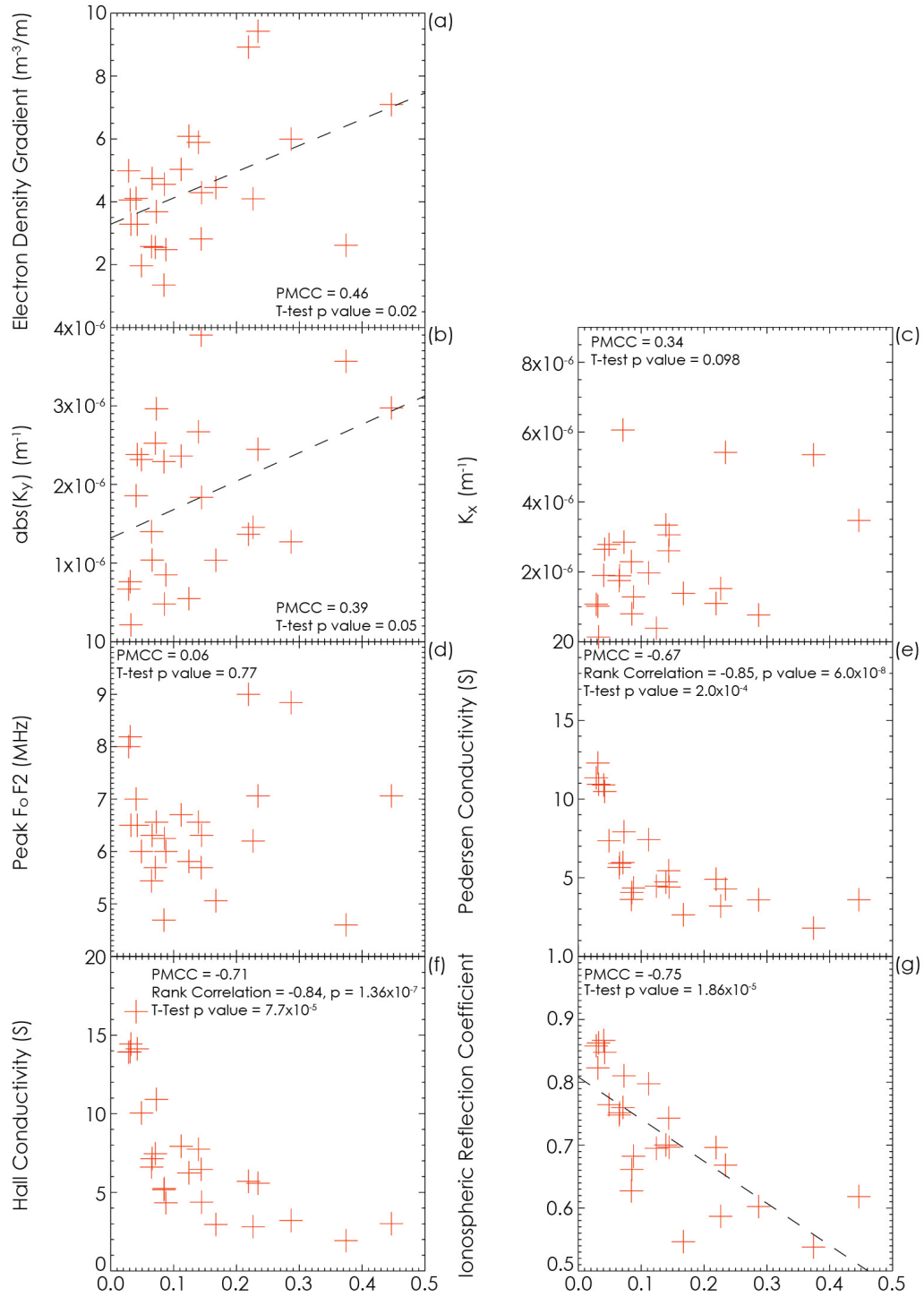


Figure 6.5: Model output statistics showing the dependence of horizontal ground magnetic field perturbation for each event as a function of the total electric field, measured in  $\text{mV m}^{-1}$ .

Panel (a) presents a comparison between the normalised model Doppler shift and the electron density gradient measured at the DOPE reflection altitude for each event. Section 4.3.5 suggests the electron density gradient provides a large contribution to the advection mechanism as can be seen from equation 4.22.

The bulk of the observed electron density gradients are in the range  $2 \text{ m}^{-3}/\text{m}$  to  $6 \text{ m}^{-3}/\text{m}$ . Section 4.3.5 predicts a trebling of the Doppler shift over this range. Panel (a) of Figure 6.6 shows results, which are consistent with the predictions, given the scatter in the data. The p-value from the two-tailed t-test is 0.02 and shows that the results are statistically significant at the 2% significance level.

The Doppler shift contributions of the east-west and north-south wavenumber will now be investigated and compared with predictions based upon the work in section 4.3.5. Panels (b) and (c) of Figure 6.6 show an observed trend for increased normalised Doppler shift as wave scale-size decreases. This trend is as expected, as small-scale waves are attenuated in the ground magnetic field. The trend is, however, weak with a low correlation coefficient. Also, the p-value from the two-tailed t-test is 0.05 and shows that the results are statistically significant at the 5% significance level.



Model Doppler shift normalised by a horizontal ground magnetic field perturbation of 1 nT (Hz)

Figure 6.6: (a – g) Model output statistics showing the dependence of the normalised model Doppler shift on seven different parameters. In each of the panels the model Doppler shift has been normalised for a horizontal ground magnetic field perturbation of 1 nT. Panel (a) presents a comparison with the electron density gradient. Panel (b) east-west wavenumber,  $k_y$ . Panel (c) north-south wavenumber,  $k_x$ . Panel (d) peak  $F_oF2$ . Panel (e) the height integrated Pedersen conductivity. Panel (f) the height integrated Hall conductivity. Panel (g) the ionospheric reflection coefficient

The majority of the 25 ULF wave events have wavenumbers smaller than  $2 \times 10^{-6} \text{ m}^{-1}$  (scale-sizes greater than 3000 km). Section 4.3.5 predicted the Doppler shift to have a negligible dependence on the north-south wavenumber, but a strong dependence on the east-west wavenumber. The range of east-west wavenumbers shown here corresponds to a region, shown in Figure 4.15, where little dependence in Doppler shift was seen. . Therefore, the east-west wavenumber dependence presented here is consistent with theory since only a weak trend is seen.

Section 4.3.5 predicted no dependence on north-south wavenumber whereas Figure 6.6 shows a similar trend in both the azimuthal and meridional scale-sizes. This may be explained by figure 6.1 (e), which shows that in the observed waves  $k_x$  and  $k_y$  are correlated, as might be expected from equation 6.1. There is scatter in the data and the p-value revealed from the two-tailed t-test has a value of 0.098 and shows that the results are statistically significant at the 10% significance level.

Peak FoF2 is another parameter, which might be expected to affect the model Doppler shift. Panel (b) of Figure 4.20 shows the impact that a changing peak FoF2 has on the normalised model Doppler shift. The statistics provide a suitable range of FoF2 to investigate this, but panel (d) of Figure 6.7 shows that the model Doppler shift is not, in fact, ordered by peak FoF2 and the p-value determined from a two-tailed t-test is 0.77, which shows that the results are not statistically significant at the 10% significance level.

Peak FoF2 is expected to indirectly affect the Doppler shift since a change in peak FoF2 affects the conductivities, which in turn affect the ionospheric reflection coefficient. These parameters will now be investigated directly.

The height integrated Pedersen and Hall conductivities clearly affect the Doppler shift. Panels (e) and (f) of Figure 6.6 show the height integrated Pedersen and Hall conductivities as a function of the normalised model Doppler shift indicating a very strong correlation between the parameters with PMCCs of -0.67 and -0.71, respectively. However, since these parameters are non-linear a more robust analysis involves using a rank correlation coefficient. The rank correlation coefficient for the Pedersen and Hall conductivity variations with model Doppler shift are -0.85 and -0.84, respectively, indicating a high

statistical dependence. The corresponding p-values determined from two-tailed t-tests performed on both of these datasets are very small ( $2 \times 10^{-4}$  and  $8 \times 10^{-5}$ , respectively) indicating a high statistical significance for both of these parameters with the normalised model Doppler shift.

Similarly to the east-west and north-south wavenumbers, the height integrated Hall and Pedersen conductivities are correlated in a real ionosphere. Therefore, the similar distributions of these two parameters with the normalised model Doppler shift, shown in panels (e) and (f) of Figure 6.7, are expected.

Equation 2.32 revealed that the height integrated Pedersen conductivity determines the reflection coefficient of the ionosphere. The top boundary of the 1-D numerical model contains both Alfvénic and compressional modes. The total electric field is composed of both downward and upward components of these two modes. The incident and reflected fast mode proportions at the top boundary are denoted by  $\beta_I$  and  $\beta_R$ , and will not be considered further.  $\alpha_I$  and  $\alpha_R$  are the incident and reflected shear mode proportions at the top boundary, where the Poynting flux is directed towards and away from the Earth, respectively. The ratio of  $\alpha_R$  to  $\alpha_I$  yields the ionospheric reflection coefficient. As has already been explained, the reflection coefficient modifies the electric field within the ionosphere and is, therefore, an important parameter affecting the recorded Doppler shift. The range of the ionospheric reflection coefficient in the 25 events studied here is 0.6 - 0.9. Using this range, and Figure 4.20, yields a predicted decrease in the normalised Doppler shift from 0.2 Hz/nT to 0.05 Hz/nT. The corresponding predicted gradient in the normalised Doppler shift with the ionospheric reflection coefficient is - 0.5 Hz nT<sup>-1</sup>. The gradient for the corresponding normalised model data presented in panel (g) of Figure 6.7 is approximately - 1.6 Hz nT<sup>-1</sup>. A two-tailed t-test performed on the data contained in panel (g) reveals a p-value of approximately  $2 \times 10^{-5}$ , which shows the result is significant at the 5% significance level.

Therefore, the dependence of normalised Doppler shift on the ionospheric reflection coefficient predicted in section 4.3.5 are in reasonable agreement with the results from the 25 events presented here, given the scatter in the data.

## 6.4.2 Normalised Observed Doppler Shift

A similar comparison as conducted with the normalised modelled data may be undertaken for the observational data from the 25 high-latitude ULF wave events studied here. The predictions, as outlined in section 4.3.5, are once again applied. Figure 6.7 presents observed statistics of the dependence of the observed normalised Doppler shift for seven parameters.

Panel (a) of Figure 6.7 presents a comparison between the normalised observed Doppler shift and the electron density gradient measured at the DOPE reflection altitude, for each event, and shows that the two parameters are weakly correlated, with a gradient of  $0.15 \text{ nT}^{-1}/\text{m}^{-3}/\text{m}$ . Also, the p-value from the two-tailed t-test is 0.29 and shows that the results are not statistically significant at the 10% significance level. Therefore, the prediction partially agrees with experimental observation but there is a lot of scatter in the data. Panels (b) and (c) show the absolute values of the east-west and north-south wavenumbers as a function of the normalised observed Doppler shift. Panels (b) and (c) show almost no trend between the azimuthal and meridional scale-sizes and the Doppler shift. Also, the p-values from the two-tailed t-tests are 0.9 and 0.85 and show that the results are not statistically significant at the 10% significance level. These results are consistent with the predictions of chapter 4. Panel (d) of Figure 6.7 shows the dependence of peak FoF2 on the normalised observed Doppler shift and suggests a reasonable correlation. Also, the p-value from the two-tailed t-test is 0.2 and shows that the results are statistically significant at the 20% significance level. Therefore, the results are not significant at the 10% significance level. There is once again a lot of scatter. Unfortunately, the sign is not what is predicted and so the results for this parameter do not agree with experimental observation. FoF2 is expected to affect the Doppler shift only in that it affects the conductivities, and in turn the reflection coefficient, so as for the model normalised Doppler shift, these parameters will now be considered. Panel (e) shows the height integrated Pedersen conductivity as a function of the normalised observed Doppler shift and also indicates a very weak correlation between the two parameters. The p-value, from the two-tailed t-test, is 0.28 and shows that the results are statistically significant at the 28% significance level,

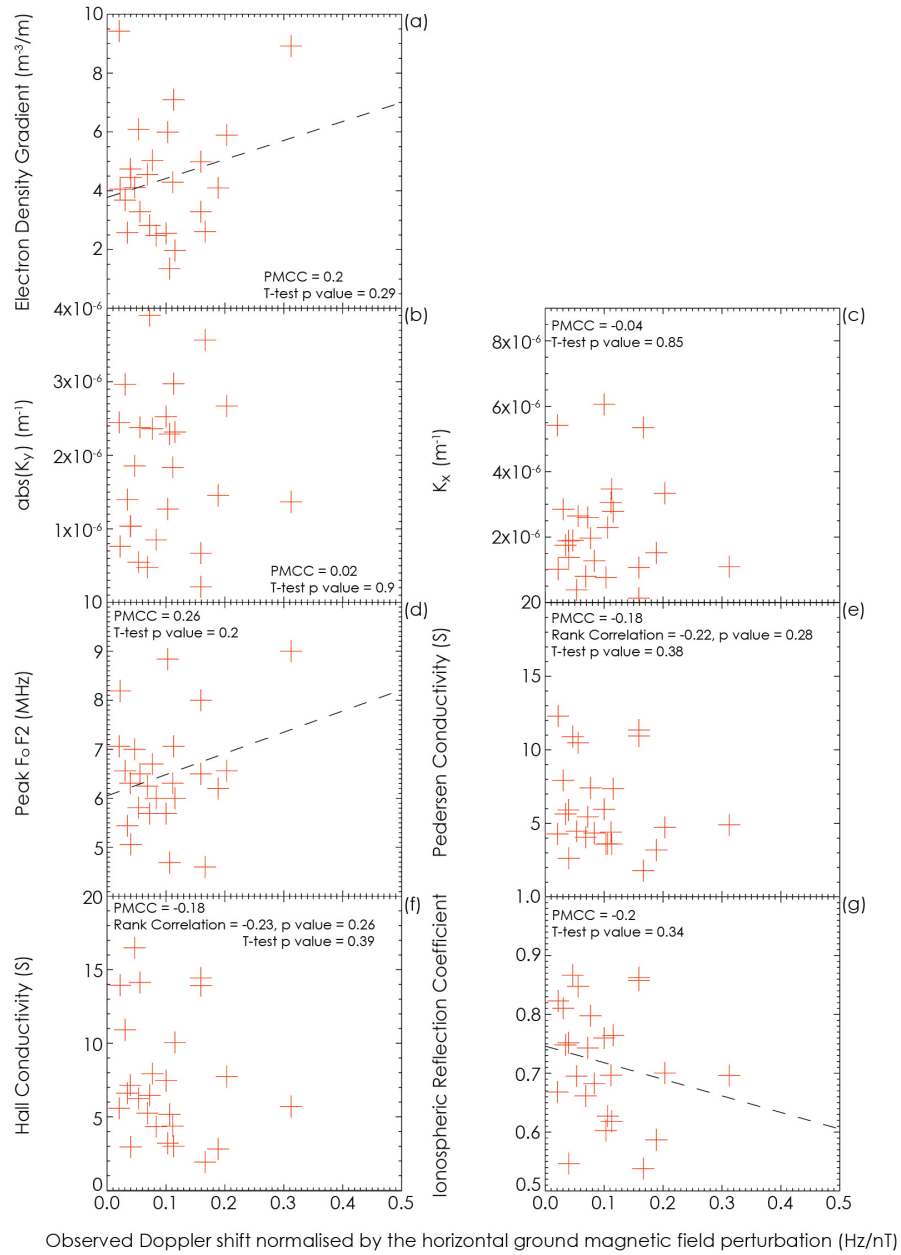


Figure 6.7: **(a – g)** Observational statistics showing the dependence of the observed normalised Doppler shift on seven different parameters. In all panels the observed Doppler shift has been normalised by the horizontal magnetic field perturbation measured on the ground. Panel (a) presents a comparison with the electron density gradient. Panel (b) east-west wavenumber. Panel (c) north-south wavenumber. Panel (d) peak FoF2. Panel (e) the height integrated Pedersen conductivity. Panel (f) the height integrated Hall conductivity. Panel (g) the ionospheric reflection coefficient.

but that the results contain a lot of scatter resulting in the data not being significant at the 10% significance level. Panel (f) shows the height integrated Hall conductivity as a function of the normalised observed Doppler shift indicating a very weak correlation between the two parameters. The p-value from the two-tailed t-test is 0.26 and shows that the results are statistically significant at the 26% significance level, but that the results also contain a lot of scatter resulting in the data not being significant at the 10% significance level. This parameter, therefore, partially agrees with experimental observation given scatter. Panel (g) of Figure 6.7 presents the effect of the ionospheric reflection coefficient on the normalised observed Doppler shift and shows a weak dependency between the parameters with a gradient of  $-3.4 \text{ nT}^{-1}$ . The p-value from the two-tailed t-test is 0.34 and shows that the results are statistically significant at the 34% significance level, but clearly not significant at the 10% significance level, which is expected due to the high levels of scatter.

Overall, the results of the normalised observed Doppler shift look similar to the normalised model Doppler shift shown in section 6.4.1 but with the quality of the correlations weakened in each case due to scatter.

### 6.4.3 Conductivity Effects on Doppler Shift

The height integrated Hall and Pedersen conductivities are investigated in more detail here to ascertain their importance, relative to the electron density gradient, in determining the normalised Doppler shift.

Removing the height integrated Pedersen conductivity effects on the Doppler shift provides a means of investigating whether the electron density gradient, as shown in panel (a) of Figure 6.6, still provides a large contribution to the Doppler shift. Panel (a) of Figure 6.8 presents model output statistics showing the Doppler shift,  $V^*$ , normalised by a horizontal magnetic field perturbation of 1 nT, but additionally normalised with respect to the height integrated Pedersen conductivity, as a function of the electron density gradient. Panel (a) shows that there is a correlation between the electron density gradient and the model normalised Doppler shift with the height integrated Pedersen conductivity depen-

dence removed. However, removing the height integrated Pedersen conductivity does not improve the correlation.

Panel (b) of Figure 6.8 presents the model Doppler shift normalised according for a ground magnetic field perturbation of 1nT as a function of the height integrated Pedersen conductivity normalised by the electron density gradient. Panel (b) shows that there is a good negative correlation between the height integrated Pedersen conductivity and the model normalised Doppler shift with the electron density contribution removed. Removing the electron density contribution again does not improve the correlation.

Panel (a) of Figure 6.9 presents the ionospheric reflection coefficient as a function of the height integrated Pedersen conductivity and shows a good correlation between these two parameters. Panel (b) of Figure 6.9 presents the height integrated Pedersen conductivity as a function of the integrated Hall conductivity for each of the 25 ULF wave signatures and indicates a near perfect positive correlation between these two parameters (PMCC = 0.98). Calculating the ionospheric reflection coefficient using the height integrated Pedersen conductivities determined here provides a near perfect reproduction of the ratio of  $\alpha_R$  to  $\alpha_I$ . The normalised Doppler shift is best ordered by the ionospheric reflection coefficient, and this in turn is well predicted by the height integrated Pedersen conductivity.

## 6.5 Doppler Shift Phase

Figure 6.10 presents model output statistics showing the observed phase difference, between DOPE and TRO, as a function of the relative phase difference for the advection mechanism to the model  $B_x$ . Only the advection mechanism is considered here as the overall Doppler shift phase closely matches the advective phase.

As in Sutcliffe and Poole (1990), the model  $B_x$  phase has been set at zero when calculating the phase differences except that here they are defined as  $B_x$  and  $B_y$  leading in order to match the observational study conducted by Wright et al. (1997). The model phase difference is calculated in this way to see if the model Doppler shift phases, for a purely shear Alfvénic incident wave, match those observed by the HF Doppler sounder. Panel

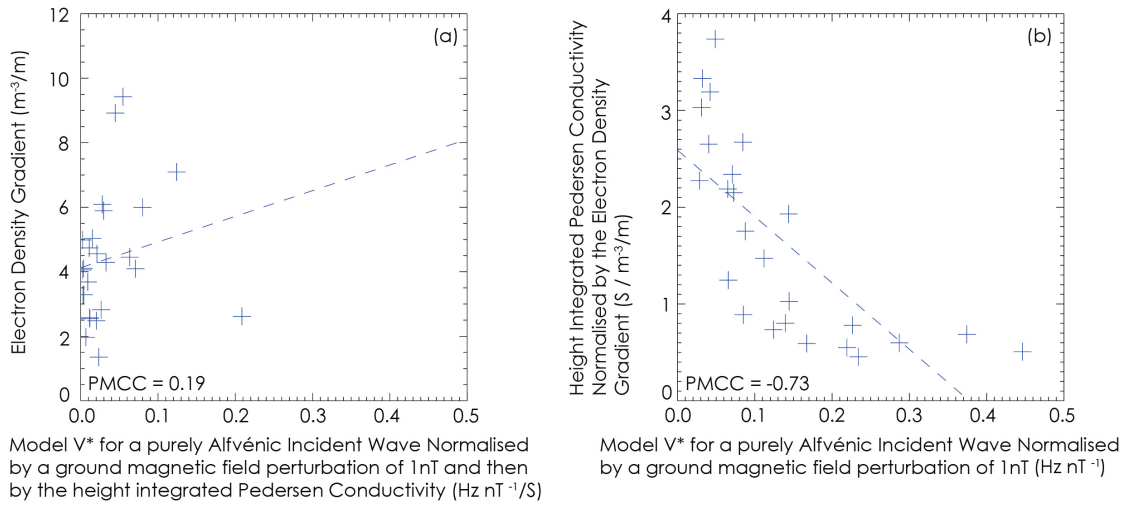


Figure 6.8: **(a and b)** Model output statistics. Panel (a) shows the model Doppler shift normalised for a horizontal ground magnetic field perturbation of 1 nT, and subsequently normalised by the height integrated Pedersen conductivity, as a function of the electron density gradient. Panel (b) presents the normalised model Doppler shift as a function of the height integrated Pedersen conductivity normalised by the electron density gradient.

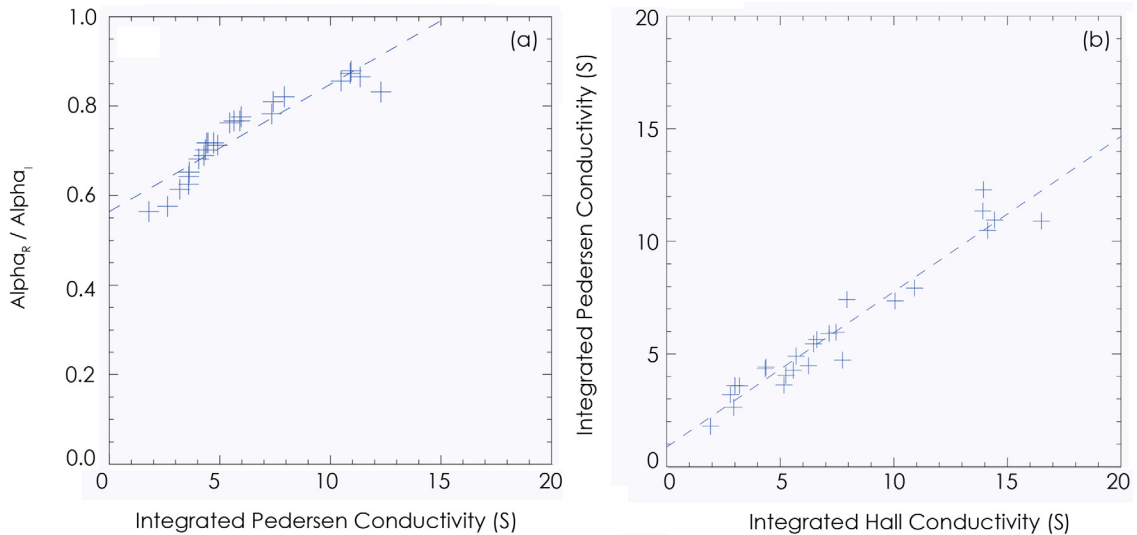


Figure 6.9: **(a and b)** Model output statistics. Panel (a) shows the amplitude ratio of the incident Alfvén mode to the reflected component as a function of the height integrated Pedersen conductivity. Panel (b) presents the height integrated Pedersen conductivity as a function of the height integrated Hall conductivity.

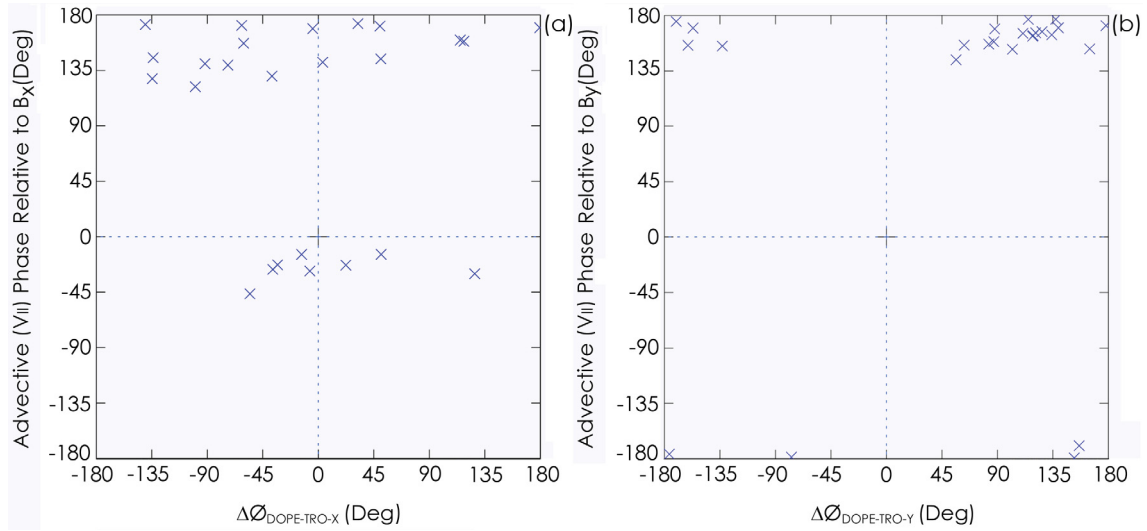


Figure 6.10: **(a and b)** Model output statistics showing the observed phase difference between DOPE and TRO as a function of the relative phase difference for the advection mechanism to a model  $B_x$  of zero phase. Panel (a) presents the observed phase difference between DOPE and TRO-X as a function of the relative phase difference for the advection mechanism. Panel (b) presents the observed phase difference between DOPE and TRO-Y as a function of the relative phase difference for the advection mechanism.

(a) of Figure 6.10 presents the observed phase difference between DOPE and TRO-X as a function of the relative phase difference for the advection mechanism. Panel (a) shows that the observed DOPE - TRO-X phase difference may take essentially any value due to the variability of this phase with latitude. The corresponding relative Doppler shift phases are structured suggesting model limitations. Panel (b) of Figure 6.10 presents the observed phase difference between DOPE and TRO-Y as a function of the relative phase difference for the advection mechanism.

In sections 4.3.2 and 4.3.3 of this thesis, the results of the model developed by Sciffer et al. (2005), which may be run at any geographic location, were used to analyse the conclusions and extrapolations made by Wright et al. (1997) whose results were detailed in section 2.7.3. Panel (d) of Figure 4.4 showed that advection would have been suggested as the explanation for the relative phase change had the Sciffer et al. (2005) 1-D numerical model been available for mid-latitudes since the mid-latitude results are consistent in the new and old model runs. However, as panel (b) of Figure 4.7 revealed previously, the phases are different when the new numerical model is run at high-latitude.

The question as to what the relative Doppler shift phases will be at high-latitudes is answered here using wave characteristics typical of FLRs at high-latitude. Panel (b) of Figure 6.10 shows that the 25 high-latitude ULF wave events show some ordering. The majority of events are ordered between  $135^\circ$  -  $180^\circ$ , agreeing with the conclusions of Wright et al. (1997). This population of events suggests that while there are still limitations, the model does appear to have the capability to predict the relative phase between the Y component of the ground magnetic field and HF Doppler signatures recorded by DOPE for both eastwards and westwards propagating events.

## 6.6 Analysis of Incident Wave Mode

As outlined in section 5.4.1, the incident wave mode may be calculated by optimising the match between the model Doppler shift and the observed Doppler shift by choosing a suitable value of the incident Alfvénic to fast mode wave mix.

Figure 6.3 showed that for all 25 ULF wave events the model predicts that advection is the dominating mechanism contributing to the overall Doppler shift for a purely shear Alfvénic incident wave. In Figure 6.11 this analysis is repeated when the 25 events have been corrected for wave mix. It is clear that the model predicts that advection remains the dominant mechanism contributing to the overall Doppler shift when the mode mix of the incident wave is matched to provide a model Doppler shift which best matches observation.

In order to see whether some of the scatter in Figures 6.6 and 6.7 is the result of not correcting for the incident wave mode, here, the analysis is repeated for the subset (of 13) events where the predicted incident wave mix is 0.95 or greater and the events which lie just below the  $y = x$  line in Figure 6.4. Figure 6.12 presents results for modelled Doppler shift.

Panel (a) of Figure 6.12 presents a comparison between the normalised Doppler shift and the electron density gradient measured at the DOPE reflection altitude for each event and shows that the two parameters are strongly correlated. The correlation is statistically

significant at the 5% significance level since the two-tailed t-test p-value is 0.034. Panels (b) and (c) show the absolute values of the east-west and north-south wavenumbers as a function of the normalised Doppler shift. Panels (b) and (c) show almost no trend between the azimuthal and meridional scale-sizes and the Doppler shift, agreeing with the predictions of chapter 4. The two-tailed t-test p-values of 0.9 and 0.62, respectively, reveal that the results from these panels are not statistically significant at the 10% significance level.

Panel (d) of Figure 6.12 shows the dependence of peak FoF2 on the normalised Doppler shift and suggests a reasonable correlation. But the correlation is not statistically significant at the 10% significance level indicated by the two-tailed t-test p-value of 0.43. Panel (e) shows the height integrated Pedersen conductivity as a function of the normalised Doppler shift and also indicates a very strong negative correlation between the two parameters. This result is also significant at the 5% significance level with a two-tailed t-test p-value of 0.014. Therefore, this parameter also agrees with the predictions of section 4.3.5. Panel (f) shows the height integrated Hall conductivity as a function of the normalised Doppler shift indicating a very strong negative correlation between the two parameters. This result is also significant at the 1% significance level with a two-tailed t-test p-value of 0.01. This parameter does, therefore, agree with the predictions of chapter 4. Finally, panel (g) of Figure 6.12 presents the effect of the ionospheric reflection coefficient on the normalised Doppler shift and shows a very strong negative dependency between the parameters with a PMCC of - 0.71. This result is also significant at the 1% significance level with a two-tailed t-test p-value of approximately 0.01. Therefore, prediction matches experimental observation.

The results of the normalised Doppler shift for the subset of 13 events where the predicted incident wave mix is 0.95 or greater and where the events lie just below the  $y = x$  line in Figure 6.4 look similar to the normalised model Doppler shift shown in section 6.4.1.

Figure 6.11 shows that the incident wave mode does not affect the dominant mechanism (advection), and hence does not affect the phase relationships a great deal as presented in Figure 6.10. Indeed, most of the events presented here would be classified as predom-

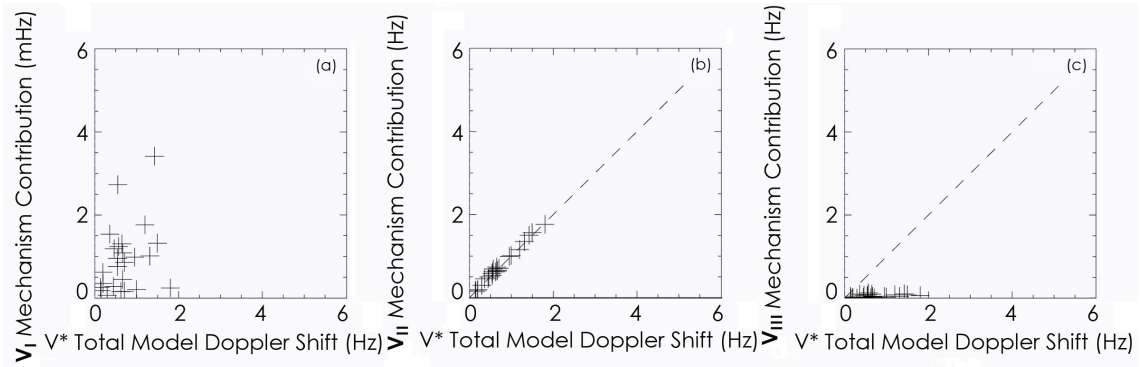


Figure 6.11: **(a – c)** Model output statistics showing the individual Doppler shift mechanism contributions to the overall Doppler shift when the incident wave mode is matched to provide a model Doppler shift which best matches observation. Panel (a) presents the total model Doppler shift, in Hz, as a function of the magnetic mechanism,  $V_I$ , in mHz. Panel (b) presents the total model Doppler shift, in Hz, as a function of the advection mechanism,  $V_{II}$ , in Hz. Panel (c) presents the total model Doppler shift, in Hz, as a function of the compressional mechanism,  $V_{III}$ , in Hz.

inantly Alfvénic with 20 out of the 25 having incident wave modes of greater than 0.8. However, it is clear from the results that the incident wave mode has a significant effect on the overall ratio of Doppler shift per nT as highlighted by Figure 6.12.

A likely candidate for providing the incident wave mode could be how close the ULF wave event is to the FLR and basic occurrence statistics for this are shown in panel (g) of Figure 6.1.

The panel shows the DOPE distance from the resonant Gaussian peak of the latitudinal power profiles for each event. A Gaussian function was fitted to each latitudinal power profile, such as panel (a) of Figure 5.5 shows with the overlaid solid red line. The peak of this Gaussian provides a resonant latitude. The distance of the resonant Gaussian peak from the HF Doppler sounder, located at Tromsø, is given in units of sigma or the number of HWHM (Half Width Half Maxima). Negative and positive values of sigma indicate that resonance is equatorward and poleward of the HF Doppler sounder, respectively.

To identify the relative location of the incident wave mode on the ionosphere to the HF Doppler sounder, which causes the ground and ionospheric ULF wave signatures for each event, the sigma distance, as shown previously in panel (g) of Figure 6.1, is plotted as a function of the incident wave mode. Figure 6.13 presents the DOPE sigma distance from

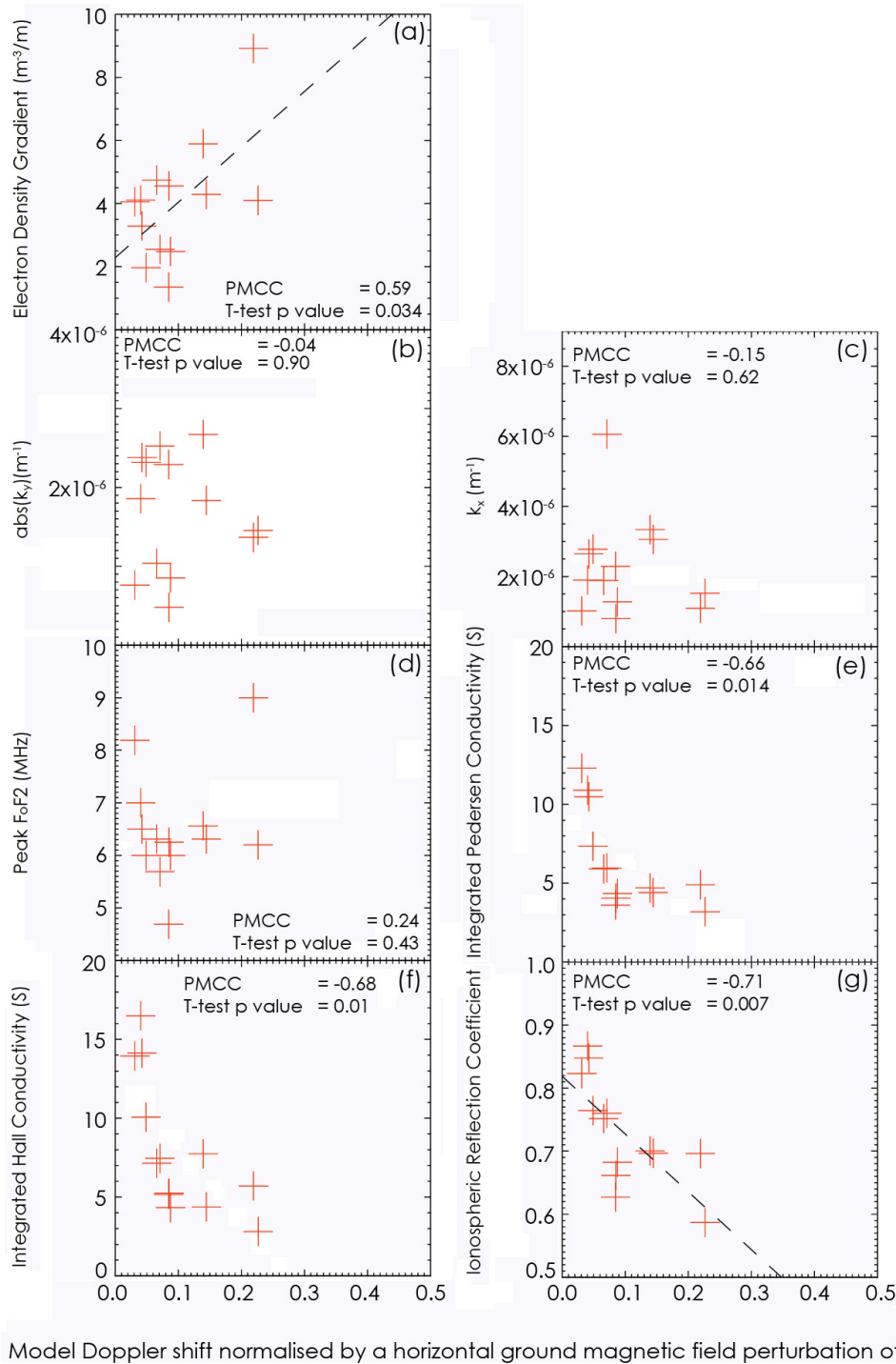


Figure 6.12: (a – g) Model output statistics showing the dependence of the normalised model Doppler shift on seven parameters for the subset of 13 events which have incident wave modes of greater than 0.95. In each of the panels the model Doppler shift has been normalised for a horizontal ground magnetic field perturbation of 1 nT. Panel (a) presents a comparison with the electron density gradient. Panel (b) east-west wavenumber,  $k_y$ . Panel (c) north-south wavenumber,  $k_x$ . Panel (d) peak FoF2. Panel (e) the height integrated Pedersen conductivity. Panel (f) the height integrated Hall conductivity. Panel (g) the ionospheric reflection coefficient.

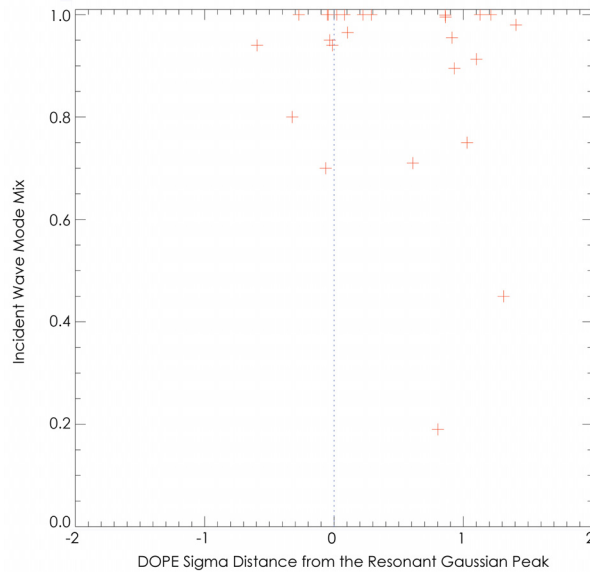


Figure 6.13: DOPE sigma distance from the resonant Gaussian peak as a function of incident wave mode found by matching the model Doppler shift to the observed Doppler shift at the DOPE reflection altitude.

the resonant Gaussian peak as a function of incident wave mode found by matching the model Doppler shift to the observed Doppler shift at the DOPE reflection altitude.

Figure 6.13 shows at high-latitudes most incident wave modes are high (greater than 0.8), and that these are not ordered by proximity to the resonance. The incident wave mode, therefore, appears to be a characteristic of the wave determined by some other factor, perhaps a characteristic of the driving source.

## 6.7 Discussion and Summary

In this chapter, a numerical one-dimensional model developed by Sciffer et al. (2005) has been employed to account for the observed relationship between the Doppler velocity oscillations of reflected radio waves from the ionosphere and geomagnetic pulsations. 25 geomagnetic pulsation events measured by the DOPE system, the IMAGE magnetometer array, and the Tromsø dynasonde, between January 1998 and September 2003 have been presented. The effect of the modelled incident wave field on an HF radio path is calculated, and compared to observation. Ground magnetic field and Doppler observa-

tions are used to find model inputs for each event. The contributing factors controlling the Doppler shift are investigated by normalising the Doppler shift relative to a horizontal ground magnetic field perturbation of 1 nT. For the ensemble of high-latitude events under investigation here, it has been demonstrated that the advection mechanism is the dominant process leading to HF Doppler frequency variations, and that a reasonable agreement between observed and model Doppler shifts is provided by this mechanism. This agreement is significantly improved if the incident wave mix is varied. When an incident fast mode is introduced the model Doppler shift is reduced, and this acts to maximise agreement between model and observation where the model Doppler shift for a purely Alfvénic mode exceeds observation. Even under these conditions it has been shown that advection remains the dominant Doppler shift mechanism. The effects of the prevailing ionospheric conditions on the modelled and observed Doppler shifts have been investigated in detail. Overall, the model dependencies shown in Figure 6.6 and in Figure 6.12 are largely consistent with the tests conducted in section 4.3.5. Figure 6.6 showed that most of the 25 ULF wave events studied here have electron density gradients of between  $2 \text{ m}^{-3}/\text{m}$  to  $6 \text{ m}^{-3}/\text{m}$ . The predictions of chapter 4 predict a trebling of the Doppler shift over this range and Figures 6.6, 6.7 and 6.12 are consistent with this. Equation 4.26 showed how important the electron density gradient is in determining the amplitude of the advection mechanism. It is, therefore, no surprise here that, since 20 out of the 25 events can be classed as almost purely Alfvénic incident modes, the electron density gradient has a significant influence on the resulting Doppler shift. Section 4.3.5 predicted the Doppler shift to have a negligible and strong dependence on the north-south and east-west wavenumbers, respectively. The majority of the 25 ULF wave events investigated here have wavenumbers smaller than  $2 \times 10^{-6} \text{ m}^{-1}$ . At these scale-sizes their effect on the observed Doppler shift is not expected to be large, as first shown in Figures 4.17 and 4.15. No convincing trend for Doppler shift is seen in Figures 6.6, 6.7 and 6.12. Panels (b) and (c) of Figure 6.6 and the same panels of Figure 6.12 show a similar trend in both the azimuthal and meridional scale-sizes, which was not predicted in chapter 4. This may be explained by equation 6.1, which showed that  $k_x$  and  $k_y$  are related through the ratio of the X and Y components

of the ground magnetic field. The analysis presented in chapter 4 predicted a strong influence on Doppler shift from peak FoF2, ionospheric conductivity and the ionospheric reflection coefficient. However, for the events under study here the Doppler shift does not appear to be strongly ordered by peak FoF2 as shown in panel (d) of Figures 6.6, 6.7 and 6.12. The height integrated Pedersen and Hall conductivities, however, show a strong negative correlation with the Doppler shift as shown in panels (e) and (f) of Figures 6.6 and 6.12, respectively. Such a relationship is expected, as the height integrated Pedersen conductivity controls the ionospheric boundary condition on the wave electric field. In a realistic ionosphere the height integrated Hall and Pedersen conductivities are themselves strongly correlated, as was shown in panel (b) of Figure 6.9. As described above, the ionospheric conductivity determines the electric field within the ionosphere, determining the reflection coefficient and is, therefore, expected to have a profound influence on the observed Doppler shift. Panel (a) of Figure 6.9 showed the strong correlation between the height integrated Pedersen conductivity and the ionospheric reflection coefficient, as is expected by equation 2.32. The effect of the ionospheric reflection coefficient on Doppler shift is examined directly in panel (g) of Figure 6.6. This panel shows the strongest correlation with normalised Doppler shift. Thus, the normalised Doppler shift is best ordered by the ionospheric reflection coefficient, and this in turn is well predicted by the height integrated Pedersen conductivity. This chapter has shown that the advection mechanism is contributing the most to the overall Doppler shift at high-latitudes for these 25 events, agreeing with previous studies of large spatial scale ULF waves (e.g., Wright et al., 1997, 1998; Waters et al., 2007; Borderick et al., 2010). The phase relationships shown within this chapter also agreed with previous work by Wright et al. (1997) since panel (b) of Figure 6.10 showed that the majority of the 25 high-latitude ULF wave events were ordered with relative phases between  $135^\circ$  -  $180^\circ$ . This is the first time that observed and modelled wave phase have been compared for a model run under the appropriate ionospheric conditions, and suggests that the model wave phase can provide a meaningful wave diagnostic. Section 6.6 showed that when the incident wave mode is accounted for, and matched for each event, the phase relationship is unaffected since 20 of the 25 events may

be classed as purely Alfvénic with incident wave modes of 0.8 or greater. Figure 6.13 has shown that most events are almost purely Alfvénic and are not ordered by the proximity to resonance indicating that the incident wave mode is determined by some other parameter, such as a characteristic of the driving source. Thus, the incident wave mode is an important parameter in accurately matching the observed and model Doppler shifts, but does not significantly affect the dominant Doppler mechanism or the relative phase between the Doppler and magnetic field wave signatures, at least for the high-latitude, large-scale waves under investigation here.

# Chapter 7

## Double-Pulse Operations with the Super Dual Auroral Radar Network

### 7.1 A Case for a Greater Super Dual Auroral Radar Network Temporal Resolution

Panels (a) and (b) of Figure 4.8 presented CUTLASS, Hankasalmi data showing a ULF wave signature, which was recorded on beam 5 on 29 December 2001 between 04:00 UT - 05:00 UT. The wave may be identified by plotting data from a single range gate as panel (b) clearly shows. Unfortunately, the temporal resolution of the data presented in panels (a) and (b) of Figure 4.8) is 120 s and is not entirely satisfactory for the study of ULF waves. Typical Pc5 high-latitude ULF waves detailed previously in chapters 5 and 6 this thesis have periods of between 200 s - 500 s. Therefore, higher resolution instrumentation would be advantageous for observing the fine-structure of these pulsations and for an accurate determination of e.g. the wave phase. One method, which can increase the temporal resolution of the SuperDARN radar, is to change the transmitted pulse sequence. A suggested pulse sequence is one that contains a set of three double-pulses in the place of the standard 7 unequally spaced pulses. The backscatter lag zero power and the Doppler velocity may be determined when using a single pair of pulses. A sequence of such pairs the same length as a multi-pulse sequence, thus, increases temporal resolution at the

expense of forming an ACF and, hence, obtaining the resulting spectral width information. This chapter details the implementation of such a pulse scheme on the Hankasalmi CUTLASS radar. To begin with, the chapter emulates the double-pulse sequence on the SuperDARN radar by using the zeroth and first lags in the standard SuperDARN multi-pulse mode (shown in Figure 3.3 as lag 0 and lag 1, respectively) to predict what might be observed experimentally with a true double-pulse. The second half of the chapter details the implementation of the double-pulse mode on channel B of the Hankasalmi CUTLASS radar, while simultaneously, in stereo (Lester et al., 2004), the standard SuperDARN multi-pulse sequence is implemented on channel A.

## 7.2 Emulation of Double-Pulse Operations

The ionospheric plasma convection velocity,  $V_{DP}$ , for a double-pulse scheme with a radar transmission frequency,  $f_{rad}$ , may be expressed in terms of the speed of light,  $c$ , as

$$V_{DP} = \frac{c}{4\pi f_{rad}} \left( \frac{\phi_1 - \phi_0}{t_1 - t_0} \right), \quad (7.1)$$

where  $t_0$  and  $t_1$  are the times associated with the zeroth and first lags, respectively, and  $\phi_0$  and  $\phi_1$  are the phases associated with  $t_0$  and  $t_1$ , respectively. The Doppler velocity may, therefore, be determined from the calculated phase difference of the first lag. Referring to Figure 3.3, the phase associated with the first lag corresponds to the phase difference between pulses 6 and 7. Data are used from these two lags, obtained from the raw ACF data, and subsequently compared to the velocities obtained from the corresponding fitted data.

### 7.2.1 Emulated Ionospheric Scatter Results

Ionospheric scatter has, characteristically, fast decorrelation times and high ionospheric plasma convection velocities, which are normally  $\geq 50 \text{ m s}^{-1}$ . Range Time Intensity (RTI) plots are a useful way of presenting data from SuperDARN.

Figure 7.1 shows a comparison between the standard SuperDARN fitted velocities and the emulated Double-Pulse Velocities (DPVs) for 0.5 hop ionospheric scatter and presents two RTI plots recorded between 30 May 2006 at 20:00 UT to 31 May 2006 at 06:00 UT. Blue and red indicate strong ionospheric plasma flow towards and away from the radar, respectively. Panel (a) of Figure 7.1 presents standard SuperDARN fitted velocity data from the Hankasalmi CUTLASS radar while panel (b) shows the emulated DPV data calculated over the same time-period. The data used to calculate the emulated DPVs were selected from only "good-lags" as determined from the standard SuperDARN fit routines. The emulation of a double-pulse experiment yields ionospheric convection velocities that are similar to those determined by the standard SuperDARN routines. In total, there are 6561 and 4385 good data points of ionospheric scatter for the standard SuperDARN data and the emulated DPV data, respectively. Fewer data points are recorded for the emulated DPV compared with the standard SuperDARN data because if the first lag is determined to be "bad" then the emulated DPV is not calculated.

Figure 7.1 suggests that using only two pulses from a single sequence lowers the standard amount of data by approximately 33%. This would imply that a single double-pulse would reduce the data coverage. However, if there are a set of three double-pulses (implying  $\sim 1,300$  points per hour) then the amount of data would be  $\sim 50\%$  greater than SuperDARN currently provides.

Examples are presented here of a good and bad emulated DPV result. Panel (a) of Figure 7.2 presents the phase of the ACF measured along beam 9 at range gate 42 at 03:02:18 UT on 31 May 2006. The fitted SuperDARN and DPV phase are shown by the overlaid dashed blue and solid red lines, respectively. The double-pulse fitted phase is calculated from only the zeroth and first lags. The double-pulse phase, in this example, shows reasonable agreement with the standard SuperDARN fitted phase. Panels (b) and (c) present the complex ACF and the velocity distribution, respectively.

Sometimes the DPV phase and the SuperDARN fitted phase are poorly correlated. Panel (a) of Figure 7.3 presents an example of this by measuring the phase of the ACF along beam 9 at range gate 42 at 03:13:19 UT on 31 May 2006. Once again, the fitted Super-

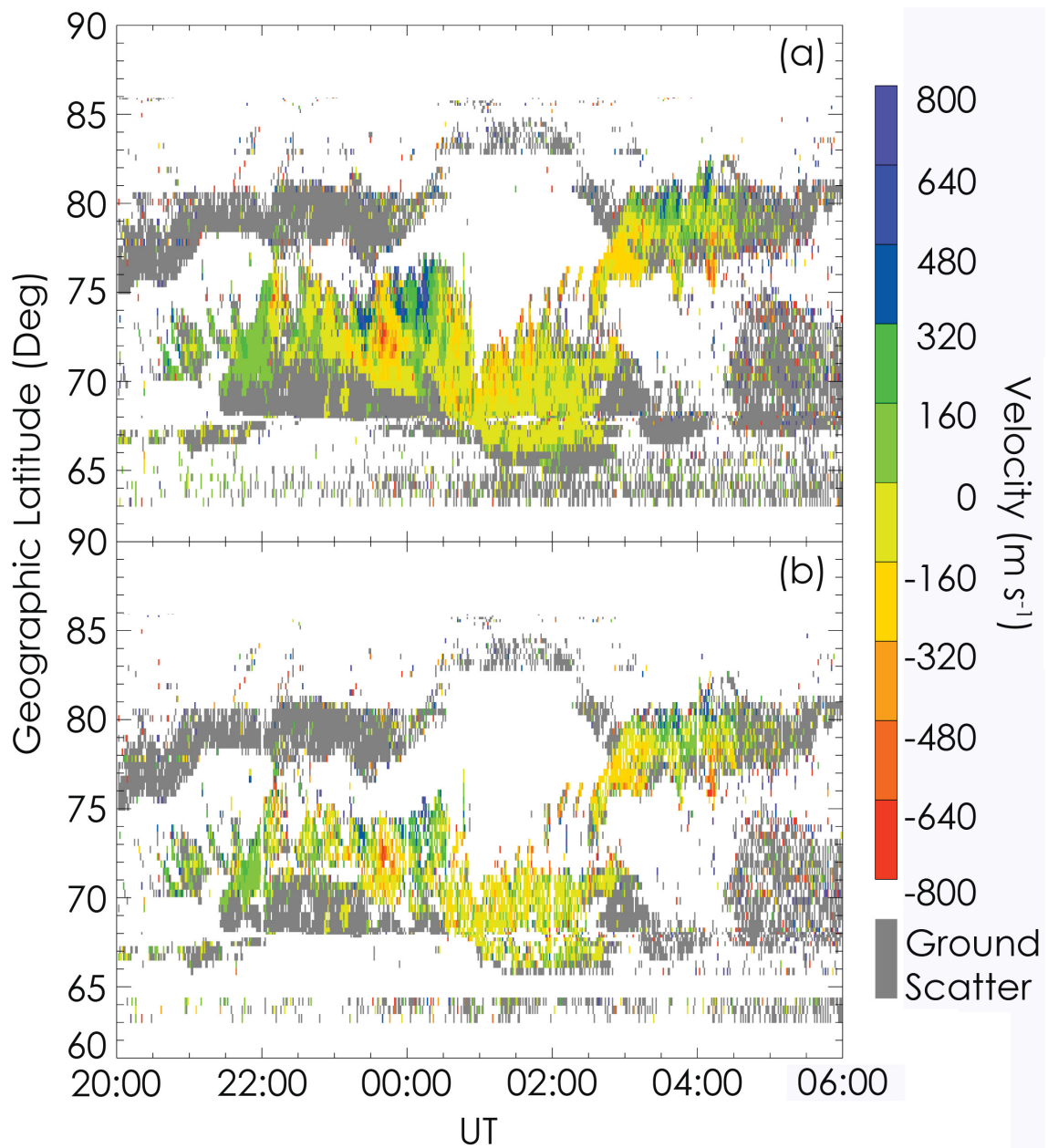


Figure 7.1: **(a and b)** An RTI plot recorded between 30 May 2006 at 20:00 UT to 31 May 2006 at 06:00 UT. Panel (a) presents the standard SuperDARN fitted velocity from Hankasalmi, Finland. Panel (b) shows the emulated Double-Pulse Velocity (DPV) over the same period as panel (a). Blue and red indicate strong ionospheric plasma flow towards and away from the radar, respectively. Ground scatter has been coloured grey in both panels.

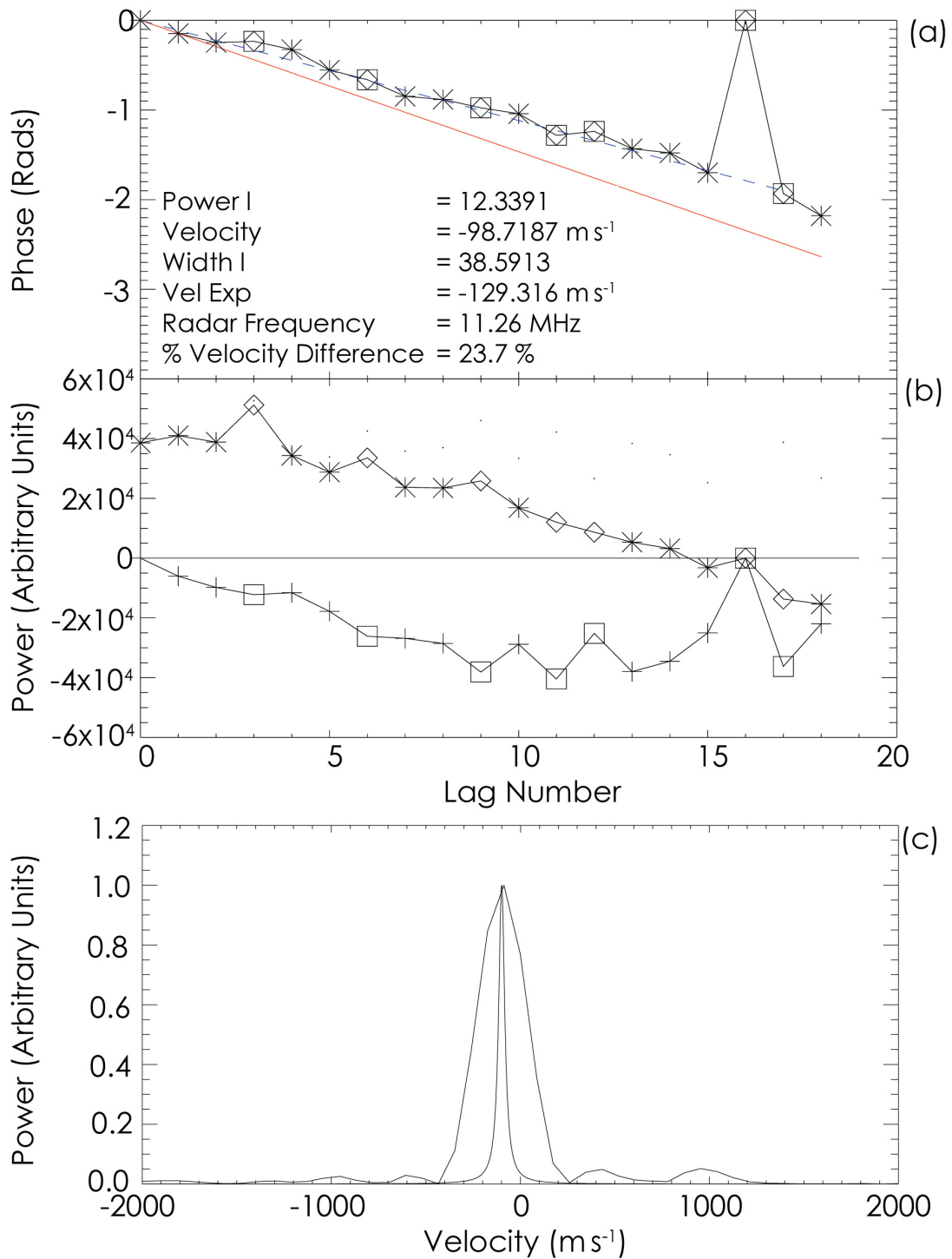


Figure 7.2: (a – c) An example of a correlated DPV fitted phase. Panel (a) presents the phase of the ACF measured along beam 9 at range gate 42 at 03:02:18 UT on 31 May 2006 by the SuperDARN radar at Hankasalmi, Finland. The fitted SuperDARN and DPV phase are shown by the overlaid dashed blue and solid red lines, respectively. Panels (b) and (c) show the complex ACF and the velocity distribution, respectively.

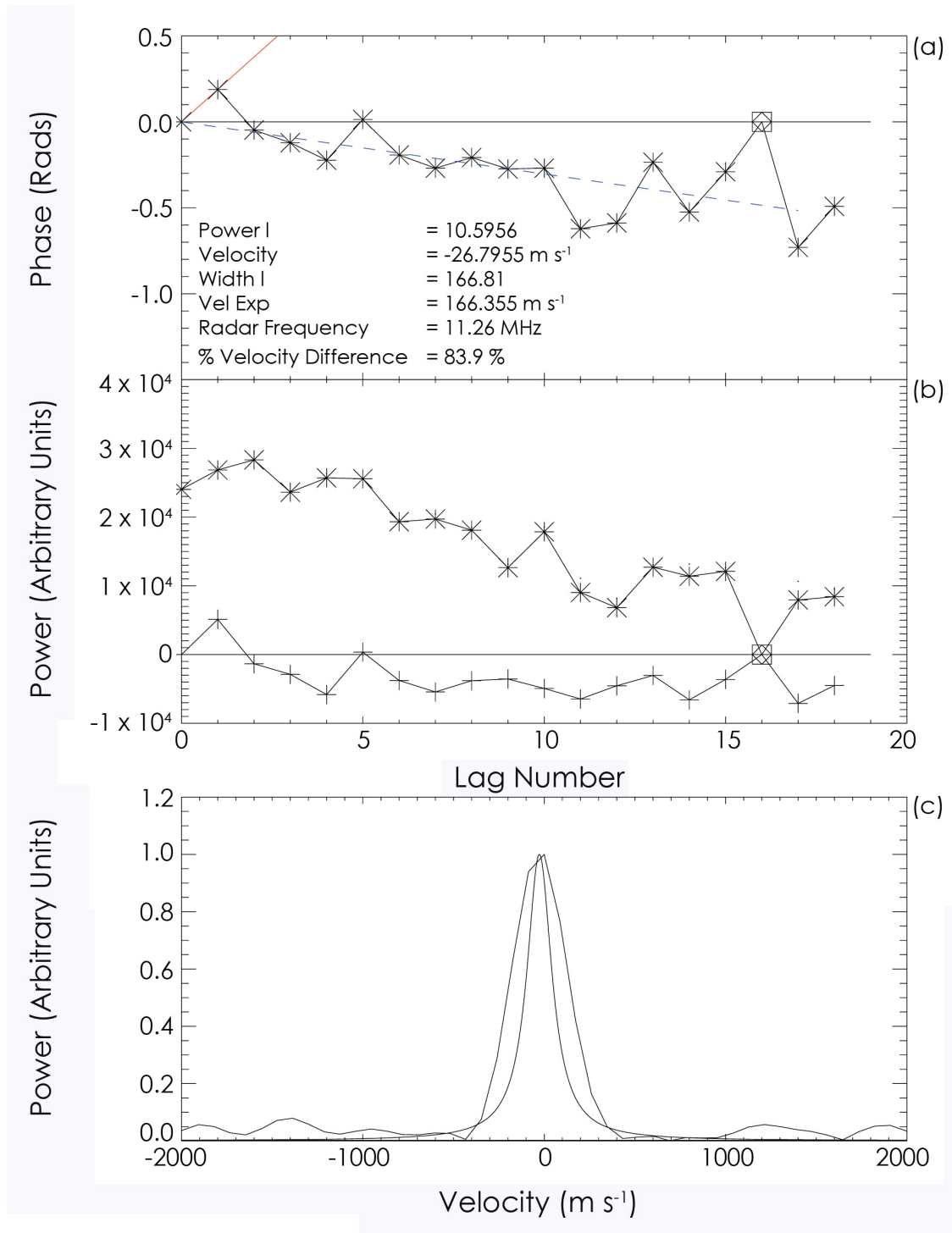


Figure 7.3: **(a – c)** An example of a poorly correlated DPV fitted phase. Panel (a) presents the phase of the ACF measured along beam 9 at range gate 42 at 03:13:19 UT on 31 May 2006 by the SuperDARN radar at Hankasalmi, Finland. The fitted SuperDARN and DPV phase are shown by the overlaid dashed blue and solid red lines, respectively. Panels (b) and (c) show the complex ACF and the velocity distribution, respectively.

DARN and DPV phase are shown by the overlaid dashed blue and solid red lines, respectively. The overlaid solid red line shows the double-pulse phase and the correspondingly poor correlation with the entire ACF.

Figure 7.4 presents a statistical analysis of the standard SuperDARN velocities compared with the emulated DPVs where the velocities are divided into  $100 \text{ m s}^{-1}$  bins and the occurrence is shown by a logarithmic colour scale. The overplotted solid black line shows  $y = x$ . The statistical analysis yields a PMCC of 0.721 between the DPVs and the standard SuperDARN fitted velocities, indicating a good correlation. Figure 7.5 presents a scatter plot comparing 1.5 hop ionospheric scatter, recorded on 1 March 2006 between 06:00 UT - 16:00 UT, calculated in the same manner as for Figure 7.4. Figure 7.5 shows a good correlation between the emulated DPV and the standard SuperDARN velocity for 1.5 hop ionospheric scatter. Both Figures 7.4 and 7.5 demonstrate that the emulated DPV agrees with the standard SuperDARN velocity for scatter of ionospheric origin.

## 7.2.2 Emulated Ground Scatter Results

Figure 7.6 presents a comparison of the ground scatter equivalent of Figure 7.4 for 1 March 2006 between 06:00 UT - 16:00 UT. Figure 7.6 shows poor statistical correlation (PMCC = 0.21) between the DPV and the standard SuperDARN velocity techniques for data of ground scatter origin. Figure 7.3 may provide an explanation for the poor correlation. The DPV method only uses phase measurements from the first two lags regardless of possible phase values from later lags. If individual phases are identified as "bad," by the standard SuperDARN routines they would be ignored by the fitting process and a velocity would be calculated based on the phases recorded at the remaining lags. A DPV, however, is always calculated from just the first lag.

In regions of rapid decorrelation, such as ionospheric scatter, the power is only associated with the first few lags implying that a double-pulse method, restricted to the first lag, would be quite good at accurately determining velocity from these targets. Slowly decorrelating ground scatter, has power that is distributed over every lag and, therefore, such backscatter is less suitable for DPV analysis.

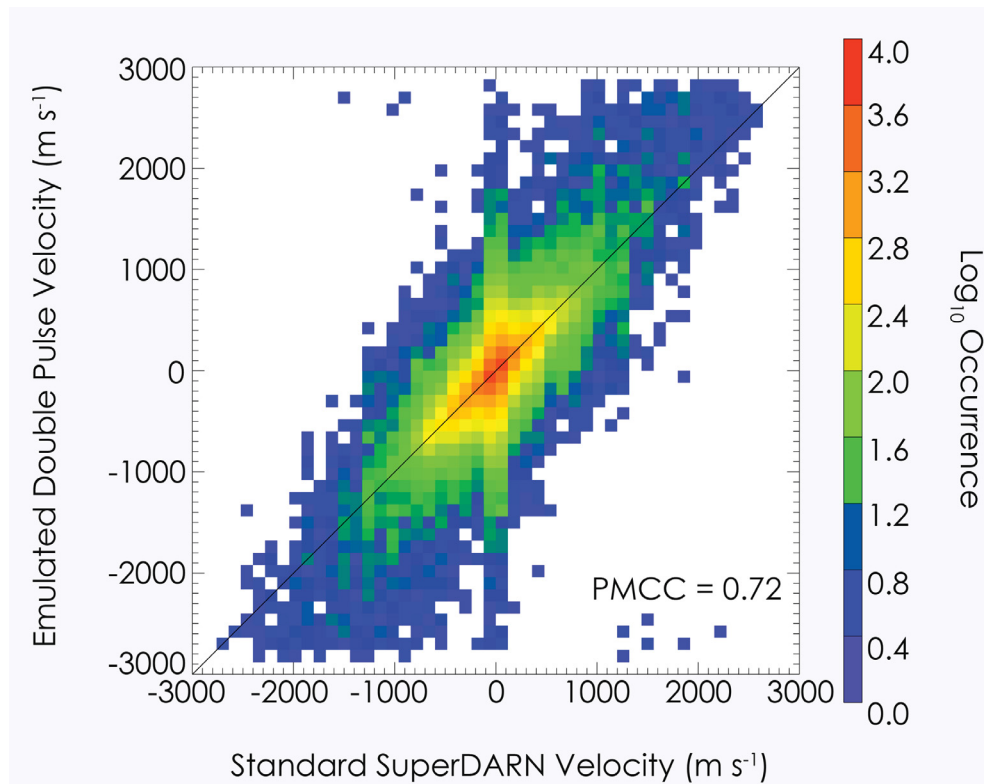


Figure 7.4: A scatter plot between the data displayed in panels (a) and (b) of Figure 7.1 for 0.5 hop ionospheric scatter. The velocities are divided into  $100 \text{ m s}^{-1}$  bins. The occurrence of the scatter is represented by a logarithmic colour scale. The overplotted solid black line shows  $y = x$ .

The phase value recorded at each lag is also subject to some measurement error. The larger number of lags associated with high powers makes the multi-pulse velocity more robust when decorrelation is slower. Such a measurement error, effectively a "phase noise" will also produce a less accurate determination of the velocity when the true phase difference in the lag is small, i.e. when the velocity is small (as in ground scatter) and when the lag itself is short (as in the first lag).

In the case of panel (a) of Figure 7.3, the phase change for the first lag is  $+0.2$  radians over  $2400 \mu\text{s}$ , whereas the phase change for the second lag is  $-0.1$  radians over  $4800 \mu\text{s}$ , and the average fitted phase gradient is  $\sim -0.03$  radians per  $2400 \mu\text{s}$ . In this particular case, the phase gradient calculated for the difference between lags 2 and 3 is in fact closer to the fitted phase gradient than the emulated DPV phase gradient.

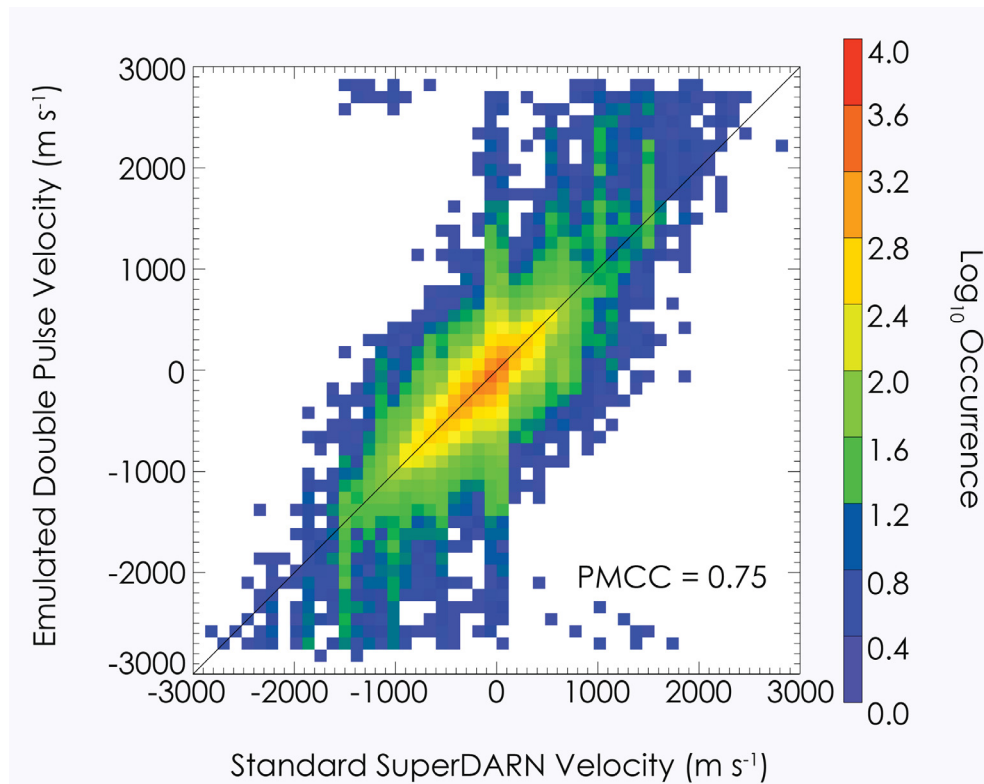


Figure 7.5: A scatter plot comparing 1.5 hop ionospheric scatter, for 1 March 2006 between 06:00 UT - 16:00 UT, calculated from the emulated DPV and the standard SuperDARN velocity methods. The overplotted solid black line shows  $y = x$ .

### 7.2.3 Lag Zero Power as a Data Quality Discriminator

It is beneficial for the double-pulse and SuperDARN multi-pulse sequences to be run simultaneously in stereo for two distinct reasons: (a) the multi-pulse SuperDARN sequence provides bad lag data for efficient removal of erroneous data from DPV returns and (b) the multi-pulse channel provides comparisons from which to determine how well the double-pulse method reproduces data using the standard pulse sequence. The lag zero power, potentially, could be used to determine high signal-to-noise ratio double-pulse data without using the standard SuperDARN fitted velocity as a discriminator. The emulation of double-pulse, presented previously, allows a test of this possibility.

The lag zero power is the backscatter power return from the zeroth lag. Figure 7.7 presents a comparison between the standard SuperDARN velocity data and the emulated DPV data for 30 May 2006 at 20:00 UT to 31 May 2006 at 06:00 UT using a threshold lag

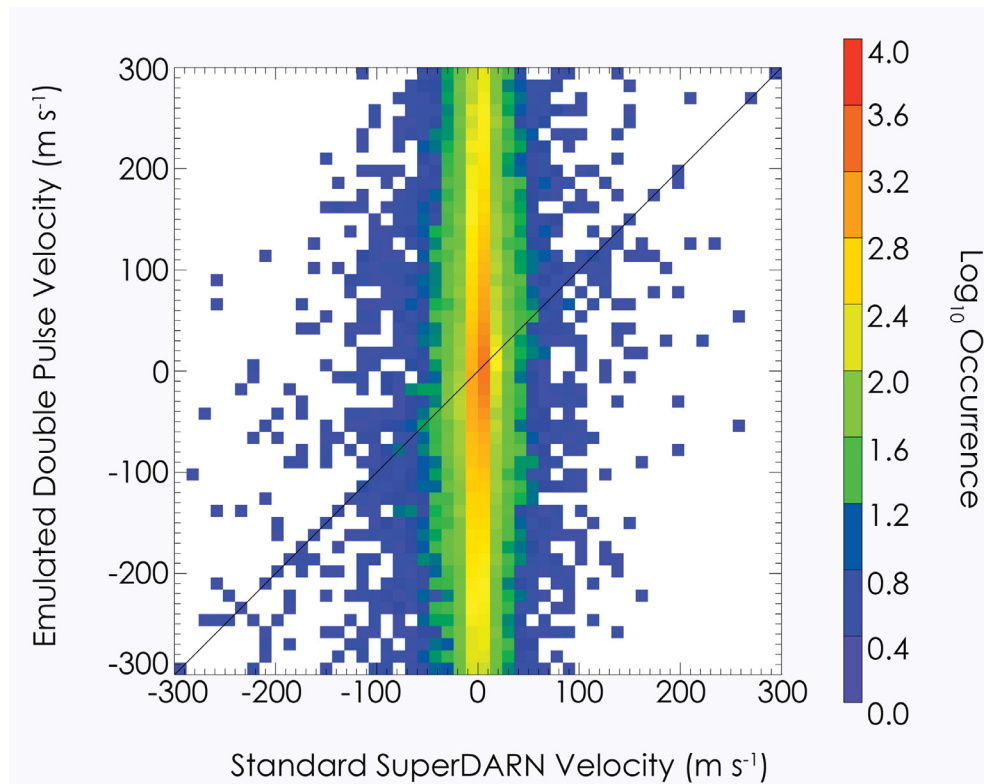


Figure 7.6: A scatter plot comparing only ground scatter, from 1 March 2006 between 06:00 UT - 16:00 UT, calculated from the emulated DPV and standard SuperDARN velocity methods. The overplotted solid black line shows  $y = x$ .

zero power of 5 dB. To remove ground scatter, a threshold of  $50 \text{ m s}^{-1}$  has been applied to the DPV data. Panel (a) of Figure 7.7 presents the original standard SuperDARN fitted velocity data for 30 May 2006 at 20:00 UT to 31 May 2006 at 06:00 UT, which is identical to panel (a) of Figure 7.1 and is shown for comparison purposes with panel (b), the double-pulse data.

Figure 7.8 presents a scatter plot between the data shown in panels (a) and (b) of Figure 7.7. Comparing Figure 7.4 and 7.7 the lag zero power threshold is not as good as the fit quality flag as an identifier of valid double-pulse measurements. Therefore, the double-pulse mode has merit, but will need to be combined with the standard multi-pulse mode operating on the other channel. This limits the advantage of the double-pulse mode as the fit quality flag data has a lower cadence.

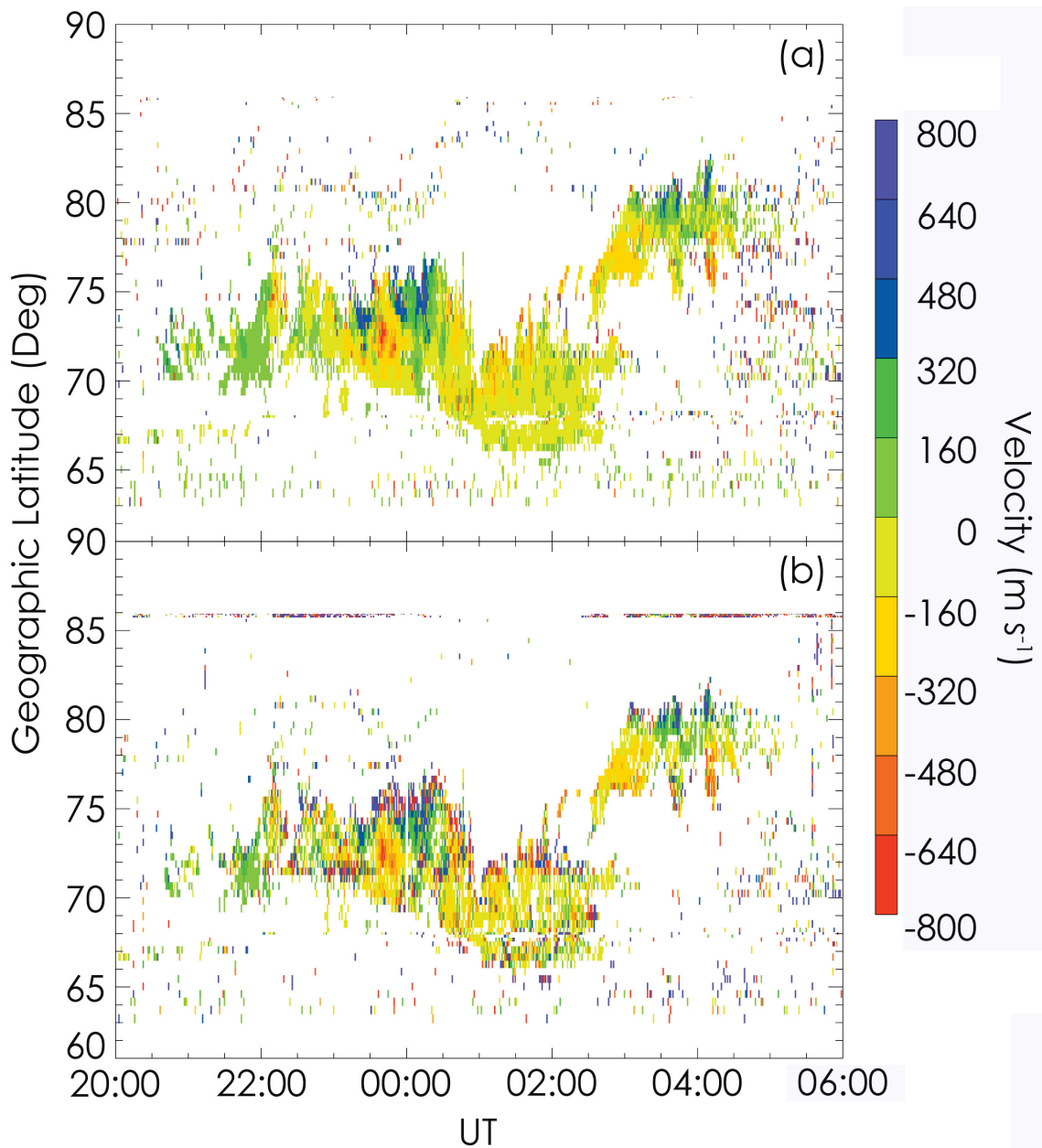


Figure 7.7: **(a and b)** A comparison between the standard SuperDARN velocity data and the emulated DPV data for 30 May 2006 at 20:00 UT to 31 May 2006 at 06:00 UT using a threshold lag zero power of 5 dB. To remove ground scatter, a threshold of  $50 \text{ m s}^{-1}$  has been applied to the DPV data. Panel (a) presents only the ionospheric scatter from the original standard SuperDARN fitted velocity data between 30 May 2006 at 20:00 UT to 31 May 2006 at 06:00 UT. Panel (b) shows the emulated double-pulse data for the same interval as panel (a) using the stated threshold velocity and lag zero power values.

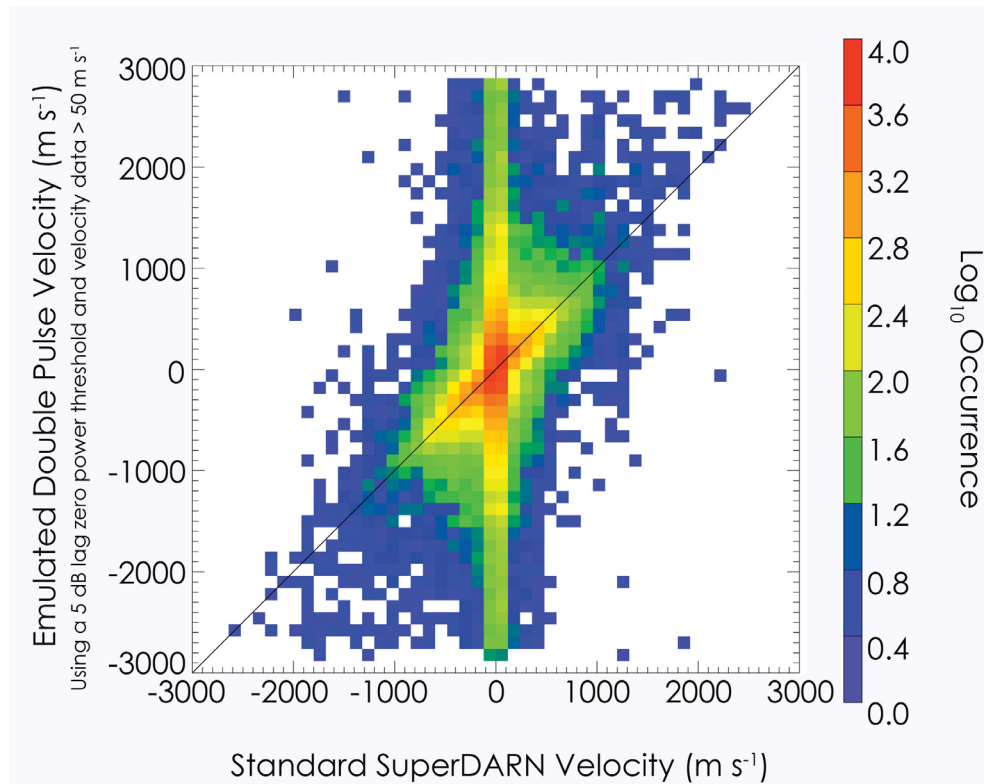


Figure 7.8: A scatter plot comparing 0.5 hop ionospheric scatter, between 30 May 2006 at 20:00 UT to 31 May 2006 at 06:00 UT, calculated from the emulated DPV using a lag zero power threshold of 5 dB.

## 7.3 Implementing a Double-Pulse Radar Mode on the Super Dual Auroral Radar Network

### 7.3.1 Enhanced Temporal Resolution with TMS

Double-pulse modes have been implemented on radar before (e.g., Nielsen, 2004), however, presented here for the first time is a double-pulse sequence operating on the Super Dual Auroral Radar Network. Raw I&Q sample returns are required because an ACF cannot be formed from three sets of two phase values. Figure 7.9 presents the stereo radar configuration that was implemented on the Hankasalmi Finland SuperDARN radar on 6 March 2008, 13:20:00 UT - 13:28:00 UT. Panels (a) and (b) of Figure 7.9 present the standard SuperDARN pulse sequence and the experimental double-pulse sequence, respectively. The configuration allows both pulse sequences to be implemented simulta-

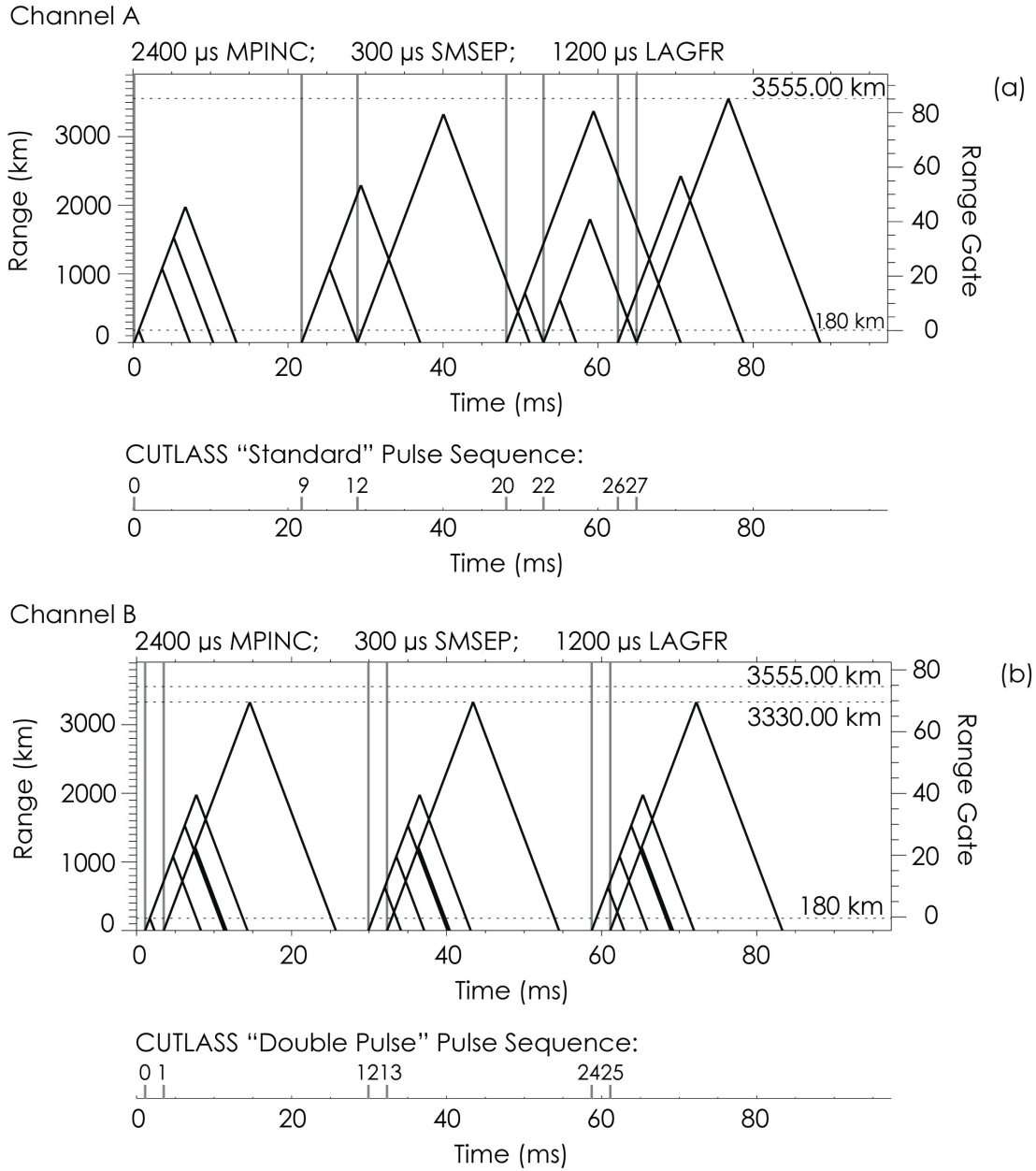


Figure 7.9: **(a and b)** Space-time diagrams for the stereo configuration of the SRM and the double-pulse mode. Panels (a) and (b) show the space-time diagram for the SuperDARN SRM on channel A and the new double-pulse sequence on channel B, respectively.

	Channel A	Channel B
Radar Frequency (kHz)	19730	19755
Cp-id	-6401	-26401
Integration Time (s)	6	6
TX Pulse Length ( $\mu$ s)	100	100
Multi-pulse Increment (MPINC) ( $\mu$ s)	2400	2400
Pulse Sequences Per Record	66	66
Number of Samples Per Sequence	848	800
Number of Pulses Per Sequence	7	6
STEREO Offset ( $\mu$ s)	-400	400
Number of Range Gates	216	200
Range Gate Separation (km)	15	15
Lag to First Range Gate ( $\mu$ s)	100	100

Table 7.1: The radar modes operating on channels A and B of the Hankasalmi Finland SuperDARN radar between 13:20:30 UT -13:30:00 UT on 6 March 2008. The column depicting channel A shows the TMS multi-pulse parameters while the column detailing channel B presents the double-pulse sequence characteristics.

neously. The backscatter during this campaign is induced artificially using the high-power RF facility at Tromsø, whose operation was outlined in section 3.6, and the RTSA method used is the TMS technique, which was outlined in section 3.2.5. The operational data for each radar channel is given in table 7.1. There are fewer bad lags when the double-pulse mode is on channel B rather than channel A, which is why the stereo configuration is implemented as shown in Figure 7.9. Table 7.1 shows that there are 216 range gates in operation for the TMS mode on channel A (each 15 km in length), while 200 range gates are used for the double-pulse TMS mode operating on channel B (also each 15 km in length). The SRM data is restricted to 75 range gates.

This knowledge allows a direct comparison between channels A and B. Figure 7.10 presents the standard RTI SuperDARN data returns for 6 March 2008 at 13:20:00 UT - 13:28:00 UT, along beam 5 from Hankasalmi Finland. Panel (a) shows the backscatter power, measured in dB. Panel (b) presents both the ionospheric and ground scatter velocities. Panel (c) shows the spectral width. All of the parameters presented in panels (a) to (c) are determined by Fitacf. Panel (b) of Figure 7.10 highlights a potential issue in using the double-pulse technique. As highlighted in section 7.2.2, low ionospheric

convection velocities ( $\leq 200 \text{ m s}^{-1}$ ) may yield poor correlation with the standard SuperDARN determined velocity data. Unfortunately, panel (b) shows that the peak velocity is approximately  $20 \text{ m s}^{-1}$ .

### 7.3.2 The Reproduction of Standard Radar Mode Data

Figure 7.11 summarises the data samples that may be used for TMS analysis recorded on 6 March 2008 at 13:21:44 UT. The data presented in Figure 7.11 is on channel A (cp-id-6401) from the Hankasalmi Finland SuperDARN radar, showing 6 s of radar operations. Panel (a) of Figure 7.11 presents the possible sample times within the pulse sequence. The vertical black lines show the pulse transmission times. Panel (b) shows the sample power found from  $I^2 + Q^2$ . The panel shows the power from each pulse sequence over the 6 s beam integration period overlaid on top of each other. The noise level acts as a discriminator between good and bad samples and is shown by the horizontal black line. Panel (c) presents the mean power profile averaged over the 6 s beam integration time using the data from panel (b). The horizontal dashed line again shows the noise level. The red rectangles and blue triangles will be explained in section 7.3.5. Panel (d) shows the mean lag zero power profile. The dotted lines show the mean power profile shifted by the pulse time delays, which are just integral multiples of MPINC. Panel (e) presents the reconstructed power profile for a single pulse sequence and is calculated by superimposing all the shifted power profiles on top of each other. Panel (f) shows the same reconstructed mean power profile as given in panel (e) but contains crosses and circles, which show unusable and usable samples for RTSA for analysing TMS range gate 68, respectively. The process must be repeated for each range gate under analysis. For this particular example, at 13:21:44 UT on 6 March 2008, all seven samples are not contaminated and may be analysed. Panel (g) presents a summary of all the samples that are available for RTSA and are marked with a +. Panels (h) to (j) present the main results of the RTSA. Panels (h), (i) and (j) show the time evolution at TMS gate 63 over 66 pulse sequences throughout the 6 s integration for power, phase and cross-phase, respectively. Using the RTSA method of TMS the raw I&Q samples, on channel A, may be partially

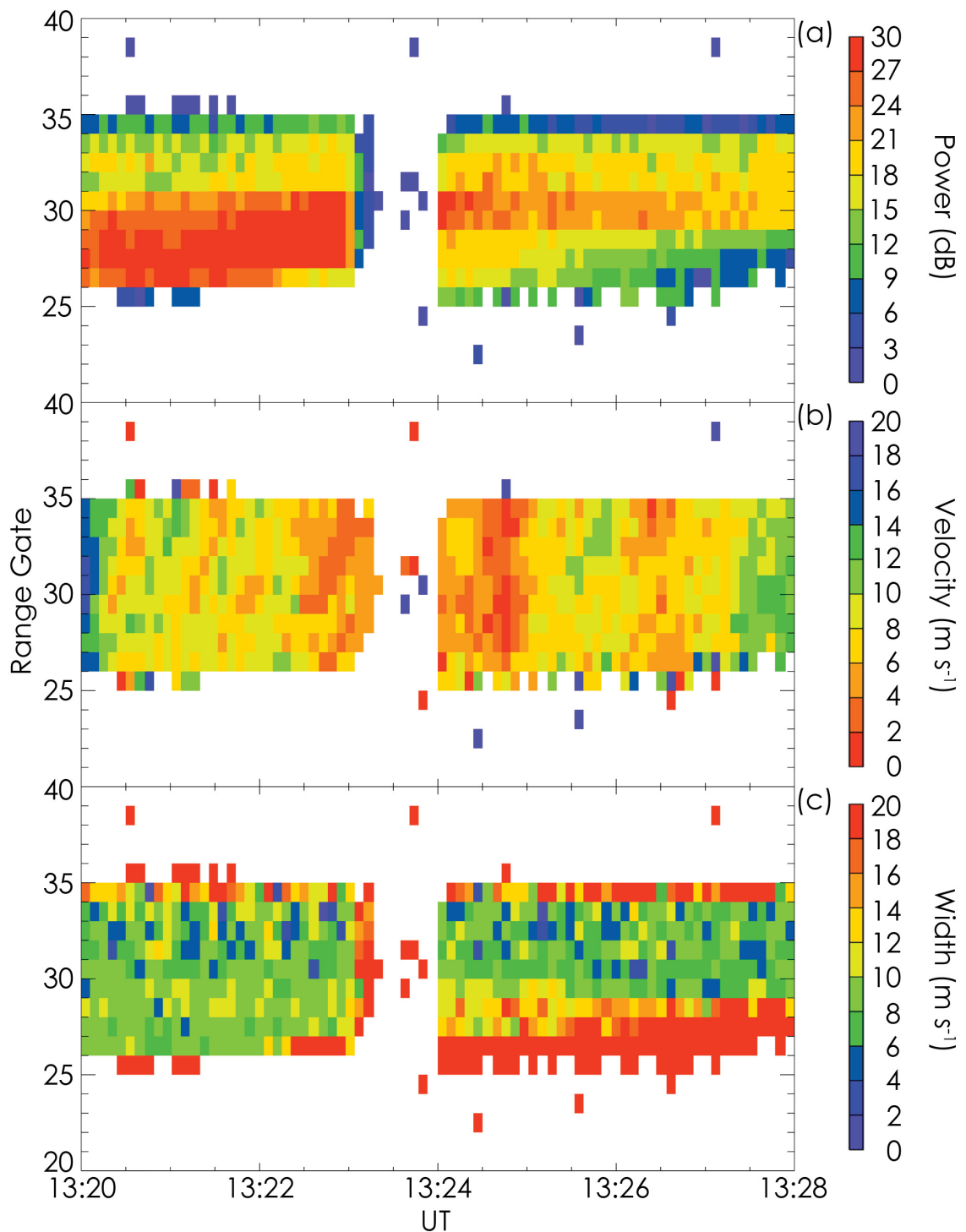


Figure 7.10: **(a – c)** An RTI plot of the standard SuperDARN data returns from 6 March 2008 at 13:20:00 UT - 13:28:00 UT, along beam 5 of the Hankasalmi Finland SuperDARN radar. Panel (a) presents the backscatter power, measured in dB. Panel (b) shows both ionospheric and ground scatter velocity measurements, in  $\text{m s}^{-1}$ . Panel (c) presents the spectral width, also measured in  $\text{m s}^{-1}$ . All of the parameters presented in panels (a) to (c) are determined by the standard SuperDARN routines.

integrated to yield a higher temporal resolution than SuperDARN normally provides. A careful balance must be found between integrating too much, which recreates the original SRM data, and integrating too little, which introduces noise. Data integration, by definition, removes noise. To test the TMS method the standard SRM data is reproduced by fully integrating the raw I&Q samples. There are 66 ACFs, which originate from the 66 pulse sequences transmitted during every integration period. These 66 pulse sequences are integrated together to yield a single fully integrated ACF.

Panel (a) of Figure 7.12 presents the complex ACF measured along beam 5 from range gate 55 at 13:24:00 UT on 6 March 2008 by the Hankasalmi Finland radar from channel A using the standard DAT data, which was introduced in section 3.2.4. Panel (b) of Figure 7.12 presents the result of integrating 66 ACFs each individually determined by the TMS method, on channel A. Panels (a) and (b) of 7.12 are identical, which demonstrates that the TMS method is valid.

### **7.3.3 Increasing Temporal Resolution using TMS**

If the integration level is lowered then the temporal resolution correspondingly increases at the expense of noise. Integration is, by definition, a noise removal process. Therefore, If the data is too noisy then lowering the integration will not improve the data set. Under ideal circumstances, with a low-noise data set, lowering the integration level would clearly be advantageous. Figure 7.13 presents the half-integrated TMS plot in the same format as Figure 7.10. Panel (a) presents the backscatter power. Panel (b) shows the line-of-sight Doppler velocities from both ionospheric and ground origin. Panel (b) of Figure 7.13 shows a doubling of the temporal resolution of the velocity measurements without a significant degradation of the data quality.

Figure 7.14 shows the raw (unintegrated) radar returns in the same format as Figure 7.10. Figure 7.14 shows that the noise level is too high to be able to discern the structures in the ionospheric plasma convection velocity as seen in panel (b) of Figure 7.13. For these data, integrating fewer than 20 ACFs per plot (approximately one third of the full integration) resulted in too much noise. Previous OUCH (Wright and Yeoman, 1999b) runs have used

# Sessaiogram: SuperDARN Raw Time Series Plot

Finland 2008/03/06 13:21:44UT, SchA cpid -6401, bm 5, frq 19730kHz, intf 6sec (nave 66), xcf 1

mppul 7, mpinc 2400us, txpl 100us(rsep 15km), smsep 100us( 15km), lagfr 100us( 15km), nrang200, maxrng 3000km, nsmp 848, seqtime 84.80mssofs -400us  
ppaf[7]=(0,9,12,20,22,26,27), noise 4341(fclr 58240), att 1(0->1), DCofs l1: 15, Q1: -1 (removed), ercod 0x0000, MaxBadRng 105km, pwrthr 6.0dB(20.0dB, finechk,

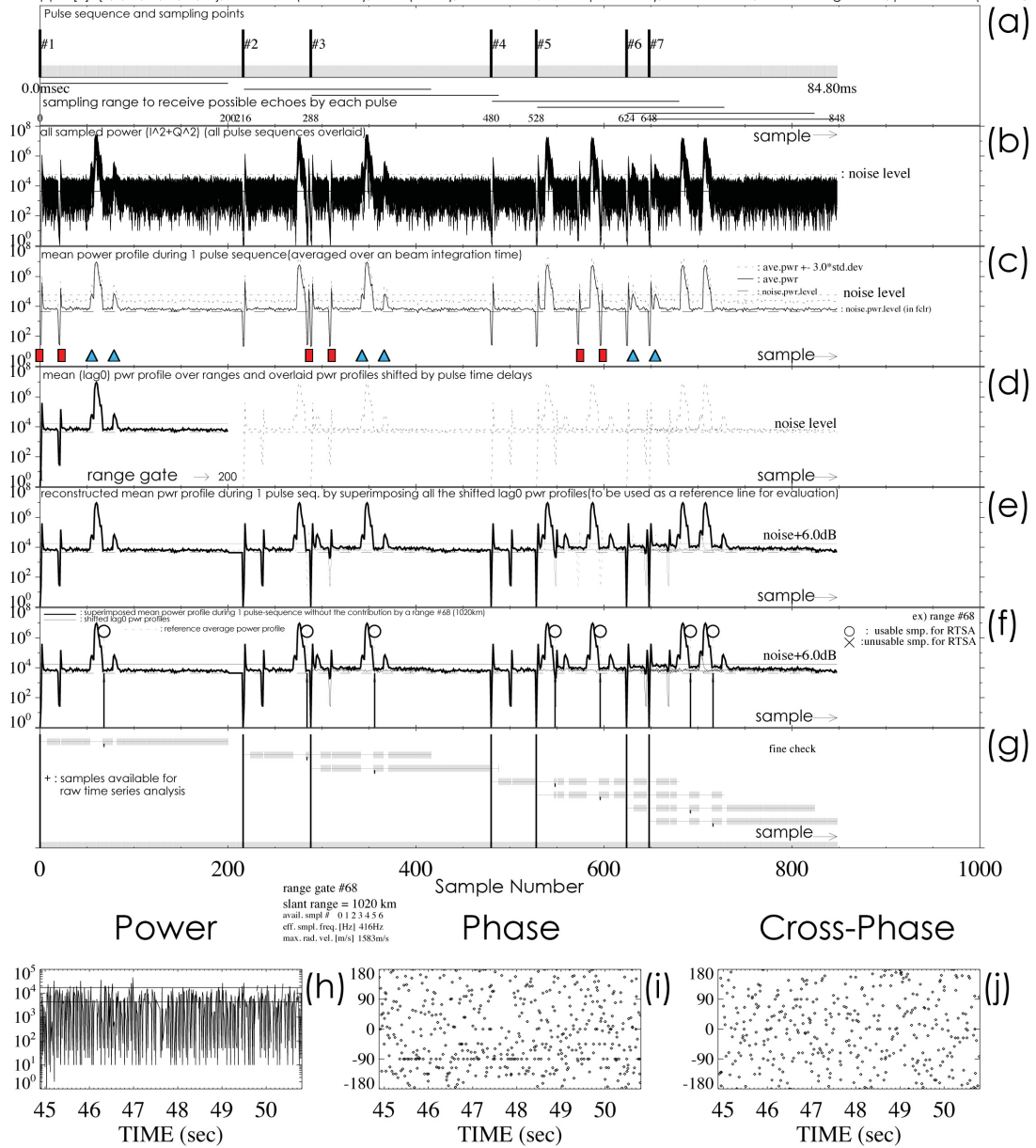


Figure 7.11: (a – j) Data samples that are available for TMS analysis for 6 March 2008 at 13:21:44 UT on beam 5 and channel A using the standard SuperDARN pulse sequence (see text for details).

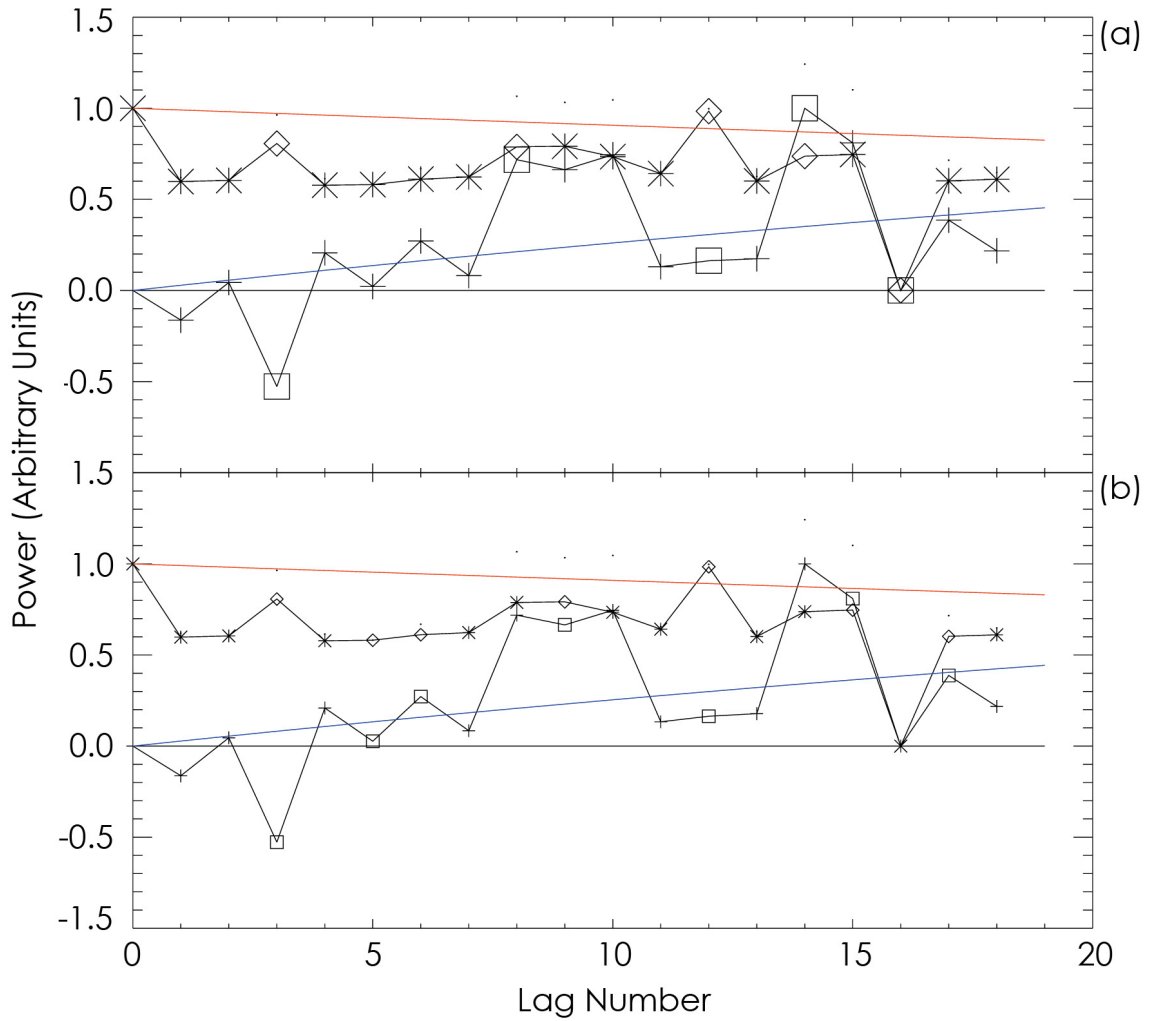


Figure 7.12: **(a and b)** A comparison between an ACF measured along beam 5 at range gate 55 at 13:24:00 UT on 6 March 2008 by the SuperDARN radar at Hankasalmi, Finland and the TMS equivalent. The complex autocorrelation function for the standard DAT data from channel A is presented in panel (a) while panel (b) shows the result when 66 individual ACFs, each determined by the TMS method, are integrated.

a 1 s integration mode (using  $\sim 10$  pulse sequences), however, no TMS data from artificial backscatter experiments have, as yet, been published using the TMS method.

### 7.3.4 Double-Pulse Lag Zero Power

Panel (a) of Figure 7.9 shows that the delay between the transmissions of the first and second pulses of the standard SuperDARN pulse sequence is sufficient for unambiguous backscatter to be recovered, at all ranges, from the first pulse. The double-pulse sequence, however, does not have a long delay between the first two transmissions. Figure 7.15 summarises the double-pulse data samples that may be used for TMS analysis recorded on 6 March 2008 at 13:21:44 UT in the same format as Figure 7.11. The data presented in Figure 7.15 is on channel B (cp-id -26401) from the Hankasalmi Finland SuperDARN radar, showing 6 s of radar operations.

Panel (b) of Figure 7.15 shows that backscatter power is received from the heater-induced irregularities from pulse 1 only after the transmission of pulse 2, revealed by the "double-humped" structure in the power profile associated with the double-pulse mode. Thus, no "clean" lag zero power profile is recorded with the double-pulse mode, unlike the standard SuperDARN multi pulse sequence. Deconvolution is a means of resolving this issue and providing a usable lag zero power. Panel (d) shows the lag zero power profile deconvolved to ensure that contamination from the pulse pair is kept to a minimum. The double-pulse mode contains 800 return samples per pulse sequence, and a subset of these represents the sampling range when echoes may be received from each pulse. Pulse 1 of the double-pulse sequence returns comprises samples 0 - 200, while pulse 2 comprises 24 - 224. Of interest is that the third pulse return samples only occur after sample number 288, therefore, all the return samples from pulse 2 are received before the samples are collected for pulse 3.

In this case samples 0 - 80 following the first pulse of each pair appear to give a clean lag zero power profile before the arrival of returns from the second pulse. Samples 105 - 184 follow on as an equivalent of samples 81 - 160 for the first pulse. It is worth mentioning that this method will not work for a general distribution of lag zero power. The dotted

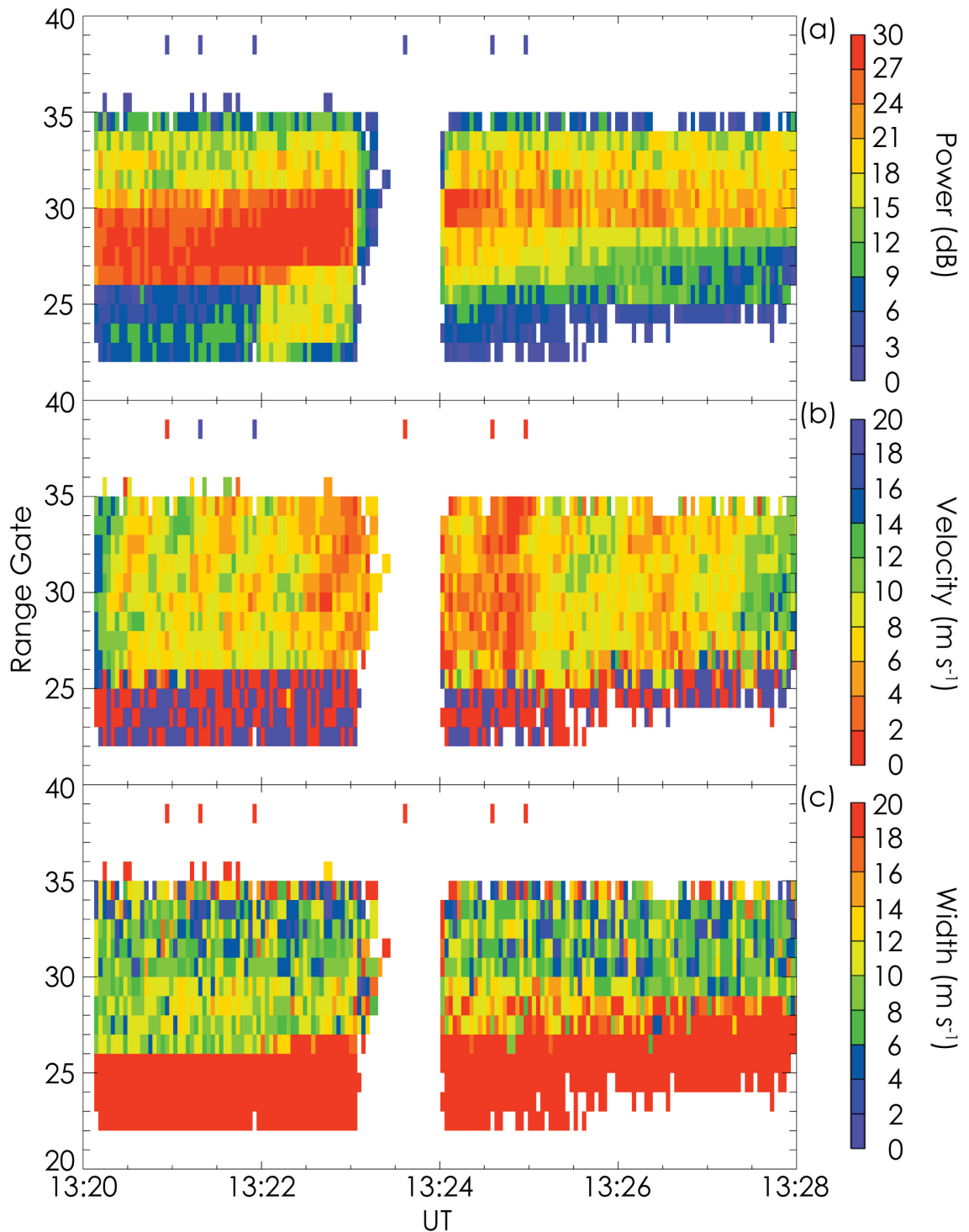


Figure 7.13: (a – c) The half-integrated TMS plot on the 6 March 2008 13:20:00 UT - 13:28:00 UT measured along beam 5, on channel A, by the SuperDARN radar at Hankasalmi, Finland. Panel (a) presents the backscatter power. Panel (b) shows the velocity, with scatter from both ground and ionospheric origin. Panel (c) shows the spectral width.

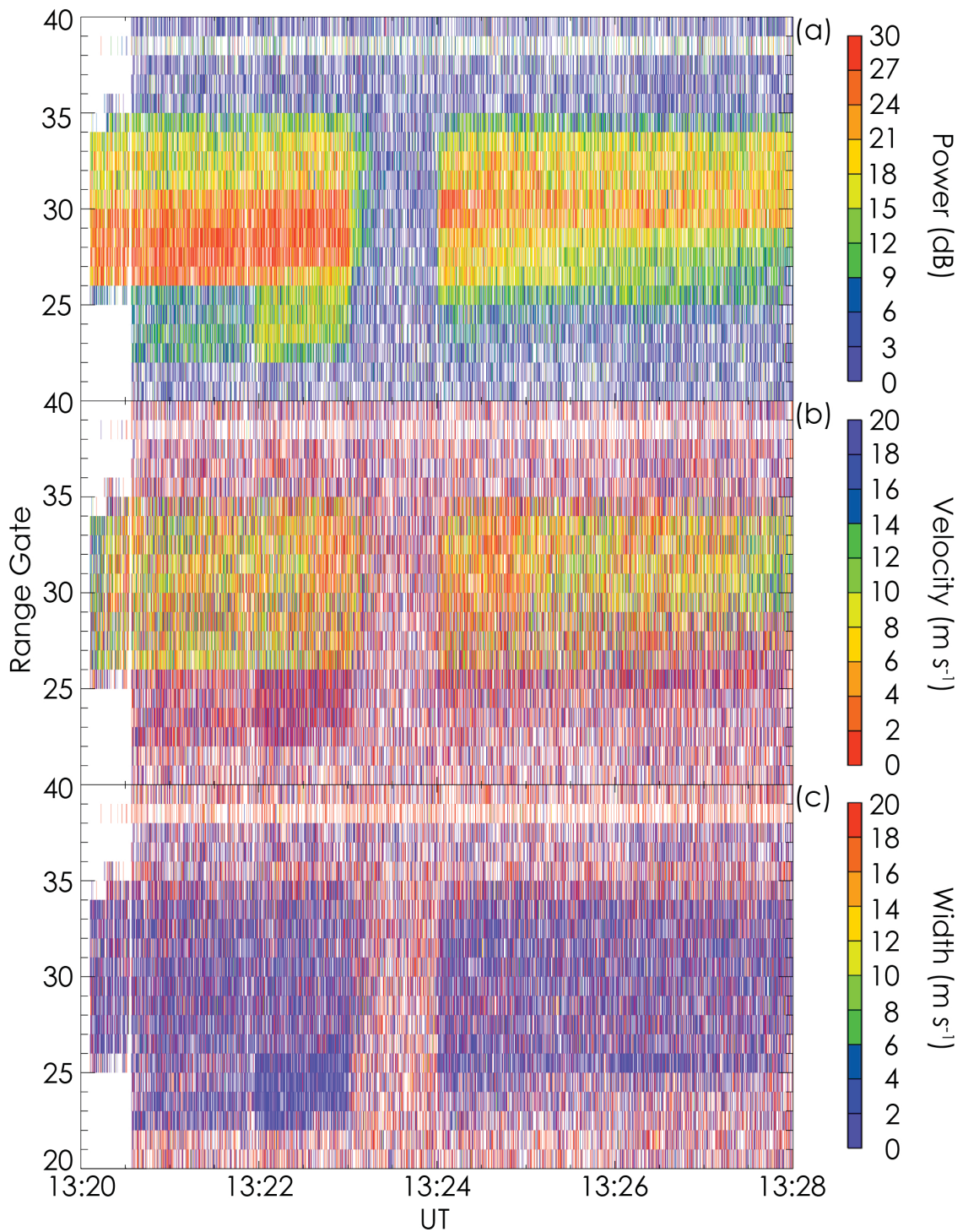


Figure 7.14: **(a – c)** The non-integrated TMS plot on the 6 March 2008 13:20:00 UT - 13:28:00 UT measured along beam 5, on channel A, by the SuperDARN radar at Hankasalmi, Finland. Panel (a) presents the backscatter power. Panel (b) shows the velocity measurements, with scatter from ground and ionospheric sources. Panel (c) shows the spectral width.

# Sessaiogram: SuperDARN Raw Time Series Plot

Finland 2008/03/06 13:21:44UT, SchB cpid -26401, bm 5, frq 19755kHz, intt 6sec (nave 66), xcf 1  
 mppul 6, mpinc 2400us, txpl 100us(rsep 15km), smsep 100us( 15km), lagfr 100us( 15km), nrang200, maxrng 3000km, nsmp 800, seqtime 80.00mssofs 400us  
 ppat[6]=(0,1,12,13,24,25), noise 715(fclr 1232), att 0(0->0), DCofs l1: 15, Q1: -1 (removed), ercod 0x0000, MaxBadRng 105km, pwrthr 6.0dB(20.0dB, finechk)

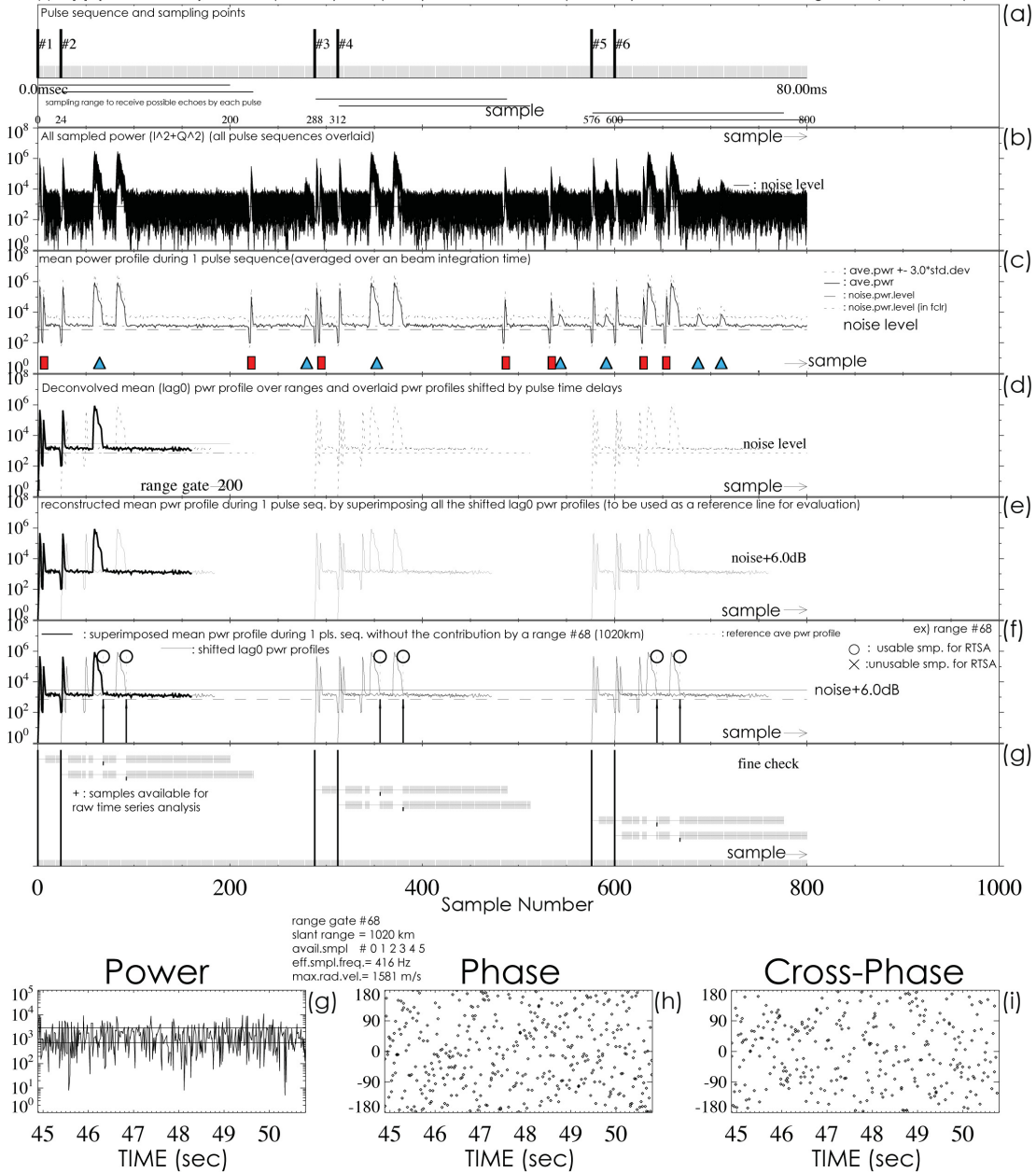


Figure 7.15: (a – j) A Sessaiogram recording the TMS double-pulse results for 6 March 2008 at 13:21:44 UT on channel B using a deconvolved lag zero power (see text for details).

lines on panel (d) show the mean deconvolved lag zero power profile shifted by the pulse time delays.

Panel (e) presents the reconstructed power profile for a single pulse sequence and is calculated by superimposing all the shifted power profiles on top of each other. Panel (f) shows the same reconstructed mean power profile as given in panel (e) but contains crosses and circles, which show unusable and usable samples for RTSA for analysing TMS range gate 68, respectively. The process must be repeated for each range gate under analysis. For this particular example, at 13:21:44 UT on 6 March 2008, all six samples were not contaminated and may be analysed. Panel (g) presents a summary of all the samples that are available for RTSA and are marked with a +. Panels (h) to (j) present the main results of the RTSA. Panels (h), (i) and (j) show the time evolution at TMS gate 63 over 66 pulse sequences throughout the 6 s integration for power, phase and cross-phase, respectively. Figure 7.15 has shown that one can distinguish returns from pulse 1 and pulse 2 in the area of heater scatter.

Figure 7.16 presents the power deconvolution on 6 March 2008 at 13:20:30 UT - 13:28:00 UT. Panel (a) shows the standard fitted power from the SRM on channel A. Panel (b) shows the standard lag zero power from the SRM on channel A. Differences between panels (a) and (b) of Figure 7.16 will be discussed in the following section. Panel (c) shows the convolved power from the double-pulse mode on channel B. Panel (d) shows the deconvolved lag zero power from the double-pulse sequence operating on channel B. A power threshold of 5 dB has been applied to the data contained in panel (d) to provide a close match to the emulation of a lag zero power contained in section 7.2.3. It is clear that the data contained in panel (d) is similar to the original power profile contained in panel (a) of Figure 7.16.

### **7.3.5 Cross-Contamination between Channels A and B**

Panels (a) and (b) of Figure 7.16 show an unexpected difference between the fitted power and lag zero power in the standard SuperDARN data from channel A. It will be shown here that this difference results from a cross-contamination between the two channels

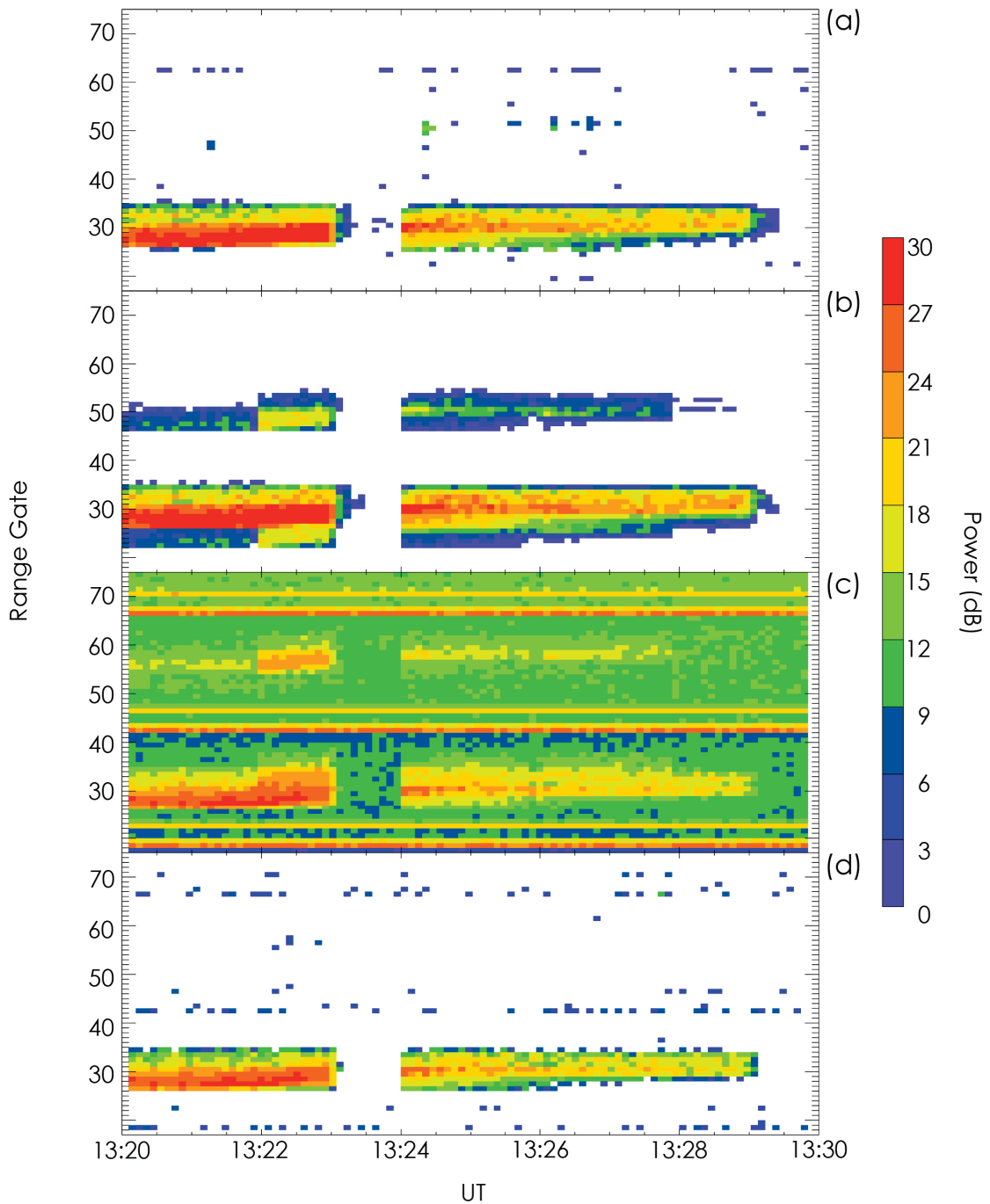


Figure 7.16: **(a – d)** Power deconvolution for 6 March 2008 at 13:20:30 UT - 13:30:00 UT. Panel (a) shows the fitted power from the SRM on channel A. Panel (b) shows the lag zero power from channel A. Panel (c) shows the convolved power from the double-pulse on channel B. Panel (d) shows the deconvolved channel B double-pulse lag zero power. The power in all of the panels is measured in dB.

operating in stereo on the SuperDARN radar.

Panel (c) of Figure 7.11 highlights the contamination seen on channel A caused by the transmissions and backscatter on channel B. The six red rectangles show the transmission times of the pulses on channel B and the corresponding six blue triangles are the times when backscatter power is received from each corresponding transmit pulse on channel B. Two effects may be noted in the channel A data as a result of the operation of the second pulse sequence on channel B. Firstly, a brief transient response is seen in channel A associated with the transmit/receive switches operating on channel B, at the times marked with red rectangles. Similar transients are seen associated with the channel A transmit pulses at the times marked in panel (a) of Figure 7.11. Secondly, when backscatter power is received from each pulse in channel B, a smaller contaminating power return is simultaneously recorded in channel A. This contaminating power is marked in panel (c) of Figure 7.11 by the blue triangles.

A clear example of this is shown by the second power peak recorded in channel A approximately between samples 76 - 89. The blue triangle located below this peak shows that this time corresponds with the arrival of backscatter from the second pulse of the double-pulse sequence transmitting on channel B.

Panel (c) of Figure 7.15 demonstrates that similar cross-contamination is recorded in channel B, caused by the pulse transmissions and backscatter returns of channel A.

The contamination issue seen here would normally be hidden when the same pulse sequence is run on both channels, as has been the case for all previous stereo operations. However, presented here for the first time are two different pulse sequences operating on the SuperDARN radar, which allows this contamination to be seen. The contamination is observed in both stereo channels even though the channels are have a frequency separation of 25 kHz, 15 kHz being the usual minimum frequency separation between the two stereo channels (Lester et al., 2004). Note, however that the contamination is not visible in the standard fitted radar data presented in panel (a) of Figure 7.16, presumably because no physically meaningful autocorrelation function could be formed from data resulting from receiving channel B data on channel A, which is operating at a different frequency.

Thus, while the cross-channel contamination will degrade the data, for instance through its effect on the lag zero power profile, which is used during the fitting process, it does not appear to result in erroneous fitted data being recorded.

### 7.3.6 Double-Pulse Velocity Analysis

Figure 7.17 presents the main results from the double-pulse campaign and shows a comparison between the different methods of determining the ionospheric convection velocity using the SuperDARN radar. Panels (a) to (c) present data from channel A while panels (d) to (g) show data from channel B. Panel (a) presents the standard SuperDARN ionospheric convection velocity measured along beam 5 of Hankasalmi, Finland. Panel (b) presents the fully integrated TMS data and highlights a satisfactory reproduction of the original SRM data. Panel (c) shows the SRM emulated DPV, as described in section 7.2. Panels (d)-(f) present the double-pulse velocities from channel B calculated from pulses 1&2, 3&4, and 5&6, respectively. Panel (d) shows for the first time a double-pulse mode working and operating on the SuperDARN radar. There is a close similarity between panel (d) and the emulated DPV shown in panel (c). The noisy nature of the plots is to be expected since during this campaign there are very low velocity plasma irregularities with slow decorrelation times. As such, high similarity between the DPV and the SRM data is not to be expected due to the issue explained in section 7.2.2: the observed ACFs, such as shown in Figure 7.12 show both a slow decorrelation and small phase gradients. Finally, panel (g) shows the concatenation of all three DPV results from panels (d)-(f) to yield a temporal resolution that is three times that of the original SuperDARN resolution. As such, this campaign is a proof that the double-pulse technique may operate on the SuperDARN radar. The temporal resolution of the SuperDARN radar may be increased by a factor of three, plus the factor of 2 (or more) gained from reducing the integration level, whilst still maintaining the same range extent of 3000 km.

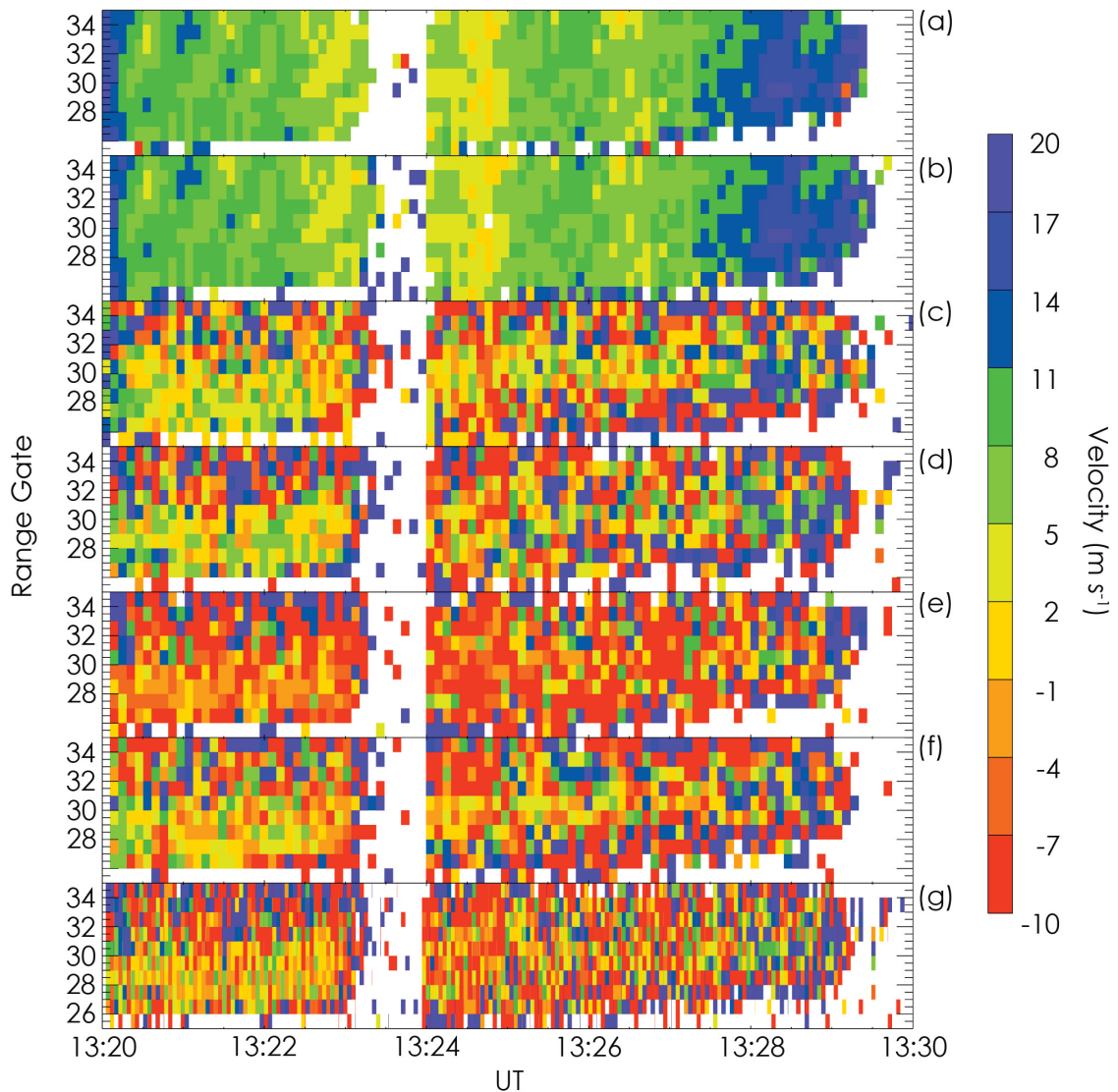


Figure 7.17: **(a – g)** A comparison of different methods for determining the ionospheric convection velocities recorded on 6 March 2008 between 13:20:30 UT - 13:30:00 UT measured along beam 5 of the Hankasalmi, Finland SuperDARN radar. Ionospheric convection velocity is shown originating from: Panel (a) the SuperDARN standard fitted velocity. Panel (b) the fully integrated TMS data. Panel (c) the standard emulated DPVs. Panels (d)-(f) the double-pulse velocities from channel B calculated from pulses 1&2, 3&4, and 5&6, respectively. Panel (g) shows the concatenation of the three DPV data sets shown in panels (d)-(f).

## 7.4 Summary

A first examination of the statistical correlation of ionospheric velocity measurements determined from an emulated double-pulse method and the standard SuperDARN routines has been undertaken. Using the first two lags of the standard SuperDARN pulse sequence, an approximation to a double-pulse mode may be emulated. The results demonstrate that while, in general, the PMCC calculated between the two data sets indicates a high statistical correlation, the discrepancies caused by the nature of this method means that there are shortcomings with the technique. If the first lag yields a phase value atypical for the ACF as a whole, as illustrated in Figure 7.3, then there will be a discrepancy between the calculated DPV and the velocity determined by the standard SuperDARN routines.

For ionospheric scatter this discrepancy produces a minor artefact in the comparison between the two velocity distributions for both the 0.5 hop ionospheric scatter as shown in Figure 7.4 and 1.5 hop ionospheric scatter presented in Figure 7.5. These two figures prove that a double-pulse scheme may be used to reproduce the velocity measurements determined by the standard SuperDARN routines. This is due to the fast decorrelation times associated with ionospheric scatter such that the majority of the backscatter power is concentrated in the earliest lags. Unfortunately, the high noise level associated with slow ionospheric convection velocities severely affects the double-pulse method as shown in Figure 7.6. The emulated DPV method yields an impressive data set for ionospheric scatter but cannot be used for ground scatter.

The TMS RTSA technique is employed here to provide a full integration of the raw ACFs on channel A in order to reproduce the standard SuperDARN data, demonstrating the correct usage of the raw I&Q samples. The technique is then used to recover I&Q samples from the new double-pulse mode on channel B. The results of the first experimental double-pulse technique on SuperDARN are promising, but unfortunately, they demonstrate the problems and challenges associated with the radar mode: its inability to reproduce the standard SuperDARN data when there is a slow but noisy phase evolution or when there are slowly decorrelating plasma irregularities.

Nevertheless, the double-pulse technique does appear to work on the Hankasalmi Finland SuperDARN radar. The success of the technique is highlighted by the similarity of the double-pulse results from channel B with the emulated double-pulse techniques from channel A in their multi-pulse SRM and multi-pulse TMS forms. The usefulness of non-integrated TMS data, and the implications of using data from less noisy data sets, has been shown and a reliable value of the lag zero power may be determined by deconvolving the power profile.

The running of two independent pulse sequences on the stereo channels of the Hankasalmi radar has enabled, for the first time, the observation of cross-contamination between the radar channels. The different pulse sequences run on channels A and B allow the observation of these cross-contaminations even though the frequency separation between the channels is 25 KHz.

A new capability for the SuperDARN radar has been demonstrated that increases the cadence of transmissions, and therefore, increases the temporal resolution by a factor of three while still maintaining the same range extent of approximately 3000 km.

# Chapter 8

## Summary and Further Work

### 8.1 Introduction

This thesis has comprised three distinct studies, which have modelled, observed, and analysed ULF waves within the terrestrial magnetosphere and ionosphere. Chapters 4, 5 and 6 detailed modelling and observational studies of ULF waves, while chapter 7 described a technique designed to improve the temporal resolution of ULF wave observation. The conclusions have been organised accordingly.

### 8.2 Summary I- Large Spatial-Scale ULF Waves

Chapter 4 detailed the testing of a 1-D numerical model (Sciffer et al., 2005), which calculates ULF wave fields, and the Poole and Sutcliffe (1988); Sutcliffe and Poole (1989, 1990) model, which uses these wave fields to determine corresponding model Doppler shifts. These models form the foundation of chapters 5 and 6. The first main study, detailed in chapter 5 of this thesis, focussed on ULF wave observations at high-latitudes in the terrestrial ionosphere using a collection of both space- and ground-based instruments. Chapter 5 used a combination of an HF Doppler sounder (DOPE), a network of ground magnetometers (IMAGE), upstream solar wind monitors (ACE and IMP-8 spacecraft) and a 1-D numerical model to examine the temporal evolution of a ULF wave. The

event occurred on 16 April 1998 and followed a solar wind density and pressure increase seen in the upstream ACE spacecraft data. The magnetometer and HF Doppler sounder data showed that the event developed into a low- $m$  ( $-6$ ) field line resonance. The ULF electric and magnetic fields were determined by a 1-D model (Sciffer et al., 2005), which calculates the wave propagation from the magnetosphere, through the ionosphere to the ground with an oblique magnetic field. These ULF wave fields were used to determine a model HF Doppler shift which was compared to DOPE observations. The ULF magnetic field at the ground and Doppler observations provided model inputs at various points throughout the event. The incident wave mode evolved from a mixture of fast and Alfvén modes at the beginning of the event to an almost purely shear Alfvénic incident mode after approximately 33 minutes. Chapter 5 has shown, for the first time, a measurement of the wave mode evolution throughout an impulse-driven ULF wave event. This event is the only one appearing to have impulse-driven characteristics out of the 25 events detailed in Chapter 6.

Chapter 6 provided a detailed observation and modelling statistical study of 25 ULF wave events. These geomagnetic pulsations were measured by the DOPE system, the IMAGE magnetometer array, and the Tromsø dynasonde between January 1998 and September 2003. During this period, the DOPE system measured approximately 300 geomagnetic pulsations. The ones included in chapter 6 were extracted because they fulfilled three simple selection criteria that (a) after passing the wave data through an FFT routine to obtain the dominant frequency of the wave, the wave signature had an identical frequency in both the DOPE instrument and the IMAGE magnetometer array, (b) the effective azimuthal wavenumber,  $m$ , was less than 10 and (c) there were data available from the Tromsø dynasonde that provided a satisfactory electron density profile using the POLAN algorithm (Titheridge, 1985). The observed HF Doppler shifts determined from the DOPE sounder were compared to model Doppler shifts calculated using a 1-D numerical model. Chapter 6 showed that the advection mechanism is contributing the most to the overall Doppler shift at high-latitudes, agreeing with previous studies of large spatial-scale ULF waves (e.g., Wright et al., 1997, 1998; Waters et al., 2007; Borderick et al., 2010). The phase re-

relationships shown within chapter 6 also agreed with previous work by Wright et al. (1997) showing that the majority of the 25 high-latitude ULF wave events were ordered with relative phases between  $135^\circ$  -  $180^\circ$ . This is the first time that observed and modelled wave phase have been compared for a model run under appropriate ionospheric conditions, and suggested that the model wave phase can provide a meaningful wave diagnostic.

Chapter 6 showed that wave mode is important in determining the Doppler shift, although advection remains the dominant mechanism even for the more compressional events. The chapter also showed that the electron density gradient and the ionospheric reflection coefficient are critical parameters in determining the Doppler shift for typical high-latitude FLRs. Chapter 6 demonstrated that most events were almost purely Alfvénic and were not ordered by proximity to resonance indicating that the incident wave mode is determined by some other parameter, such as a characteristic of the driving source. Thus, the incident wave mode is an important parameter in accurately matching the observed and model Doppler shifts, but does not significantly affect the dominant Doppler mechanism or the relative phase between the Doppler and magnetic field wave signatures.

### **8.3 Future Work I- Large Spatial-Scale ULF Waves**

Chapter 6 revealed that the incident wave mode of each of the 25 ULF wave events is not ordered by their proximity to resonance. A future study could investigate what determines the incident wave mode of a ULF wave and could use a more complex ULF wave field model, with a higher dimensionality, such as that detailed in Waters and Sciffer (2008). Future investigations could increase the number of events, extend to higher effective azimuthal wavenumbers, look for more impulse-driven events, and investigate other classes of pulsation, e.g. Pi2.

## 8.4 Summary II- Double-Pulse Operations

Chapter 7 described the double-pulse radar technique, which aimed to provide an unprecedented resolution of ULF waves. An initial analysis emulating a double-pulse using the first two lags of the standard SuperDARN pulse sequence showed poor correlation between the double-pulse method and the standard SuperDARN velocity data for ground scatter but good correlation for data of ionospheric origin.

An experimental campaign followed and the new pulse sequence did indeed increase the temporal resolution of one of the CUTLASS SuperDARN radar by a factor of three. Preliminary findings suggested, as predicted from the earlier emulation, that this technique is valid for use with ionospheric scatter with steady phase values. Results showed that the double-pulse method cannot be used when the phase is rapidly changing or when data originates from slowly decorrelating FAIs.

Chapter 7 described the first time that two independent pulse sequences have been run in stereo on the SuperDARN radar and allowed, also for the first time, observations of cross-contamination between the radar channels to be seen.

## 8.5 Future Work II- Double-Pulse Operations

Several aspects of the double-pulse study detailed in chapter 7 could be explored further. More experimental campaigns, currently not possible due to funding constraints, would increase the probability of observing (a) ionospheric backscatter with slowly changing phase values and/or fast decorrelating FAIs and (b) ULF wave structures.

# Bibliography

- Alfvén, H.: Existence of Electromagnetic-Hydrodynamic Waves, *Nature*, 150, 405–406, 1942.
- Allan, W. and Poulter, E. M.: ULF waves- Their relationship to the structure of the Earth's magnetosphere, *Rep. Prog. Phys.*, 55, 533–598, 1992.
- Allan, W., Poulter, E. M., and White, S. P.: Hydromagnetic wave coupling in the magnetosphere - Plasmapause effects on impulse-excited resonances, *Planet. Space Sci.*, 34, 1189–1200, 1986.
- Allan, W., White, S., and Poulter, E. M.: Impulse-excited Hydromagnetic Cavity and Field-line Resonances in the Magnetosphere, *Planet. Space Sci.*, 34, 371–385, 1986b.
- Anderson, B. J., Engebretson, M. J., Rounds, S. P., Zanetti, L. J., and Potemra, T. A.: A statistical study of Pc 3-5 pulsations observed by the AMPTE/CCE magnetic fields experiment. 1. Occurrence distributions, *J. Geophys. Res.*, 95, 10,495–10,523, 1990.
- Armstrong, T. P., Krimigis, S. M., and Lepping, R. P.: Magnetosheath burst of predominantly medium nuclei observed with IMP 8 on February 16, 1974, *J. Geophys. Res.*, 83, 5198–5206, 1978.
- Baddeley, L. J.: Wave-particle interactions in the terrestrial magnetosphere, Ph.D. thesis, University of Leicester, University Road, Leicester, LE1 7RH, 2003.
- Baddeley, L. J., Yeoman, T. K., and Wright, D. M.: HF Doppler sounder measurements of the ionospheric signatures of small scale ULF waves, *Ann. Geophys.*, 23, 1807–1820, 2005.

- Birkeland, K. R.: The Norwegian Aurora Polaris Expedition 1902-1903, vol. I, Aschehoug and Co., Christiania, 1908.
- Borderick, J. D., Yeoman, T. K., Waters, C. L., and Wright, D. M.: Observations and modelling of the wave mode evolution of an impulse-driven 3 mHz ULF wave, *Ann. Geophys.*, 28, 1723–1735, 2010.
- Bougher, S. W. and Roble, R. G.: Comparative Terrestrial Planet Thermospheres 1. Solar Cycle Variation of Global Mean Temperatures, *J. Geophys. Res.*, 96, 11,045–11,055, 1991.
- Chapman, S. and Ferraro, V. C. A.: A new theory of magnetic storms, *Terr. Magn. Atmosph. Elec.*, 36, 77–97, 1931.
- Chen, L. and Hasegawa, A.: A Theory of Long-period Magnetic Pulsations, 1. Steady State Excitation of Field Line Resonances, *J. Geophys. Res.*, 79, 1024–1032, 1974a.
- Chen, L. and Hasegawa, A.: A Theory of Long-Period Magnetic Pulsations 2. Impulse Excitation of Surface Eigenmode, *J. Geophys. Res.*, 79, 1033–1037, 1974b.
- Chisham, G., Lester, M., Milan, S. E., Freeman, M. P., Bristow, W. A., Grocott, A., McWilliams, K. A., Ruohoniemi, J. M., Yeoman, T. K., Dyson, P. L., Greenwald, R. A., Kikuchi, T., Pinnock, M., Rash, J. P. S., Sato, N., Sofko, G. J., Villain, J. P., and Walker, A. D. M.: A decade of the Super Dual Auroral Radar Network (SuperDARN): scientific achievements, new techniques and future directions, *Surv Geophys*, 28, 33–109, 2007.
- COESA: U.S. Standard Atmosphere, 1976 (NOAA Document S/T 76-1562), U. S. Government Printing Office, Washington, D. C., 1976.
- Cowley, S. W. H.: Magnetosphere-Ionosphere Interactions: A tutorial Review, American Geophysical Union, 2000.
- Cowley, S. W. H., Davies, J. A., Grocott, A., Khan, H., Lester, M., McWilliams, K. A., Milan, S. E., Provan, G., Sandholt, P., Wild, J. A., and Yeoman, T. K.: Solar wind-

magnetosphere-ionosphere interactions in the Earth's plasma environment, *Phil. Trans. R. Soc. Lond. A*, 361, 113–126, 2003.

Cowling, T. G.: *Magnetohydrodynamics*, Adam Hilger Ltd, 2nd edn., 1980.

Davies, K.: Doppler studies of the ionosphere with vertical incidence, *Proc. Inst. Rad. Engng*, 50, 94–95, 1962.

Davies, K., Watts, J. M., and Zacharisen, D. H.: A Study of F2-Layer Effects as Observed with a Doppler Technique, *J. Geophys. Res.*, 67, 601–609, 1962.

Dieminger, W., Goubau, G., and Zenneck, J.: Die Störungen der Ionosphäre, *Hochfrequenz. u. Elektroakust.*, 44, 2–17, 1934.

Dungey, J.: Interactions of solar plasma with the geomagnetic field, *Planetary and Space Science*, 10, 233–237, 1963.

Engebretson, M. J., Glassmeier, K.-H., and Stellmacher, M.: The dependence of high-latitude Pc5 wave power on solar wind velocity and on the phase of high-speed solar wind streams, *J. Geophys. Res.*, 103, 26,271–26,271, 1998.

Fenrich, F. R., Samson, J. C., Sofko, G., and Greenwald, R. A.: ULF high- and low-m field line resonances observed with the Super Dual Auroral Radar Network, *J. Geophys. Res.*, 100, 21 535–21 547, 1995.

Fenwick, R. C. and Villard, O. G.: Continuous Recordings of the Frequency Variation of the WWV-20 Signal after Propagation over a 4000-Km Path, *J. Geophys. Res.*, 65, 3249–3260, 1960.

Georges, T. M.: Ionospheric effects of atmospheric waves, ESSA Technical Report IER 57-ITSA 54, U. S. Department of Commerce., 1967.

Glassmeier, K.-H., Buchert, S., Motschmann, U., Korth, A., and Pedersen, A.: Concerning the generation of geomagnetic giant pulsations by drift-bounce resonance ring current instabilities, *Ann. Geophys.*, 17, 338–350, 1999.

- Glassmeier, K.-H., Klimushkin, D., Othmer, C., and Mager, P.: ULF Waves at Mercury: Earth, the giants, and their little brother compared, *Adv. Space Res.*, 33, 1875–1883, 2004.
- Greenwald, R. A., Weiss, W., Nielsen, E., and Thomson, N. P.: STARE: A new radar auroral backscatter experiment in northern Scandinavia, *Radio Sci.*, 13, 1021–1039, 1978.
- Greenwald, R. A., Baker, K. B., Dudeney, J. R., Pinnock, M., Jones, T. B., Thomas, E. C., Villain, J.-P., Cerisier, J.-C., Senior, C., Hanuise, C., Hunsucker, R. D., Sofko, G., Koehler, J., Nielsen, E., Pellinen, R., Walker, A. D. M., Sato, N., and Yamagishi, H.: DARN/SUPERDARN A global view of the dynamics of high-latitude convection, *Space Sci. Rev.*, 71, 761–796, 1995.
- Grocott, A.: Radar Observations of Convection in the Nightside High-Latitude Ionosphere, Ph.D. thesis, Department of Physics and Astronomy, University of Leicester, The University of Leicester, University Road, Leicester, LE1 7RH, 2002.
- Hanuise, C., Villain, J. P., Gresillon, D., Cabrit, B., Greenwald, R. A., and Baker, K. B.: Interpretation of HF radar ionospheric Doppler spectra by collective wave scattering theory, *Ann. Geophys.*, 11, 29–39, 1993.
- Harang, L.: Pulsations in an ionized region at a height of 650-800 km during the appearance of giant pulsations in the geomagnetic records, *Terr. Magn. Atmos. Elect.*, 44, 17–19, 1939.
- Hargreaves, J. K.: The upper atmosphere and solar terrestrial relations. An introduction to the aerospace environment., New York, NY (USA): Van Nostrand Reinhold Company, 1979.
- Hasegawa, H., Fujimoto, M., Phan, T.-D., Reme, H., Balogh, A., Dunlop, M. W., Hashimoto, C., and TanDokoro, R.: Cluster Detection of Rolled-up Kelvin-Helmholtz Vortices at the Magnetopause: Comparison with Simulations, *ISSS-7 Proceedings*, 2005.

- Hedin, A. E., Biondi, M. A., Burnside, R. G., Hemandez, G., Johnson, R. M., Killeen, T. L., Mazaudier, C., Meriwether, J. W., Salah, J. E., Sica, R. J., Smith, R. W., Spencer, N. W., Wickwar, V. B., and Viridi, T. S.: Revised global model of thermosphere winds using satellite and ground-based observations, *Journal of Geophysical Research-Space Physics*, 96, 7657–7688, 1991.
- Hughes, W. J.: The Effect of the Atmosphere and Ionosphere on Long Period Magnetospheric Micropulsations, *Planet. Space Sci.*, 22, 1157–1172, 1974.
- Hughes, W. J.: Hydromagnetic waves in the magnetosphere, in: *Solar-Terrestrial Physics*, edited by: Carovillano, R. L. and Forbes, J. M., D. Reidel Pub. Co., 1983.
- Hughes, W. J.: The magnetopause, magnetotail, and magnetic reconnection, in *Introduction to Space Physics*, ed. M. G. Kivelson and C. T. Russell, Cambridge University Press: New York., pp. 227–287, 1995.
- Hughes, W. J. and Southwood, D. J.: An Illustration of Modification of Geomagnetic Pulsation Structure by the Ionosphere, *J. Geophys. Res.*, 81, 3241–3247, 1976a.
- Hughes, W. J. and Southwood, D. J.: The screening of micropulsation signals by the atmosphere and ionosphere, *J. Geophys. Res.*, 81, 3234–3240, 1976b.
- Hunsucker, R. D. and Hargreaves, J. K.: *The High-Latitude Ionosphere and its Effects on Radio Propagation*, Cambridge University Press, 1st edn., 2003.
- Imber, S. M., Milan, S. E., and Hubert, B.: The auroral and ionospheric flow signatures of dual lobe reconnection, *Ann. Geophys.*, 24, 3115–3129, 2006.
- Institute, T. F. M.: The IMAGE Magnetometer Network, <http://www.space.fmi.fi/image/stations.html>, Last Checked: 20th October 2010, 2009.
- Jacobs, J. A., Kato, Y., Matsushita, S., and Troitskaya, V. A.: Classification of Geomagnetic Micropulsations, *J. Geophys. Res.*, 69, 180–181, 1964.
- JHUAPL: SuperDARN- Location of Radars, <http://superdarn.jhuapl.edu/fov/north.html>, Last Checked: 20th October 2010, 2009.

- Kallenrode, M.-B.: Space Physics: an Introduction to Plasmas and Particles in the Heliosphere and Magnetospheres, Springer-Verlag Berlin Heidelberg, 3rd edn., 2004.
- Khan, H. and Cowley, S. W. H.: Observations of the response time of high-latitude ionospheric convection to variations in the interplanetary magnetic field using EISCAT and IMP-8 data, *Ann. Geophys.*, 17, 1306–1335, 1999.
- King, J. H. and Papitashvili, N. E.: Solar wind spatial scales in and comparisons of hourly WIND and ACE plasma and magnetic field data, *J. Geophys. Res.*, 110, 1–8, 2005.
- Kivelson, M. G. and Pu, Z.-Y.: The Kelvin-Helmholtz instability on the magnetopause., *Planet. Space Sci.*, 32, 1335–1341, 1984.
- Kivelson, M. G. and Russell, C. T.: Introduction to Space Physics, Cambridge University Press, 3rd edn., 1997.
- Kivelson, M. G. and Southwood, D. J.: Coupling of global magnetospheric MHD eigenmodes to field line resonances, *J. Geophys. Res.*, 91, 4345–4351, 1986.
- Kivelson, M. G. and Southwood, D. J.: Hydromagnetic Waves and the Ionosphere, *Geophys. Res. Lett.*, 15, 1271–1274, 1988.
- Kivelson, M. G., Etcheto, J., and Trotignon, J. G.: Global compressional oscillations of the terrestrial magnetosphere: the evidence and a model, *J. Geophys. Res.*, 89, 9851–9856, 1984.
- Klostermeyer, J. and Röttger, J.: Simultaneous geomagnetic and ionospheric oscillations caused by hydromagnetic waves, *Planet. Space Sci.*, 24, 1065–1071, 1976.
- Lee, D.-H. and Lysak, R. L.: Magnetospheric ULF Wave Coupling in the Dipole Model: the Impulsive Excitation, *J. Geophys. Res.*, 94, 17,097–17,103, 1989.
- Lester, M., Chapman, P. J., Cowley, S. W. H., Crooks, S. J., Davies, J. A., Hamadyk, P., McWilliams, K. A., Milan, S. E., Parsons, M. J., Payne, D. B., Thomas, E. C.,

- Thornhill, J. D., Wade, N. M., Yeoman, T. K., and Barnes, R. J.: Stereo CUTLASS-A new capability for the SuperDARN HF radars, *Annales Geophysicae*, 22, 459–473, 2004.
- Luhr, H.: The IMAGE magnetometer network, *STEP International Newsletter*, 4, 4–6, 1994.
- Mann, I. R. and Wright, A. N.: Diagnosing the excitation mechanisms of Pc5 magnetospheric flank waveguide modes and FLRs, *Geophys. Res. Lett*, 26, 2609–2612, 1999.
- Matsushita, S. and Saito, T.: Geomagnetic pulsations associated with sudden commencements and sudden impulses (Morphological behavior of damped type geomagnetic pulsations associated with storm sudden commencements and sudden impulses), *Planet. Space Sci.*, 15, 573–587, 1967.
- Maxwell, J. C.: On Physical Lines of Force, *Philosophical Magazine. The London, Edinburgh and Dublin Philosophical Magazine and Journal of Science (Fourth Series)*, XXV., 1861.
- McDiarmid, D. R.: Simultaneous observation of a travelling vortex structure in the morning sector and a field line resonance in the postnoon sector, *J. Geophys. Res.*, 99, 8891–8904, 1994.
- McWilliams, K. A.: Ionospheric Signatures of Dayside Reconnection Processes, Ph.D. thesis, Department of Physics and Astronomy, University of Leicester, The University of Leicester, University Road, Leicester, LE1 7RH, 2001.
- Menk, F. W.: Characterization of ionospheric Doppler oscillations in the Pc 3-4 and Pi2 magnetic pulsation frequency range, *Planet. Space Sci.*, 40, 495–507, 1992.
- Menk, F. W., Cole, K. D., and Devlin, J. C.: Associated geomagnetic and ionospheric variations, *Planet. Space Sci.*, 31, 569–572, 1983.

- Milan, S. E., Yeoman, T. K., Lester, M., Thomas, E. C., and Jones, T. B.: Initial backscatter occurrence statistics from the CUTLASS HF radars, *Annales Geophysicae*, 15, 703–718, 1997.
- Newton, I.: *Philosophiæ Naturalis Principia Mathematica*, Halley, 1686.
- Nielsen, E.: Mean velocities measured with the double pulse technique, *Ann. Geophys.*, 22, 3531–3536, 2004.
- Nishida, A.: Ionospheric Screening Effect and Storm Sudden Commencement, *J. Geophys. Res.*, 69, 1861–1874, 1964.
- Parker, E. N.: Dynamics of the Interplanetary Gas and Magnetic Fields, *Astrophysical Journal*, 128, 664–675, 1958.
- Peredo, M., Slavin, J. A., Mazur, E., and Curtis, S. A.: Three-dimensional position and shape of the bow shock and their variation with Alfvénic, sonic and magnetosonic Mach numbers and interplanetary magnetic field orientation, *Journal of Geophysical Research-Space Physics*, 100, 7907–7916, 1995.
- Poole, A. W. V. and Sutcliffe, P. R.: Mechanisms for observed total electron content pulsations at mid latitudes, *J. Atmos. Terr. Phys.*, 49, 231–236, 1987.
- Poole, A. W. V. and Sutcliffe, P. R.: The Relationship Between ULF Geomagnetic Pulsations and Ionospheric Doppler Oscillations: Derivation of a Model, *J. Geophys. Res.*, 93, 14,656–14,664, 1988.
- Primdahl, F.: The fluxgate magnetometer, *J. Phys. E: Sci. Instrum.*, 12, 241–253, 1979.
- Provan, G. and Yeoman, T. K.: A comparison of field-line resonances observed at the Goose Bay and Wick radars, *Annales Geophysicae*, 15, 231–235, 1997.
- Rietveld, M. T., Kohl, H., Kopka, H., and Stubbe, P.: Introduction to ionospheric heating at Tromsø—Experimental overview, *J. Atmos. Terr. Phys.*, 55, 577–599, 1993.

- Rietveld, M. T., Wright, J. W., Zabolin, N., and Pitteway, M. L. V.: The Tromsø Dyna-sonde, *Polar Science*, 2, 55–71, 2008.
- Rishbeth, H. and Garriott, O. K.: Relationship between simultaneous geomagnetic and ionospheric oscillations, *Radio Sci.*, 68D, 339–343, 1964.
- Ruohoniemi, J. M. and Baker, K. B.: Large-scale imaging of high-latitude convection with Super Dual Auroral Radar Network HF radar observations, *J. Geophys. Res.*, 103, 20,797–20,811, 1998.
- Ruohoniemi, J. M., Greenwald, R. A., Baker, K. B., and Samson, J. C.: HF Radar Observations of Pc 5 Field Line Resonances in the Midnight/Early Morning MLT Sector, *J. Geophys. Res.*, 96, 15,697–15,710, 1991.
- Samson, J. C.: Geomagnetic pulsations and plasma waves in the Earth's magnetosphere. In Jacobs, J. A. (ed.), vol. 4, London: Academic Press, 481-592, 1991.
- Samson, J. C., Harrold, B. G., Ruohoniemi, J. M., Greenwald, R. A., and Walker, A. D. M.: Field line resonances associated with MHD waveguides in the magnetosphere, *Geophys. Res. Lett.*, 19, 441–444, 1992.
- Sandholt, P. E., Farrugia, C. J., Stauning, P., and Cowley, S. W. H.: Auroral signature of lobe reconnection, *Geophys. Res. Lett.*, 23, 1725–1728, 1996.
- Sciffer, M. D. and Waters, C. L.: Propagation of ULF waves through the ionosphere: Analytic solutions for oblique magnetic fields, *J. Geophys. Res.*, 107, 1297–1310, 2002.
- Sciffer, M. D., Waters, C. L., and Menk, F. W.: A numerical model to investigate the polarisation azimuth of ULF waves through an ionosphere with oblique magnetic fields, *Ann. Geophys.*, 23, 3457–3471, 2005.
- Siebert, M.: Geomagnetic Pulsations with Latitude-Dependent Periods and their Relation to the Structure of The Magnetosphere, *Planet. Space Sci.*, 12, 137–147, 1964.

- Smith, E. J., Tsurutani, B. T., and Rosenberg, R. L.: Observations of the Interplanetary Sector Structure up to Heliographic Latitudes of  $16^\circ$ : Pioneer 11, *J. Geophys. Res.*, 83, 717–724, 1978.
- Southwood, D. J.: The behaviour of ULF waves and particles in the magnetosphere, *Planet. Space Sci.*, 21, 53–65, 1973.
- Southwood, D. J.: Some Features of Field Line Resonances in the Magnetosphere, *Planet. Space Sci.*, 22, 483–491, 1974.
- Southwood, D. J.: A general approach to low-frequency instability in the ring current plasma, *J. Geophys. Res.*, 81, 3340–3348, 1976.
- Southwood, D. J. and Hughes, W. J.: Theory of hydromagnetic waves in the magnetosphere, *Space Sci. Rev.*, 35, 301–366, 1983.
- Southwood, D. J. and Kivelson, M. G.: The Effect of Parallel Inhomogeneity on Magnetospheric Hydromagnetic Wave Coupling, *J. Geophys. Res.*, 91, 6871–6876, 1986.
- Spreiter, J. R., Summers, A. L., and Alksne, A. Y.: Hydromagnetic flow around the magnetosphere, *Planet. Space Sci.*, 14, 223–250, 1966.
- Stewart, B.: On the Great Magnetic Disturbance Which Extended from August 28 to September 7, 1859, as Recorded by Photography at the Kew Observatory, *Phil. Trans. R. Soc. Lond. A*, 151, 423–430, 1861.
- Stone, E. C., Frandsen, A. M., Mewaldt, R. A., Christian, R. E., Marglies, D., Ormes, J. F., and Snow, F.: The Advanced Composition Explorer, *Space Sci. Rev.*, 86, 1–22, 1998.
- Sutcliffe, P. R. and Poole, A. W. V.: Ionospheric Doppler and electron velocities in the presence of ULF waves, *J. Geophys. Res.*, 94, 13,505–13,514, 1989.
- Sutcliffe, P. R. and Poole, A. W. V.: The relationship between ULF Geomagnetic Pulsations and Ionospheric Doppler Oscillations: Model Predictions, *Planet. Space Sci.*, 38, 1581–1589, 1990.

- Tamao, T.: Transmission and Coupling Resonance of Hydromagnetic Disturbances in the Non-uniform Earth's Magnetosphere, *Sci. Rep. Tohoku Univ., Ser. 5*, 17, 43–72, 1965.
- Tanner, B. K.: Introduction to the Physics of Electrons in Solids, Cambridge University Press, 3rd edn., 1995.
- Titheridge, J. E.: Ionogram Analysis with the Generalized Program POLAN, Report UAG-93, World Data Center A for Solar-Terrestrial Physics. U.S. Dept. of Commerce, Boulder. CO 80301, USA., pp. 1–189, 1985.
- Villain, J. P., André, R., Hanuise, C., and Grésillon, D.: Observation of the high latitude ionosphere by HF radars: Interpretation in terms of collective wave scattering and characterization of turbulence, *J. Atmos. Terr. Phys.*, 58, 943–958, 1996.
- Voelker, H.: Observations of Geomagnetic Pulsations Pc3,4 and Pi2 at Different Latitudes, *Ann. Geophys.*, 24, 245–252, 1968.
- Walker, A. D. M., Ruohoniemi, J. M., Baker, K. B., and Greenwald, R. A.: Spatial and temporal behavior of ULF pulsations observed by the Goose Bay HF radar, *J. Geophys. Res.*, 97, 12,187–12,202, 1992.
- Waters, C. L.: Corrections to Equations in: A numerical model to investigate the polarisation azimuth of ULF waves through an ionosphere with oblique magnetic fields, [http://plasma.newcastle.edu.au/~colin/ionosn/eqn\\_corrections.pdf](http://plasma.newcastle.edu.au/~colin/ionosn/eqn_corrections.pdf), Last Checked: 20th October 2010, 2006.
- Waters, C. L. and Sciffer, M. D.: Field line resonant frequencies and ionospheric conductance: Results from a 2-D MHD model, *J. Geophys. Res.*, 113, 1–10, 2008.
- Waters, C. L., Yeoman, T. K., Sciffer, M. D., and Ponomarenko, P.: Modulation of radio frequency signals by ULF waves, *Ann. Geophys.*, 25, 1113–1124, 2007.
- Watts, J. M. and Davies, K.: Rapid frequency analysis of fading radio signals, *J. Geophys. Res.*, 65, 2295–2301, 1960.

- Wing, S., Newell, P. T., and Meng, C.-I.: Cusp Modeling and Observations at Low Altitude, *Surveys in Geophysics*, 26, 341–367, 2005.
- Wright, A. N.: Dispersion and Wave Coupling in inhomogenous MHD Waveguides, *J. Geophys. Res.*, 99, 159–167, 1994.
- Wright, D. M.: HF Doppler Observations of ULF Waves: System Development and High Latitude Results, Ph.D. thesis, University of Leicester, University Road, Leicester, LE1 7RH, 1996.
- Wright, D. M. and Yeoman, T. K.: High-latitude HF Doppler observations of ULF waves: 2. Waves with small spatial scale sizes, *Annales Geophysicae*, 17, 868–876, 1999a.
- Wright, D. M. and Yeoman, T. K.: CUTLASS observations of a high-m ULF wave and its consequences for the DOPE HF Doppler sounder, *Ann. Geophys.*, 17, 1493–1497, 1999b.
- Wright, D. M. and Yeoman, T. K.: High resolution bistatic radar observations of ULF waves in artificially generated backscatter, *Geophys. Res. Lett.*, 26, 2825–2828, 1999c.
- Wright, D. M., Yeoman, T. K., and Chapman, P. J.: High-latitude HF Doppler observations of ULF waves. 1. Waves with large spatial scale sizes, *Ann. Geophys.*, 15, 1548–1556, 1997.
- Wright, D. M., Yeoman, T. K., and Davies, J. A.: A comparison of EISCAT and HF Doppler observations of a ULF wave, *Ann. Geophys.*, 16, 1190–1199, 1998.
- Wright, D. M., Yeoman, T. K., Baddeley, L. J., Davies, J. A., Dhillon, R. S., Lester, M., Milan, S. E., and Woodfield, E. E.: High resolution observations of spectral width features associated with ULF wave signatures in artificial HF radar backscatter, *Ann. Geophys.*, 22, 169–182, 2004.
- Yeoman, T. K., Wright, D. M., and Chapman, P. J.: High-latitude observations of ULF waves with large azimuthal wavenumbers, *J. Geophys. Res.*, 105, 5453–5462, 2000.

Yukimatu, A. S. and Tsutsumi, M.: A new SuperDARN meteor wind measurement: Raw time series analysis method and its application to mesopause region dynamics, *Geophys. Res. Lett.*, 29, 1–4, 2002.

Zhang, D. Y. and Cole, K. D.: Formulation and computation of hydromagnetic wave penetration into the equatorial ionosphere and atmosphere, *J. Atmos. Terr. Phys.*, 57, 813–819, 1995.

Zhang, X. Y., Zong, Q. G., Yang, B., and Wang, Y. F.: Numerical simulation of magnetospheric ULF waves excited by positive and negative impulses of solar wind dynamic pressure, *Science in China Series E: Technological Sciences*, 52, 2886–2894, 2009.